University of Strathclyde
Department of Mechanical & Aerospace Engineering

On the evaluation of high temperature creep-fatigue responses of structures

Daniele Barbera

A thesis presented in fulfilment of the requirements
for the degree of Doctor of Philosophy

2017

Declaration of author's rights

Daniele Barbera
March 1, 2017

Acknowledgements

I would like to say thanks to my supervisors Dr Haofeng Chen and Professor James Boyle. I appreciated your support and help. Your guidance over the past 3 years has been invaluable in making me a good researcher and hopefully a good engineer, even if sometime I know that *"I should better understand the concepts of solid mechanics"*. Thanks so much I wish you all the best.

Considerable thanks also go to Dr Yevgen Gorash from WARC, for his advices and support over the years. I look forward to keeping in touch with you once my studies are completed.

I would like also to thanks all the SILA group mates, Dario, Graeme, Ross and Cho. Thanks for your friendship and support given during this long period together. A special thanks to Dario, for all the time that you dedicated to me when everything was not very good, and for your total and unconditioned friendship. Even if I will not get this degree, I got a very good friend. Thanks also to all the friends outside my research group in particular David, Jonathan, Lorenzo, Chiara, Marilena and Annalisa. I enjoyed the work also because of you all, thanks for the long talks, coffes and metafit/boxe classes!

My sincerest thanks go to my beloved Francesca because all my achievements are the results of your love. I will love you forever despite any adversity.

Last but not least my family, for their support during all my life, for their love and for being capable of trusting this boy that loved science, rockets and computers.

To Marisa and Mario,
to their strength and resilience

For a successful technology,
reality must take precedence over public relations,
for nature cannot be fooled.
Richard Feynman, Rogers Commission Report(1986)

Abstract

This thesis details the research and development steps undertaken to improve and enhance the Linear Matching Method Framework (LMMF) for high temperature structural integrity assessment. Firstly, a more accurate interpolation method is developed to calculate the revised yield stress, which is necessary to calculate the creep rupture limit. Convergence issues are also investigated to improve the numerical difficulties often suffered by the "fluctuating" revised yield stress. Secondly, the extended Direct Steady Cycle Analysis (eDSCA) is used to solve two complex case studies and a comprehensive theoretical study is undertaken on the effect of combined creep and cyclic plasticity. This subroutine is enhanced by adding many new features, including the possibility to calculate the fatigue damage using only few tensile constants. Multiple creep dwells within the load cycle can be considered and improvements are made to the cyclic loop construction. In order to make the eDSCA more accurate for creep damage assessment, the stress modified ductility exhaustion method is implemented combining the advantages of both stress and strain based methods. Thirdly, several case studies on creep-fatigue interaction are discussed thanks to the flexibility of the LMMF including the detrimental effect of creep-ratchetting. Furthermore, a new potentially dangerous mechanism involving the sudden accumulation of plastic strain during the creep dwell is identified and studied by numerical means.

Publications

Journal Papers

Barbera, D, Chen, H & Liu, Y 2017, 'Advances on creep-fatigue damage assessment in notched components' Fatigue & Fracture of Engineering Materials & Structures, accepted for publication

Barbera, D, Chen, H & Liu, Y 2016, 'Creep-fatigue life assessment of a pipe intersection with a dissimilar metal weld by Linear Matching Method' Applied Mechanics and Materials, vol 853, pp. 366-371, 10.4028/www.scientific.net/AMM.853.366.

Giugliano, D, **Barbera, D** & Chen, H 2016, 'Effect of fiber cross section geometry on cyclic plastic behaviour of continuous fiber reinforced aluminum matrix composites' European Journal of Mechanics - A/Solids, Vol. 61, pp. 35-46, 2017.

Barbera, D, Chen, H & Liu, Y 2016, 'Creep-fatigue behaviour of aluminium alloy-based metal matrix composite' International Journal of Pressure Vessels and Piping.Apr 30;139:159-72, 10.1016/j.ijpvp.2016.02.004

Barbera, D, Chen, H & Liu, Y 2015, 'On the creep fatigue behavior of Metal Matrix Composites' Procedia Engineering, vol 130, pp. 1121-1136, 10.1016/j.proeng.2015.12.277

Barbera, D, Chen, H & Liu, Y 2015, 'On creep fatigue interaction of components at elevated temperature' Journal of Pressure Vessel Technology, Transaction of the ASME, 138(4), pp. 041403-1 - 041403-8

Barbera, D & Chen, H 2015, 'Creep rupture assessment by a robust creep data interpolation using the linear matching method' European Journal of Mechanics - A/Solids, vol 54, pp. 267-279, 10.1016/j.euromechsol.2015.07.003

Conference Papers

Barbera, D, Chen, H & Liu, Y , 2016,'Review and case study of the linear matching method framework for structural integrity assessment', ASME Pressure Vessels and Piping Conference, July 17-21, Vancouver, Canada.

Barbera, D, Chen, H & Liu, Y , 2016, 'Creep fatigue life assessment of a pipe intersection with dissimilar material joint by Linear Matching Method', International Symposium on Structural Integrity (ISSI-2016), May 26-30, Tianjin, China.

Barbera, D, Giugliano, D, Chen, H & Liu, Y , 2015, 'Micromechanical modeling on plastic and creep behaviors of MMCs using the Linear Matching Method', 5th International Workshop on Direct Methods, University of Oxford, Department of Engineering Science, September 6-8th, Oxford, UK.

Contents

List of figures

List of tables

Nomenclature

α	Multiaxial factor for creep damage model
Δt	Dwell time
$\Delta\rho_{ij}^{r}$	Varying residual stress field increment
$\Delta\theta$	Temperature increment
$\Delta\varepsilon_{ij}^{p}(x,t_n)$	Plastic strain increment
$\Delta\bar{\varepsilon}^{c}$	Creep strain increment
$\Delta\varepsilon_r$	Ratchet strain increment per cycle
$\Delta\varepsilon_{ij}^{c}$	Associated compatible strain increment
$\frac{\Delta\sigma}{2}$	Stress amplitude
$\dot{\varepsilon}_{ij}^{c}$	Strain rate
${\varepsilon_p}^{L}$	Plastic strain during loading
ε_c	Creep strain during creep dwell
$\dot{\varepsilon_c}$	Creep strain rate
${\varepsilon_p}^{UL}$	Plastic strain during unloading loading
${\epsilon_f}^{*}$	Multiaxial creep ductility
ϵ_f	Uniaxial creep ductility
θ_0	Reference temperature
μ	Shear modulus
λ	load multiplier
λ_{creep}	Creep rupture limit multiplier
λ_{cavity}	Cavity spacing
$\bar{\rho}_{ij}^{c}(x)$	Constant residual for creep rupture stress field
$\bar{\rho}_{ij}(x)$	Constant residual stress field
$\rho_{ij}^{r}(x,t)$	Changing residual stress field
σ_c	Creep rupture stress by LMM
σ_y	Yield stress
σ_y^{r}	Revised yield stress
$\hat{\sigma}_{ij}$	Elastic stress field
$\hat{\sigma}_{ij}^{\theta}$	Elastic thermal stress field
$\hat{\sigma}_{ij}^{P}$	Elastic mechanical stress field
σ_{ij}^{in}	Scaled elastic stress component
$\sigma_y^{R}(x,t_n)_m$	Iterative von Mises yield stress
σ_m	Mean stress
σ_1	Maximum principal stress
$\bar{\sigma}$	Equivalent stress
σ_r	Creep rupture stress
σ_{ref}^{R}	Creep rupture reference stress
σ_{ref}	Reference stress
C_{lm}	Larson Miller constant
$\dot{r}$	Cavity radius growth rate
r_0	Initial cavity radius
T	Temperature
T_0	Characteristic temperature
t_f	Time to fracture
x_i	integration point position

Acronyms

AGR	Advanced Gas cooled Reactor
CDM	Constitutive Damage Modelling
CFCI	Creep Fatigue Crack Initiation
CGF	Creep Cavity Factor
CTE	Coefficient of Thermal Expansion
CRF	Creep Ratcheting Failure
DCA	Direct Cyclic Analysis
DE	Ductility Exhaustion
DMW	Dissimilar Metal Weld
DSCA	Direct Steady Cycle Analysis
eDSCA	extended Direct Steady Cycle Analysis
EPP	Elastic Perfect Plastic
ES	Elastic Shakedown
LCF	Low Cycle Fatigue
LM	Liu-Murakami
LMM	Linear Matching Method
LMMF	Linear Matching Method Framework
LPD	Load Point Displacement
MDF	Multiaxial Ductility Factor
MM	Median Method
MMC	Metal Matrix Composite
MMM	Modified Mitchell's Method
MUSM	Modified Universal Slopes Method
N_{CF}	Number of cycles to fail for creep-fatigue crack initiation
N_{CR}	Number of cycles to fail for creep-ratcheting
N_f	Number of cycles to failure
P_{LM}	Larson-Miller Parameter
P_{MH}	Manson-Haferd Parameter
P_{OSD}	Orr-Sherby-Dorn Parameter
PS	Plastic Shakedown
RK	Robotov-Kachanov
RF	Ratcheting Failure
RO	Ramberg Osgood
SENB	Single Edge Notched Bar
SBS	Step-by-Step analysis
SMDE	Stress Modified Ductility Exhaustion
TF	Time Fraction
USM	Universal Slope Method

Chapter 1

Introduction

1.1 Structural integrity and power industry

The UK's greenhouse gas emissions are estimated to be 514 $MtCO_2e$ per year, and it is committed to reduce this to 371.2 $MtCO_2e$ by 2020 and to 159 $MtCO_2e$ by the end of 2050 [1]. The use of nuclear power has been identified as a part of the solution to the decarbonisation challenge by combating global warming and preserving a cleaner environment for future generations. However, the ageing of nuclear power plants such as the UKs Advanced Gas-cooled Reactor fleet requires costly decommissioning after a very long operating life. This leads to the necessity of a newer, more efficient and safer nuclear fleet to supply reliable cost effective and carbon-free electricity. In the scenario of an ageing and more reliable new nuclear power plant fleet, structural integrity plays an important role, for both the old and new generation of the UK's nuclear power station fleets. Due to the necessity of supporting national energy demand, the AGR fleet life has recently been extended up to 2030. In this additional operation phase, monitoring the structures and assessing crack initiation in aged structures such as boilers is mandatory, since due to their design, replacement is not practical. The safe operation and end of life of these nuclear power plants have a crucial impact not only on the national demand for electricity but also on financial investments of several industries related to the nuclear power generation in the UK. At least four different types of reactors have been selected to be built in the UK (i) AP1000 (Westinghouse), (ii) ABWR (Hitachi-GE), (iii) SMR (NuGen) and (iv) EPR (EDF Energy). Operating temperatures and load can vary in each design, and there is also a growing interest in High-Temperature Reactors capable of reaching temperatures of up to $1000°C$.

Structural integrity assessment has been a crucial aspect of conventional and nuclear power industries and has a remarkable impact on the latter. Subsequent efforts have been made to solve new emerging issues, since the beginning of the commercial nuclear power era, with the Calder Hall grid connection in 1956. Structure integrity has played a major role due to the increasing ageing of the power plants, and the ageing of material increased concern over the safety of reactor components. Different problems due to the ageing have been encountered, such as the Reactor Pressure Vessel embrittlement for the UK Magnox reactor, the graphite core cracking and the crack initiation of the boiler weldment [2] in the AGR.

International design codes including ASME Boiler and Pressure Vessel Code (NH)

[3] and the UK's R5 high-temperature assessment procedure [4] are used to develop and assess power plant components and are always under development to improve their capabilities. However, these design codes have limitations in anticipating unknown phenomena, such as the remarkable material degradation or the effect of secondary loads on the fatigue life and stress corrosion. Furthermore, they are rule-based methods and rely on elastic finite element analyses that may produce very conservative results. Although inelastic analyses may be used to relax the conservatism mentioned above, they are computationally inefficient and not always practicable. This can be an issue when a life extension program is going to be undertaken, which requires a much deeper understanding of all the possible failure mechanisms. For this purpose not only is a detailed material description necessary, but it is also essential to have a more accurate, robust and efficient methodology for calculating the structural response under complex cyclic loading conditions.

In recent decades an alternative approach, which uses a numerical direct method, has been developed and tested to solve different engineering problems. It has been capable of generating a sequence of parameters necessary to evaluate the response of a structure subjected to severe cycling loading conditions. The Linear Matching Method (LMM) has been developed to calculate, in the most efficient way, the cyclic plastic response of a structure subjected to a cyclic thermal and mechanical load. It was demonstrated to be capable of calculating shakedown, ratchetting and plastic collapse limits, more efficiently than other numerical procedures such as the Direct Cyclic Analysis (DCA) for a broad range of problem [5–9].

1.2 High temperature structures

High-temperature structures will play a major role for power industry in the short and long term period. Depending on the operating conditions and the environmental effects several failure mechanisms are possible. Structures such as pressure vessels, piping, welds, turbine blades or protective coating are exposed to complex cyclic loading histories during their operating life. The aforementioned complex scenario makes challenging the assessment of both new and ageing structures. Furthermore, due to design and manufacturing requirements, these structures have grooves or changes of thickness and in many cases also the presence of multi-material joints. These characteristics introduce stress concentrations and material mismatch, which pose a serious danger to the integrity of the components. Due to high temperature and cyclic loading creep-fatigue cracking is possible and must be assessed. Fatigue cracking is known to start from the surface of the part, and the damage propagates in a transgranular way. The creep damage instead initiates in the material, developing in an intergranular way. When particular loading conditions are considered, the creep and fatigue damage interaction reduces the life of the component remarkably. Examples of structures that have suffered from creep-fatigue cracking are present in UK's AGR experience. The superheater tailpipe welds, shown in Figure 1.1, have experienced this kind of failure since the late 1980s. The component was designed for a 35-year service life and up to 33 cold shutdowns. The dwell times were estimated between 8000 and 12500 hours, with a start of creep dwell at 170 MPa. All the observations done in this case study by [10] confirmed the importance of creep-fatigue interaction on the component integrity.

The crack has initiated between the parent and heat affected zone (Figure 1.1). In Figure 1.1 it is shown how the creep damage (cracks inner in the component) interacted with the fatigue crack started from the external surface. Furthermore, fatigue crack is distinguishable from creep cracking due to the absence of any oxidation layer in the latter one.

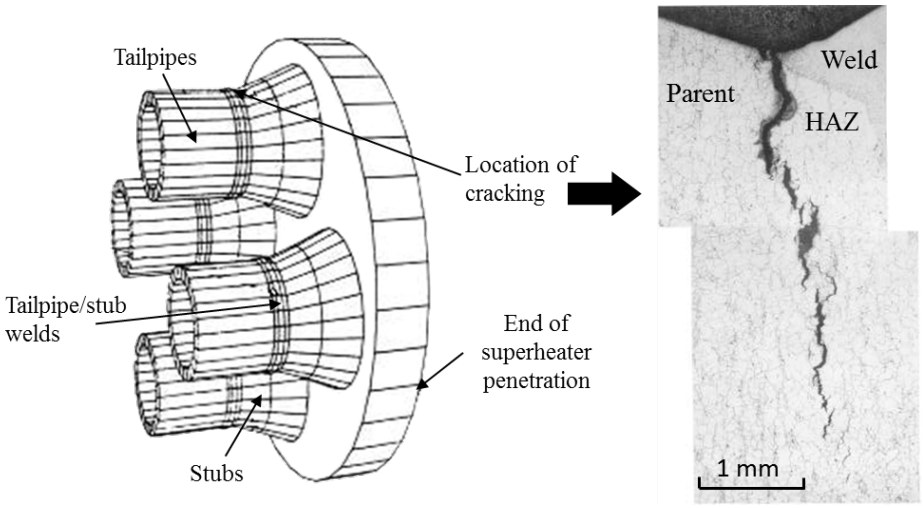

Figure 1.1: Cracking in superheater tailpipe weld type 316H [10].

Another component that demonstrated the importance of creep-fatigue interaction assessment is the boiler tube plate and the steam boiler header. Due to a particular loading condition, the ligaments between the holes in the boiler tube plate (Figure 1.2) experienced severe thermal cycling. This phenomenon occurred during start-up and shutdown with a minor intermediate thermal cyclic during the boiler operation. Critical creep dwell has been identified, with a start of the creep dwell at 302 MPa at a maximum temperature of $550°C$ for 16 hours.
Instead, the reheat cracking has been observed in the nozzle weld of the steam boiler header (Figure 1.2). It has been a very challenging issue for this type of component. This mechanism is defined as a creep driven cracking, which occurs when welding residual stresses relax during the creep dwell. However, to make it possible for the reheat cracking to occur in 316H weld, other effects were also investigated. It has been identified by Spindler [11] that the multiaxial stress state is capable of reducing the material creep ductility up to on the order of magnitude. This has a significant impact on the assessment done, which was based on the uniaxial creep ductility, producing an overly optimistic result. This last example further explains how it is important to accurately simulate the stress state of a component, and how this has a substantial impact on the life assessment prediction.

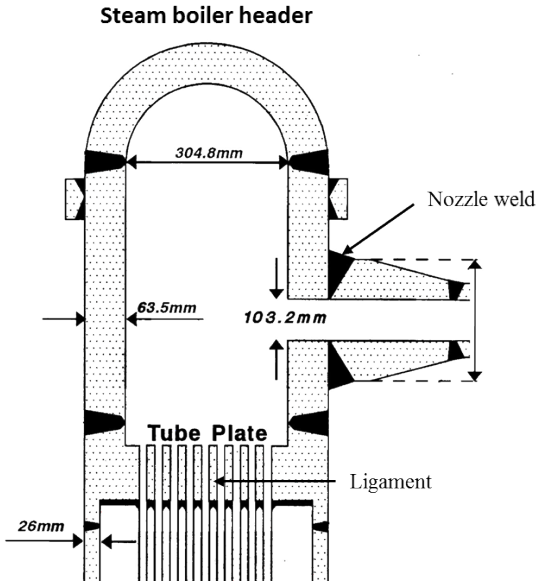

Figure 1.2: Critical locations for creep-fatigue interaction of the AGRs Steam Boiler header and tube plate [11].

These examples highlight the importance of accurately estimating the fatigue and creep damage occurring in a component subjected to severe thermal and cyclic mechanical loads. To produce an accurate assessment of both the creep and cyclic plastic response should be quantified. However, depending on the load case their interaction must be considered by empirical rule based approach provided by design codes or by performing numerical analyses. This latter approach is convenient to relax the conservatism of design procedures, or to evaluate specific non-linear phenomena. The efforts done so far to improve creep-fatigue assessment method will be crucial for the successful design and operation of GEN IV nuclear reactors. An example of GEN IV high temperature reactor is the Sodium Fast Reactor (SFR), which is schematically represented in Figure 1.3. Many components are expected to experience high temperature cyclic load due to the changes of pressure and temperature during normal operation, start-up and shut-down. Over all the possible failure mechanisms, two are the most likely to occur, creep-fatigue damage and high temperature ratchetting. These failure mechanisms are very complex due to the nature of the load applied, leading to complex interaction between creep and fatigue.

In this future scenario design code needs to be coupled to efficient and robust numerical procedure to further validate the accuracy of the assessment. In the last decade, remarkable efforts have been made to accurately represent the viscous and plastic behaviour of materials subjected to cyclic load conditions at high temperatures. In addition to this, numerous research works on accurate creep damage modelling were conducted [12–15] by implementing the Continuum Damage Mechanics (CDM) approach in finite element analyses. However, few researchers have concentrated on the creep-fatigue interaction and damage prediction using all the aforementioned techniques 15. The use of these full inelastic analyses safely reduces the conservatism of rule based methods. Despite this, they require numerous and precisely calibrated material parameters in order to guarantee accurate results. Moreover, they have a high

computational cost, especially when 3D finite element models are considered. In order to assess the stabilised response of a structure, the Direct Cyclic Analysis (DCA) has recently been implemented within the commercial finite element software, ABAQUS [16]. This numerical method is capable of obtaining the stabilized cyclic response in an iterative way by using a combination of Fourier series and time integration of the non-linear material response. However, it introduces numerical errors and convergence problems, meaning the DCA is not always a viable solution. In order to fill the gap between material science and industrial practical problems, direct methods such as the Linear Matching Method have been adopted.

The Linear Matching Method (LMM) represents an alternative to those full inelastic analyses. The LMM is a numerical procedure based on direct methods, which allow to calculate the cyclic response of a structure without the necessity to consider complex constitutive equations. The key capability of this method is to accurately calculate the constant and varying residual stress field occurring within the structure due to the cyclic plasticity or creep behaviours. The LMM has already been shown to provide an accurate, and less conservative solutions on components operating under cyclic loads [17–20].

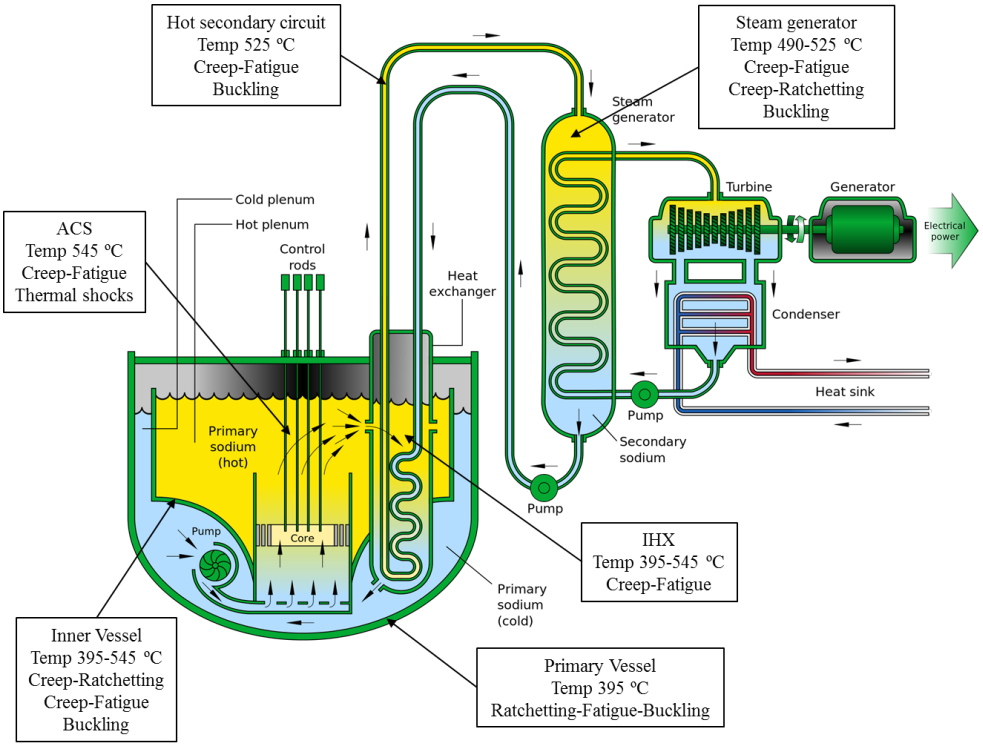

Figure 1.3: Expected location and damage modes in a SFR type GEN IV reactor (source: Wikipedia).

1.3 Objectives and scopes

The Linear Matching Method has been demonstrated to be a useful tool for structural assessment of industrial components, in particular for the power industry sector. Fur-

thermore, several industry partners such as EDF Energy and Siemens UK expressed their interest in developing the LMM for high-temperature creep assessment. Three key issues need to be investigated to deliver the largest impact to the UK's industrial and academic community.

The first is about improving the numerical procedure for the creep rupture limit assessment, based on the revised yield stress concept. This method, despite its effectiveness, still does not consider real experimental results. This is a barrier for the use of LMM for the creep rupture limit calculation. By replacing the over conservative procedure based on the shakedown reference stress concept currently available in the R5 a large dissemination of the method is expected. The second issue is about testing and further developing the extended Direct Steady Cyclic Analysis (eDSCA). The present eDSCA numerical procedure has not been standardised, and still requires many modifications. Furthermore, it has been used for simple loading cases and only for relatively simple problems. Many questions are still open and need an answer to allow this procedure to be fully implemented in the LMM plug-in. This is also requested by many industrial partners such as EDF Energy. The final issue relates to the assessment of particular failure mechanisms that involves high temperature creep dwell. The impact of creep is very complex, and it is capable of generating complex stress redistribution within the component. This issue is crucial for the design of new components, which are intended to operate at very high temperature. However, it is also necessary for particular extreme loading conditions that can occur in emergency/accident scenario.

By taking into account these issues, this project has the following objectives:

1. Create a new algorithm to extrapolate and interpolate creep rupture stresses from real experimental data. This procedure will fully replace the present strategy, and also convergence issues related to the fluctuating revised yield stress will be sorted out. Such a method will be capable of providing a more accurate creep rupture limit than the actual practice in the UK's R5 procedure. This will improve the robustness of the assessment delivered, relaxing the conservatism present in the current design practice.

2. Consider complex case studies, varying the cyclic loading history, testing several creep and fatigue damage interaction rules and also evaluate multi-materials problems. The accuracy of the method in predicting the stress state and the stress level will be tested, and improvements will be delivered as well. Several creep damage criteria will also be considered and implemented within the eDSCA. The creep ductile exhaustion and stress modified ductile exhaustion methods, which are currently adopted by EDF Energy, will be applied and tested. A comparison will be made between the LMM predictions and the real creep-fatigue endurance. The procedure will be modified to consider multiple creep dwells within the cycle, with particular attention to intermediate and compressive creep dwell.

3. By adopting the LMM and other numerical procedures, new insights into the understanding of failure mechanisms occurring at high temperature will be delivered. Also, a better understanding of creep-fatigue interaction and creep-ratchetting will be presented within this work.

1.4 Outline of the Dissertation

This thesis is composed of 8 chapters, each dealing with a specific topic. Chapter 2 gives an overview of the effect of high temperature and cyclic mechanical load on structural design. This includes the effect cyclic plasticity and creep on structure's behaviour. It also examines the high-temperature design procedure, comparing in first instance UK's R5 and ASME NH codes. In the same chapter, the LMM Framework is introduced showing its capabilities for high-temperature assessment, and a numerical example is provided. Chapter 3 discusses the new method developed within this PhD project for creep rupture limit calculation. A robust creep rupture data interpolation algorithm is formulated and implemented within the LMM. A benchmark study is presented for a 3D plate with an hole subjected to cyclic thermal and constant mechanical load. A more complex two thin pipes example is introduced for additional verification. Furthermore, investigations on convergence issues are discussed. Chapter 4 proposes an in-depth insight into the creep-fatigue crack initiation assessment. The procedure for creep-fatigue crack initiation evaluation by LMM is discussed. Two cases studies are introduced within the chapter, a Metal Matrix Composite volume element and a dissimilar metal weld. Both the structures are subjected to severe cyclic thermal and mechanical loads. Several theoretical discussions are presented about the impact of load levels and creep dwell length to the cyclic response of the structure. Chapter 5 details the implementation of the Stress Modified Ductile Exhaustion (SMDE) method in the LMM. A detailed comparison between SMDE and other creep damage models is provided. A numerical example is presented to show the accuracy of the method, and a comparison between the prediction and the experimental results is given. Chapter 6 deals with a novel unexpected structural behaviour, which occurs at high temperature under particular loading condition. Several numerical tests are presented, and a clear theoretical and practical explanation is provided. Finally, a summary of all the findings obtained within this project is given in Chapter 7. Furthermore, in this chapter conclusions and future work are also presented reflecting the undergoing research at the Structural Integrity and Life Assessment research group (SILA).

Chapter 2

High temperature design and assessment

2.1 Introduction

The fundamentals of creep and plasticity behaviour are found in many undergraduate texts books. However, only in more advanced books [21, 22] they are discussed together in a comprehensive manner. Furthermore, due to the enormous research efforts carried out to date, it is very difficult to have a clear picture of all of the possible responses of structures and the associated failure mechanism.

The following literature review provides a deep insight into already established concepts, and forms the basis for all of the work contained within this thesis. Furthermore, many concepts are re-assessed and deeply analysed giving more accurate definitions. Significant efforts are made in understanding how the failure mechanisms can be assessed using a rule-based method, or the more refined finite element analyses even with a limited amount of material data. Two of the most used design codes for creep-fatigue crack initiation assessment are reviewed. Both the ASME NH and R5 procedures are described and the main differences pointed out.

The numerical procedures based on continuum damage mechanics or on direct methods are both revised. The main advantages and disadvantages of these methodologies are presented and discussed. The Linear Matching Method Framework is presented and carefully reviewed showing its effectiveness in addressing several structural integrity problems. The overall aim of this chapter is to provide the most comprehensive review of the concepts for high-temperature design assessment of structures.

2.2 Creep on structures under monotonic load

2.2.1 Creep mechanism

Creep is a mechanism that affects materials subjected to a certain load at high temperature. It starts affecting materials when the temperature is in a range between 0.3 and 0.5 time the melting temperature. It is a time, stress and temperature-dependent mechanism, which can be represented by a strain-time curve. This curve is usually divided into three subsequent stages, and generic creep curves are described in Figure 2.1.

The three curves are obtained for an increasing mechanical load at the same constant temperature.

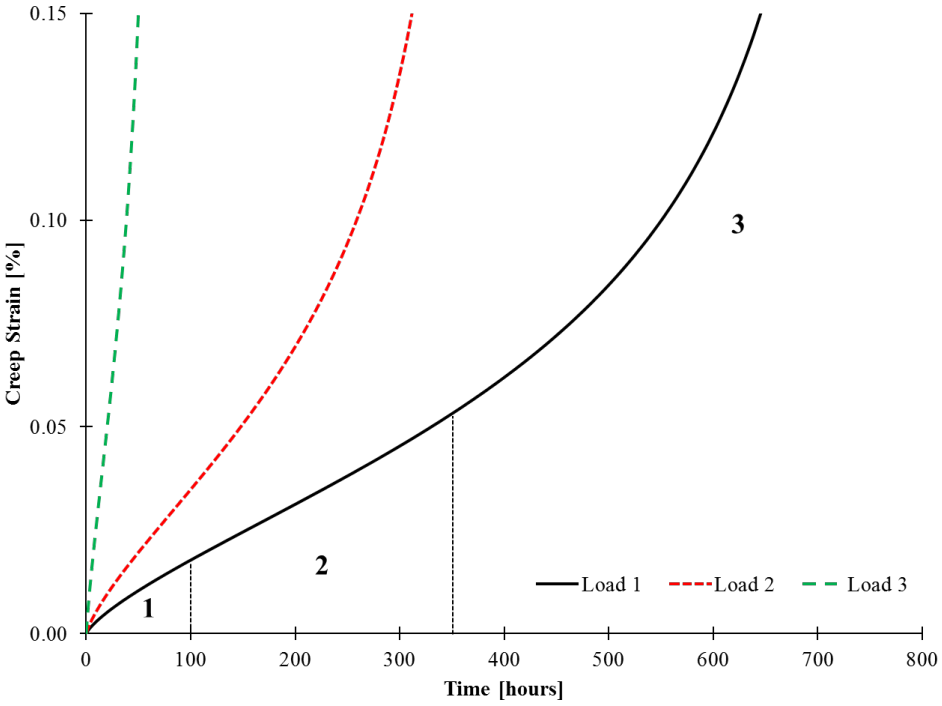

Figure 2.1: Generic tensile creep test curves at increasing load levels.

From the continuous black curve, the three stages are visible, primary (1), secondary (2) and tertiary (3). During the primary phase, a hardening mechanism occurs, and the initial creep strain rate slowly reduces. Following this the secondary stage starts, which is the longest stage during which the creep strain rate is constant. During this period the material starts to develop intergranular damage, and the effective cross section area reduces. This mechanism leads to the tertiary phase which ends with the component rupture. During this phase, a progressive increase of the strain is shown in Figure 2.1. However, for the others curves, this categorization is less evident. This is due to the high level of stress applied to those load cases. For such a high level of stress, the tertiary phase will occur in a very short period (dashed green curve). The effect of these three stages on the creep strain rate is also shown in Figure 2.2. The creep strain rate at the beginning exhibits a reduction up to the steady state value, this is due to the hardening phenomenon. The secondary phase will continue until the damage caused by creep will not be significant. This depends on the material and loading conditions applied. When the tertiary phases start an exponential increase of the creep strain rate is observed.

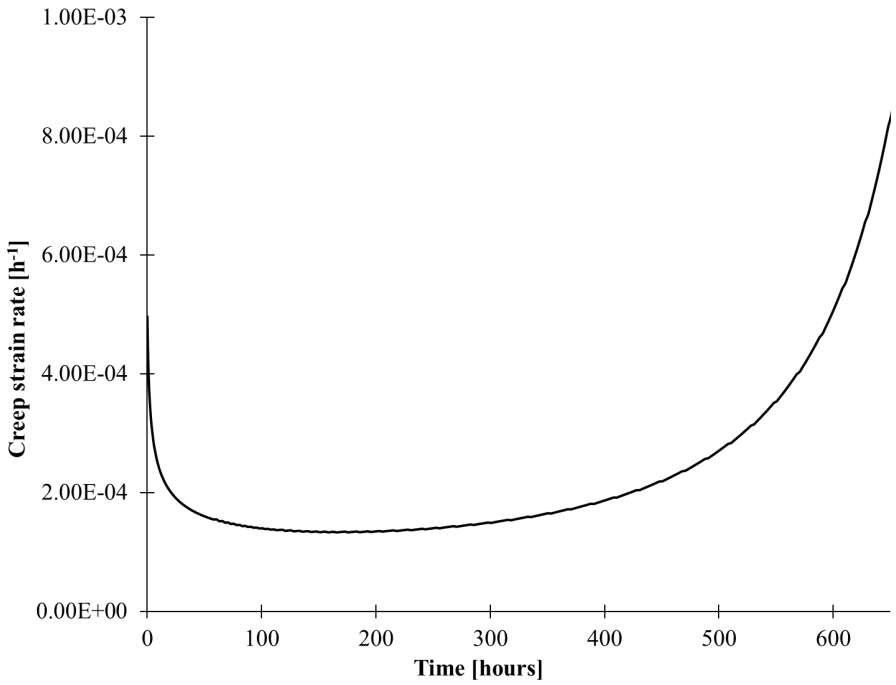

Figure 2.2: Generic tensile creep strain rate curve at constant tensile load levels.

Another important mechanism, which occurs when a structure is subjected to a secondary load and the creep strain accumulates, is the so-called relaxation. Stress relaxation is a crucial mechanism that affects high-temperature structures in a different way. However, if the stress distribution is not uniform in the component, like a notched bar, the initial stress distribution will change as well. The regions with a high level of stress will exhibit stress reduction (relaxation) and the regions with low stress will exhibit an increase of stress. This mechanism is not only caused by creep, but it can also be triggered by plasticity and is known as stress redistribution. This process in real practical cases occurs simultaneously and needs to be carefully assessed. The creep strain accumulation is the engineering effect of an internal material change. Three phenomena are the cause of creep strain and are affected by the load level and temperature. These mechanisms are the dislocation glide or slip, the grain boundary sliding and the diffusion of atoms and vacancies. A way to represent all of these possible mechanisms is by using a creep deformation mechanism map. An example of deformation mechanism map for a generic material is reported in Figure 2.3. The stress normalised to the yield and the homologous temperature T_m are reported on the vertical and horizontal axes respectively. For stress above the yield, dislocation glide is expected, and the rupture will be ductile. Dislocation creep mechanism occurs for a wide range of temperature and mechanical load, and it is one of the most relevant for practical applications. The grain boundaries subjected to the normal tensile stress will draw atoms. Contrary to this, the boundaries subjected to the compressive stress will release atoms. This region can be divided into two distinct sub-regions, the pipe diffusion (left to UV) and the lattice diffusion (right UV). Furthermore, depending on the temperature the aforementioned regions can be subdivided into two parts (from line XY). The two regions above XY line exhibit rigid grain boundaries, conversely below the XY line sliding grain

boundaries are observed. If the temperature is extremely high, and the stress very low, a particular type of creep mechanism occurs, this is called Nabarro-Herring creep. In this case, the diffusion occurring across the crystal matrix will be dominant.

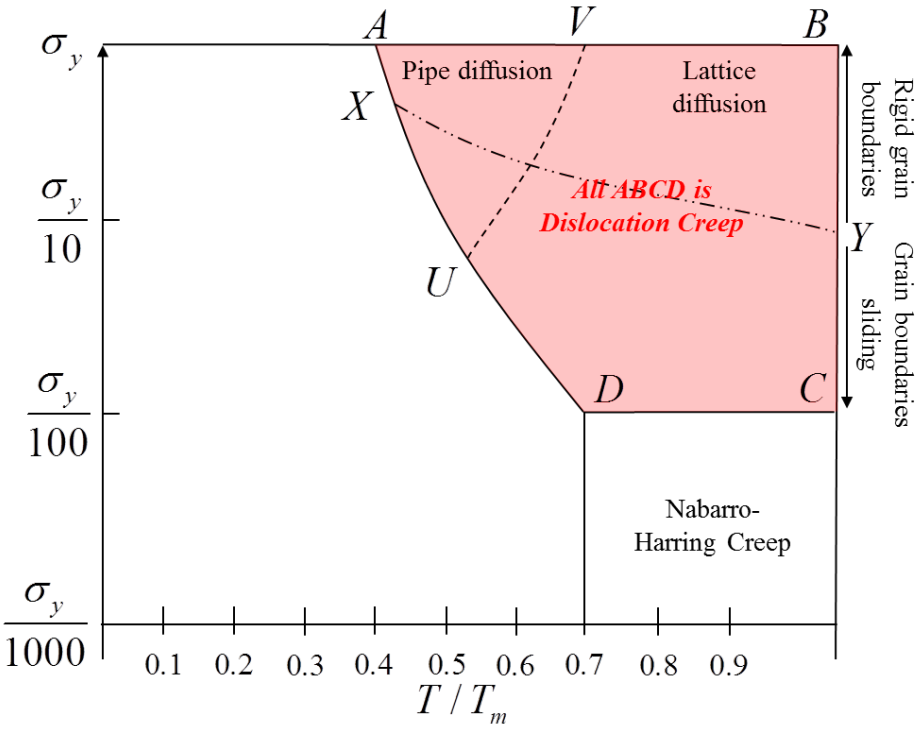

Figure 2.3: Generic creep deformation mechanism map.

2.2.2 Primary and secondary creep

In order to describe the primary and secondary creep stage, two assumptions must be made. The first is about the strain separation; the total strain can be separated into elastic, plastic and creep strain. The second is that the creep strain is a function of three separable functions, which are stress, time and temperature. The creep strain then has the form of:

$$\varepsilon_c = f_1(\sigma)\, f_2(T)\, f_3(t) \tag{2.1}$$

If only the secondary creep is relevant the function of time is neglected and several formulations have been proposed such as the Norton:

$$f_1(\sigma) = A\bar{\sigma}^n \tag{2.2}$$

If the time dependence cannot be neglected several functions have been proposed, and one of the most known is the Bailey:

$$f_3(t) = Bt^m \tag{2.3}$$

Combining equation 1 and 2 the Norton-Bailey law is obtained $\varepsilon_c = B\bar{\sigma}^n t^m$. This simple mathematical representation of the creep behaviour is capable of representing both the primary and secondary stage. In Figure 2.4 the experimental data is interpolated with the Norton-Bailey law, and good agreement is obtained. However, it is clear that this mathematical relationship does not represent the tertiary phase, where a large increase of the creep strain rate is present. When the temperature effect needs to be considered the Arrhenius law can be used to model such a dependency.

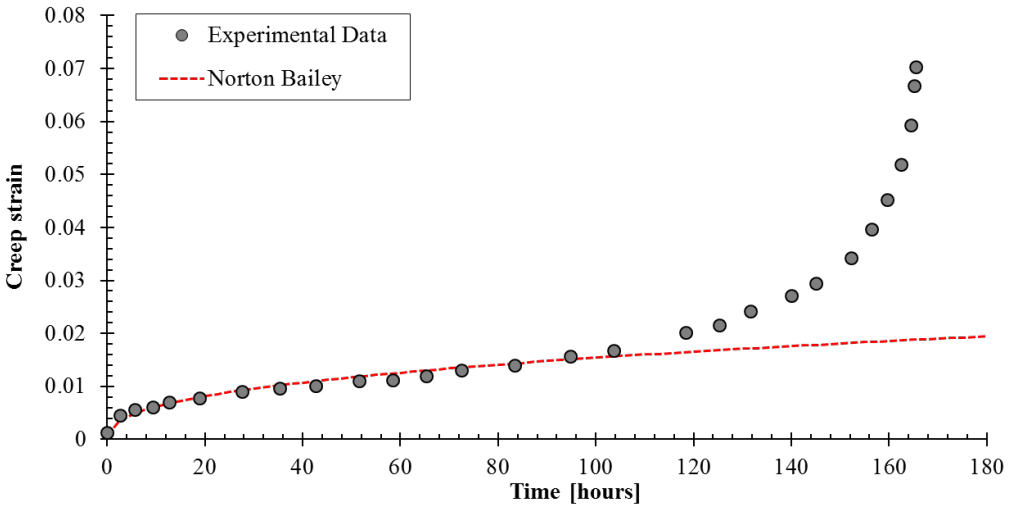

Figure 2.4: Experimental data, interpolated by the Norton-Bailey law.

For several materials, the Norton law is capable of modelling the steady state creep strain rate for precise load levels, as it is shown if Figure 2.5a. In this plot, the steady-state creep strain rate is reported against the applied stress, and a linear relationship at a different temperature is obtained. However, when considering other materials for a larger range of stress levels this is not true and creep strain rate is strongly affected by the stress level. This is shown in Figure 2.5b where steady creep rate of 0.5Cr0.5Mo0.25V is reported. In this case for low-stress n is equal to the unity, for the intermediate stress, it is equal to 4 and for the high stress, it reaches a value of 12 [23].

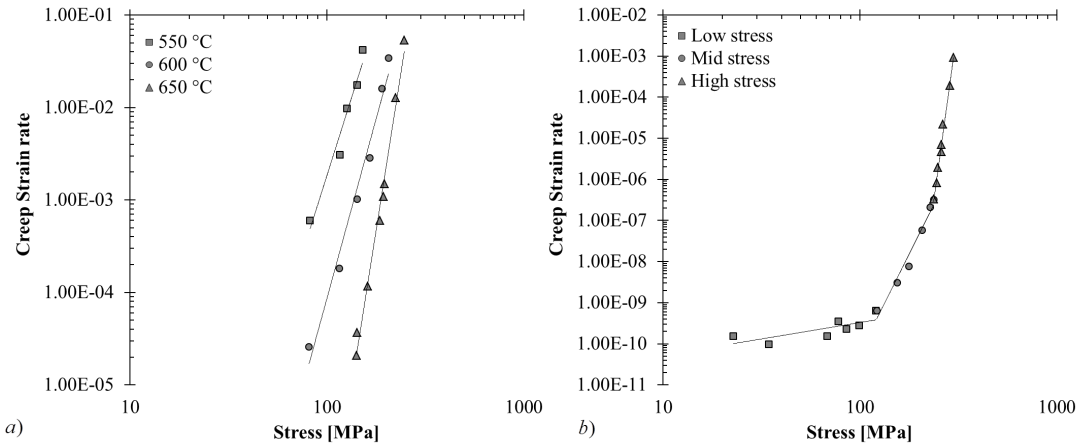

Figure 2.5: a) Creep strain rate against stress for 316L(N) at different temperatures, b) Creep strain rate against stress for 0.5Cr0.5Mo0.25V. [14]

This demonstrates the inaccuracy of Norton Bailey equation to model such a change of the creep strain rate. Several attempts have been done to characterise this phenomenon with a single continuous equation. Two recent developments have been put forward by [24] who proposed the Modified Power Law formulation and by [25] who proposed the Characteristic Strain Model. The main assumption made by Naumenko and his colleagues concerns the definition of creep strain rate. They assumed that the creep strain rate could be represented by the sum of a linear and power contribution, using the following formulation:

$$\frac{\dot{\varepsilon}_{\min}}{\dot{\varepsilon}_0} = \frac{\sigma}{\sigma_0} + \left(\frac{\sigma}{\sigma_0}\right)^n \tag{2.4}$$

where $\dot{\varepsilon}_0$, σ_0 and n are material constants. The stress σ_0 is necessary to specify the stress level required to allow the change of behaviour, from linear viscous to power law. These parameters can be identified easily from the plots shown in Figure 2.5b. When the component is subjected to a low stress the response of the equation is linear, as expected from experimental results. When the stress is further increased the transition from linear to viscous response initiates. If the stress reaches high levels, the power law breakdown regime occurs. One of the most significant benefits of this formulation over others, such as the hyperbolic sine, is to be able to also catch the linear behaviour at low stress. This latter one is relevant for industrial application, where creep occurs at low stress and for long periods.

The Characteristic Strain Method introduced by Bolton is even more versatile than Naumenko's one. It only requires the minimum creep strain rate data, two creep rupture strengths obtained from creep rupture data and a single complete creep test performed at a characteristic stress. It is worth noting that it is capable of modelling all three creep stages. This result is remarkable because it requires less material data than other complex constitutive models. Boltons main assumption is to consider the slope of the creep strain rate stress dependent. This stress dependency is introduced by considering

the ratio between the applied stress and the rupture stress as follows:

$$\frac{d\left(\log\left(\varepsilon_c\right)\right)}{d\left(\log\left(\sigma\right)\right)} = \frac{1}{1-\frac{\sigma}{\sigma_r}} \tag{2.5}$$

where ε_c is the total creep strain, σ is the applied stress and σ_r is the rupture stress at the appropriate time. When the stress is very small the stress exponent tends to the unit, conversely when it approaches to the rupture stress the n diverges to infinity. By integrating equation (2.5) the creep strain is then obtained as a function of the stress:

$$\varepsilon_{\min} = \frac{\varepsilon_{ch}}{\frac{\sigma_r}{\sigma}-1} \tag{2.6}$$

where ε_{ch} is a material constant and can be estimated by using a single creep rupture strength and a creep tensile test adopting the following equation:

$$\varepsilon_{ch} = \varepsilon_d\left(\frac{\sigma_{r1}}{\sigma_d}-1\right) \tag{2.7}$$

where σ_{r1} is the rupture stress at time t_1, and σ_d is the stress that produces a creep strain ε_d within t_1. The last parameter that needs to be calculated is the rupture stress σ_r in equation (2.5), which can be calculated as:

$$\begin{aligned} \sigma_r &= \sigma_{r1}\left(\tfrac{t_1}{t}\right)^{\frac{1}{m}} \\ m &= \tfrac{\log(t_2/t_1)}{\log(\sigma_{r1}/\sigma_{r2})} \end{aligned} \tag{2.8}$$

where σ_{r2} is another rupture stress associated to the rupture time t_2. The entire procedure requires a total of six parameters to be derived from two creep rupture tests and a single creep tensile test.

2.2.3 Tertiary creep: creep rupture

Creep rupture is the third and final stage of the creep deformation process shown in Figure 2.1, which occurs when a material is subjected to a mechanical load, at high temperature. Creep damage growth and propagation across the material is related to the growth and coalescence of voids in the microstructure of the material. This is a general description that is behind a very complex process, which can be expressed as the results of three different behaviours. The first one regards the cross section reduction due to the material deformation. Such a reduction of area is mandatory to respect the volume constancy. The second regards the material behaviour at high temperature that can exhibit particular phenomena like recrystallization and the development of precipitates. The third one is the development of the defects. The introduction of these defects causes a local increase in the stress and the local intergranular cracking. Assessing creep rupture is the first step in the assessment of a structure operating at high temperature. Due to the increasing demand of rupture data for long-term assessment (100000 hours), typical for power generation industry, many efforts have been done to extrapolate rupture data from laboratory test. To do this, a series of different temperature dependent parameters were developed. When the data available covers times and temperatures adequately a master curve can be obtained. Once this

procedure is completed the rupture time for any stress at the appropriate temperature can be calculated, also estimating the residual life. Three of the most used temperature dependent parameters are Larson-Miller [26], Manson-Haferd [27] and Orr-Sherby-Dorn [28]. Larson-Miller parameter is one of the first methods used to determine the creep master curves, compensating time with temperature to predict long term creep data.

$$P_{LM} = (T + 273.15) \cdot (\log(t_f) + C_{lm}) \tag{2.9}$$

It relies on the assumption that a coincident point exists for all iso-stress plots. Such a coincident point corresponds to the C_{lm} material parameter which can vary between 20-22. Authors [29] suggested that the wide use of this parameter, which is designed for low-temperature creep may lead to inaccurate predictions, especially for cases where the material is subjected to high temperature and low stresses. The Manson Haferd parameter is based on the assumption that a coincident point must exist when plotting the logarithm of the rupture time against the temperature. This point defines two parameters, which are related to the material T_a and t_a . The Manson Haferd parameter is calculated using the following equation:

$$P_{MH} = \frac{\log t_r - \log t_a}{T - T_a} \tag{2.10}$$

This parameter is normally accepted and widely adopted, and it is capable of producing better predictions at high temperature with low-stress level, but this capability is related more to its mathematical approach than its physical background. Conversely, the Orr-Sherby-Dorn parameter combines both the physical behaviour and the mechanical and thermal behaviour for a wide range of temperatures. The plot of the logarithmic rupture times against the inverse of the temperature results in a series of parallel lines at different stresses. The slope of each line represents a constant value which includes the activation energy Q for the damaging process and the universal gas constant R. The Ordd-Sherby-Dorn parameter can be defined by the following equation:

$$P_{OSD} = \log t_r - \frac{Q}{RT} \tag{2.11}$$

This parameter is more efficient in predicting the rupture stresses and is capable of covering a wider range of temperatures than the previous parameters. Based on the aforementioned parameters the rupture life can be estimated by calculating the stress within the structure. Design codes adopt approximated procedure to calculate the stress required to enter the parameter-based rupture time curves. The UK's R5 is based on the calculation of the reference rupture stress σ^R_{ref}. This calculation is performed only when the loading condition produces significant creep behaviour in the structure. Depending on the material creep ductility, different reference stresses formulation can be adopted, for creep ductile materials the following is considered:

$$\sigma^R_{ref} = \{1 + 0.13\,[\chi - 1]\}\,\sigma_{ref} \tag{2.12}$$

where σ_{ref} is the reference stress, and it is calculated using different formulation depending on load condition. For an isothermal and homogeneous structure it is equal

to $\sigma_{ref} = \frac{P\sigma_y}{P_U}$, where P is the primary load, σ_y is the yield stress of the material and P_U is the plastic collapse load. χ is the stress concentration factor, and it is used to adjust the reference stress for local strain concentration. For an isothermal and homogeneous structure, it is obtained as the ratio between the maximum elastic equivalent stress and the maximum reference stress calculated. This approach is acceptable if this ratio is lower than 4. Conversely, if the stress raiser is sharp enough to be considered as a crack-like defect a different assessment procedure is required. If the material is creep brittle or the creep stress exponent n is higher than 7 the following formulation can be adopted:

$$\sigma_{ref}^{R} = \left\{1 + \frac{1}{n}\left[\chi - 1\right]\right\}\sigma_{ref} \tag{2.13}$$

Another way to model the creep rupture comes from the increasing computational efficiency and the better understanding of creep mechanics. Several damaging models have been proposed and validated. Two of the most used are the Kachanov-Rabotnov model [30, 31] (RK) and the Liu Murakami [32] (LM), which introduce a scalar damage parameter.

Consider a continuum body with an associated volume V and surface S representing an undamaged notched bar, which is subjected to an axial mechanical load at high temperature. A creep damage parameter is considered to regulate the stress and strain relationship. At the start of the creep dwell, no damage is present within the volume, or it is too small to affect the stress-strain response. However, when sufficient time has passed the damage will initiate and grows as shown in Figure 2.6 at 250 hours. At this point, a failure front can be identified in a red semicircular shape (or doughnut-shaped for the full model). The increase of the damage rate depends on the material properties and load conditions. A progressive smaller volume V of the body will be capable of bearing the applied load. At around 750 hours the failure front is unified, and the damage affects the central part of the notched bar. The loading bearing capability of the structure is related to its capability of redistributing the stresses when a region has failed. When the undamaged volume reaches a limit beyond which it cannot bear the applied load, the rupture will occur. In the proposed example this occurs at 1066 hours, and the damage front is localised in the centre of the bar.

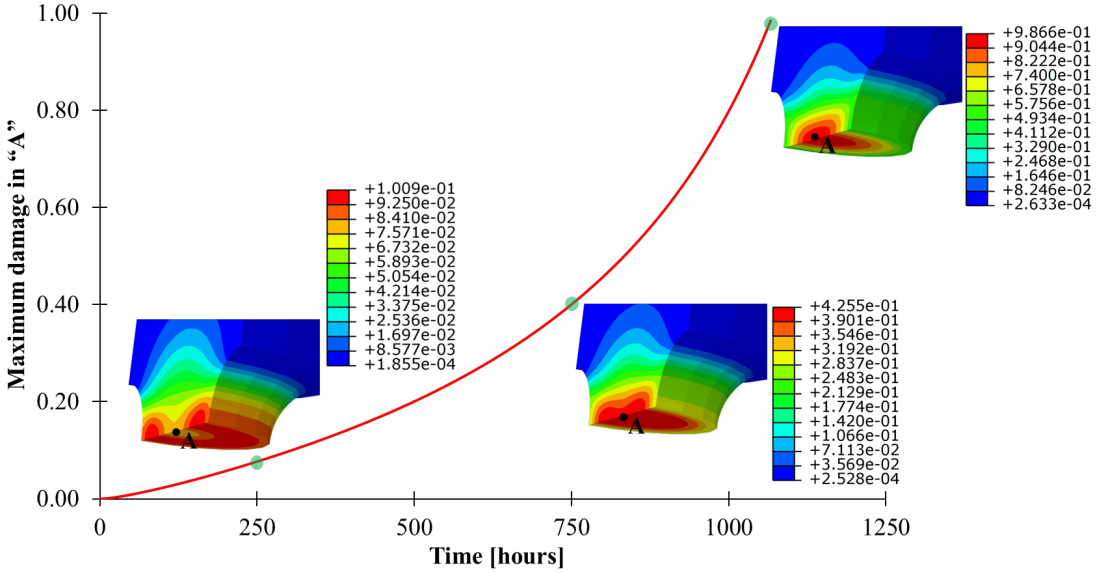

Figure 2.6: Damage evolution for a notched bar subjected to a monotonic load. The contour of the damage accumulated is shown at 250, 750 and 1066 hours.

This process can be described by an accurate mathematical representation of the creep strain rate and damage rate. For a uniaxial creep problem the creep strain rate and the damage rate has been defined as follow:

$$\begin{aligned} \dot{\varepsilon}_{ij}^{c} &= \frac{3}{2} A \left(\frac{\bar{\sigma}}{1-\omega}\right) t^{m} \left(\frac{S_{ij}}{\bar{\sigma}}\right) \\ \dot{\omega} &= B \frac{{\sigma_r}^{\chi}}{(1-\omega)^{\phi}} \end{aligned} \tag{2.14}$$

where $\bar{\sigma}$ is the von Mises stress, S_{ij} is the deviatoric stress component and σ_r is the rupture stress and t is the time. All the others multipliers or exponents are material parameters, which require being calculated by tensile creep tests. However, this constitutive damage model is not complete because it requires the definition of the rupture stress for the damage rate calculation. The rupture stress is calculated considering the effect of both principal stress and equivalent stress, using the following formulation:

$$\sigma_r = \alpha\sigma_1 + (1-\alpha)\,\bar{\sigma} \tag{2.15}$$

α is the multiaxial parameter, and it describes the effect of principal and von Mises stress on the failure mechanism. To obtain such a creep parameter, a tensile test needs to be done on a notched bar specimen. When the rupture life is known at different applied stresses, FE-analyses are performed varying α and an optimum value is identified. However, this procedure is tedious and requires many experimental and numerical tests. Furthermore, it has been demonstrated that the rupture life is significantly affected by the predicted parameters [33]. Despite its simplicity, the Kachanov creep damage model has a clear weakness in its mathematical formulation. When the damage parameter approaches to the unity, the creep strain rate and damage rate tend to diverge to infinite. This problem has been resolved by the model presented by

Liu-Murakami and then successfully applied to several engineering problems [34]. The mathematical representation of this model is shown:

$$\dot{\varepsilon}_{ij}^{c} = \frac{3}{2} A \bar{\sigma}^{n-1} S_{ij} t^{m} \exp\left[\left(\frac{2(n+1)}{\pi\sqrt{1+\frac{3}{n}}}\right)\left(\frac{\sigma_1}{\bar{\sigma}}\right)\omega^{\frac{3}{2}}\right]$$
$$\dot{\omega} = B\frac{(1-\exp(-q_2))}{q_2}\sigma_r^{\chi}\exp\left(\omega q_2\right) \tag{2.16}$$

This model follows the same principle of the one proposed by Kachanov, but the damage does not cause any numerical problem when it approaches unity. Furthermore, the various material parameters required can be obtained by the same creep test of uniaxial and notched specimens. A comparison is shown in Figure 2.7, where the creep damage against the time is reported for both the damage models. Both models produce similar rupture times, however the LM approaches the failure with a more realistic trend. Furthermore, the damaged area is not localised and it is homogeneously distributed. Conversely, RK shows an unrealistic diverging trend and the damage contour is more localised than in LM. The RK formulation is not capable of reaching the desired critical damage (0.99) and for this case the analysis has been aborted when it is 0.79. This phenomenon becomes even more severe if the mesh is refined due to the presence cracks [35].

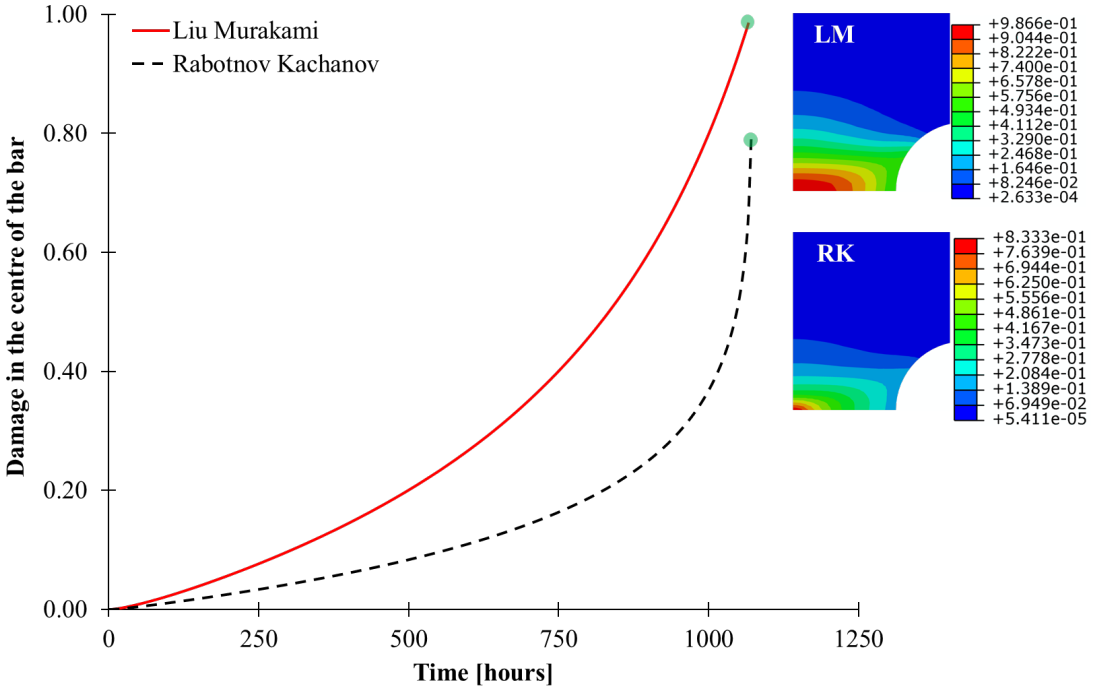

Figure 2.7: Damage evolution of a notched bar subjected to a monotonic load, for the Liu-Murakami and Robotonov-Kachanov creep damage model. Damage contours for both models are reported at the rupture.

Several local creep damage models have been developed, with even more damage parameters. However these stress based damage models have two major drawbacks,

the first one regards their applicability. The material parameters need to be calibrated using precise testing conditions, such as load level and temperature. In some cases such as the Dyson model, this procedure can be very complex [12, 15]. This makes it very challenging to apply these models for standard design procedure, where versatility and flexibility are preferred. The second drawback is the computational cost, which needs to be considered especially when a complex structure is analysed. These models require many increments to get the convergence, and the time step can reduce significantly when the damage propagates. In some cases, even 30000 increments are required to cover an entire dwell time of just 1200 hours, for a simple geometry. For these reasons such a strategy is adopted only when a particularly refined damage model is required.

2.3 Cyclic response of structures

2.3.1 Shakedown, ratchet and limit load

When a structure is subjected to a cyclic load, four cyclic responses are possible. In the last 30 years, several efforts have been made to predict these behaviours. One of the most famous works was carried out by [36]. In his work Bree identified that a component subjected to cyclic temperature and constant mechanical load could exhibit elastic shakedown, plastic shakedown or ratchetting. To represent the interaction between the cyclic and constant load, he proposed an interaction diagram as shown in Figure 2.8.

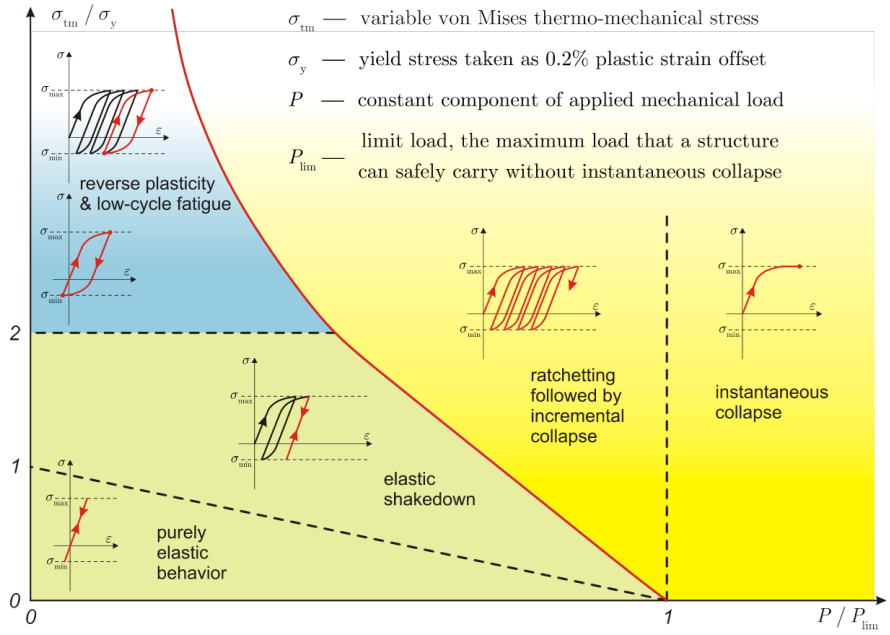

Figure 2.8: Classical Bree's like diagram for a cylinder subjected to cyclic thermal load and constant mechanical load.

Within the diagram (Figure 2.8) the thermal stress and the constant mechanical load are normalised for the yield stress and limit load respectively and are reported on the vertical and horizontal axes. If the combined loads applied are small enough the entire component will remain elastic during the operating life. However, if the load is

increased the component can exhibit elastic shakedown. At the early stage of its life, the component accumulates plastic strain. However, when the steady state is reached the response returns to be elastic and no more plastic strain is accumulated. Parts are designed in many cases to operate in this region because their operating life is very high (over than 10000 cycles). If the cyclic thermal load is increased, which is crucial for the power industry that is seeking to operate at high temperatures to improve the efficiency, the component may exhibit plastic shakedown. In this region the cyclic response is characterized by the typical closed hysteresis loop shown in Figure 2.8. In this region the component exhibits plasticity during both the loading and unloading phases, and its life is affected by Low Cycle Fatigue (LCF). The most important task for engineers is about assessing in the most accurate way the total strain range. This parameter is fundamental to assess the fatigue damage per cycle, and then the component life.
In order to evaluate the fatigue damage within each load cycle the low cycle fatigue life curves should be used. However, these curves are not always available, especially at high temperatures. For this reason several robust and efficient methods have been created by [37–40] and recently modified even further [41, 42]. These approaches are based on the assumption to separate the elastic and plastic contribution to the fatigue life. Using the following relationship for the elastic $\Delta\varepsilon_e$ and plastic strain range $\Delta\varepsilon_p$ are given:

$$\Delta\varepsilon_e N_f^{\alpha_1} = C_1 \tag{2.17}$$

$$\Delta\varepsilon_p N_f^{\alpha_2} = C_2 \tag{2.18}$$

where α_1, α_2, C_1 and C_2 are material parameters related to the fatigue ductility. By combining equations (2.17) and (2.18) the Coffin-Manson relationship is derived, which relates the total strain range $\Delta\varepsilon_t$ with the number of cycles to fail N_f.

$$\frac{\Delta\varepsilon_t}{2} = \frac{\sigma_f^{'}}{E} \cdot (2N_f)^b + \varepsilon_f^{'} \cdot (2N_f)^c \tag{2.19}$$

The right hand part of equation (2.19) represents the elastic strain range and the plastic strain range. The coefficient $\sigma_f^{'}$ is related to the material fatigue strength, instead $\varepsilon_f^{'}$ represents the material fatigue ductility strength. Manson and others researchers developed and modified equation (2.19) obtaining the Universal Slope Method (USM) [40, 43] assuming that the coefficients b and c are material independent. Furthermore, empirical equations for $\sigma_f^{'}$ and $\varepsilon_f^{'}$ were developed by Manson in his work where the total strain range was defined as follows:

$$\Delta\varepsilon_t = \frac{3.5 S_u}{E} N_f^b + D^{-c} N_f^c \tag{2.20}$$

where S_u is the ultimate strength of the material, D is the ductility failure strain due to the section area reduction both of which are given by a tensile test. The two exponents b and c do not depend on the material considered. Despite its theoretical simplicity the main downsize is the necessity to define the reduction area to estimate the ductility. However, this material data is not always available. In order to avoid the use of the

reduction of area the Modified Universal Slopes Method (MUSM) has been developed. The USM is enhanced by replacing the cyclic strength and ductility with an equation based on the tensile ductility and strength:

$$\frac{\Delta\varepsilon_t}{2} = \frac{\sigma_f^{'}}{E} \cdot (2N_f)^b + \varepsilon_f^{'} \cdot (2N_f)^c \tag{2.21}$$

The fatigue strength coefficients and the fatigue ductility are calculated using the following equations:

$$\begin{aligned} \sigma_f^{'} &= E \cdot 0.623 \cdot \left(\tfrac{S_u}{E}\right)^{0.832} \\ \varepsilon_f^{'} &= 0.0196 \cdot {\varepsilon_f}^{0.155} \cdot \left(\tfrac{S_u}{E}\right)^{-0.53} \end{aligned} \tag{2.22}$$

The exponents instead are assumed constant b = -0.09 and c = -0.56. The ultimate strength is selected for the appropriate temperature and hold time if creep is present. An example of its effectiveness and the reliability is given in Figure 2.9. A benchmarking on low cycle fatigue behaviour of Al2024 T3 at high temperature [44] is shown. A comparison between the MUSM, the experimental data and other approximated methods recently reviewed by [45], the Median Method (MM) and the Modified Mitchell's Method (MMM), are presented in Figure 2.9.

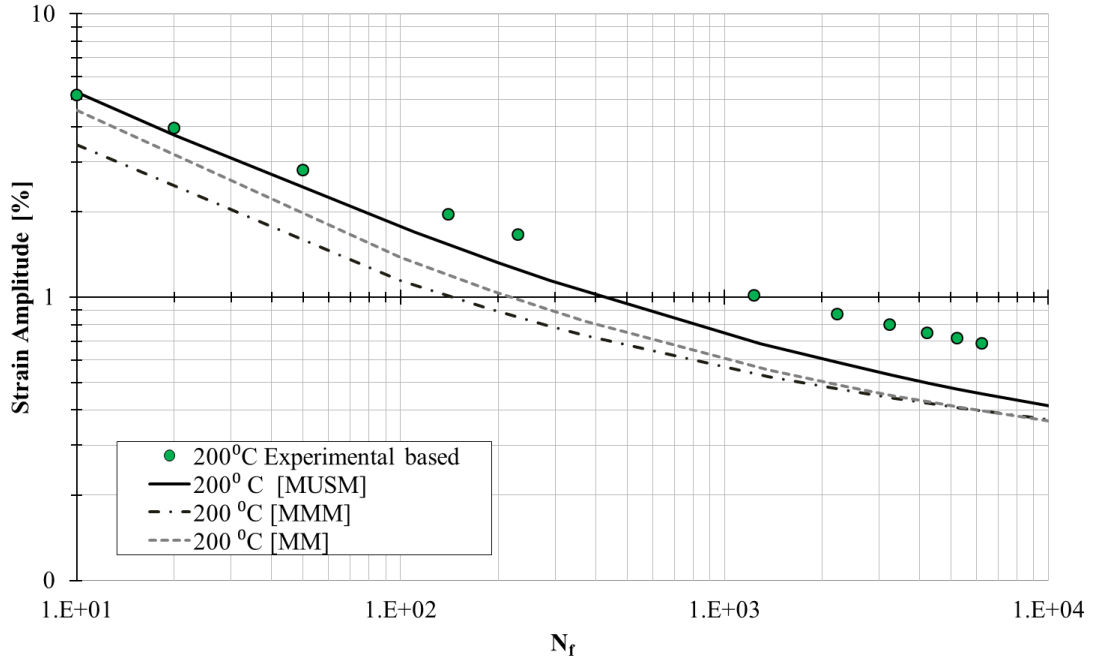

Figure 2.9: Experimental low cycle fatigue life (solid circles) of Al2024T3 at 200°C and approximated low cycle fatigue curves.

These approximated methods demonstrate an ability to produce accurate results, especially at high levels of strain. Conversely, at low levels of strain, in all the methods adopted the final result is always conservative. For this particular case, the MUSM approach is always the most accurate and least conservative. These approximated laws

are useful for the early design stage when the fatigue life of the material at certain conditions may be unknown.

If the mechanical load is further increased ratchetting mechanism can occur in the component, and incremental collapse might affect the life of the component (Figure 2.8). This mechanism is considered very dangerous for industrial components, and must be avoided. When a component fails due to ratchetting the failure mechanism is different from the failure for plastic shakedown. Ratchetting failure affects the component globally, and it is accompanied by a larger reduction of the section area. Conversely, when low cycle fatigue affects the part a local failure, in the form of a crack, initiates in a very small location. If the mechanical load is increased even further the structure may fail immediately after the application of the load, and in this case, the limit load has been reached, and the collapse is instantaneous. Usually, this type of failure is related to bad design and assessment of the component. Due to its importance, it is the first failure mechanism assessed in any international design code present today. Several procedures are developed to ensure no plastic collapse and will be discussed in a more detailed way later. These include analytical solution based on elastic analyses, detailed non linear finite element analyses or refined finite element analyses based on direct methods.

2.4 Creep on structures under cyclic load

2.4.1 Creep-fatigue interaction

Creep and fatigue are complex mechanisms that involve different types of damaging processes. Creep produces intergranular cavitation damage, while fatigue propagates cracks through transgranular paths, with surface striations and wide surface cracks. Relevant works on mapping this interaction was done by Hales [46] and recently reviewed by Yan [47] for 316 stainless steel. Hales used the direct metallographic observation to explain the cyclic creep experimental results. A direct correlation is established between the hold time and the magnitude of the cavitation processes, which increases in magnitude for a longer dwell time. Furthermore, the creep damage process is strongly affected by the position of the hold time within the loading cycle. The most critical condition occurs when the creep dwell starts at the peak of the tensile stress, introducing signs of intergranular damage even for short periods. In components operating at high-temperature creep and fatigue are competing mechanisms, depending on strain range [48] and dwell time. Hales [46] identified four cases of interaction, further extended by Plumbridge [49]. The first case involves Pure Fatigue behaviour where surface cracking is dominant. The second case is Transgranular Competing, which has a transgranular crack propagating during the tensile hold time, and cavitation damage begins to occur. The third case is Mixed Interaction, where the transgranular cracking becomes intergranular. The last case is a Pure Creep process, where the hold time is long enough to allow the loading cycle to be considered as a monotonic load case. Other parameters like the total strain range were found to be important in this competitive mechanism. For large strain ranges, fatigue is dominant, while creep is more damaging for small strain ranges.

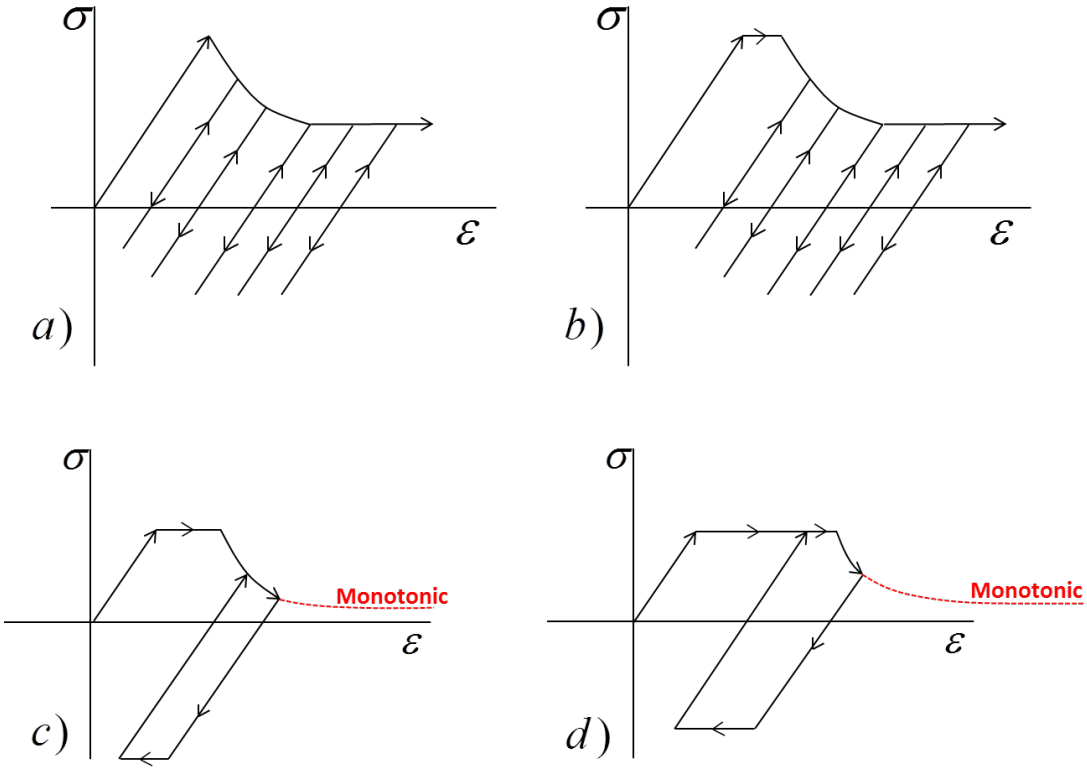

Figure 2.10: Different material responses due to cyclic loading with creep dwell period at the tensile peak a) elastic response, b) elastic shakedown, c) creep enhanced reversed plasticity and d) creep enhanced plastic shakedown

Figure 2.10 shows a schematic representation of the possible mechanisms, which can occur when considering a creep dwell that starts at the peak of the tensile stress. When the load level is below the elastic limit, no plastic behaviour takes place at the first cycle (Figure 2.10a). The subsequent creep dwell causes a progressive stress relaxation, without any plastic strain during the unloading and loading phases. When the load level is greater than the elastic limit but significantly below the shakedown limit, plastic behaviour occurs in the first cycle (Figure 2.10b). If the progressive stress relaxation during the subsequent creep dwell is not significant, again there is no plastic strain during the subsequent cycles. The resulting steady state cyclic response is similar to shakedown, and the accumulated creep damage is identical to the monotonic load case. Figure 2.10c shows the response of the structure when creep enhanced plasticity occurs during unloading due to the higher load level. In this case, a steady-state closed loop response appears, and the creep strain range is compensated by the reverse plasticity. If the applied load level continues to increase, the hysteresis loop response shows plasticity during both the loading and unloading phases, causing more severe fatigue damage which interacts with the creep damage (Figure 2.10d). In both Figure 2.10c and Figure 2.10d, the accumulated creep damage is larger than obtained by a monotonic load, due to the higher stress level which cyclically occurs during the creep dwell. For this reason, this response is known as Cyclically Enhanced Creep. In some particular conditions, an open hysteresis loop response is possible. This mechanism is known as Creep ratchetting and this will be discussed in the next subsection.

2.4.2 Creep-ratchetting mechanism at high temperature

Ratchetting is a cyclic phenomenon, which results in the progressive accumulation of plastic strain. This process can be driven by high mechanical or thermal load level. Thermal ratchetting can occur with very small primary load due to the flow of high-temperature fluids, which causes a severe cycling thermal gradient. This behaviour leads to an accumulation of plastic strain [50, 51]. From Bree [36] it is known that if the structure operates in a region of strict or global shakedown, no inelastic strain accumulation occurs. This statement as discussed in the previous subsection becomes imprecise if creep occurs [52]. Although creep dwell can introduce a closed hysteresis loop response (Figure 2.10c-d) for cyclic loading conditions within the shakedown limit. The closure of the hysteresis loop is due to the compensation of all the inelastic strains within the entire cycle. However, the non-closed hysteresis loop would still be possible, when an inelastic strain accumulation occurs due to the dominant creep or reversed plastic strains [53]. For example, a large dwell time could produce a creep strain greater than the limited plastic strain, leading to an inelastic strain accumulation dominated by creep. In other loading conditions a large stress relaxation, which results in a low level of overall creep stress, leads to insignificant creep strain but large plastic strain during the unloading phase. This could produce an open hysteresis loop dominated by the reversed plastic strain. Hence creep ratchetting is instead a much more complex mechanism, and it is dependent on the dwell time, the type of load applied and load levels. To better understand the Creep Ratchetting mechanism, a diagram showing creep ratchetting interaction boundary is given in Figure 2.11.

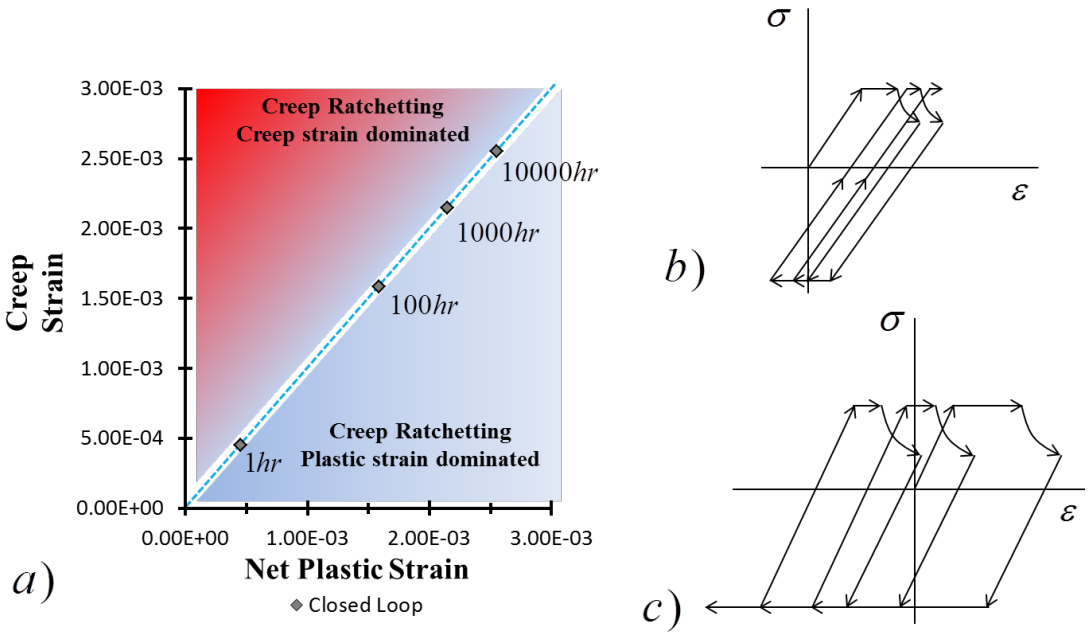

Figure 2.11: a) Creep ratchetting interaction boundary and steady state response for creep ratchetting b) creep stain and c) plastic strain dominated.

The straight 45-degree line shown indicates the closed hysteresis loop limit. If the loading conditions are within the shakedown limit and no primary load is applied, for

any dwell time an identical magnitude of creep strain and net plastic strain is obtained and the closed loop response is possible. In this case, the plastic strain at loading and the creep strain are totally recovered by the reversed plasticity. Instead, if a primary load is applied depending on its level different behaviours are possible. If the ratio between creep and net plastic strain is above the closed loop limit a creep ratchetting mechanism dominated by creep strain occurs (Figure 2.11a), and the entire cycle shifts rightward. Otherwise, when the ratio is below the closed loop line a creep ratchetting mechanism dominated by plastic strain occurs (Figure 2.11b), and the steady-state cycle moves leftward due to the large reverse plasticity. In both cases, the creep ratchetting mechanism is driven by the creep dwell period, and the creep ratchet life of the component must be assessed as well as the creep fatigue life. In all design and assessment codes, ratchetting must be avoided [3, 4], and the Creep Ratchetting Failure (CRF) could be dealt in the same way. It is suggested by [54], that Ratchetting Failure (RF) and Low Cycle Fatigue (LCF) are distinct competitive mechanisms, which can be assessed separately. If the hysteresis loop is closed, then there is no inelastic strain accumulation and the fatigue failure mechanisms can be predicted using the Manson-Coffin relationship [54]. However, if the failure occurs due to necking (RF or CRF) the ductility exhaustion approach is used to calculate the number of cycles to failure N_r:

$$N_r = \frac{\varepsilon_f}{\Delta\varepsilon_r} \tag{2.23}$$

where ε_f is the tensile ductility of the material, and $\Delta\varepsilon_r$ is the accumulation of inelastic strain per cycle. Recent development in non-linear material modelling allows for more detailed consideration [55]. It is shown that the ratchetting mechanism can affect the LCF life, only when the loading level is near the static limit load of the structure. The intensified plastic strain accumulation due to ratchetting affects the crack initiation and propagation, especially where stress concentration is present. It is reasonable to assume that creep-ratchetting can be assessed independently from the creep-fatigue process in the most cases.

2.4.3 Creep-fatigue total damage calculation

In order to estimate the total damage caused by creep and fatigue interaction, a damage diagram must be defined. Different relationships between fatigue and creep can be established, and the most commonly used is the bi-linear relationship adopted by ASME NH [3];

$$\phi_f + \phi_c \leq D \tag{2.24}$$

where ϕ_f and ϕ_c are the accumulated fatigue and creep damage, and D is an allowable creep-fatigue damage factor which depends on the material. If the total damage D is equal to unity, the linear diagram is obtained, as shown in Figure 2.12, where the creep-fatigue damage diagrams and experimental data for type 304SS at different total strain ranges are presented as an example [56].

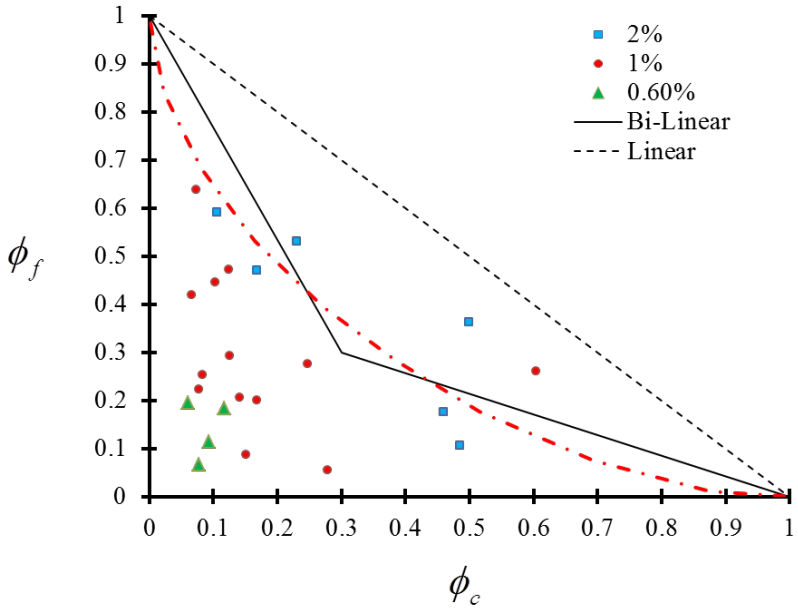

Figure 2.12: Type 304SS (595°C) damage diagram for bi-linear, linear and combined damage rules.

The bi-linear locus shows a focal point where the creep and fatigue damage is equal to 0.3, which is a material constant. Another way to model this interaction is given by Skelton [57], who introduced a coupled model for creep-fatigue damage interaction shown in Figure 2.12. It is based on the assumption that a creep fatigue interaction exists and the total damage is not equal to unity. When the total damage to failure is lower than unity, the failure locus has a concave shape with an upward facing curve. The failure locus is described by the following relationship:

$$\frac{\phi_f}{1-\phi_c} + \frac{\phi_c}{1-\phi_f} = 1 \tag{2.25}$$

The focal point on the diagram is 0.33, close to the one predicted by the bi-linear method. This relationship can be easily modified if a damage de-coupling is necessary, introducing two interaction coefficients I_{fc} and I_{cf} attenuating effect of fatigue on creep and vice versa. Equation (2.25) is then modified in the following way:

$$\frac{\phi_f}{1-I_{cf}\phi_c} + \frac{\phi_c}{1-I_{fc}\phi_f} = 1 \tag{2.26}$$

By the adoption of such a formulation and by accurately calculating the interaction coefficients, it is possible to model the different interaction mechanisms.

2.5 Key Parameters for the Creep-Fatigue Assessment

When creep and fatigue affect a structure, a series of parameters need to be calculated to perform the crack initiation assessment. These parameters are defined in Figure 2.13, where a typical steady state cycle with a tensile peak creep dwell is shown.

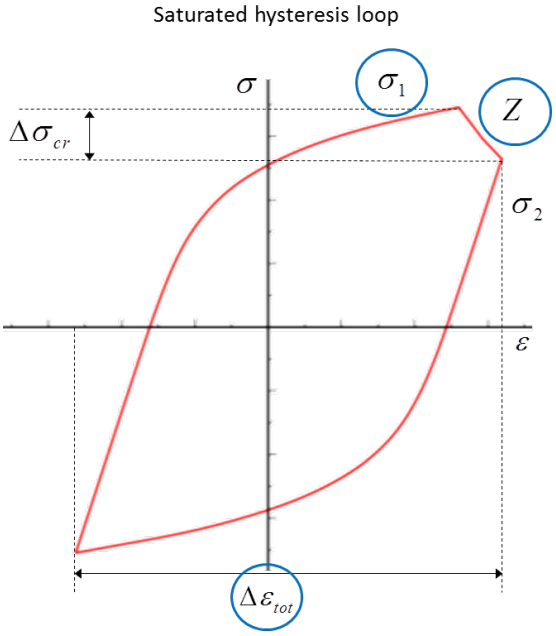

Figure 2.13: Saturated Steady State Cycle with creep dwell at tensile peak.

The three most important parameters are highlighted in blue, which are the stress at the start of the dwell σ_1 , the elastic follow up factor Z and the total strain range $\Delta\varepsilon_{tot}$. The Z factor expresses the ratio between the equivalent creep strain increment and the associated elastic strain decrease. When the load applied is primary, Z is very big and can tend to infinity conversely if the load is classified as secondary it corresponds to the unity. However, in real structures it assumes intermediate values. Other parameters can be used to accurately define the hysteresis loop such as the creep stress drop $\Delta\sigma_{cr}$, the associated creep strain $\Delta\varepsilon_{cr}$ and the plastic strain $\Delta\varepsilon_p$ accumulated within the cycle. The only way to obtain these parameters and assess the steady state cycle is by adopting inelastic step-by-step finite element analyses, or by using a more convenient direct methods such as the Linear Matching Method. Inelastic incremental finite element analyses can identify the structural response due to creep and fatigue interaction. However, these are computationally inefficient especially when 3D elements are used, and convergence issues can occur. Conversely, direct methods such as the LMM have been demonstrated to be capable of providing alternative solutions to engineering problems, providing all the required parameters for crack initiation analysis, and can easily be adapted to any design code. The design codes such as R5 or ASME, are widely adopted and capable of calculating the aforementioned key parameters by adopting a series of design rules and procedures. In the majority of cases, these procedures rely on linear elastic analysis. However, in certain cases when conservatisms need to be relaxed, then an inelastic material response can be implemented. Despite

this, there is no real interaction between creep and fatigue, which are evaluated separately. Their interaction relies mostly on safety factors, which enhance the calculated parameter. These design rules provide a conservative but safe assessment for a large class of components used by industry.

2.5.1 International design codes; R5 and ASME NH

The most crucial aspect of any creep-fatigue assessment procedure is to identify the structural response due to a cyclic load. This means constructing an accurate hysteresis loop, in order to evaluate the creep and fatigue damage. All assessment codes consider an open loop response unacceptable and for this reason, only the closed loop response will be considered (Figures 2.10c-d), and creep ratchetting is neglected. Both ASME NH and R5 procedures rely on simplified methods to address the stress calculation, and make extensive use of stress categorization. Different types of analyses can be utilised, for the pessimistic elastic analyses to the more sophisticated and less conservative inelastic analyses. As shown in Figure 2.13 a series of parameters are crucial for the accurate assessment of crack initiation with creep-fatigue interaction. The first parameter is the stress at the start of the creep dwell, which is estimated by both codes in different ways. ASME NH calculates this stress by adopting a revised effective creep stress, which is equal to 1.25 times the effective creep stress. The effective creep stress is obtained by multiplying the yield stress of the material at creep temperature by a stress factor Z^{NH}, which is not the elastic follow up factor. The value of Z^{NH} depends on the level of primary and secondary stress for the cyclic loading condition considered, which is adequately described by NH-T-1332 [3]. R5 instead has two options to calculate the start of the dwell stress; the first adopts the shakedown reference stress. Otherwise, a second alternative can be considered if the peak stress is not included in the shakedown reference stress. A revised steady-state equivalent stress at the start of the creep dwell is obtained by subtracting the shakedown stress limit from the maximum equivalent elastic stress range. Once the start of the dwell stress is calculated the second parameter, the creep strain, is assessed by both the codes with different procedures. ASME NH calculates the creep strain by using the isochronous stress-strain curve at the revised effective creep stress for the holding temperature and time. Whereas, in R5, the creep strain range $\Delta\bar{\varepsilon}_c$ is obtained using the following relationship:

$$\Delta\bar{\varepsilon}_c = -\frac{Z}{\bar{E}}\Delta\bar{\sigma} \tag{2.27}$$

where $\bar{E}$ is the effective Young's modulus, Z is the elastic follow-up factor and $\Delta\bar{\sigma}$ is the equivalent stress drop during the dwell period. The inaccurate calculation of the stress reduction and Z factor may introduce an overly conservative creep strain. The concept of the elastic follow up factor was introduced in R5 to avoid fully inelastic time-dependent analyses. There are three options available to calculate it, and the most accurate are the one which uses an elastic-creep inelastic analysis. In such a type of analysis, no plastic behaviour is considered, and a monotonic load is applied rather than a cyclic one. This procedure does not take into account cyclic plasticity, to reduce the computational effort. The last parameter which needs to be calculated to start the crack initiation assessment is the total strain range $\Delta\varepsilon_{tot}$. Both assessment

procedures adopt the Neuber correction in order to calculate the plastic strain from the elastic solution, but R5 differs by also using the Ramberg-Osgood material model for the cyclic material response. Furthermore, both procedures consider different modifiers to account for the local geometric concentration factor and multiaxial plasticity. In the ASME NH, the total strain range is defined as:

$$\Delta\varepsilon_{tot}^{NH} = K_\nu \cdot \Delta\varepsilon_{\text{ mod}} + K \cdot \Delta\varepsilon_c \tag{2.28}$$

where K is the local concentration factor, K_ν is the multiaxial plasticity and Poisson ratio adjustment, $\Delta\varepsilon_{\text{ mod}}$ is the modified maximum strain range and $\Delta\varepsilon_c$ is the creep strain range [56]. The modified maximum strain range can be calculated using three options, with an increasing amount of conservatism. All three methods use the maximum equivalent elastic strain range as starting point. Different factors are considered to enhance the elastic strain range due to non-linear effects. The R5 has a similar procedure and calculates the total equivalent strain range as follows:

$$\Delta\varepsilon_{tot}^{R5} = \Delta\varepsilon_{el,r} + \Delta\varepsilon_p + \Delta\varepsilon_{vol} \tag{2.29}$$

where the first term is the revised equivalent elastic strain range, which is obtained by dividing the sum of maximum equivalent elastic stress and stress drop due to creep by the effective Young's modulus. The second term represents an enhancement of the elastic strain range due to plasticity. The last term is a correction to the change of constant volume during plastic deformation and creep (Appendix A7) [4]. Once these parameters are determined the fatigue and creep damage can be calculated and the total damage is determined by using the appropriate interaction rule. Both codes produce similar results regarding fatigue damage, but differences can occur if the creep strain is dominant [58]. Both codes address the fatigue damage by adopting the Miner's law. R5 accounts for the crack initiation by calculating the number of cycles N_i necessary to produce a crack of size a_i, and the number of cycles N_g to make the crack grow to the final size a_0. This allows separating the crack initiation and growth processes. Therefore the size effect issue can be assessed. The two design codes address the creep damage in different ways. ASME NH adopts the Time Fraction (TF) rule to calculate the creep damage:

$$d_c^{TF} = \int_0^{t_h} \frac{dt}{t_f\left(\sigma, T\right)} \tag{2.30}$$

where t_f is the creep rupture time obtained by creep rupture tests, and it is function of stress and temperature.dt is the time increment and t_h is the hold time. Despite its simplicity this approach is not conservative for a small strain range without proper safety factors, and becomes overly conservative for high stress dwell period [58, 59]. In contrast to this, the R5 procedure adopts the Ductility Exhaustion (DE), which is determined by using the following relationship:

$$d_c^{DE} = \int_0^{t_h} \frac{\dot{\bar{\varepsilon}}_c}{\bar{\varepsilon}_c\left(\dot{\bar{\varepsilon}}_c, T\right)} dt \tag{2.31}$$

where t_h is the dwell time, $\dot{\bar{\varepsilon}}_c$ is the instantaneous creep strain rate and $\bar{\varepsilon}_c$ is the material creep ductility. The results generated by the DE produces less scattering results when compared with the TF, making DE more accurate [47]. Despite the reasonable conservative predictions given by the DE, when the initial stress is low, overly conservative results are obtained. This behaviour was studied by Spindler [59], who developed a *"Stress Modified Ductility Exhaustion"* approach to overcome this issue. Furthermore, this approach gives a better prediction of the creep damage due to intermediate creep dwell during the load cycle, in a typical power plant operating scenario [60, 61].

2.6 The Linear Matching Method Framework

The R5 procedure is composed of several steps, which require being accomplished in order to fully assess the integrity a component. A simplified representation of all the major steps is presented in Figure 2.14 in the form of a flowchart, a more extensive description can be found in [62]. Alongside, all the deliverables provided by the LMMF are shown. Both the R5 and LMMF share as starting point the problem description, the thermal and elastic analyses. The first stage of the assessment regards the definition of safe margins against the plastic collapse and creep rupture, if creep is significant. When these checks are not passed, the use of detailed numerical analyses it is recommended. However, full inelastic analyses have two major drawbacks. The first one is the requirement of detailed material constitutive equations. The second one is the high computational cost and inherent convergence issues.

Conversely, the Linear Matching Method has been developed to accurately and efficiently solve these and other design problems, without relying on conservative assumptions or complex constitutive formulations. Once the plastic and creep rupture limits have been determined, a check on the existence of shakedown is performed by a sequence of steps with an increasing complexity. If at least global shakedown cannot be demonstrated, detailed inelastic analyses are recommended. As depicted in Figure 2.14 the LMMF provides numerical procedures to address this crucial step. Both the elastic and global shakedown limits can be calculated for any arbitrary load history, providing upper and lowerbound solutions. Hence if creep is relevant, and the associated dwell time is relatively short the overall load history still the same as for shakedown but stress relaxation cannot occur. Once again the LMMF provides a numerical procedure to calculate the accumulated creep strain in such a loading case, which is always more accurate than the R5 procedure [4].

The last part of the assessment deals with the characterization of the saturated cycle, necessary to evaluate the pure fatigue and creep-fatigue damage. This is done by evaluating the total strain and stress ranges, the start of dwell stress, the associated stress drop, the creep strain rate and creep strain accumulated during the dwell. It is also crucial to properly identify compressive and tensile creep dwells in order to not

introduce produce overly conservative assessments. The LMMF provides two numerical procedures to estimate the steady state cycle, considering pure fatigue or full creep and cyclic plasticity interaction. This approach is different from the R5 procedure, which relies on approximations to calculate the aforementioned quantities. Hence, the use of the LMMF safely reduces conservatisms, but also improves the understanding of the cyclic response of the structure by characterizing complex mechanisms such as creep-ratchetting or cyclically enhanced creep.

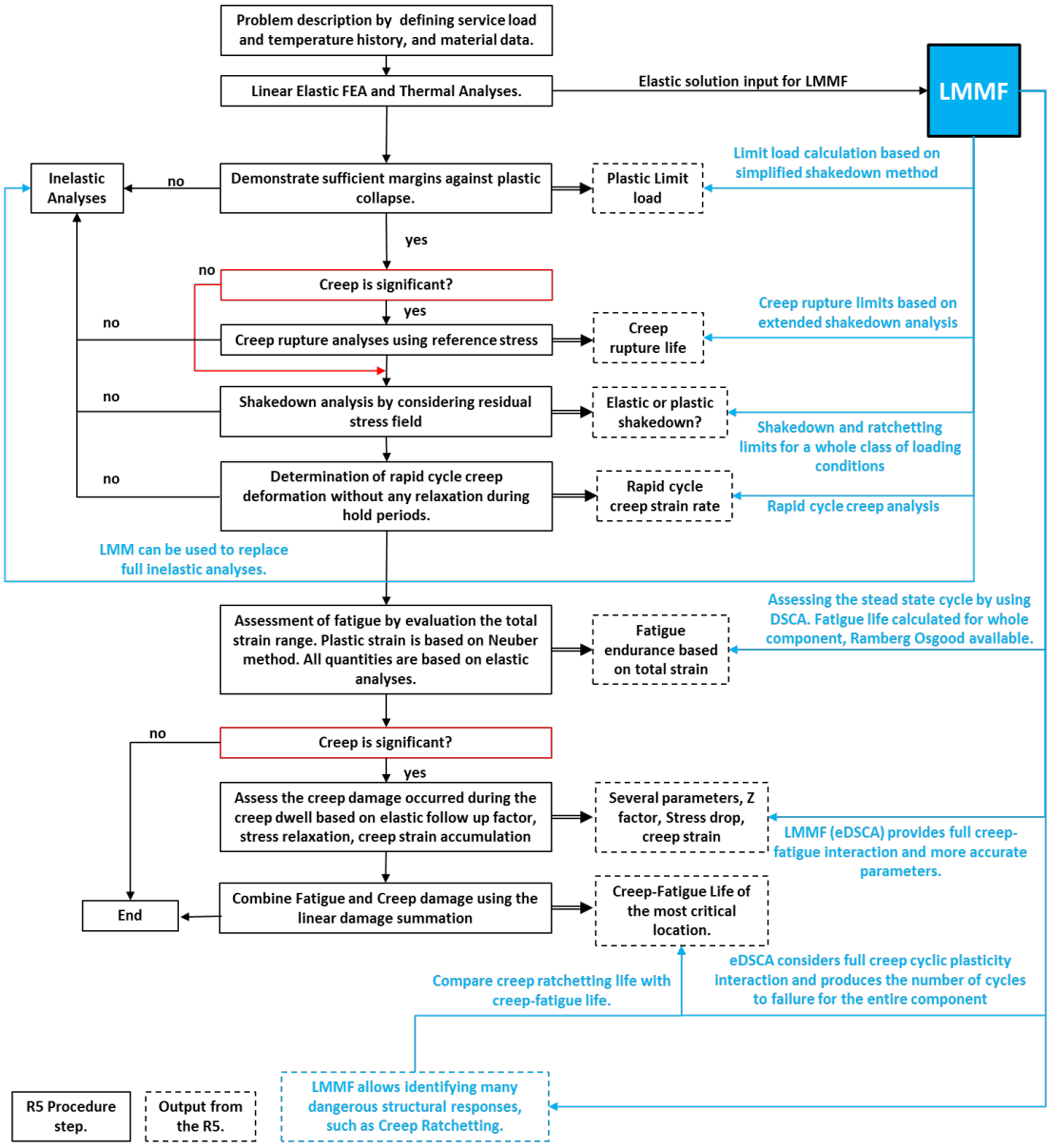

Figure 2.14: Schematic flowchart showing the R5 procedure for structural integrity assessment and LMMF capabilities in support of the R5.

2.6.1 Basic numerical procedure for the LMM

Consider an Elastic-Perfectly Plastic (EPP) body with a volume V and a surface S, which is subjected to a general cyclic load condition. On such body volume is applied a cycling temperature $\lambda_\theta \theta(x,t)$ instead on the surface a constant load $\lambda_p P(x,t)$ acting over part of the structure's surface S_T. The remaining surface is constrained to have no displacement. The time variation considered over a typical cycle is $0 \leq t \leq \Delta t$. Corresponding to these loading histories there exists a linear elastic stress history:

$$\hat{\sigma}_{ij}(x,t) = \lambda_\theta \hat{\sigma}^\theta_{ij}(x,t) + \lambda_p \hat{\sigma}^p_{ij}(x,t) \tag{2.32}$$

where $\hat{\sigma}^\theta_{ij}$ and $\hat{\sigma}^p_{ij}$ denotes the varying elastic stresses due to $\theta(x,t)$and $P(x,t)$, respectively. By selecting the proper values for λ_θ and λ_p a whole class of loading histories can be considered. The general stress field for the cyclic problem involves three different components, the elastic, the constant and the changing residual stress fields.

$$\sigma_{ij}(x,t) = \hat{\sigma}_{ij}(x,t) + \bar{\rho}_{ij}(x) + \rho^r_{ij}(x,t) \tag{2.33}$$

where $\hat{\sigma}_{ij}(x,t)$ represents the linear elastic solution depicted in equation (2.32), $\bar{\rho}_{ij}(x)$ denotes the constant residual stress field which is in equilibrium with zero primary loading and corresponds to the residual stress field at the start and end of the cycle, which is responsible for the elastic shakedown behaviour. Instead, $\rho^r_{ij}(x,t)$ represents the changing residual stress field within the load cycle, responsible for the reverse plasticity and ratchetting behaviours. In order to characterize the critical limits mentioned in the previous section and the steady state cyclic response a minimization process of a functional dependent by an appropriate class of kinematically admissible strain rate history $\dot{\varepsilon}^c_{ij}$ has been created within the LMMF. This minimization process can be expressed in an incremental form as follow:

$$I\left(\dot{\varepsilon}^c_{ij}, \lambda\right) = \sum_{n=1}^{N} I^n \tag{2.34}$$

$$I^n\left(\Delta\varepsilon^n_{ij}, \lambda\right) = \int_V \left\{\sigma^n_{ij}\Delta\varepsilon^n_{ij} - \left[\hat{\sigma}_{ij}(x,t) + \bar{\rho}_{ij}(x) + \rho^r_{ij}(x,t)\right]\Delta\varepsilon^n_{ij}\right\} dV \tag{2.35}$$

$$\rho^r_{ij}(x) = \sum_{n=1}^{N} \Delta\rho_{ij}\left(t_n\right) \tag{2.36}$$

where N represents the total number of load instances considered within the load cycle and $\rho^r_{ij}(x)$ is the summation of all the previous changing residual stress field increments $\Delta\rho_{ij}\left(t_n\right)$. The strain rate history is replaced by a series of strain increments $\Delta\varepsilon^n_{ij}$, as shown by equation (2.35), that occurs at each load instance n within the load cycle. Depending on the design problem the cyclic stress history represented by equation (2.33) can be varied. For elastic shakedown and creep rupture analyses, the changing residual stress field is neglected otherwise a $\rho^r_{ij}(x) \neq 0$ can be considered. A

set of linear incremental relationships for the strain increment can be defined for all these class of problems as follow:

$$\Delta\varepsilon_{ij,l+1}(t_n)' = \frac{1}{2\bar{\mu}_l(t_n)}\left[\hat{\sigma}_{ij}(t_n) + \rho_{ij,l+1}(t_{n-1}) + \Delta\rho_{ij,l+1}(t_n)\right]' \tag{2.37}$$

$$\Delta\varepsilon_{kk,l+1}(t_n)' = 0 \tag{2.38}$$

where notation (') refers to the deviator component of stresses and $\bar{\mu}_l(t_n)$ is the iterative shear modulus obtained from the iterative step l. This iterative shear modulus is obtained by the following linear matching equation:

$$\bar{\mu}_{l+1}(x,t_n) = \bar{\mu}_l(x,t_n)\frac{\sigma_y(x,t_n)_l}{\bar{\sigma}\left(\hat{\sigma}_{ij}(x,t_n) + \rho^r_{ij}(x,t_n)_l\right)} \tag{2.39}$$

where $\bar{\mu}_{l+1}(x,t_n)$ is the iterative shear modulus at the iteration *l+1* for n^{th} load instance associated to the previous iterative step *l*. $\rho^r_{ij}(x,t_n)_l$ is the sum of the constant residual stress field and all the previous changing residual stresses at different load instances. $\sigma_y(x,t_n)_l$ is the iterative von-Mises yield stress model at load instance t_l for the Elastic Perfect Plastic model or for the more refined Ramberg-Osgood one. When one or more creep dwells affect the loading cycle at a predefined load instance n^{th}, the yield stress is replaced by the minimum of the yield stress and creep flow stress. The extended numerical method is fully detailed in chapter 4.

2.6.2 The LMM software tool

From the earliest stage of the LMM development, efforts have been focused on the development of the ABAQUS user subroutines. The user has to interact with the FORTRAN source code to modify it accordingly to perform the desired analysis. A few actions such as the definition of the loading history need to be carefully taken by the user. Such procedure is not straightforward for engineers without any programming experience, and can introduce errors that invalidate the results. To solve this issue, and to enhance the usage of the LMMF from industries, a Graphical User Interface (GUI) and an autonomous ABAQUS plug-in have been developed recently [63]. The aim of the plug-in is to adopt the information provided by the user through a GUI, to automatically modify the finite element model in the Abaqus/CAE environment, and the particular keywords required to output all the required parameters. This informations include material properties, boundaries conditions and loading cycle definition. This solution allows a convenient use of the LMM, but at the same time, it reduces the possibility to introduce errors. The user can select the model and the analysis type required through the GUI (Figure 2.15a). When this is done, the user can either extract or provide the material constants required (Figure 2.15b).

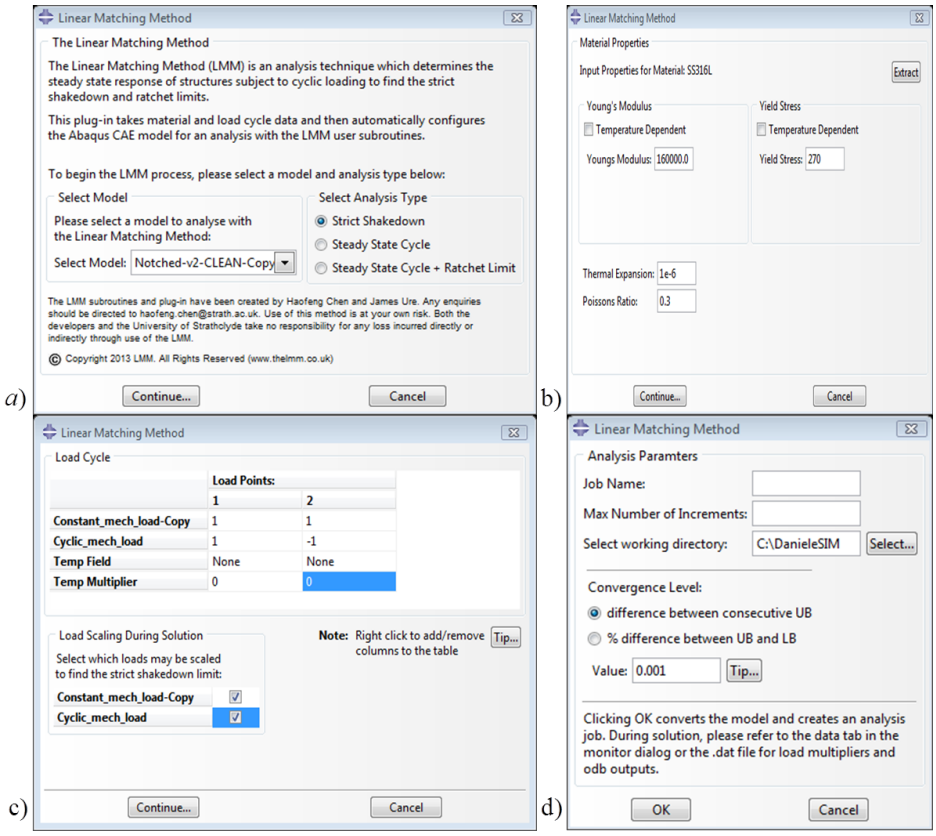

Figure 2.15: a) LMM main menu for analysis type and model selection, b) material properties selection, c) load cycle construction menu, d) analysis parameters and convergence methods and level menu.

The plug-in checks each value provided by the user to identify any possible error. When an error occurs a dialog box appears, with an error code and a brief explanation that is useful for debugging. The definition of the loading cycle is performed by compiling a load table (Figure 2.15c), where multiple load points can be created by using individual load or temperature field defined in the CAE. This approach allows the user to consider a whole class of different loading conditions. Once the load history is defined the desired convergence rule can be selected (Figure 2.15d). The maximum number of increments and the name of the analysis file can be decided to generate a successful LMM job. It is worth noting that the LMM software tool has the capability to perform multiple Computer Processing Units (CPUs) analysis. This feature is crucial for the large model when 3D complex geometries are considered.

2.6.3 Case study: notched bar

To show the capabilities of the LMMF, a benchmark numerical example is presented. A bar with a circumferential round notch is considered. Its geometry and mesh are represented in Figure 2.16a. Due to the symmetry of the problem, an axisymmetric model is adopted.

Table 2.1: 316(N)L mechanical properties at $550°C$

Youngs modulus [MPa]	160000		
Poissons ratio	0.3		
Yield stress [MPa]	270		
Ramberg-Osgood	B = 1741.96		$\beta = 0.2996$
Norton-Bailey	A = $6.604 \cdot 10^{-19}$	n = 5.769	m = −0.55

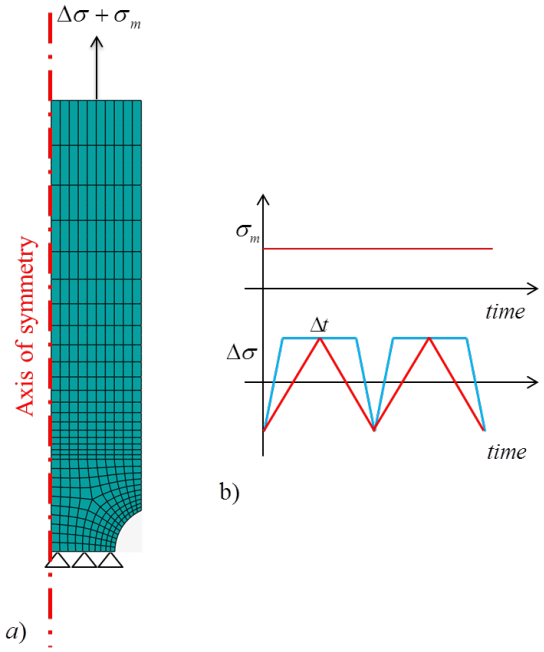

Figure 2.16: a) Finite element model of the circumferential notched bar, b) and the different loading histories considered.

The mesh is composed of 336 quadratic quadrilateral elements CAX8R in ABAQUS, with a reduced integration scheme. Both the cyclic and constant mechanical loads are applied and their loading histories are shown in Figure 2.16b. $\Delta\sigma$ is a cyclic axial load with R=-1, and σ_m is a constant load. The bar is exposed homogeneously to a high and constant temperature of $550°C$. This type of loading condition allows for the consideration of a large number of different loading histories. For creep-fatigue interaction study a hold time Δt is considered at the tensile peak, where significant creep damage is expected. The material used for this example is stainless steel 316(N) L, and all the elastic and inelastic material properties are presented in Table 2.1.

2.6.4 Cyclic response, plastic collapse and creep rupture

By using the Elastic Perfect Plastic (EPP) material model, the shakedown and ratchet limit interaction diagram obtained for this notched bar subjected to a cyclic load history are shown in Figure 2.17. The vertical and horizontal axes correspond to the cyclic and constant mechanical load respectively, both normalised to the material yield stress. In Figure 2.17, the shakedown limit is represented by a continuous black line, the ratchet

limit and limit load by a dashed dot green and violet line respectively. When subjected to a cyclic load within the shakedown limit the response of structure becomes Elastic Shakedown (ES), where the material responses entirely elastically except for an initial plastic strain occurred at the beginning of load cycle.

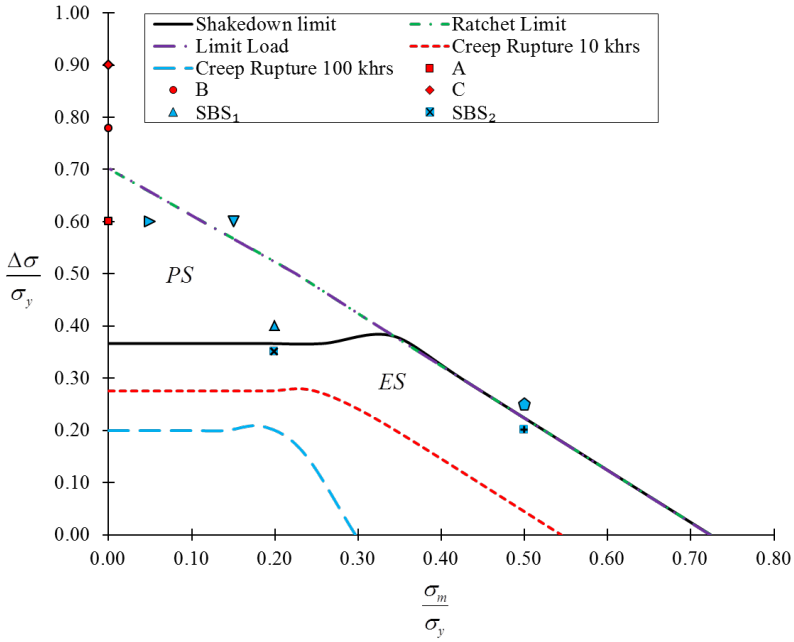

Figure 2.17: Notched bar interaction diagram, shakedown, ratchet and creep rupture limit.

If the component operates in the Plastic Shakedown (PS) region, low cycle fatigue is expected, and a closed loop cycle is present. Contrary to the Bree-like diagram for a cycling thermal load and a constant mechanical load, the ratchet limit and the limit load are coincident as shown in Figure 2.17. This is due to the presence of a cycling and constant primary loads, which make ratchet limit and limit load identical. The results obtained provide a clear picture of the cyclic behaviour of the structure, for different magnitudes of the loads applied. To demonstrate the accuracy of the limits predicted a series of Step-by-Step (SBS) analyses had been performed for six cyclic load points shown in Figure 2.17. Figure 2.18a presents the obtained plastic strain magnitude histories for the cyclic load points SBS_2 and SBS_4. Both cyclic load points exhibit a clear shakedown behaviour. Figure 2.18b shows calculated plastic strain magnitude histories for the cyclic load points SBS_1 and SBS_5, both exhibiting a reverse plasticity behaviour. The analyses for the last two cyclic load points SBS_3 and SBS_6 aborted before completing. Both the cyclic load points are over the limit load, hence it is impossible to meet the equilibrium. These results from the SBS analyses demonstrate the accuracy of the shakedown limit and ratchet limit (limit load) prediction obtained by the LMM. Furthermore, it is worth nothing that the computational cost required by incremental analyses is much higher than the LMM. For the shakedown and ratchet analysis, the advantage of the LMM over the SBS is that the LMM is a direct method that exploits the bounding theorems and is able to calculate the limits directly and accurately. Instead, the SBS analysis needs a significant number of trial and error

attempts to locate these limits. Indeed a single SBS calculation can only determine whether the component is in shakedown or ratchetting.

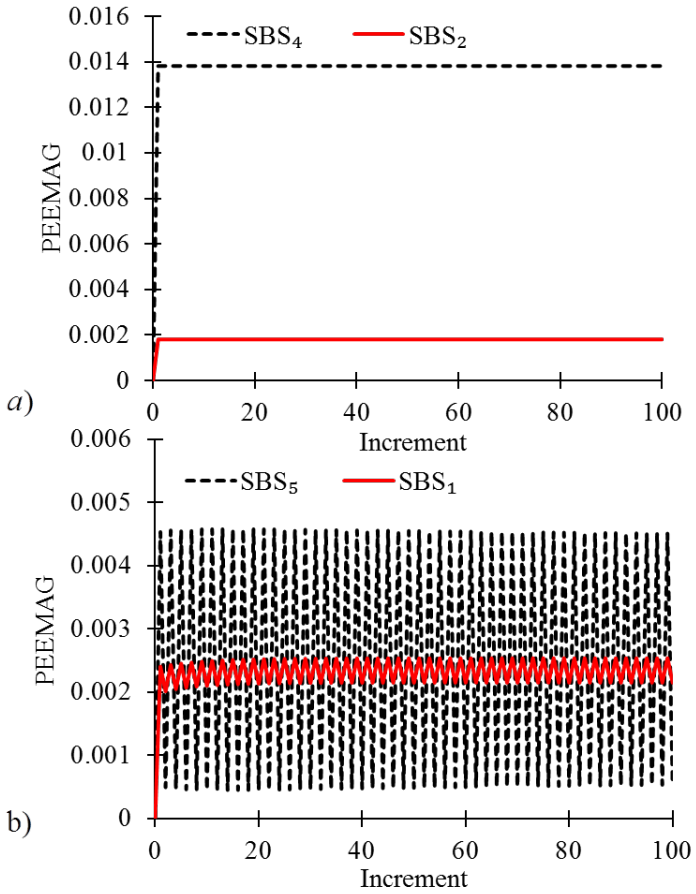

Figure 2.18: Plastic strain magnitude histories for different cyclic loading points obtained by Step-by-Step analyses.

When the component is subjected to an elevated temperature the creep rupture limit, need to be assessed. For this purpose, the LMM has recently been extended in order to accurately calculate the rupture limit for the desired rupture time, by an extended shakedown procedure, as used in the R5, but in a much more accurate and robust way. In the LMM creep rupture analysis, the steady state cyclic stress is accurately evaluated by considering the associated residual stress at each integration point. Furthermore, the temperature dependent creeps rupture stresses are also considered for the entire structure without any conservative assumptions. In Figure 2.17, two creep rupture limits are shown for 10000 (short dash) and 100000 (long dash) hours. In this assessment, the reduction of material strength across the entire specimen is homogeneous due to the constant and homogeneous temperature.The most critical location is always located at the root of the notch. If the applied cyclic loading point is outside the creep rupture limit, the component will rupture at a stage earlier than its designed life.

2.6.5 Creep fatigue assessment

Low cycle fatigue assessment is needed when the component operates in the plastic shakedown (PS) domain, or when the cyclic response results in a closed hysteresis loop due to a creep dwell. In order to predict the number of cycles to failure, the maximum total strain range is calculated by the LMM for the notched specimen. Then the strain-life relations obtained from the experimental test are used to predict the number of cycles to failure. These predictions are then compared in Figure 2.19 with the scaled strain-life curve taking into account the notch factor, due to experimental data being unavailable for the geometry studied.

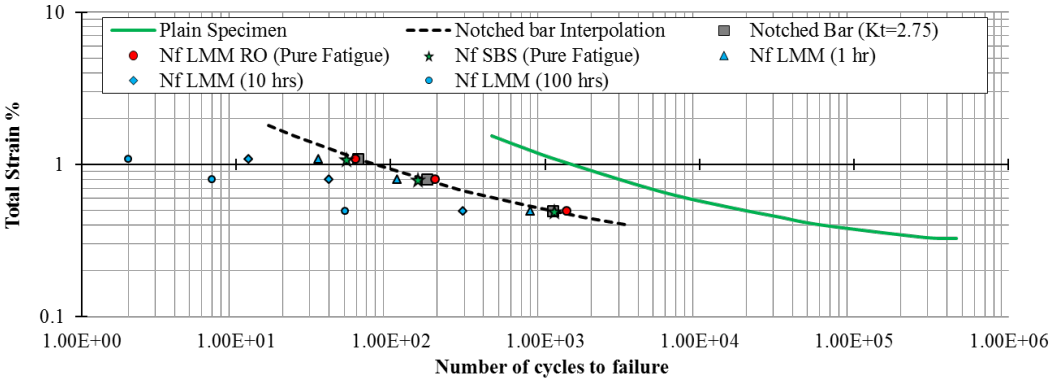

Figure 2.19: Results for pure fatigue and creep-fatigue assessment of a circumferential round notched bar with pure fatigue life curve.

In order to study the effect of the material hardening on the low cycle fatigue life, the Ramberg-Osgood material model is adopted, to fully describe the steady state cycle response. The parameters for the material are reported in Table 2.1. For this work, only small applied strain amplitudes between 0.25-0.6 % are considered, which correspond to more practical industrial application [64]. For the LCF assessment with creep-fatigue interaction, three tensile peak dwell periods of 1, 10 and 100 hours are considered. A series of parameters is required to assess fully the creep-fatigue interaction, which leads to the crack initiation at the most critical location. These parameters are discussed by [65], and are the total strain range, the stress at the start of the dwell, the creep stress drop, the associated creep strain increment and the elastic follow up factor. Contrary to the R5, which bases the calculation of many of the parameters mentioned above on a series of approximate quantities obtained by the elastic solution, the LMM fully considers the creep-fatigue interaction during the cycle and accurately calculates the elastic, plastic and creep strains and associated stresses by adopting robust solid mechanics concepts. Figure 2.19 shows the results of pure fatigue and creep-fatigue assessment of the specimen subjected to the cyclic loading point A, B and C illustrated in figure 2.17. Figure 2.19 illustrates the comparison between the number of cycles to failure between those expected by taking into account the notch factor (grey square), the predicted endurances by the LMM (red dot), and by the SBS (green star) adopting a non-linear kinematic hardening present in ABAQUS. A good agreement is achieved for the pure fatigue predictions, especially for intermediate and large strain ranges (cyclic load point B and C). However, a slightly less conservative result is observed for

the smallest applied total strain (cyclic load point A), with an error of 23 % over the expected number of cycles to failure by taking into account the notch factor. The SBS results match with the expected results for small strain and become more conservative for large strains. However, the CPU time required by the SBS analysis is around 1104 seconds. Instead, only 116 seconds for the LMM adopting the Ramberg-Osgood material model. The SBS requires 16650 increments to complete all 150 steps. Instead, the LMM needs only 150 increments for the single analysis step. The impact of creep dwell on the life of the specimen is investigated, and it is also shown in 2.19. The creep-fatigue assessment results are presented for the three dwell times considered. For 1 hour dwell, the life reduction is around 42%, and the damage due to fatigue is larger but comparable to the one produced by creep. However, when the creep dwell increases creep-fatigue interaction becomes relevant, and the life reduction is more significant. The further stress relaxation due to the increase of the dwell time enhances the reversed plasticity during the reverse loading. Figure 2.20 shows how the cyclic response is affected by the increase of the creep dwell.

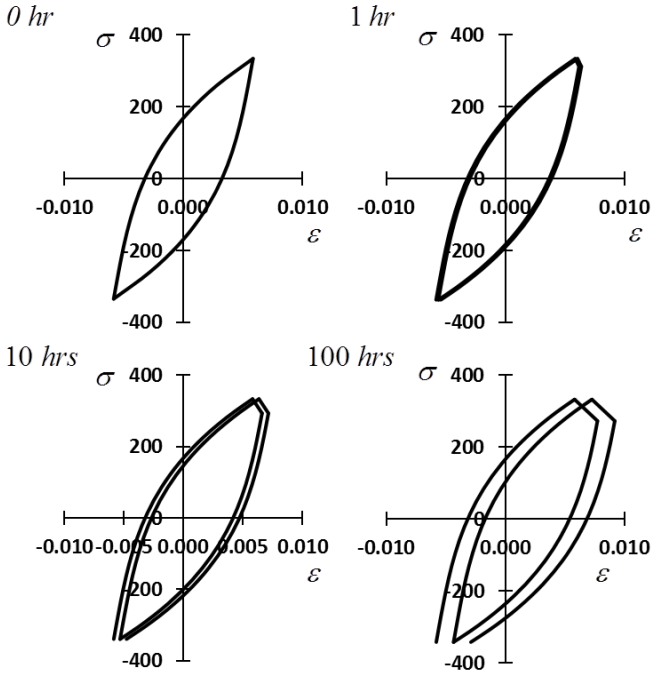

Figure 2.20: Cyclic response at different creep dwells time for cyclic loading point A at the most critical location.

The effect of creep fatigue interaction on the notched bar life is shown in Figure 2.21, for cyclic load point A (0.25% applied strain amplitude) at different dwell times. From the plot on the left the creep damage increase with the dwell time, and after a precise threshold it is larger than the fatigue damage. Despite the stress relaxation, the fatigue damage is not enhanced significantly. The hardening allowed by considering the Ramberg-Osgood material model allows better prediction of the reversed plasticity. By focusing on the same figure up to 30 hours, a turning point can be identified, which is about 10 hours. Between 10 and 15 hours, the creep-fatigue interaction is maximum. After 15 hours the creep damage increases and becomes the most important failure

mechanism.In Figure 2.22 the creep strain against the net plastic strain is reported for each dwell time considered.

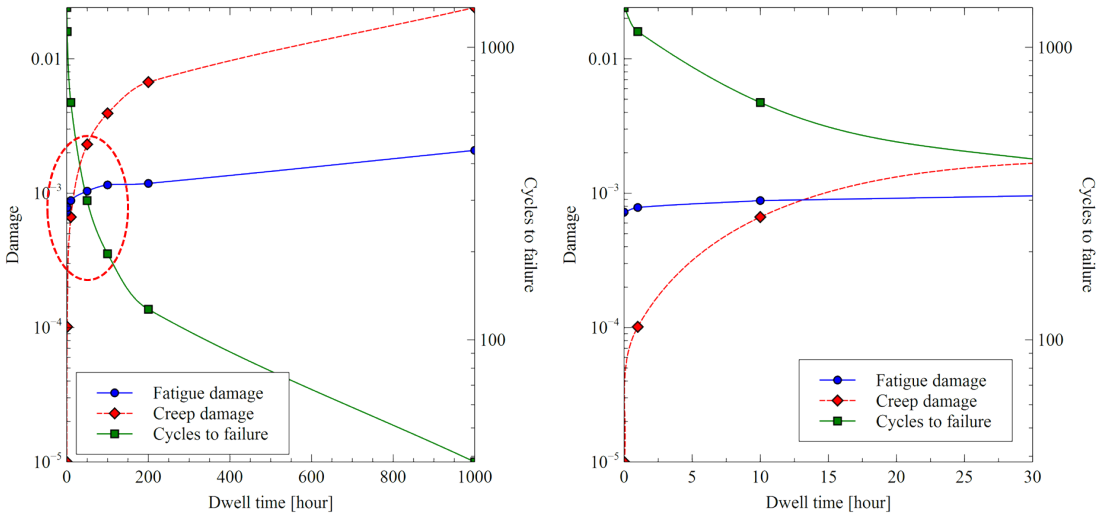

Figure 2.21: Creep and fatigue damages against dwell time, and notched bar endurance.

When the net plastic strain due to the loading and unloading phase is not equal to the creep strain accumulated over the dwell creep-ratchetting occurs. For this loading condition and a dwell time larger than 10 hours, the results are above the closed loop limit (dashed line). The associated creep-ratchetting mechanism is creep strain dominated. However, it is important to clarify if this mechanism is relevant for the specimen integrity. For this case, which corresponds to an applied strain amplitude of 0.25 %, the creep ratchetting is not so severe. For 1000 hours (Figure 2.22) it does not produce significant damage compared to the creep-fatigue interaction. The expected failure is at 98 cycles, but the creep-fatigue cycles to failure have been estimated to about 40 cycles.

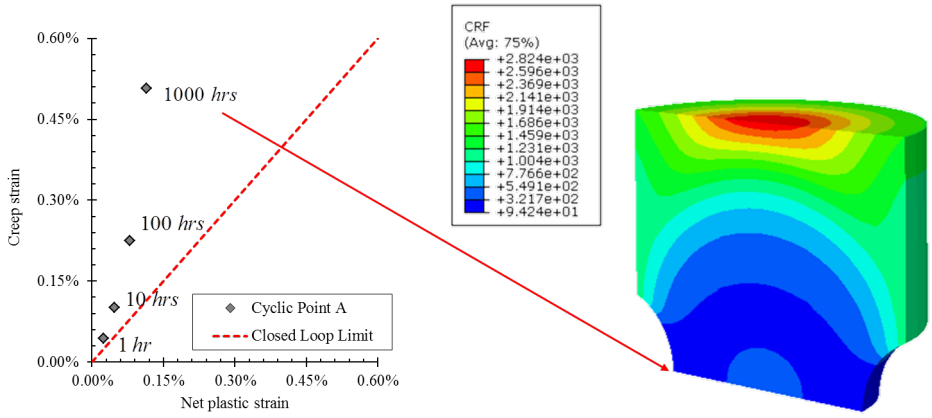

Figure 2.22: Creep-ratchetting interaction diagram at different creep dwells time for cyclic loading point A at the most critical location, and contour of the cycles to failure for creep-ratchetting at 1000 hours.

2.7 Conclusions

A detailed review of the main aspects of creep and creep-fatigue interaction in structures at high temperature is given. For creep-fatigue interaction, the creep dwell within a cyclic load is confirmed to cause a series of dangerous mechanisms, including the creep enhanced plasticity/fatigue, cyclically enhanced creep damage, and creep ratchetting. If the creep-fatigue interaction produces a closed hysteresis loop response, the damage originates due to the combined action of the cyclically enhanced creep and the increased fatigue damage due to the stress relaxation during the dwell period. Alternatively, if the creep strain becomes too large to be compensated by the reverse plastic strain, or the significant stress drop during the dwell period leads to a significantly reversed plastic strain, the closed hysteresis loop may become open. This inelastic strain accumulation is known as *Creep Ratchetting*, and it has been recommended for this to be assessed separately with the creep-fatigue damage assessment.

The main differences and crucial points for the creep-fatigue interaction assessment of both ASME NH and R5 have been reviewed. It is worth noting that both codes adopt conservatisms in the entire creep-fatigue assessment procedure. In terms of creep damage assessment, the use of creep ductility and stress modified creep ductility allows R5 to produce less conservative results for any strain range. Another point of difference is the material selection, which is very strict for the ASME, whereas the R5 is flexible and allows the user to make the appropriate selection. This difference becomes crucial when assessing new components, which are intended to operate at extremely high temperatures where creep-fatigue interaction is dominant. R5 can be used in addition to the ASME NH when this provides overly conservative results due to extreme cyclic loading conditions.

The assessment of creep rupture and creep-fatigue interaction through incremental finite element analyses have also been reviewed. For creep rupture the use of continuum damage mechanics using stress-based methods is demonstrated to be effective. However, these methods are very sensitive to the material parameters, requiring a very detailed optimisation process. This also requires many experimental tests, which are not always feasible. Furthermore, the stress-based methods are recognised to be mesh sensitive and highly affected by the load level within the structures. Finally, the computational cost is significant when 3D structures are modelled. For creep-fatigue interaction, incremental analyses have been used demonstrating how these are in several cases inefficient compared to direct methods such as the LMM.

A complete overview of high-temperature design and assessment capabilities of the Linear Matching Method Framework is given. The LMM has been demonstrated to be capable of improving the assessment in a robust and reliable way by reducing the unnecessary conservatism present in the design code. The introduction of the LMM software tool using an ABAQUS CAE plug-in with an intuitive GUI makes the LMMF easily accessible to a wide range of users, including those who have little knowledge in theory and programming skills. The benchmark example of the notched bar demonstrates the effectiveness of the method, and several of analysis types are achieved with the minimum number of material properties.

Chapter 3

Creep rupture assessment by a robust creep data interpolation using the LMM

3.1 Introduction

In engineering a great number of structures are subjected to the action of combined loads, especially mechanical and thermal loading. In particular fields of engineering like aerospace and nuclear among many others, creep is a remarkable phenomena. Creep rupture is identified during uni-axial testing, and is observed as a rapid strain increase in a short time period. The source of creep damage is related to the growth and coalescence of voids in the material microstructure. The assessment of this degenerative process is necessary to establish in which location and how the component will fail. Various of creep damage models have been proposed, such as the Kachanov-Rabotnov model [30, 31], or others [15, 32, 66, 67]. Approaches like these relying on detailed creep strains are able to simulate the entire damage process during creep analysis, but require numerous creep constants in the constitutive equation, which are not always available. Furthermore, the applied load is typically monotonic in these creep analyses, and greater effort is necessary when simulating a cyclic loading condition. For industrial applications, usually it is important to employ methods based upon the creep rupture data [4] which are able to simulate a precise phenomenon with fewer constants as possible, and efficiently consider practical cyclic thermal and mechanical loading conditions.

For this consideration the Linear Matching Method (LMM) introduced an approach to simulate the creep rupture effect by extending the shakedown analysis method [68, 69]. This approach evaluates the creep rupture limit using an extended shakedown method by the introduction of a revised yield stress, which is calculated comparing the material yield stress with a creep rupture stress obtained by an analytical formulation. The assessment of creep rupture limit in this way does not need to explicitly calculate the creep strain during the component lifetime, thus avoiding difficulties from using detailed creep constitutive equation. The advantages of this approach on the basis of creep rupture data are the limited amount of material data required, and the capability to construct a complete creep rupture limit for different rupture times. The method is

capable of identifying the most critical areas where the failure will occur, and also to highlight which type of failure mechanisms (plasticity failure or creep rupture) will be dominant. It is worth noting that the LMM creep rupture analysis method for cyclic load condition is also able to evaluate the monotonic loading condition as a special case, associated with an extended limit analysis. The proposed LMM creep rupture concept has been verified [69]), however, it does not provide an accurate model for various alloys, where creep rupture mechanisms can be notably different, and the analytical function in [19] can provides inaccurate predictions.

The aim of this study is to develop a more flexible and accurate numerical method capable of providing an accurate creep rupture stress to replace existing analytical creep rupture stress function adopted within the LMM creep rupture analysis, by investigating various interpolation and extrapolation methods for the calculation of creep rupture stress for the entire range of temperature and creep rupture time using limited creep rupture experimental data. For this purpose, three distinct methods a) linear interpolation method, b) logarithm based polynomial relationship and c) the Larson Miller parameters, are investigated and compared to produce the most accurate prediction. The aim of this chapter is also to implement the interpolation and extrapolation methods on creep rupture data into the LMM creep rupture analysis method, and apply this new procedure to a couple of practical examples of creep rupture analysis. The first example provides a benchmarking, which analyses creep rupture limits of a plate with a hole subjected to a cyclic thermal load and a constant mechanical load. The second example performs creep rupture analyses of a two-pipe structure under combined action of a cyclic thermal load and a constant mechanical load, and is used to further confirm the efficiency and effectiveness of the new method, and to discuss distinct failure mechanisms associated with various creep rupture limits. For both numerical examples, step-by-step analysis is also used to verify the accuracy of the proposed creep rupture assessment method.

3.2 LMM approach to creep rupture analysis

The LMM approach to creep rupture analysis is performed through an extended shakedown analysis [69, 70], where the original yield stress of material in the analysis is replaced by so-called revised yield stresses at each integration points for all load instances in the finite element model. Using the strategy of extended shakedown analysis, the creep rupture limit can be assessed for both the cyclic and monotonic load conditions depending upon the number of load instances in a cycle. In the method, the revised yield stress σ_y^r is determined by the minimum of original yield stress of material σ_y and a creep rupture stress σ_C for a predefined time to creep rupture t_f. With this scheme, the creep rupture limit of a structure can be evaluated efficiently and conveniently by using the creep rupture data only, without the usage of detailed creep constitutive equations. Apart from the time to rupture t_f, the creep rupture stress σ_C also depends on the applied temperature T . [69] proposed an analytical formulation for the calculation of the creep rupture stress, which is the product of the yield stress of material and two analytical functions as shown below:

$$\sigma_c\left(x_i, t_f, T\right) = \sigma_y \cdot R\left(\frac{t_f}{t_0}\right) \cdot g\left(\frac{T}{T_0}\right) \tag{3.1}$$

where x_i is the position of the integration point, t_0 and T_0 are material constants, $R\left(\frac{t_f}{t_0}\right)$ is the dimensionless function of a given time of creep rupture t_f, and $g\left(\frac{T}{T_0}\right)$ is the function of the applied temperature T. It is worth noting that for several of practical materials a unique equation 3.1 of creep rupture stress is not available. Hence a compromised scheme was provided by [69] for a particular case of plate with a hole, where the function $R\left(\frac{t_f}{t_0}\right)$ was a known parameter, and therefore no detailed formulation was needed for it. The function $g\left(\frac{T}{T_0}\right)$ that reflects the creep rupture stress dependency on temperature is formulated by:

$$g\left(\frac{T}{T_0}\right) = \frac{T_0}{T - T_0} \tag{3.2}$$

However, in practical applications with limited experimental creep rupture data, it would be impossible to formulate equation (3.1) for the analysis. To overcome this, a new numerical scheme to calculate the creep rupture stress using limited rupture experimental data is proposed within this work. Once the revised yield stress σ_y^r is obtained from the creep rupture stress for a given time to creep rupture and temperature, it allows an extension of the shakedown procedure for the creep rupture analysis. In the rest of this section, the applied LMM numerical procedure [69] for the creep rupture assessment is summarised. The material is considered isotropic, elastic-perfectly plastic. The stress history has to satisfy both the yield and the creep rupture condition. In order to define a loading history an elastic stress field $\hat{\sigma}_{ij}$ is obtained by the sum of different elastic thermal stress $\hat{\sigma}_{ij}^{\theta}$ and mechanical stress $\hat{\sigma}_{ij}^{P}$. Such elastic stress fields are associated with load parameter λ, which allows considering a wide range of loading histories:

$$\lambda\hat{\sigma}_{ij} = \lambda\hat{\sigma}_{ij}^{\theta} + \lambda\hat{\sigma}_{ij}^{P} \tag{3.3}$$

The method relies on a kinematic theorem [71], which can be expressed by the incompressible and kinematically admissible strain rate history. This strain rate $\dot{\varepsilon}_{ij}^{c}$ is associated with a compatible strain increment $\Delta\varepsilon_{ij}^{c}$ using an integral definition:

$$\int_0^{\Delta t} \dot{\varepsilon}_{ij}^{c} dt = \Delta\varepsilon_{ij}^{c} \tag{3.4}$$

A creep rupture limit multiplier can be calculated, taking into account the load history

introduced:

$$\lambda_{creep} \int_V \int_0^{\Delta t} \left(\hat{\sigma}_{ij}\dot{\varepsilon}^c_{ij}\right) dtdV = \int_V \int_0^{\Delta t} \sigma^c_{ij}\dot{\varepsilon}^c_{ij} dtdV \tag{3.5}$$

For creep rupture analysis, σ^c_{ij} is the stress at the revised yield associated with the strain rate history $\dot{\varepsilon}^c_{ij}$, $\hat{\sigma}_{ij}$ and is the linear elastic stress field associated with the load history for $\lambda = 1$. Combining the associated flow rule, equation (3.5) can be simplified and the creep rupture limit multiplier λ_{creep} can then be calculated by the following equation:

$$\lambda_{creep} = \frac{\int_V \int_0^{\Delta t} \sigma^R_y(t) \cdot \bar{\dot{\varepsilon}} \left(\dot{\varepsilon}^c_{ij}\right) dtdV}{\int_V \int_0^{\Delta t} \left(\hat{\sigma}_{ij} \cdot \dot{\varepsilon}^c_{ij}\right) dtdV} \tag{3.6}$$

where $\sigma^R_y(t)$ is the revised yield stress which is determined by the minimum of the yield stress of material $\sigma_y(t)$ and the creep rupture stress $\sigma_C(t)$ depending on the temperature at each integration point and the predefined creep rupture time. Equation (3.6) contains two volume integrals, which can be calculated via plastic energy dissipations from the Abaqus solver [16]. An iterative solving process based on a number of linear problems can be arranged [70]. The first step initiates with plastic strain rate $\dot{\varepsilon}^i_{ij}$, from which a linear problem is posed for a new strain history $\dot{\varepsilon}^c_{ij}$,

$$\dot{\varepsilon}^{c\prime}_{ij} = \frac{1}{\mu}\left(\lambda^i_{creep}\hat{\sigma}_{ij} + \bar{\rho}^c_{ij}\right)' \tag{3.7}$$

$$\dot{\varepsilon}^c_{kk} = 0 \tag{3.8}$$

$$\mu = \frac{\sigma^R_y}{\bar{\dot{\varepsilon}}^i} \tag{3.9}$$

where notation ($'$) refers to the deviator component of stress and strain, $\bar{\rho}^c_{ij}$ is the constant residual stress field. Equation (3.9) describes the matching condition between the linear and non-linear materials, where the shear modulus μ is defined as the ratio between the revised yield stress σ^R_y and the equivalent strain rate $\bar{\dot{\varepsilon}}^i$. To obtain the solution over the cycle, the equation (3.8) is further integrated over the cycle time producing the following relations:

$$\Delta\varepsilon^{c\prime}_{ij} = \frac{1}{\bar{\mu}}\left(\bar{\rho}^c_{ij} + \sigma^{in}_{ij}\right)' \tag{3.10}$$

$$\sigma_{ij}^{in} = \bar{\mu} \left(\int_0^{\Delta t} \frac{1}{\mu(t)} \lambda_{creep}^{i} \hat{\sigma}_{ij}(t) dt \right) \tag{3.11}$$

$$\frac{1}{\bar{\mu}} = \int_0^{\Delta t} \frac{1}{\mu_n} dt \tag{3.12}$$

where $\Delta\varepsilon_{ij}^{c}$ is the plastic strain increment, σ_{ij}^{in} is the scaled elastic stress component over the cycle and $\bar{\mu}$ is the overall shear modulus for the cycle period Δt. Once the solution for this incompressible linear problem is calculated, a load multiplier λ_{creep}^{f} can be obtained using the strain rate history $\dot{\varepsilon}_{ij}^{c}$ in equation (3.6). For each increment the creep rupture limit calculated has to satisfy this inequality $\lambda_{creep}^{f} \leq \lambda_{creep}^{i}$. The repeated use of this procedure generates a monotonically reducing sequence of creep rupture limit multipliers, which will converge to a minimum upper bound when the difference between two subsequent strain rate histories has no effect on creep rupture limit. When convergence occurs, the stress at every Gauss point in the finite element mesh is either equal or lower than the revised yield stress. For a practical case of study, a load history can be defined as a sequence of straight lines in the load space, and the entire load history can be fully described by the vertices. These vertices represent a number of stress fields, which create the stress history associated with the corresponding loading history. Considering a strictly convex yield condition that includes the von Mises yield condition, the plastic strain occurs only at these vertices. In such a case the strain rate history over the cycle can be expressed by a sum of plastic strain increments at these vertices in the load space. By adopting this procedure the creep rupture limit can be calculated by an iterative process which leads to a unique solution, considering only the most relevant points of the loading cycle [69], and avoiding the use of creep constitutive equations which are normally difficult to be obtained.

3.3 Numerical schemes on creep rupture stress using limited experimental data

Equation (3.1) provides an analytical solution to the creep rupture stress, with no direct relationship with experimental data. The aim of this new approach is to use limited experimental rupture data to calculate the correct creep rupture stress. The interpolation and extrapolation on creep rupture experimental data is a challenging field, on which many other researchers [26, 27, 29, 72, 73] worked to produce reliable long term creep rupture data. In order to interpolate and extrapolate creep rupture data required for the LMM creep rupture analysis, different approaches and strategies are investigated. The first strategy investigated is a linear interpolation. The requested material property is estimated by linear interpolation in the smallest temperature range available. When the temperature is out of the range provided, extrapolation needs to be performed. This approach is straightforward, but has a serious weakness. The accuracy relies on the number of data points provided. If the temperature range of simulation is wider than the available experimental one, a remarkable overestimation of creep rupture stress is possible. Furthermore, such a method is not capable of fitting complex non-linear material behaviour especially at high temperature with scattering

data. The second approach uses a polynomial logarithmic relationship between the stress and temperature, and least square method is adopted to perform the calculation of polynomial coefficients. The "best" fit is the one that minimizes the square of the error, expressed by the following equation [74]:

$$err = \sum_{i=1}^{n} (y_i - (a \cdot x_i + b))^2 \tag{3.13}$$

To minimize the error the constants have to be precisely evaluated. The derivatives of the error with respect to the variables are fixed to zero, obtaining two linear equations. These equations can be solved, gathering a matrix formulation for a first order linear interpolation, which does not always provide a good agreement with experimental data. Therefore, to overcome this issue, a more general formulation is introduced. The error that has to be minimized is expressed by the following relationship:

$$err = \sum_{i=1}^{n} \left(y_i - \left(a_0 + \sum_{k=1}^{j} a_k x^k \right) \right)^2 \tag{3.14}$$

In order to do this a derivative for each coefficient is needed, and each equation is set to zero. For j that represents the order and n the number of data points the following equation is obtained:

$$\frac{\partial err}{\partial a_j} = -2 \sum_{i=1}^{n} \left(y_i - \left(a_0 + \sum_{k=1}^{j} a_k x^k \right) \right) x^j = 0 \tag{3.15}$$

This general formulation can be represented in a matrix formulation, and the Gaussian elimination is used to achieve the system solution.

$$\begin{bmatrix} n & \sum x_i & \sum x_i^2 & \cdots & \sum x_i^j \\ \sum x_i & \sum x_i^2 & \sum x_i^3 & \cdots & \sum x_i^{j+1} \\ \sum x_i^2 & \sum x_i^3 & \sum x_i^4 & \cdots & \sum x_i^{j+2} \\ \vdots & \vdots & \vdots & \ddots & \vdots \\ \sum x_i^j & \sum x_i^{j+1} & \sum x_i^{j+2} & \cdots & \sum x_i^{j+j} \end{bmatrix} \begin{bmatrix} a_0 \\ a_1 \\ a_2 \\ \vdots \\ a_j \end{bmatrix} = \begin{bmatrix} \sum y_i \\ \sum x_i y_i \\ \sum x_i^2 y_i \\ \vdots \\ \sum x_i^j y_i \end{bmatrix}$$

Using this formulation different interpolating equations can be constructed for the temperature (T) dependent creep rupture stress σ_C. The polynomial formulation considered for a specific $j$order is the following:

$$\log(\sigma_c) = a_0 + a_1 (\log(T)) + a_2 (\log(T))^2 + \ldots + a_j (\log(T))^j \tag{3.16}$$

The third method evaluated is the Larson Miller parameter which is based on time-temperature parameters [26]. Such a method is used to determine the creep master curves, compensating time with temperature to predict long term creep data. The Larson Miller parameter is widely used for long term creep rupture data prediction and for master curve extrapolation using short term experimental results. It relies on the assumption that a coincident point exists for all iso-stress plots. The Larson-

Miller parameter can be used to establish a relationship between the rupture stress, the temperature and rupture time allowing extrapolation for long term creep. This parameter is defined by the following expression:

$$P_{LM} = \frac{(T + 273.15) \cdot (\log(t_f) + C)}{1000} \tag{3.17}$$

where T is the temperature expressed in Celsius degree, t_f is the time to rupture measured in hours and C is a material constant, normally around 20-22. The first step is to calculate the P_{LM} values of all the data available, obtaining a P_{LM} versus $\log(\sigma)$ plot. A second order polynomial equation is used to fit the data points:

$$\log(\sigma) = a_0 + a_1 P_{LM}(T) + a_2 (P_{LM}(T))^2 \tag{3.18}$$

The three parameters $[a_0, a_1, a_2]$ are calculated using the least square method. Adopting these parameters it is possible to extrapolate data over the temperature for the same rupture time. If necessary such method is capable of extrapolating the rupture stress over the time. Equation (3.18) makes the creep stress directly related to the Larson Miller parameter, for a defined rupture time, temperature, and constant C that is shown in equation (3.17) and is material dependent.

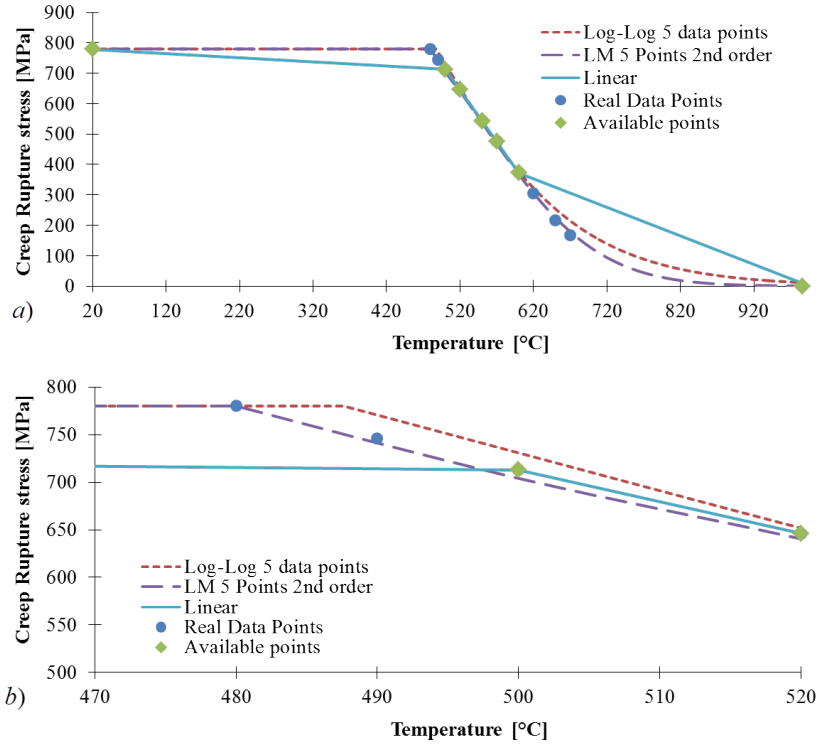

Figure 3.1: a) Interpolation of experimental creep rupture data with three methods b) Close view of creep rupture interpolation at lower temperatures

In order to find the best numerical scheme, a comparison between these approaches is shown in Figure 3.1, which is obtained by interpolating and extrapolating Nimonic 80-A rupture data. In order to reproduce the common lack of availability of data

for a wide range of temperatures only five data points are used ("Assumed Available points") over the nine presented on the data sheet ("Real Data Points"). Figure 3.1a shows a complete view of the interpolation results. It is clear how linear interpolation overestimates rupture stress for high temperatures and contrary underestimates it for low temperatures.

The other two methods instead are able to provide much more accurate rupture data, and the Larson Miller approach is the one which leads to the most precise prediction. Figure 3.1b presents a closer view for temperatures between $480°C$ and $520°C$. It can be seen clearly that the Larson-Miller approach is still the best option due to its capability of providing an accurate prediction; instead linear and logarithmic approaches respectively underestimate and overestimate the real experimental rupture stress. For each method the maximum and minimum temperatures are imposed. The maximum allowable working temperature is a material constant, and is an upper bound limit for the simulation. The minimum creep temperature is a material constant too, and depends on the rupture time. All the methods described in this section are implemented in the solution process through a FORTRAN subroutine called by the LMM creep rupture analysis via Abaqus user subroutine UMAT [16], where the Larson Miller method is the default method to calculate the creep rupture stress, but the user is allowed to use other two schemes as well during the analysis.

3.4 Plate with a hole

3.4.1 Finite element model for the plate with a hole example

The first example analysed is a square plate with a hole subjected to a constant mechanical load and a cycling thermal load. A quarter of the plate is modelled due to the symmetry condition (Figure 3.2). The mesh used is composed by 642 20-node solid isoparametric elements, with reduced integration scheme.

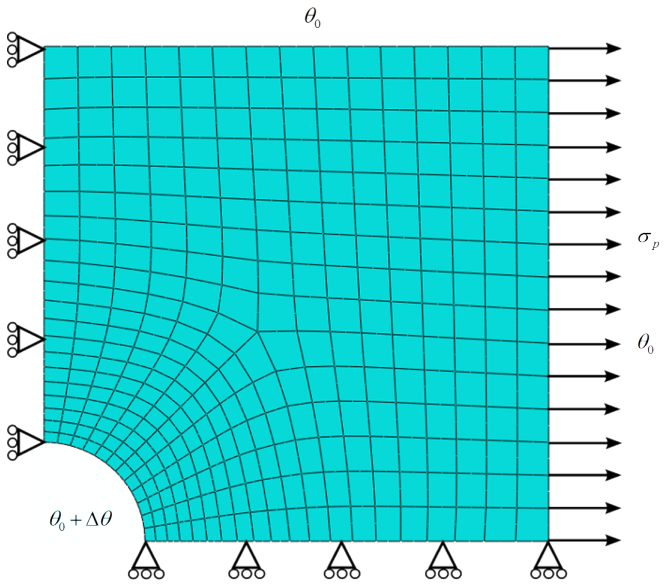

Figure 3.2: Finite element model of plate with a hole

The following geometric ratios are used in this study, $\frac{D}{L} = 0.2$ where D is the hole diameter and L the length of the plate, and $\frac{t}{L} = 0.05$ where t is the plate thickness. In order to benchmark the new approach the same material properties used by [74] are considered. The material has a Youngs modulus $E = 208\ GPa$, Poissons ratio $\nu = 0.3$ and a constant yield stress $\sigma_y = 360$ MPa. A reference uni axial tensile load $\sigma_p = 360$ MPa is applied on the external face surface, and plain conditions are applied to the two external faces. The reference thermal elastic stress field is generated by imposing a thermal gradient over the component. The coefficient of thermal expansion of the material is $\alpha = 1.25 \times 10^{-5}\ ^{\circ}C^{-1}$. In order to generate the appropriate temperature field a user defined subroutine is used, *UTEMP within Abaqus [16], where the temperature gradient of the plate with a hole is defined using the following equation:

$$\theta = \theta_0 + \Delta\theta \cdot \ln(\frac{5a}{r}) / \ln(5) \tag{3.19}$$

where a is the radius of the hole, temperature $\theta_0 = 200$ and $\Delta\theta = \Delta\theta_0 = 400$ for the reference thermal elastic stress. This analytical formulation computes the temperature for each integration points using the coordinates to calculate the appropriate distance from the plate centre. In order to compare the results obtained by using the new methodology with the previous approach a table of creep rupture stresses are calculated using equations (3.1) and (3.2).

3.4.2 Results and discussion for the plate with a hole example

An initial investigation has been performed for a given creep rupture time corresponding to R=0.5. A fictional rupture stress data is obtained using equations (3.1) and (3.2). To determine which is the most robust interpolation/extrapolation method three creep rupture batches are adopted (Table 3.1). The first batch contains creep rupture stresses at low temperature ($300^{\circ}C$ to $340^{\circ}C$), the second one at high temperature ($450^{\circ}C$ to $480^{\circ}C$) and the last one contains both.

Table 3.1: Creep rupture data of fictional steel

		Temperature [C]	Creep rupture stress [MPa] for R = 0.5
Batch-3	Batch-1	300	360
		310	327
		320	300
		330	276
	Batch-2	340	257
		450	144
		460	138
		470	133
		480	128

A single creep rupture limit calculation is performed, for the plate with a hole subjected to the reference thermal load and nil mechanical load. Direct comparison between linear interpolation method and Larson Miller method using different data batches is showed in Figure 3.3a.

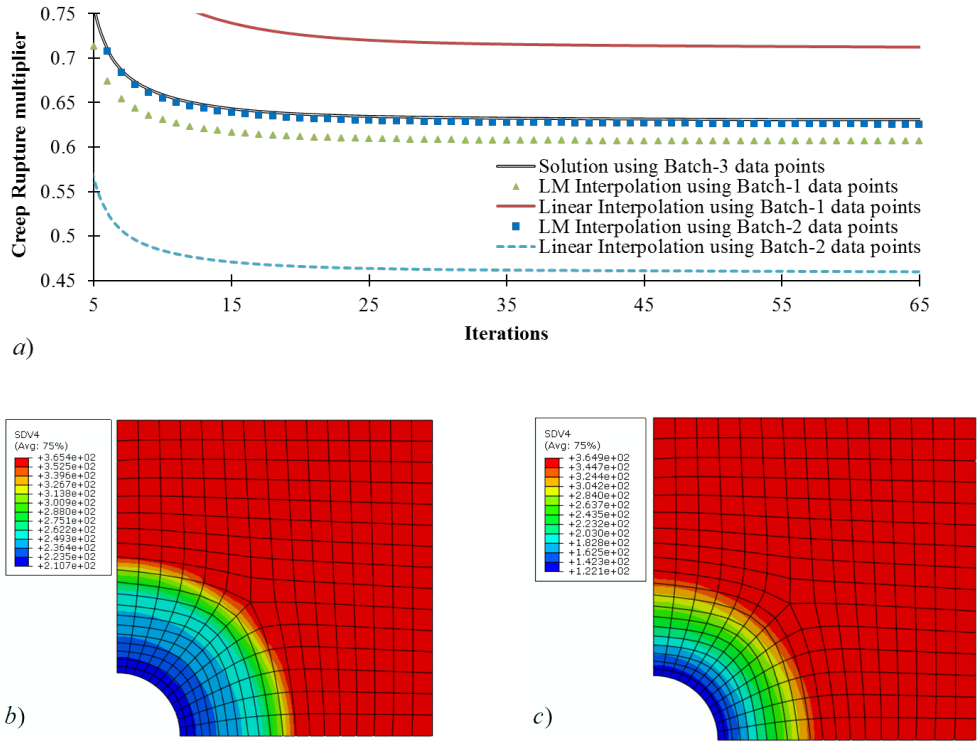

Figure 3.3: a) Convergence of creep rupture limit for different interpolation techniques, b) and c) Revised yield stress contour obtained by linear interpolation and Larson Miller method [MPa], respectively

Using data batch-3 equal creep rupture limit multipliers are obtained (black line) for both methods. Instead using data batch-1, the solution provided by the linear interpolation is the less conservative. This outcome is due to the lower extrapolation accuracy of creep rupture stress over temperature. Instead the Larson-Miller approach is capable of interpolating and extrapolating a more precise creep rupture stress, which brings to a safer solution for data batch-1. If creep rupture stress data points provided are at high temperature (batch-2) the Larson Miller method produces very accurate creep rupture limit, contrary the linear interpolation method is over conservative. Figure 3.3b and Figure 3.3c show the converged revised yield stress calculated by using the linear interpolation method and Larson Miller method respectively. The creep rupture stress around the hole with the highest temperature calculated by the linear interpolation is about higher than the one predicted by the Larson Miller approach. For these reasons the Larson-Miller parameter is considered to be the most appropriate approach leading to the accurate solution to the creep rupture stresses for the creep rupture analysis. Therefore, only the Larson-Miller parameter is considered in the rest of this chapter. Figure 3.4 presents a creep rupture limit diagram of a plate with a hole under constant mechanical load and cycling thermal load for different time to rupture, using the creep rupture data calculated by both the analytical function (3.1) and the new approach using the new scheme. It can be seen clearly in Figure 3.4 that the new approach and previous method in [69] using the analytical function (3.1) produce identical creep rupture limit curves.

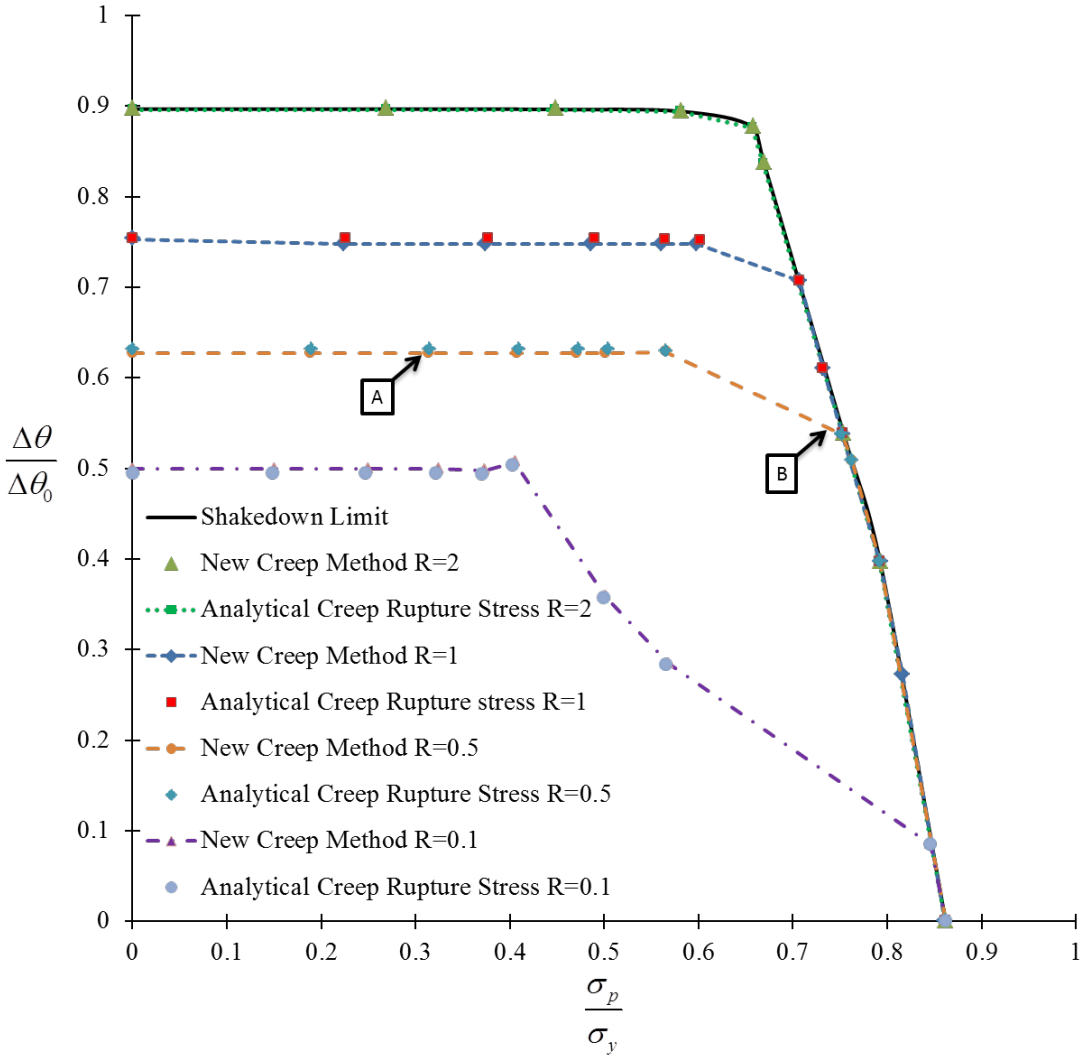

Figure 3.4: Creep rupture limit diagram for a plate with a hole, under constant mechanical load and cycling thermal load for different time to rupture

It is worth noting that the creep rupture limit curve obtained for R=2 matches perfectly with the shakedown limit, as for this required time to rupture (R=2) the calculated creep rupture stress is greater than the yield stress of material (i.e. the revised yield stress is equal to the yield stress of material), causing a failure of the component dominated by the plastic yield rather than the creep rupture. In all other cases as expected a remarkable creep rupture limit reduction takes place when the reduction of the creep rupture stress leads to a lower revised yield stress, due to a lower value of R (i.e. longer allowable time to creep rupture). Figure 3.5a and Figure 3.5b show the creep effect due to load cases at points A and B, which are taken from the curve with R=0.5 in Figure 3.4. When temperature is high enough creep is dominant (load point A), the revised yield stress is lower than the initial yield stress across a big component volume (Figure 3.5a). Instead for load point B creep effect is highly reduced, and the reduction of the revised yield stress due to the high temperature is limited to a small volume around the hole (Figure 3.5b).

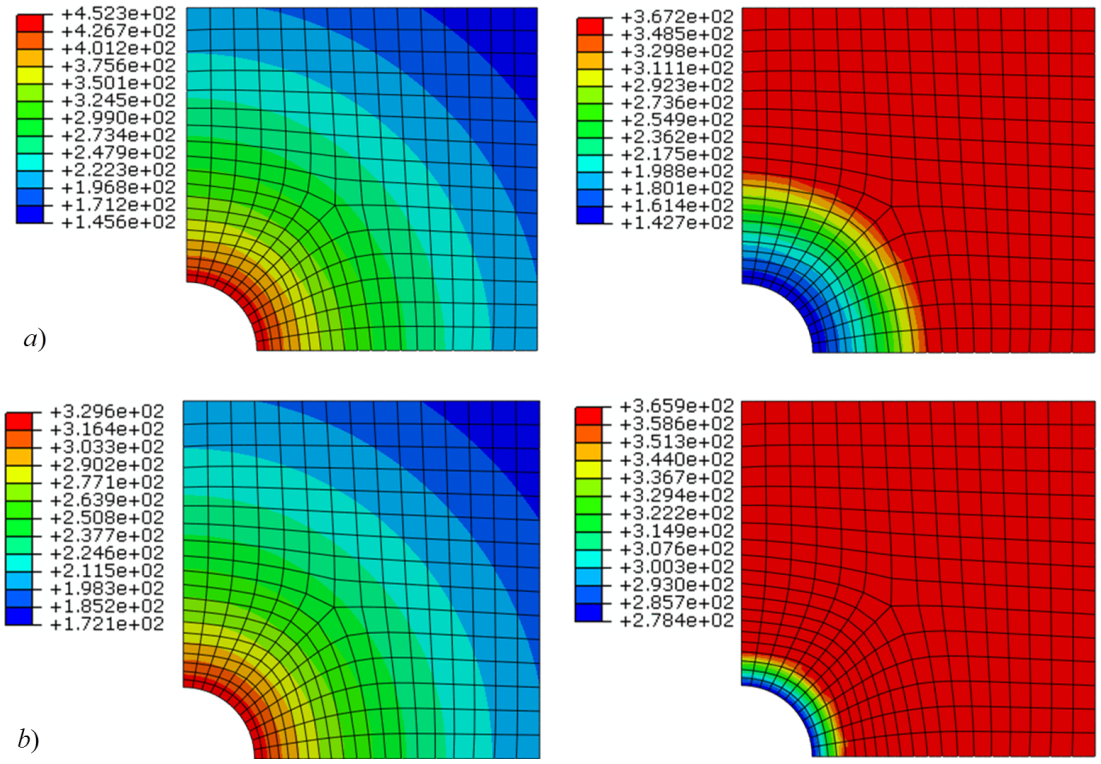

Figure 3.5: a)Effect of temperature (left contour) on the revised yield stress (right contour) for load point A (Figure 3.4) b) Effect of temperature (left contour) on the revised yield stress (righ1t contour) for load point B (Figure 3.4).

In order to confirm the obtained LMM creep rupture limit interaction curves in Figure 3.4, the creep rupture limit for R=0.5 is verified through a step-by-step analysis, considering the following cyclic load points, A_1(0.2,0.65), A_2(0.2,0.55), B_1(0.6,0.65), B_2(0.6,0.55), C_1(0.85,0.2), C_2(0.8,0.2) shown in Figure 3.6, where cyclic load points A_1, B_1 and C_1 are just outside the creep rupture limit curve for R=0.5, and points A_2, B_2 and C_2 are slightly below the creep rupture limit curve.

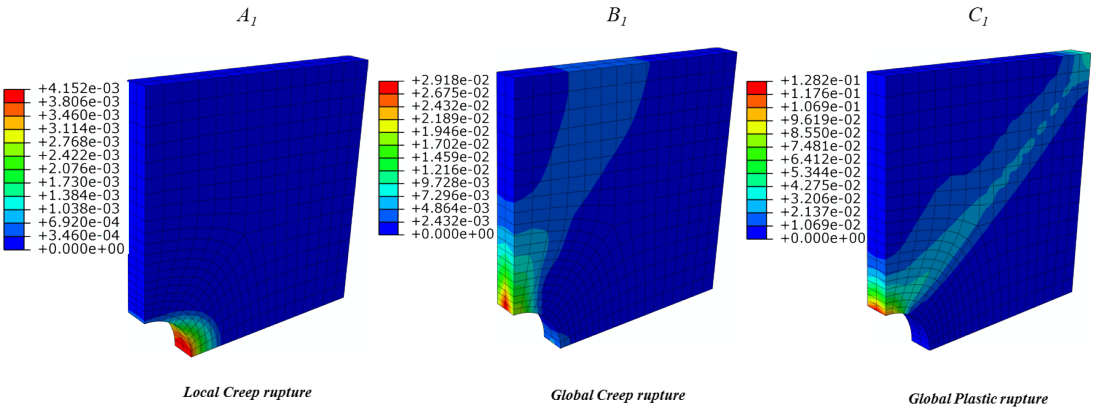

Figure 3.6: Different creep rupture and plastic collapse mechanisms of the plate with a hole corresponding to load points A_1, B_1 and C_1, respectively for R=0.5

In order to introduce the creep rupture effect in the step-by-step analysis and validate the creep rupture limit obtained (Figure 3.7a), the revised yield stress by the creep rupture stress is used to replace the yield stress. By comparing plastic strain histories for these cyclic load points (Figure 3.7b) calculated by the step-by-step analysis, it can be seen that all the cyclic load points exhibit a shakedown behaviour when using the original yield stress of the material except for load point C_1 which shows a ratchetting mechanism.

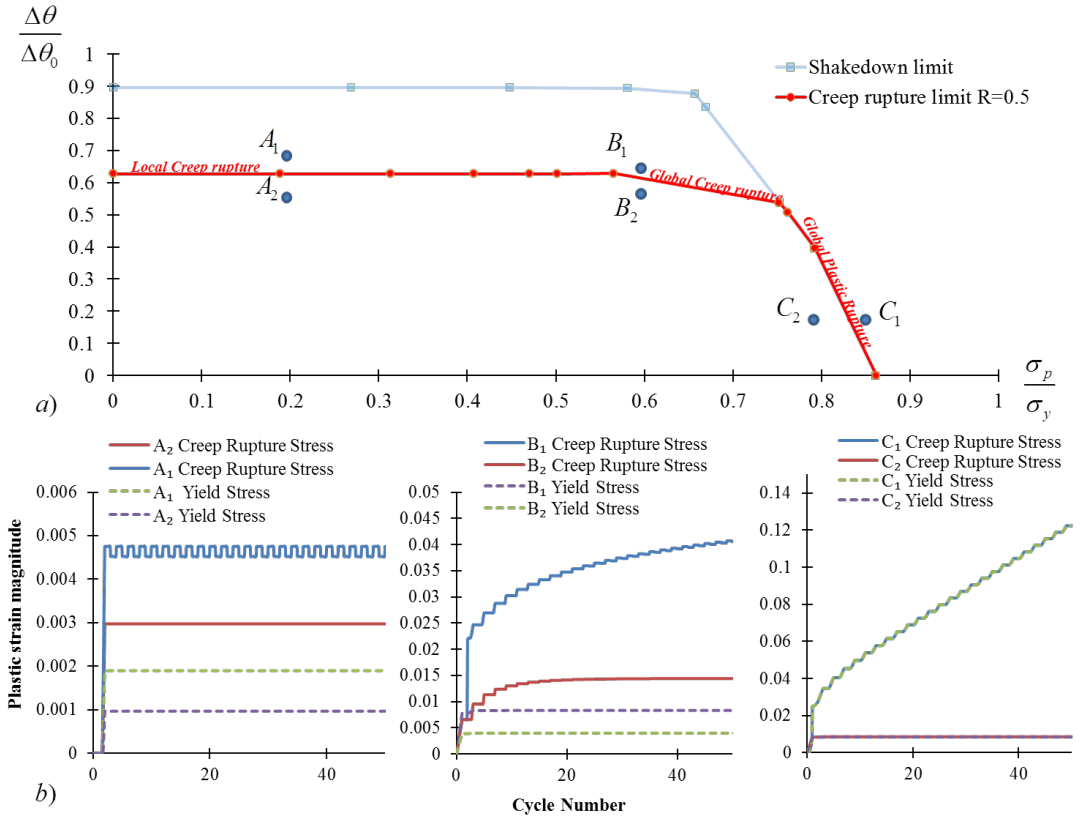

Figure 3.7: Verification of the a) LMM creep rupture limit for the plate with a hole by comparing the b) plastic strain histories from detailed step-by-step analyses.

Contrary when the creep rupture stress is considered, cyclic load points A_1, B_1 and C_1 exhibit a non-shakedown behaviour, and cyclic load points A_2, B_2, C_2 show a shakedown mechanism. These significant mechanism changes between cyclic load points $A_1/B_1/C_1$ and $A_2/B_2/C_2$ indicate the applicability of the calculated creep rupture limit interaction curve for R=0.5. It can also been observed that the creep rupture limit interaction curve for R=0.5 exhibits three distinct areas according to the applied constant mechanical load ranges,and respectively. In the first load range local creep rupture behaviour is dominant, instead a global creep rupture is present in the second one. The upper bound of the second mechanical load range represents the end of creep rupture effect on the component. In the third load range, where, the creep rupture does not take any effects due to the relatively low temperature. The corresponding creep rupture limit curve is actually determined by a global ratchetting mechanism and results

are equal to the shakedown procedure. This threshold is not constant and varies with the defined rupture time. An extreme case is represented by the creep rupture limit for R=0.1 (Figure 3.4). In this case the revised yield stress is widely affected by the creep rupture and global ratchetting failure occurs only for temperature ratio below. Figure 8 presents three typical failure mechanisms of plate with a hole corresponding to load points A_1, B_1 and C_1, respectively, by showing the plastic strain magnitude contours calculated by the step-by-step analysis using the revised yield stress with R=0.5. Local creep rupture occurs for load point A_1 which affects strictly a local area at high temperature, contrary the global creep rupture mechanism occurs for the cyclic load point B_1 which affects a larger area across the thickness. For the cyclic load point C_1, a global ratchetting rather than the creep rupture becomes the failure mechanism, which is totally driven by the larger mechanical load and lower temperature.

3.5 Two-pipe structure

3.5.1 Finite element model for the two-pipe structure

In the second example, the component is composed of two pipes with different lengths, which was originally created by [75] as a one dimensional problem made by two bars. Later [76] modified it by replacing the bars by pipes, and an internal pressure to the longer pipe was introduced. Both pipes were subjected to an axial force F and the longer one having a cycling temperature. This example was also adopted by [5] to predict ratchet limit and it is useful to investigate different failure mechanisms. This study further extends the example by cycling the temperature over each of the two pipes and considering creep rupture, as shown in Figure 3.8.

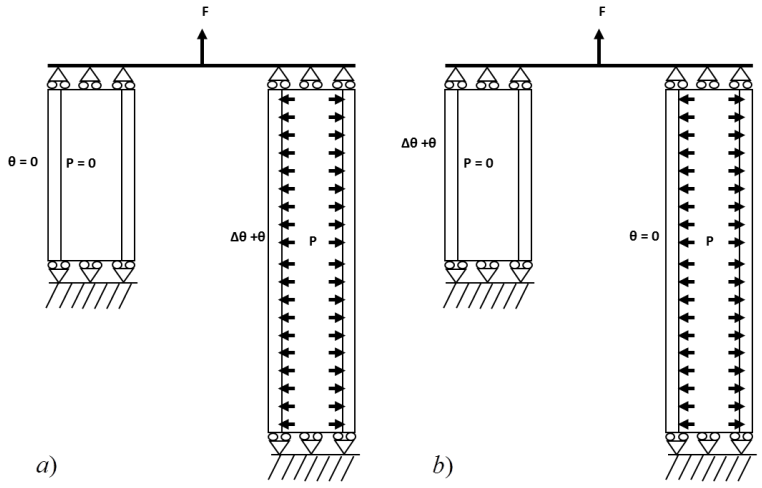

Figure 3.8: Finite element model of the two-pipe structure subjected to an axial force F and an internal pressure P on the longer pipe, with a fixed force over pressure ratio of F/P=10, as well as a thermal cycling load on a) the longer pipe , and b) the shorter pipe

Two thermal load cases are considered in this study; in case (a) the shorter pipe is at constant uniform temperature of $0°C$ and the longer one has a cycling uniform temperature between $0°C$ and the operating one. Contrary in case (b) the shorter pipe is subjected to that cyclic temperature and the longer pipe is set to constant uniform temperature of $0°C$. In addition to this thermal load, the two-pipe structure is also subjected to an axial force F, given in Newton [N], and an internal pressure P given in [MPa] is applied on the longer pipe, a fixed force over pressure ratio of F/P=10 is considered. This ratio was adopted by [17] demonstrating how it affects the ratchet limit. The ratio adopted here is considered to be the worst case scenario due to the severity of hoop stress comparing with the axial force. Despite the simple geometry, such an example is complex in terms of failure mechanisms and it is an ideal example to investigate the effect of creep rupture. The entire model is composed of 1460 20-node solid isoparametric elements, with reduced integration scheme. The geometric dimensions adopted are given in Table 3.2.

Table 3.2: Two-pipe structure dimensions

Property	Pipe 1	Pipe 2
Length	100	200
Outside radius (mm)	2.68	3.22
Inside radius (mm)	2.00	2.00

The two pipes have one end constrained in the axial direction and plane condition is applied to the other end allowing the two pipes to deform together. The material adopted is Nimonic 80A which has a Youngs modulus of 219 GPa , a Poissons ratio of 0.3, and a coefficient of thermal expansion $1.61 \times 10^{-5}\ °C^{-1}$. It is worth noting that the LMM is capable of considering temperature dependent material properties. However in this study the effect of temperature on the Youngs modulus and coefficient of thermal expansion is not significant comparing with the effects of temperature on both the yield and creep rupture stress. Hence the temperature dependent yield stress of material is used and it is reported in Table 3.3, as well as the temperature dependent creep rupture stresses for different times to rupture shown in Table 3.4.

Table 3.3: Temperature dependent yield stress of Nimonic 80A steel alloy

$\sigma_y(T)$[MPa]	780	725	700	455	50
T $[°C]$	0	200	650	800	990

The creep rupture data of Nimonic 80A steel shown in Table 3.4 are obtained using the LM extrapolation procedure for 300 khrs of time to rupture and also 200 khrs when temperature is greater than $570°C$.

3.5.2 Results and discussions for the two-pipe structure

Both the shakedown limit and creep rupture limit interaction curves for different times to rupture for the two-pipe structure subjected to thermal load case (a) are obtained by the proposed method and shown in Figure 3.9. Axial force F is given in Newton [N], and the cyclic temperature range in degree Celsius $[°C]$. The blue line represents

Table 3.4: Creep rupture data of Nimonic 80A steel at different rupture times, [*] extrapolated data

Temperature [$°C$]	Creep rupture stress 100 khrs [MPa]	Creep rupture stress 200 khrs [MPa]	Creep rupture stress 300 khrs [MPa]
480	779	742	693*
490	746	709	662*
500	713	675	628*
510	680	640	592*
520	646	606	555*
570	475	412*	366*
600	372	312*	264*
620	306	253*	206*
650	217	177*	135*
670	168	135*	99*

the shakedown limit calculated using the original yield stress of the material. Instead the dashed lines represent the creep rupture limits for rupture time of 100, 200 and 300 khrs, respectively.

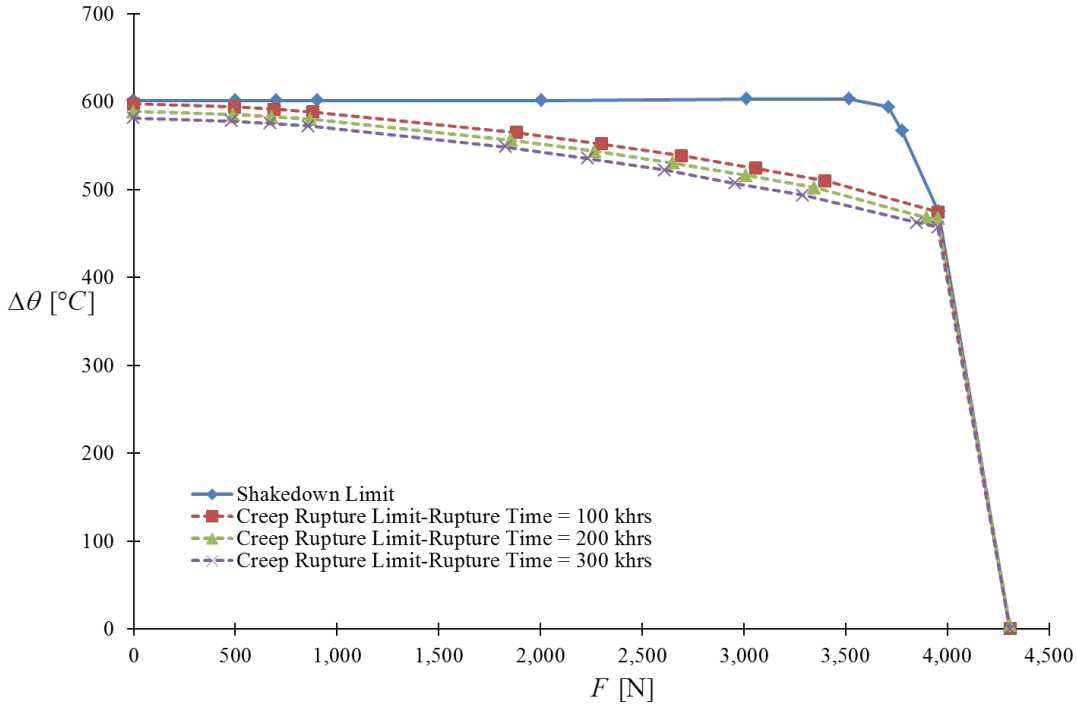

Figure 3.9: Shakedown limit (continuous line) and creep rupture limit diagram (dashed line) at different time to rupture for a two-pipe structure (case a).

The creep rupture limit for a given rupture time of 100 khrs under cyclic thermal load case (a) (Figure 11) is verified by a series of step-by-step analyses, considering three cyclic load points just outside the creep rupture limits $C_1(2000,570)$, $C_3(3500,520)$, $B_1(4200,300)$ and three inside $C_2(2000,540)$, $C_4(3500,490)$, $B_2(4000,300)$ as shown in

Figure 3.10. In order to confirm the LMM creep rupture limit for a given rupture time of 100 khrs by the step-by-step analysis, both the original yield stress and the revised yield stress (determined by the minimum of the creep rupture stress and the original yield stress of material) are adopted.

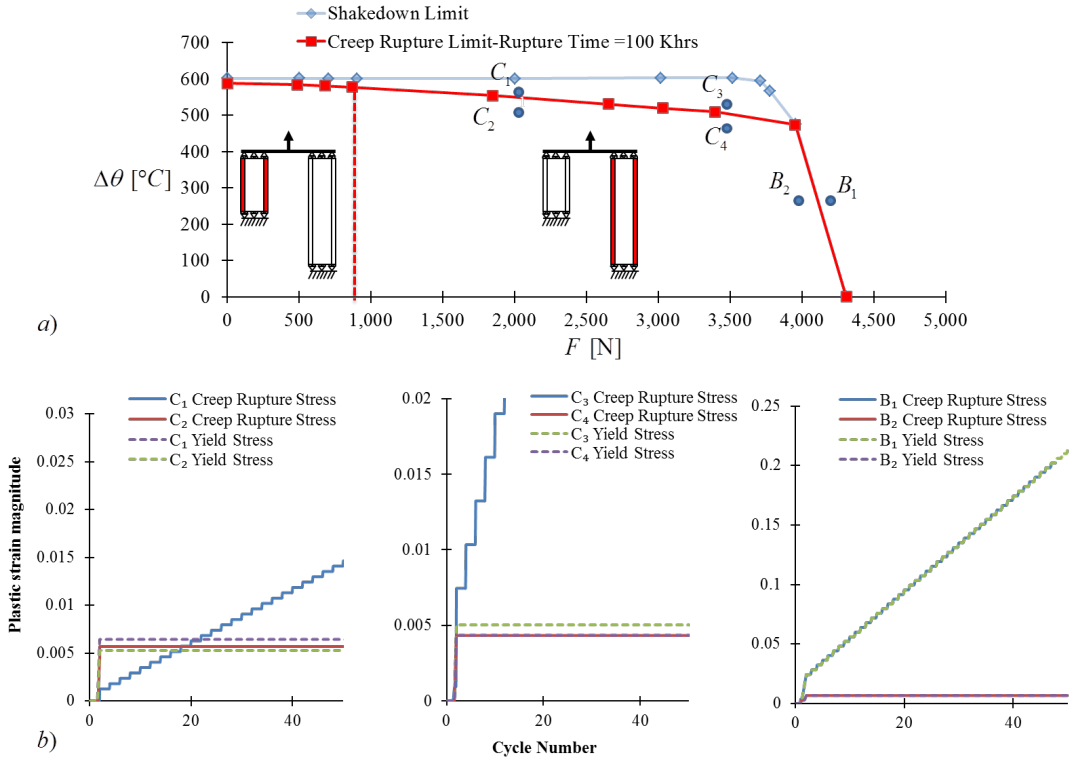

Figure 3.10: Verification through step-by-step analysis of the a) LMM creep rupture limit for a two pipe structure by comparing the b) plastic strain histories.

By comparing plastic strain histories for these cyclic load points (Figure 3.10b) calculated by the step-by-step analysis, it can be seen that all cyclic load points exhibit shakedown behaviour when adopting the original yield stress except for load point B_1, which shows a ratchetting mechanism. Instead considering the revised yield stress, cyclic load points C_1, C_3 and B_1 show a non-shakedown behaviour (Figure 3.10b), the cyclic load points C_2, C_4 and B_2 which are just inside the creep rupture limit curve show a shakedown behaviour. These significant mechanism changes between cyclic load points $C_1/C_3/B_1$ and $C_2/C_4/B_2$ confirm the accuracy of the calculated creep rupture limit interaction curve for a given rupture time of 100 khrs. As for the plate with a hole problem, in this example creep effect also depends on the operating temperature, and for temperatures below $480°C$ creep does not occurs (Table 4). For this reason both cyclic load points B_1 and B_2 with a temperatures below $480°C$ have identical plastic behaviour using either the yield stress or the revised yield stress. It can be further identified from Figure 3.10b that in load case (a) for axial load up to 900 N the creep rupture limit is very close to the shakedown limit, and the failure initiates in the shorter pipe (highlighted in red) due to the dominating cyclic thermal load instead of the constant mechanical load. In this case due to the applied cyclic thermal condition,

creep takes effect only on the longer pipe, which is however still capable of bearing higher load under such a loading conditions comparing with the shorter pipe. For this reason creep does not affect the plastic behaviour of the shorter pipe significantly for low axial forces and internal pressures, which makes the creep rupture limit close to the shakedown limit. Instead for higher axial forces and internal pressures, the failure mechanism switches to the longer pipe (highlighted in red), and the difference between the shakedown and creep rupture limits is much more significant. In order to further investigate the effect of different high temperature condition on the creep rupture, the cyclic thermal load case (b) is also calculated the proposed method, and the corresponding shakedown and creep rupture limit interaction curves for different allowable times to creep rupture are presented in Figure 3.11.

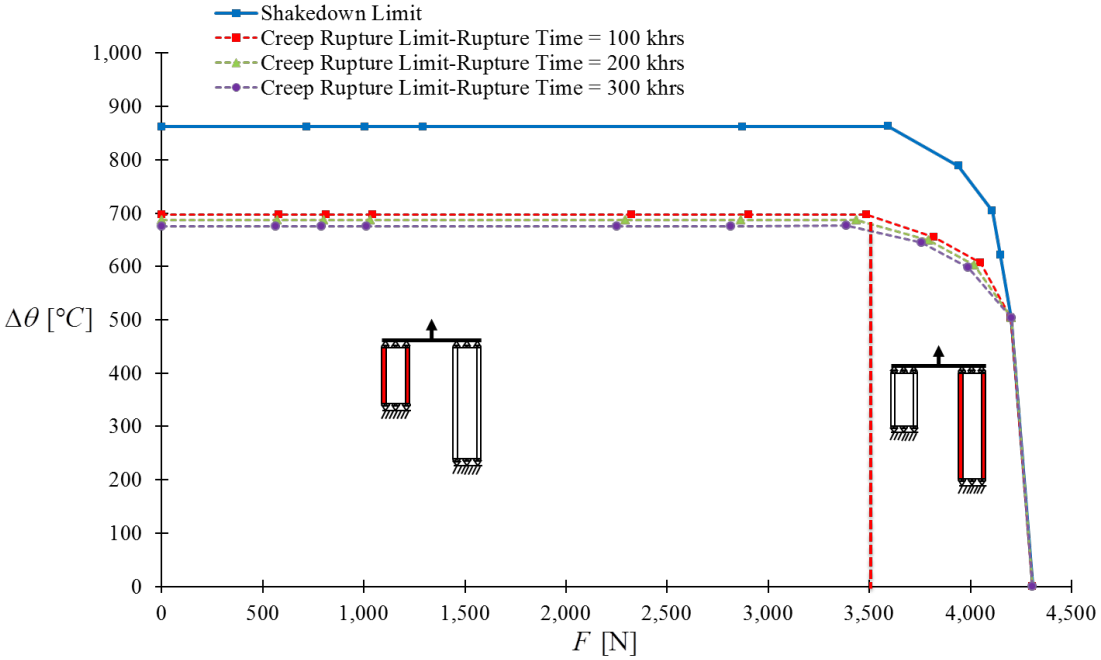

Figure 3.11: Shakedown limit (continuous line) and creep rupture limit diagrams at different time to rupture for a two-pipe structure (case b).

In this case failure occurs in the shorter pipe (highlighted in red) for an axial force up to 3500 N, where the failure of the shorter pipe is dominated by the creep rupture due to the applied high temperature on it. As expected, comparing with the shakedown limit, the applied cyclic thermal load on the shorter pipe causes a significant reduction in the creep rupture limits of a two-pipe structure. Instead when axial force is higher than 3500 N and temperature is above $500°C$ failure initiates in the longer pipe due to the larger internal pressure on it.

During the creep rupture limit calculation, convergence issue was emerged for high temperature loading points, which make the creep rupture limit load multiplier fluctuating even after numerous increments. During this iterative analysis, the convergence of the algorithm is supposed to reduce the creep rupture limit multiplier at each iteration, which leads to a same reduction in the applied temperature. However this temperature reduction will increase the creep rupture stress and the revised yield stress, which in

turn increases the creep rupture limit multiplier in the next iteration. This will inevitably cause a fluctuation on the calculated creep rupture limit multiplier as shown in Figure 3.12.

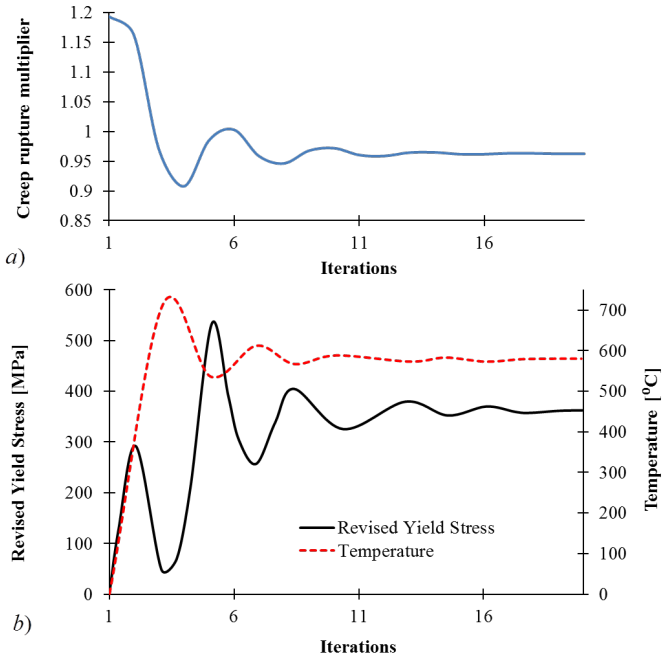

Figure 3.12: a) Convergence plot of creep rupture limit for the two-pipe structure at rupture time equal to 100 khrs for a pure reference thermal load, b) Convergence plot of temperature and revised yield.

Furthermore, in this two-pipe structure the temperature has no gradient through the pipe thickness and it is scaled uniformly across the entire structure. This implies that the algorithm is largely sensitive to the temperature changes, enhancing the creep limit multiplier oscillation. To solve this convergence problem, during each iteration a new scaling factor is calculated using the mean of previous creep rupture limit multipliers determined by the last two iterations, and it is used to scale temperature, and the associated thermal stress field. In this way the oscillating behaviour is damped and with few iterations convergence is reached as shown in Figure 3.12a. In order to ensure the convergence speed and avoid an excessive damping due to the introduction of such a scheme, this numerical treatment is only applied when the oscillations are observed. The actual convergence condition after this treatment is presented in Figure 3.12b, which shows a large oscillating behaviour of the creep rupture limit multiplier, revised yield stress and scaled temperature during the first 10 iterations. However, after 10 iterations, the oscillating behaviour is damped and the creep rupture limit multiplier converges after 15 iterations.

3.6 Conclusions

This chapter presents a new method for creep rupture stress calculation based on limited creep rupture experimental data in the creep rupture limit assessment, which is

developed within the Linear Matching Method Framework. The approach developed demonstrated to be more reliable than the previous one, and capable of better modelling creep rupture data. Three distinct approaches including linear interpolation, polynomial interpolation and Larson Miller parameter are considered for interpolation and extrapolation of creep rupture stresses. It has been identified by an initial investigation using fictional rupture stress data that the Larson Miller approach is the most robust and reliable in interpolating and extrapolating creep rupture stress among these three methods, especially when fewer rupture stress experimental data points are available.

The numerical example consisting of a 3D plate with a hole is used for benchmarking purposes. The creep rupture limits obtained by the proposed approach match with the results from previously published work. It can also been observed that the creep rupture limit interaction curve exhibits three distinct mechanisms, depending on the magnitude of the applied constant mechanical load. The three observed mechanisms are local creep rupture, global creep rupture and global ratchetting mechanism.

A second numerical example investigates creep rupture limits of a two-pipe structure considering two loading cases. Both shakedown limit and creep rupture limits for different rupture times are calculated for these two loading cases, which show a remarkable distinction in the creep rupture limit interaction diagram. In the first case for an axial load up to 900 N the failure starts from the shorter pipe due to a reverse plastic mechanism. For a higher axial load the failure is always located at the longer pipe exhibiting a global creep rupture mechanisms. In the second case where the cyclic thermal load is applied to the shorter pipe, the difference between shakedown limit and creep rupture limit is remarkable, and the failure mechanism is located at the shorter pipe for axial load up to 3500 N. This example demonstrates how creep rupture can affect the same structure in different ways due to the different temperature load conditions.

The initial convergence problem due to the fluctuation of the revised yield stress and scaled temperature is solved by introducing a damping factor during the scaling process when a fluctuation of the creep rupture limit multiplier takes place. The further convergence study shows that with the proposed numerical scheme the oscillating behaviour is damped within the limited number of iterations and the creep rupture limit multiplier converges quickly. The accuracy of the obtained creep rupture limits is also verified by the detailed step-by-step analyses, which are further used to investigate the interaction between the different failure mechanisms.

Chapter 4

Study of creep-fatigue crack initiation by LMM

4.1 Introduction

One of the most crucial concerns in assessing structures operating at high temperature and subjected to cyclic load is the estimate of the number of service cycles to initiate a crack. This information is relevant for two reasons. First, the accurate estimate of the cycles to initiate the crack is required to minimise the downtimes and improve the safety of the plant. Second, the accurate prediction of the location allows for better inspection planning and maintenance outages. Furthermore, if the location of the crack is not accessible, more sophisticated inspections can be planned, even before the start of plant operations.

This assessment is done, as it has been discussed in chapter 2, by using rule-based methods. However, these methods do not rely on full creep and fatigue modelling and do not directly consider their interaction. In many cases, especially for a new design or new operating conditions, they may produce overly conservative results. Engineers have two choices, proceed with more detailed inelastic finite element analyses or perform tests to validate the results obtained from the design code. In many cases, this latter option is very expensive, and not always practicable due to the long term testing that creep and fatigue involve. The traditional incremental finite element analyses provide a very good degree of accuracy but they have a low efficiency and they are not versatile due to the necessity of many material parameters.

Conversely, The LMMF, reviewed in chapter 2, is capable of assessing different structural integrity aspects including the crack initiation assessments of an un-cracked body by adopting the extended Direct Steady Cycle Analysis (eDSCA). In this chapter, the eDSCA is presented in a very detailed way, and two case studies are provided to further test and develop the method. Two numerical models are considered, the Representative Volume Element (RVE) of a Metal Matrix Composite and a Dissimilar Metal Weld (DMW) pipe intersection. Both case studies are very complex and offer the possibility to fully demonstrate the capabilities of the LMM. Furthermore, thanks to the large number of results, several insights on creep-fatigue interaction are discussed.

4.2 Numerical procedure for creep-fatigue assessment

4.2.1 An extended Direct Steady Cycle Analysis considering creep

In the present work an extended procedure of the LMM Direct Steady Cycle Analysis (DSCA) is adopted to evaluate the low cycle fatigue response with creep dwell. As in other works the LMM procedure requires as input a series of linear elastic solutions, generated at discrete time points within the cycle where a significant stress range occurs and hence the most relevant plastic strain. This strategy is quite important concerning efficiency because it saves computing time by targeting the steady state cycle directly and neglecting insignificant loading conditions. These are assumed to lie in the von Mises yield surface, comparing with other cycle-by-cycle analysis methods which must consider the entire load history.

The aim of this extended DSCA procedure is to calculate the cyclic stress history at the steady state due to the accumulation of the residual stress field by either plastic or creep responses. The associated inelastic plastic or creep strains are also evaluated for the steady state load cycle. The extended DSCA procedure is based on a series of iterative cycles which are defined as m = 1, 2... M. Within each iterative sub-cycle, there will be a series of increments N, corresponding to each time points within the cycle ranging from n = 1, 2... N. Each individual varying residual stress $\Delta\rho^r_{ij}(x,t_n)_m$ associated with each elastic solution $\hat{\sigma}^e_{ij}(x,t_n)$ at sub-cycle m will be calculated by the extended DSCA procedure in an iteratively way [19, 53]. Upon reaching a converged solution, the constant residual stress can be determined by;

$$\bar{\rho}_{ij}(x) = \sum_{m=1}^{M}\sum_{n=1}^{N}\Delta\rho^r_{ij}(x,t_n)_m \tag{4.1}$$

The accumulated residual stress for n^{th} load instance at m^{th} cycle of iterations can be defined as;

$$\rho^r_{ij}(x,t_n)_m = \sum_{k=1}^{m-1}\sum_{n=1}^{N}\Delta\rho^r_{ij}(x,t_n)_k + \sum_{k=1}^{n}\Delta\rho^r_{ij}(x,t_k)_m \tag{4.2}$$

A flowchart of the LMM extended DSCA procedure is presented in Figure 4.1, which shows how to evaluate steady state plastic and creep behaviours of structures in an iterative way. For the load instance t_n without creep dwell period, the plastic strain amplitude $\Delta\varepsilon^p_{ij}(x,t_n)$ can be calculated by;

$$\Delta\varepsilon^p_{ij}(x,t_n) = \frac{1}{2\bar{\mu}(x,t_n)}\left[\hat{\sigma}_{ij}(x,t_n)' + \rho^r_{ij}(x,t_n)'\right] \tag{4.3}$$

where notation ($'$) refers to the deviator component of stresses and $\bar{\mu}$ is the iterative shear modulus. When adopting the Ramberg-Osgood (RO) material model, this plastic strain amplitude can be used to update the iterative yield stress. For the load instance with creep dwell period , the effective creep strain can be calculated by equation (4.4)

when considering a time hardening creep constitutive equation (17) in [53].

$$\Delta\bar{\varepsilon}^c = \frac{B(n-1)\Delta t^{m+1}(\bar{\sigma}_s - \bar{\sigma}_c)}{(\frac{1}{\bar{\sigma}_c^{n-1}} - \frac{1}{\bar{\sigma}_s^{n-1}})(m+1)} \tag{4.4}$$

where B , m and n are the creep constants of the material. $\bar{\sigma}_c$ denotes the creep flow stress, which is the sum of the start-of-dwell stress $\bar{\sigma}_s$ and the residual stress $\Delta\rho_{ij}^r$ induced during the dwell period. The creep flow stress can be evaluated by equation (25) in [53], using the information of the creep strain rate at the end of dwell time, which is calculated by equation (23) and (24) in [53]. The calculation of the residual stress $\Delta\rho_{ij}^r$ at each increment is through the solution of a formulated linear problem (10). When the procedure is completed the residual stress field is obtained and the iterative shear modulus $\bar{\mu}_m(x, t_n)$ is updated at each sub-cycle for each load instance by adopting the linear matching equation;

$$\bar{\mu}_{m+1}(x, t_n) = \bar{\mu}_m(x, t_n) \frac{\sigma_y^R(x, t_n)_m}{\bar{\sigma}\left(\hat{\sigma}_{ij}(x, t_n) + \rho_{ij}^r(x, t_n)_m\right)} \tag{4.5}$$

where $\bar{\mu}_m(x, t_n)$ is the iterative shear modulus at the sub-cycle m for n^{th} load instance. $\sigma_y^R(x, t_n)_m$ is the iterative von-Mises yield stress for RO material model or yield stress for the Elastic Perfectly Plastic (EPP) material model at load instance t_n. This yield stress $\sigma_y^R(x, t_n)_m$ will be replaced by creep flow stress $\bar{\sigma}_c$ when considering a load instance involving creep relaxation due to the introduced dwell period. At the end of each sub-cycle, the convergence will be checked. If the convergence criterion is not satisfied a subsequent sub-cycle starts, otherwise the results are outputted to provide all the crucial parameters for creep fatigue assessment.

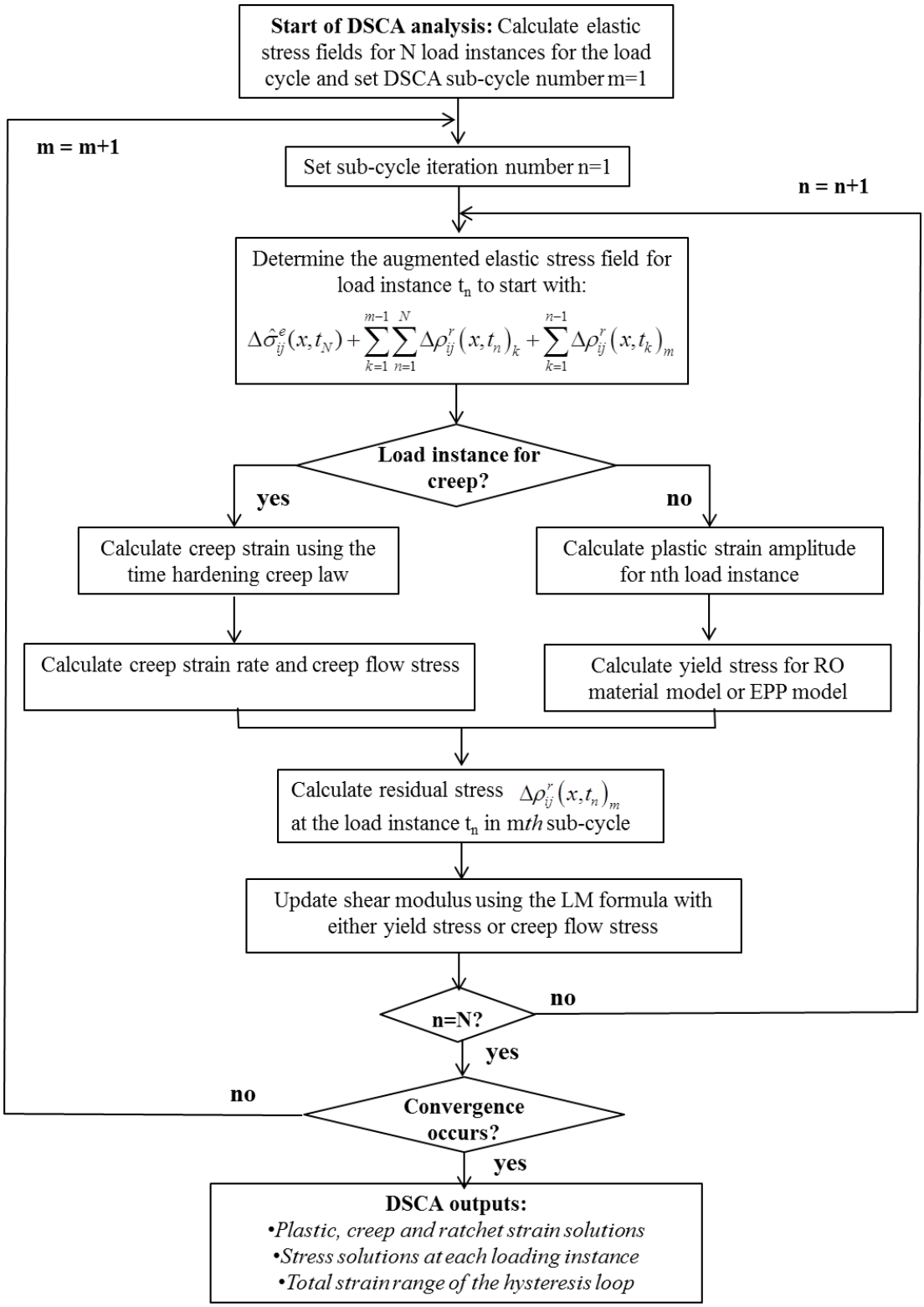

Figure 4.1: Flow chart illustrating the LMM extended DSCA numerical procedure.

Once the whole procedure shown in Figure 4.1 is converged the creep fatigue life of any component subjected to a cyclic thermal and mechanical load can be evaluated. All the required parameters for the assessment can be estimated from the steady state cyclic response obtained, using the procedure depicted in Figure 4.2 and it is based on the procedure developed by [77]. The fatigue and creep damage are calculated separately by the accurate evaluation of total strain range, stress at the start of creep dwell, stress drop, creep strain rate and creep strain accumulated during the dwell. However, the interaction between creep and cyclic plasticity is considered during the saturated hysteresis loop calculation. Furthermore, compressive and tensile creep dwells are identified in order to not introduce produce overly conservative assessments. It worth noting that the creep and fatigue damage models can be modified, depending on the standard required.

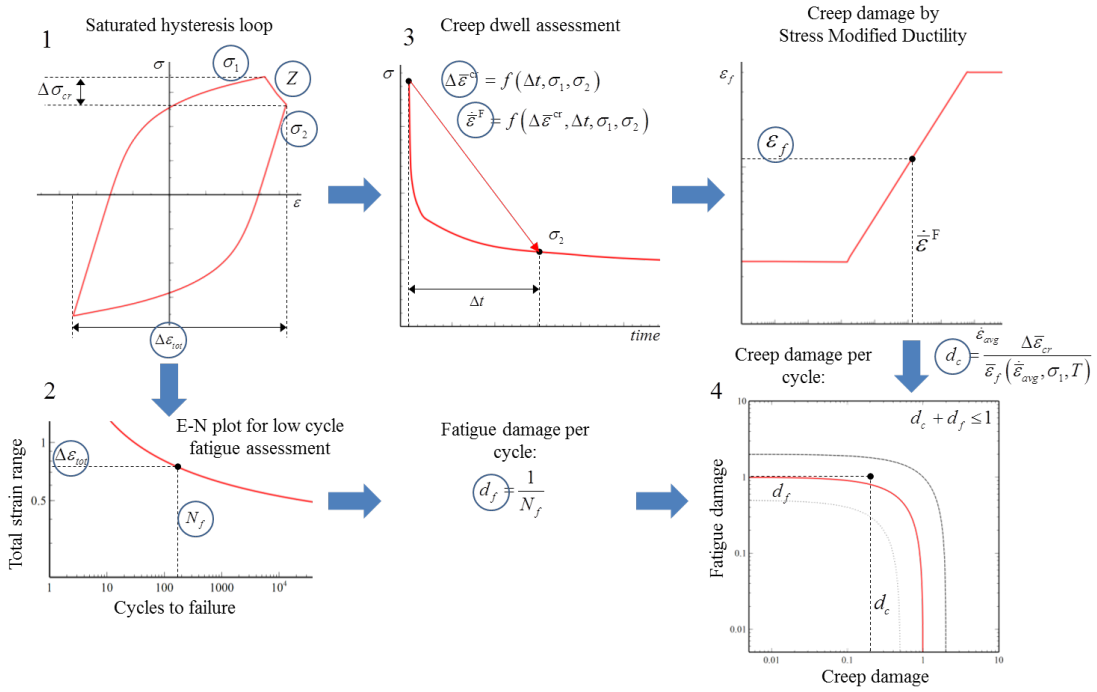

Figure 4.2: Creep fatigue assessment procedure adopted for crack initiation assessment. 1)The saturated hysteresis loop is characterised by the eDSCA, 2) the total strain range is used to estimate the number of cycle to failure due to fatigue and the associated damage per cycle, 3) the creep dwell is assessed determining the damage per cycle, 4) the total damage is calculated.

4.3 On the creep-fatigue interaction of Metal Matrix Composites

4.3.1 Overview on the Metal Matrix Composite

The increasing demand for machines operating at a high level of efficiency requires high operating temperatures, and for particular application also a light weight design. Metal Matrix Composites (MMCs) are composite materials which are capable of delivering the requirements mentioned above. Different types of reinforcement can be

introduced into the metal matrix, including randomly dispersed particles, short fibres and homogeneously aligned long fibres. This work is concentrated on the latter type of reinforcement, which has a high strength in the fibre direction and low weight ratio as well. However, these advantages are seriously downsized by creep behaviour, thermal fatigue, manufacturing processes and environment problems like oxidation [78]. Especially creep-fatigue behaviour becomes an area of research interest, due to the lack of a unified and universal method to assess it, although different standard codes were developed for the assessment of the creep-fatigue life of a high-temperature component, including ASME BPV code and UK R5 [3, 4].

When creep is present, the structures response to a cyclic loading condition changes dramatically [52, 53, 68], for the low-temperature case. Due to the induced residual stresses by creep and plasticity, a closed stress-strain cycle may be formed when the reverse plastic strains completely recover the inelastic strain created during loading and creep dwell periods. With this situation, the lifetime of the MMCs is dominated by the combined damages from cyclically enhanced creep and increased fatigue by the stress relaxation during the dwell period. Alternatively, the hysteresis loop may become non-closed if the creep strains become too large for the reverse plastic strains to recover or vice versa. This leads to a critical failure mechanism called creep ratchetting, which is similar to the plastic ratchetting, for both the inelastic strain will be accumulated during each load cycle. However, the accumulation of inelastic strain for creep ratchetting is driven by either the creep strain or stress relaxation during the dwell period. In order to evaluate creep-fatigue interactions and combined damages of MMCs under cyclic load and high-temperature condition, various factors that affect creep and fatigue behaviours of composites need to be investigated, including effects of the applied cyclic load level, dwell period and temperature on the MMCs performance. Numerical simulations and modelling of fibre or particle reinforced aluminium based MMC have been performed by many researchers [79–87], in particular for the low cycle fatigue damage due to the cyclic plasticity, and creep rupture under the high-temperature condition. Traditional Finite Element Analysis was adopted, using for each case the most suitable material model, able to fit the experimental results. The micro-mechanical model was also used to study the size effect of fibre or particle on the MMC response. The Linear Matching Method (LMM), as a powerful Direct Method for the shakedown and ratchet analysis, has been used to investigate the shakedown and ratchetting response of fibre [88] or particle [8] reinforced MMC. However, very little research focused on the numerical modelling of creep-fatigue interaction into MMC has been done, and considerable efforts are necessary when simulating different interacting mechanisms.

The LMM has been recently extended for the evaluation of fatigue-creep interaction and validated by [53] and further used for a more practical application, i.e. creep fatigue life assessment of weldment [89, 90]. But despite this, no study on the creep-fatigue interaction of MMCs was performed by using the LMM. Therefore, the aim of this research study is to adopt the latest extension of the LMM to evaluate the steady state cycle response of a silicon carbide fibre reinforced 2024T3 aluminium alloy based MMC, subjected to a cyclic thermal and mechanical load with a creep dwell between the loading and unloading phase. The interaction between all the failure mechanisms as mentioned earlier is described and investigated for different loading conditions. This work is intended to be a general and fundamental attempt in understanding the micro-structural response to high-temperature environment and cyclic loading.

4.3.2 Metal Matrix Composite numerical model

A long fibre reinforced MMC is analysed in this work. Due to the periodic dispersion of the fibres in the matrix, a unit cell can be identified for the micro-mechanical modelling. The MMC unit cell is subjected to a constant mechanical load on the right external face and uniform cycling temperature from 0 to θ_0 in the body (Figure 4.3). The creep effect on the cyclic behaviour of MMC is investigated by introducing a dwell period at each load cycle as shown in the Figure 4.3. Due to geometric symmetries a quarter of the unit cell is adopted with two planes of symmetry applied as boundary conditions, in addition to the plain condition on the two external faces to introduce the periodic constraints.

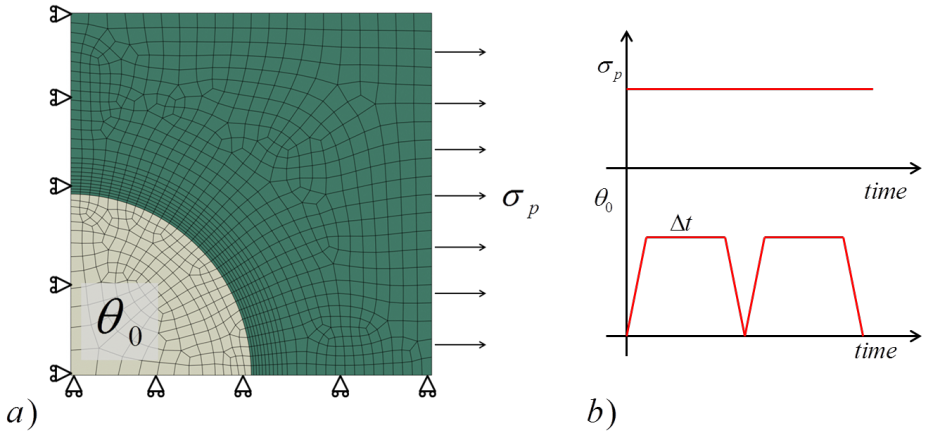

Figure 4.3: a) Finite element model of the MMC unit cell and b) applied loading history.

The mesh is composed of 1039 8-node biquadratic plane strain quadrilateral elements, with a reduced integration scheme. The model is composed of two parts, a left corner spherical fibre and a surrounding metal matrix (Figure 4.3). Due to the interaction between the fibre and the matrix a refined mesh is adopted in the "Interaction Boundary" where the failure mechanisms are mostly expected. The material properties for both the matrix and fibre are reported in Table 4.1. Creep behaviour is evaluated

Table 4.1: MMC material properties.

	Al2O3 Fibre	Al 2024 T3 Matrix
E [MPa]	450000	73000
ν	0.15	0.33
α	$4 \cdot 10^{-6}$	$2.3 \cdot 10^{-5}$
σ_y[MPa]	10000	345

using a time hardening creep constitutive relationship;

$$\dot{\varepsilon}^{cr} = A \cdot \sigma^{n} \cdot t^{m} \tag{4.6}$$

where n is the stress exponent, m is the time exponent for the primary creep stage and A is the power law multiplier. Creep is considered only for the matrix and the data for tensile creep is taken from [91] and reported in Table 4.2.

Table 4.2: Creep parameters A, n and m for 2024T3 aluminum alloy.

	$150°C$	$175°C$	$200°C$	$225°C$
A	$0.763 \cdot 10^{-12}$	$3.461 \cdot 10^{-12}$	$4.079 \cdot 10^{-12}$	$5.118 \cdot 10^{-12}$
n	3.246	3.299	3.395	3.5526
m	-0.303	-0.573	-0.535	-0.519

In order to verify the LMM results, ABAQUS step-by-step analyses are used and the single operating load cycle consists of three ABAQUS load steps. The first one is a *STATIC step, which represents the loading phase where both temperature and mechanical load are applied. Then a *VISCO step is present to simulate the creep dwell time where mechanical load and temperature are constant. To implement equation (4.6) during the second step a user defined *CREEP subroutine is necessary, and the time-hardening formulation is adopted. The third step is a *STATIC step representing the unloading phase, where the mechanical load is constant and the temperature goes to zero.

4.3.3 Effect of creep dwell on hysteresis loop

In order to provide a benchmark to define reasonable cyclic load conditions for the creep fatigue assessment of MMC, a shakedown limit interaction curve was calculated as shown in Figure 4.4 by using the LMM shakedown analysis method, where a reference uniform cycling temperature range from $0°C$ to θ_0 (where $\theta_0 = 200°C$) is applied over the entire model. The ordinate and abscissa axes in Figure 4.4 show the temperature and mechanical load, normalised to the reference temperature $0°C$ and yield stress (345 MPa) of matrix respectively.

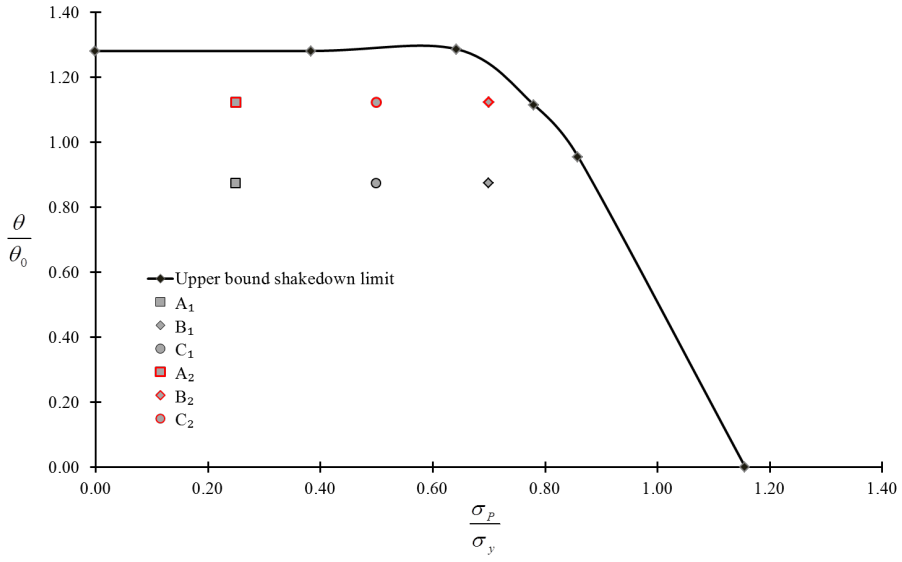

Figure 4.4: Shakedown limit for the MMC under constant mechanical load and cycling thermal load.

The adopted LMM analysis is also able to estimate the overall failure mechanism of

MMC including the most critical location, by showing the contour of cyclic plastic strain range. Figure 4.5a shows the cell response to a cyclic load point at (0.7, 1.0) (Figure 4.4), whereas Figure 4.5b corresponds to the limit load. It is clear from Figure 4.5 that the "Interaction Boundary" is the most critical location, and this will be the location where the fatigue and creep damage will accumulate, ultimately initiating cracking in the matrix. The evaluation of creep-fatigue behaviour of MMCs is performed by a series of analyses considering six cyclic load points inside the shakedown limit: A_1(0.25,0.875), A_2(0.25,1.125), B_1(0.7, 0.875), B_2(0.7,1.125), C_1(0.5, 0.875) and C_2(0.5,1.125) as shown in Figure 4.4. If without creep effect, all these cyclic load points within the shakedown limit should exhibit shakedown behaviour only. The aim of our analysis is to investigate how the cyclic behaviour of MMC changes with creep response due to the introduced high-temperature dwell period. To understand the creep-fatigue interaction, each load point is evaluated for different dwell times 1, 100, 1000 and 10000 hours, respectively.

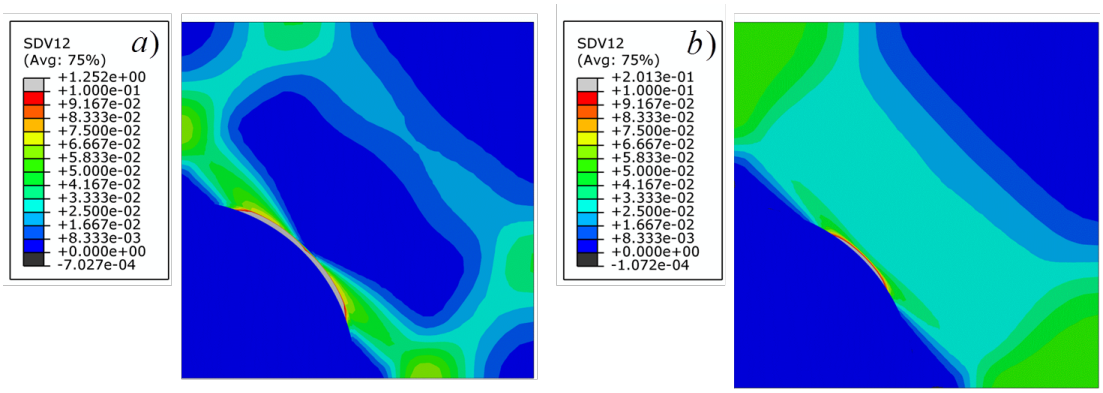

Figure 4.5: Effective plastic strains at different cycling load points.

Four hysteresis loops are generated and presented in Figure 4.6 for cyclic load points A_1 and C_1, where the blue and red line correspond respectively to a dwell time of 1 hour and 100 hours at $175°C$. For a dwell time of 1 hour, the closed hysteresis loop is present only for A_1, instead for C_1 a small total strain increment is present. Creep affects both cases and enhances the unloading plasticity, but no plastic straining occurs during loading due to the overall stress level since it is below the yield. The loop shape changes when a larger dwell time is considered and non-closed loop behaviour is observable also for A_1. In Figure 4.6, the accumulation of total strain is entirely driven by the creep strain. Under such conditions, the damage caused by creep is necessary even for a low-level primary load as seen for load point A_1.

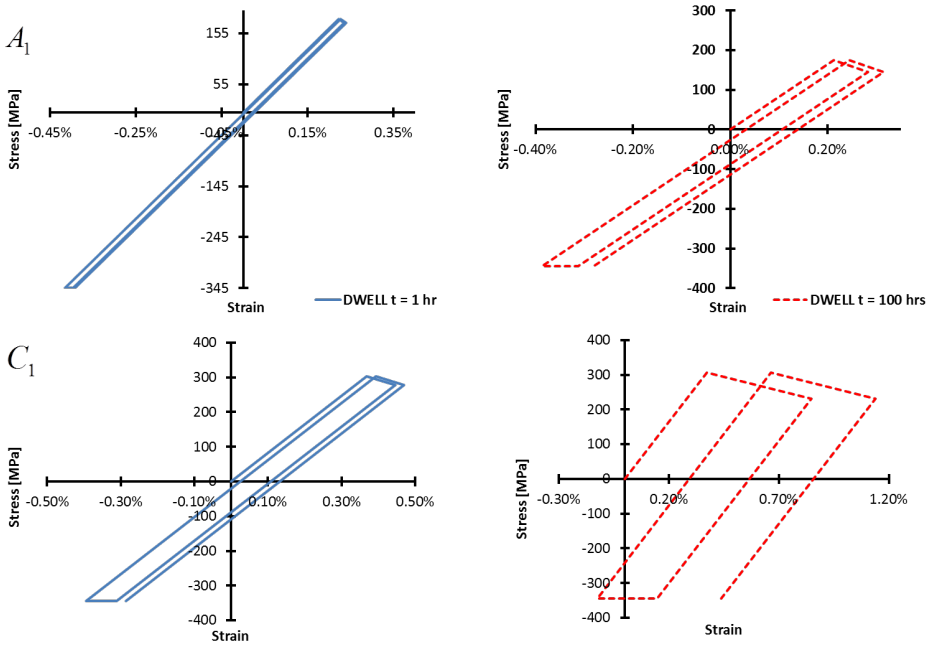

Figure 4.6: Response of the steady state stress-strain path at location with the maximum plastic strain for different dwell time for load points A_1 and C_1.

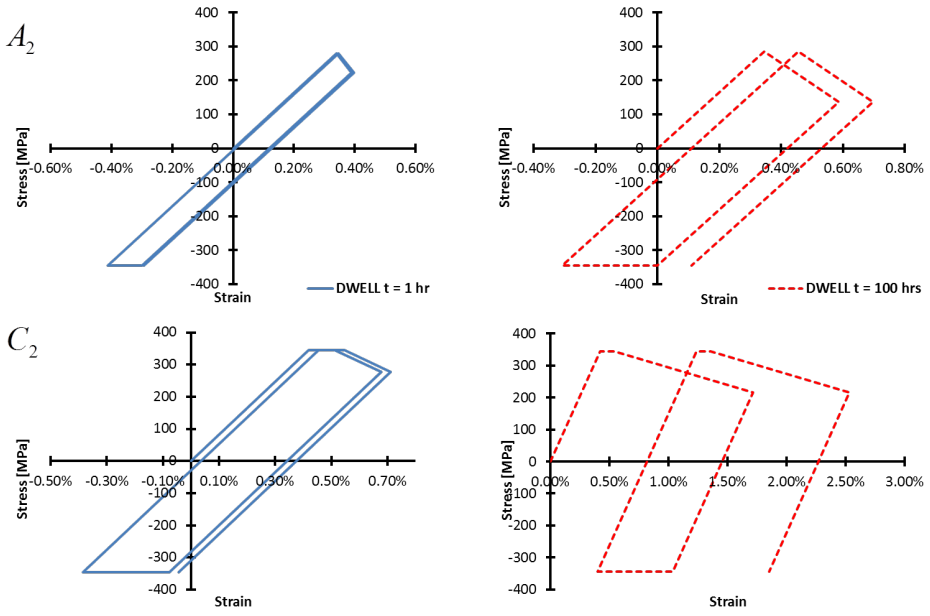

Figure 4.7: Response of the steady state stress-strain path at location with the maximum plastic strain for different dwell time for load points A_2 and C_2.

Figure 4.7 shows the MMC response to the cyclic load points A_2 and C_2 for different dwell times at $225°C$. The load point A_2 with smaller mechanical load also exhibits a closed loop for a 1 hour dwell time (blue line) as the load point A_1 (Figure 4.6), but with a larger strain range due to the higher thermal load applied. Conversely load point C_2 with larger mechanical load shows a small creep ratchetting mechanism even for 1 hour dwell time. Furthermore, for cyclic load point C_2 a small plastic strain also accumulates during the loading phase. Such behaviour is due to the larger mechanical load and the accumulated residual stresses during the cycle which lead some regions to yield also during the loading phase. For the 100 hours of dwell time both loading points behave in a similar way, where creep ratchetting become the dominant mechanism.

To have a complete overview of structure response to such cyclic loading conditions, cyclic load points B_1 and B_2 (Figure 4.4) are investigated and the corresponding stress-strain responses at the steady state are presented in Figure 4.8. For both dwell times, both points B_1 and B_2 show the plastic loading phase and creep ratchetting behaviour due to the very large mechanical load. However point B_2 has a higher strain level due to the higher temperature of $225°C$ applied. When the dwell time is increased from 1 hour to 100 hours, creep strain is increased significantly for both load points, and more significant creep ratchetting mechanism is present.

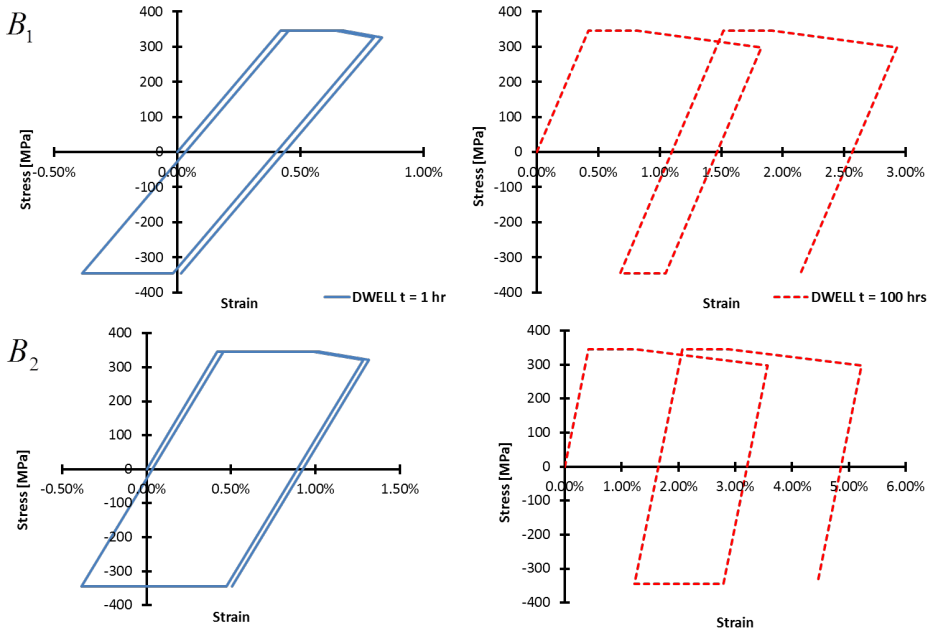

Figure 4.8: Response of the steady state stress-strain path at location with the maximum plastic strain for different dwell time for load points B_1 and B_2.

The detailed effects of different creep dwell times on plastic strains for both cyclic loads points B_1 and B_2 are reported in Figure 4.9. Figure 4.9a and Figure 4.9b show the plastic strain range during loading phase for point B_1 and B_2 respectively, which involves a small and localised area in the "Interaction Boundary". When the creep dwell time is increased the plastic region does not increase significantly and still highly localised, but with a greater plastic strain magnitude. For point B_2 with a higher temperature of $225°C$ the plastic region becomes bigger and also slightly increases for

longer creep dwell. A similar trend is shown by Figure 4.9c and Figure 4.9d for cyclic load points B_1 and B_2 respectively, where the plastic strain at unloading phase is reported.

Both figures confirm the major plastic damage occurs at the unloading phase and involves a quite large area of the matrix. The increase of both the dwell time and the thermal load enhances such behaviour significantly by dramatically increasing the plastic strain magnitude as shown in Figure 4.9c and Figure 4.9d. For both load points B_1 and B_2, the creep ratchetting behaviour becomes very significant as it is enhanced by the high level of primary load. Dwell time is also crucial for the cell response to the cyclic load

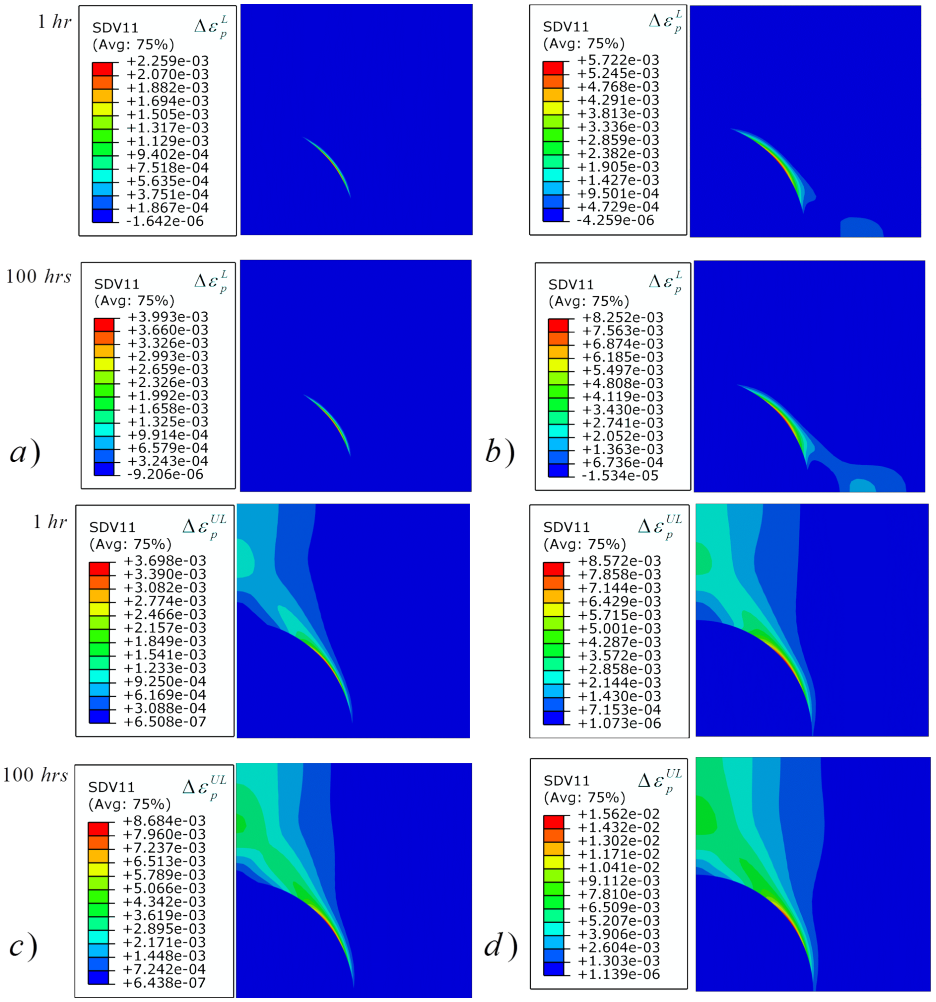

Figure 4.9: Effect of dwell time on plastic strain increments at loading and unloading for cyclic load points B_1 and B_2.

All the results confirm that creep ratchetting mechanisms are affected by two key parameters, dwell time and the primary load level. The analyses performed for cyclic load case A_1 and A_2 showed a closed hysteresis loop. The increase of dwell time drastically changed the MMC response, introducing an evident creep strain accumulation even for such cases. In order to confirm the importance of the primary load

on the creep ratchetting behaviour, the pure cyclic thermal load case is investigated, i.e.. $\frac{\sigma_P}{\sigma_y} = 0.0$ $\frac{\theta}{\theta_0} = 1.0$ This loading condition is investigated by considering varying dwell times from 1 hour to a maximum of 10000 hours. The calculated hysteresis loops for different dwell times are shown in Figure 4.10. It is evident that when there is no primary load, despite the increase of creep dwell, the secondary thermal load is not capable of causing creep ratchetting in the MMCs. However, the increase of dwell time enhances the creep strain and the stress relaxation during the dwell period and consequentially enhances the plastic behaviour during the unloading phase. This will inevitably increase the total strain range of the closed hysteresis loop until a limiting state is reached, where all thermal stresses are fully relaxed to zero, no further creep strain is induced, and hence there is no additional enhancement of reverse plasticity during the unloading phase. As presented in Figure 4.10, when there is no primary load, the creep strain occurred during the dwell period will be fully recovered by the plastic strain during the unloading phase, leading to a closed hysteresis loop.

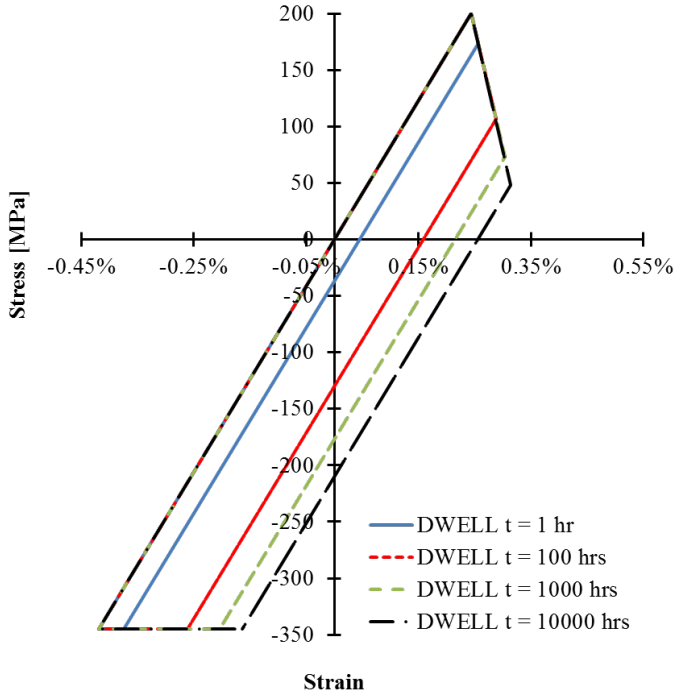

Figure 4.10: Response of the steady state stress-strain path at location with the maximum plastic strain for different dwell times.

In Figure 4.11 an overview of the stress fields at the end of creep and unloading phase for different dwell times is presented. Due to the material mismatch, at both loading phases, the highest stress of matrix develops around the fibre, starting from the "Interaction Boundary". When the creep dwell is increased, a significant stress relaxation occurs and the affected area becomes larger. Longer dwell time allows a wider area to yield during the unloading phase, as shown in Figure 4.11. The increase of creep dwell also causes higher plastic strain during unloading, and such mechanism makes the size of the hysteresis loop larger.

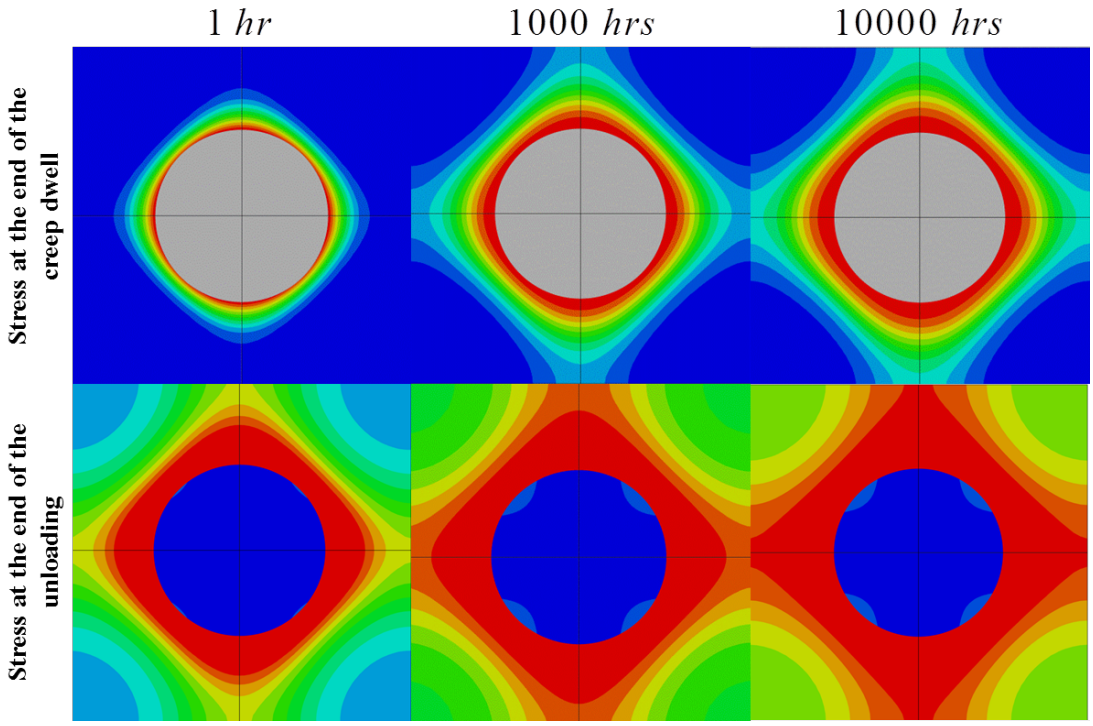

Figure 4.11: Effect of dwell time on stress levels at the end of creep and unloading phase respectively. The progressive relaxation of secondary stress induced by creep enhances the reversed plasticity producing a substantial increase of the fatigue damage at the interface between the matrix and the fibre.

4.3.4 Further studies on the effect of creep dwell on hysteresis loop and verification

To further understand the effect of dwell time on the cyclic response of MMC, the plot of magnitudes of maximum plastic strain increments during loading and unloading phases against the applied dwell time is presented in Figure 4.12a. The plot of maximum creep ratchet strain (i.e. the accumulated inelastic strain) per cycle against the applied dwell time is given in Figure 4.12b. It can be seen clearly from Figure 4.12a that when the applied dwell time is more than 1000 hours, the plastic strain magnitudes at both loading and unloading phases nearly keep unchanged. This behaviour occurs as the creep stress at the end of the dwell period reaches a steady state. By this point, the creep stress cannot relax anymore and the plastic strain magnitude during the unloading phase cannot increase with the further increase of the dwell time. However, it is observed from Figure 4.12b that the maximum creep ratchet strain almost increases linearly with the dwell time when the applied dwell time is more than 1000 hours. This highlights the effects of creep dwell time on both the shape of the hysteresis loop, and the creep-fatigue life of the MMC. For a long dwell time, creep damage dominates and a creep ratchetting mechanism occurs. This highlights the importance of the dwell time for the life assessment of component operating under such loading conditions, even when the operated loading condition is below the shakedown limit.

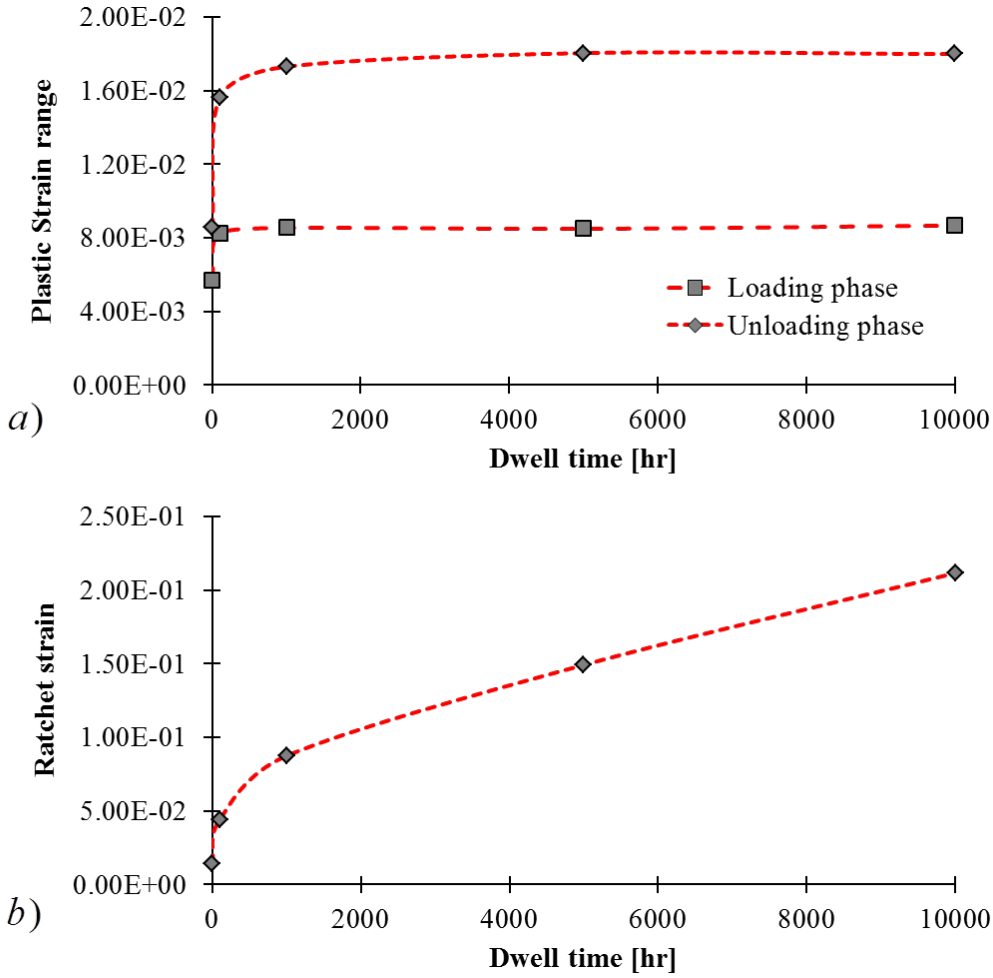

Figure 4.12: a) Plastic strain increments and b) Creep ratchet strain per cycle against dwell time at cyclic loading point B_2.

During the dwell period, both the stress relaxation and creep strain accumulation are observed for MMC. This is related to a phenomenon called elastic follow-up and is typically quantified by an elastic follow up factor Z, defined by the ratio of the creep strain increment to the elastic strain increment during stress relaxation. Under constant displacement loading, the stress relaxation results in no change in the total strain, as creep strain replaces elastic strain with time, where Z=1. The elastic follow-up factor is known to be influenced by loading conditions, and larger primary loads combined with long dwell times produce larger Z. For the MMC investigated, the detailed elastic follow up factors at the location of maximum creep strain for different dwell times and 4 considered cyclic load conditions are presented in Table 4.3. This shows how the magnitude of the primary load affects the Z factor. When the MMC is subjected to a low mechanical load (A_1 A_2) only moderate increases occur when the dwell time is increased, whereas radical changes are observed when the primary load is increased (B_1 and B_2).

Table 4.3: Values of elastic follow-up factor at location with maximum creep strain, for different loading conditions and creep dwell times expressed in hours.

Load point	Z $\delta t = 1$	Z $\delta t = 100$	Z $\delta t = 1000$	Z $\delta t = 10000$
A_1	2.45	2.91	3.80	6.15
B_1	7.65	22.8	51.8	128
A_2	1.72	2.35	3.77	8.04
B_2	11.4	60.4	159	441

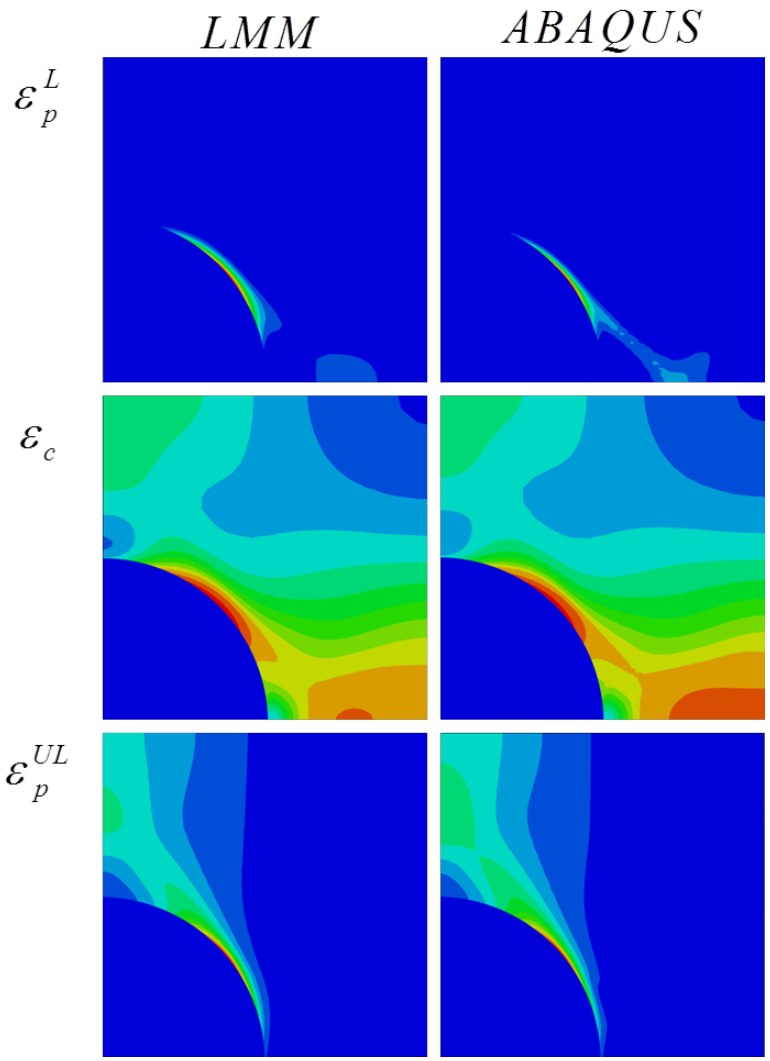

Figure 4.13: Comparisons between LMM and ABAQUS step-by-step analysis for strain increments at loading, creep and unloading phase.

In order to verify the LMM results a direct comparison with the ABAQUS step-by-step analyses is performed. Three quantities are considered in the verification procedure, the creep strain increment (ε_c), the plastic strain increment at loading (ε_p^L) and the plastic strain increment at unloading (ε_p^{UL}). Direct comparisons of contours and magnitudes of these plastic and creep strains obtained by the LMM and ABAQUS

step-by-step analyses are given in Figure 4.13 and Table 4.4, respectively, and a perfect agreement is observed. It is evident that the LMM is capable of producing accurate solutions to estimate the cyclic response of MMC to the applied cyclic load condition with creep dwell. Furthermore, it is worth noting that the LMM creep-fatigue analysis is much more efficient than the standard ABAQUS step-by-step analysis procedure. Based on a standard PC, the computational CPU cost to solve one cyclic loading case for any the dwell time required by the LMM analysis is approximately 149 seconds (150 total increments). Conversely, the ABAQUS step-by-step analysis needs 792 seconds (810 total increments) and 1268 seconds (2600 total increments) for 1 hour and 10000 hours dwell times respectively. This comparison verifies the efficiency superiority of LMM.

Table 4.4: Comparison between LMM and Step-by-Step Abaqus analyses, for different cyclic loading points.

	ε_p^L		ε_c		ε_p^{UL}	
Load point	LMM	ABAQUS	LMM	ABAQUS	LMM	ABAQUS
A_1	0	0	$2.21 \cdot 10^{-4}$	$2.53 \cdot 10^{-4}$	$1.80 \cdot 10^{-4}$	$2.00 \cdot 10^{-4}$
B_1	$2.26 \cdot 10^{-3}$	$2.01 \cdot 10^{-3}$	$1.76 \cdot 10^{-3}$	$1.74 \cdot 10^{-3}$	$3.70 \cdot 10^{-3}$	$3.51 \cdot 10^{-3}$
A_2	0	0	$1.20 \cdot 10^{-3}$	$1.25 \cdot 10^{-3}$	$1.13 \cdot 10^{-3}$	$1.20 \cdot 10^{-3}$
B_2	$5.72 \cdot 10^{-3}$	$5.15 \cdot 10^{-3}$	$3.22 \cdot 10^{-3}$	$3.14 \cdot 10^{-3}$	$8.57 \cdot 10^{-3}$	$8.15 \cdot 10^{-3}$

4.3.5 Discussions on MMC damaging and response to the cyclic load

Among the six cyclic loading points shown in Figure 3, the most critical one is B_2. Hence for this loading point a complete cell view is presented in Figure 4.14a and Figure 4.14b for the discussion. In previous sections it is well established that creep dwell time affects dramatically the structure response, due to the stress relaxation and redistribution, which are particularly damaging and responsible for the plasticity during the unloading and loading phase when the primary load level is high enough. Figure 4.14a shows the stress distribution at the end of the creep dwell for two cases, 1 hour and aluminium alloy metal matrix composite 1000 hours of dwell time. The associated residual stress during the creep dwell makes it possible to yield regions which normally dont exhibit a plastic behaviour. This is highlighted by Figure 4.14b where the plastic strain increment at unloading phase is reported. Both the plastic strain magnitude and area at unloading phase largely increases by longer dwell times. Due to the transverse direction of the mechanical load, the reinforcement fibre does not improve the tensile strength of MMC significantly under such load condition, which is the most critical load condition the structure may experience. The most dangerous mechanism shows plasticity in both loading and unloading phase. In such condition creep and creep ratchetting become extremely damaging when the dwell time increases.

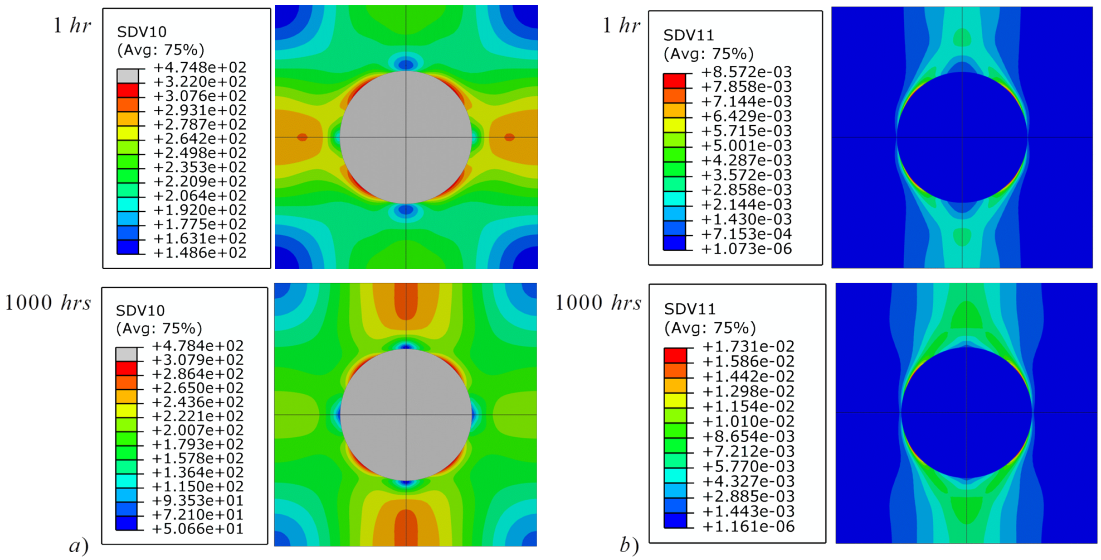

Figure 4.14: a) Effect of dwell time on the stress distribution for the complete unit cell at the end of creep dwell, for cyclic load point B_2, b) Effect of dwell time on the plastic strain increment of the complete unit cell during unloading phase, for cyclic load point B_2.

The effect of dwell time on the strain evolution is presented in Figure 4.15, where the plastic and creep strains contours are shown for different dwell times. The loading phase is not affected by the increase of the dwell duration because it starts after the tensile peak. Instead, the unloading phase is remarkably enhanced by the increase of the creep dwell, which increases the stress drop at the most critical location, and enhances the reverse plasticity by increasing the total strain range. Furthermore, the creep strain increases remarkably over the different dwells analysed. For this particularly dangerous cyclic loading condition (B_2), the matrix experiences a large stress redistribution during the creep dwell and also a high level of stress during both the creep and unloading phase (Figure 4.16). Such a high level of stress makes the creep damage dominant for dwell times up to 1000 hours. Instead for dwell time up to 10000 hours classical monotonic creep rupture occurs. The creep rupture failure always initiates in the interface area but rapidly involves the entire surrounding matrix. Then it is not capable of withstanding the applied load condition, and a fast increase of the creep strain is expected due to the increasing creep damage. It is important to underline that these failure analyses are performed within the shakedown limit. Without the presence of the creep dwell, none of those above failure mechanisms can be observed.

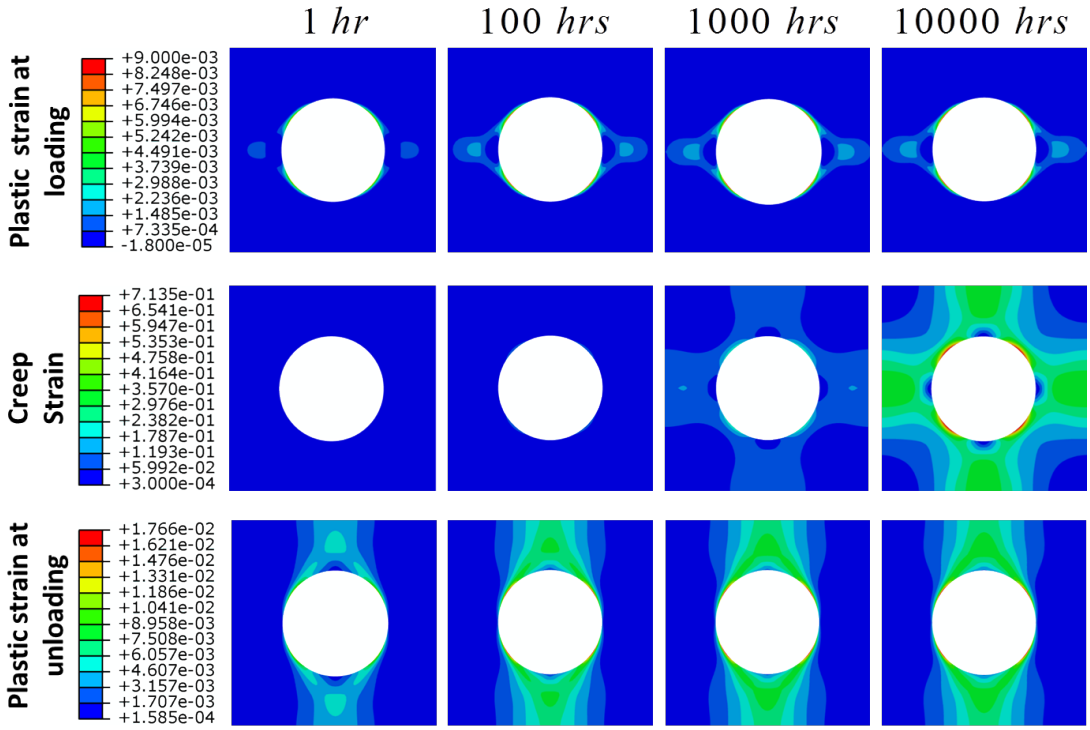

Figure 4.15: Strain contours at loading, creep and unloading for a uniform cycling temperature $\sigma_0 = 225^{\circ}C$ and a constant mechanical load $\sigma_P = 241.5$ MPa for different dwell times.

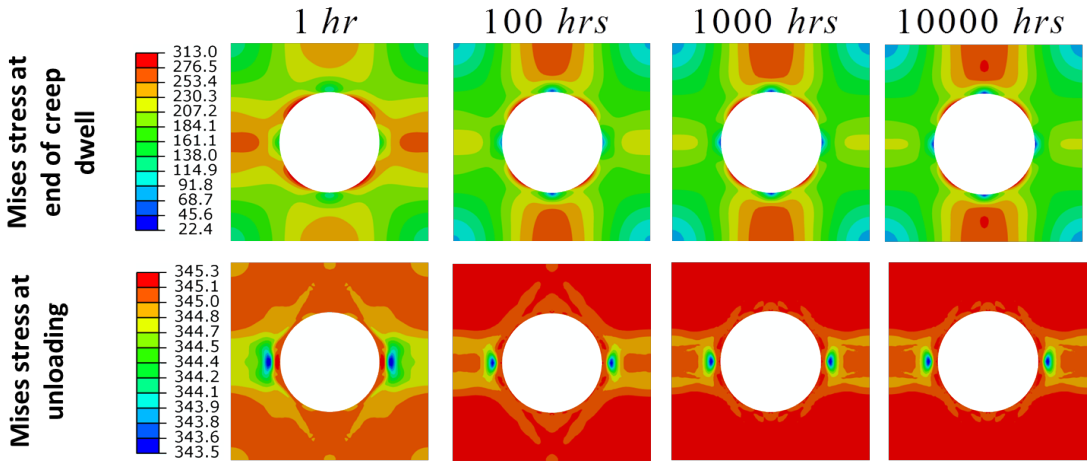

Figure 4.16: Stress contours at end of the creep dwell and unloading phase for a uniform cycling temperature $\sigma_0 = 225^{\circ}C$ and a constant mechanical load $\sigma_P = 241.5$ MPa for different dwell times.

4.3.6 Creep ratchetting failure in the MMCs

Creep ratchetting is a dangerous mechanism, which can interact with creep and fatigue and it may become dominant. Figure 4.17 shows the creep ratchetting interaction diagram, which is useful to understand the response of the micro-structure. The creep strain and net plastic strain, which is the difference between the plastic strain at loading and unloading phase, are displayed on the vertical and horizontal axes respectively. Closed loop is possible only if the creep strain is fully recovered from the net plastic strain. However, this closed loop condition is remarkably affected by both the dwell time and the stress relaxation. The closed loop limit can be represented by a 45-degree line as shown in Figure 4.17. The cyclic loading points A_1, B_1, C_1 are investigated for increasing dwell times. Only for short hold period, a closed loop is possible especially for high mechanical load level (up to 1 hour). Otherwise, the results diverge on the upper part of the limit (Figure 4.17). This means that the creep-ratchetting mechanism is creep strain dominated.

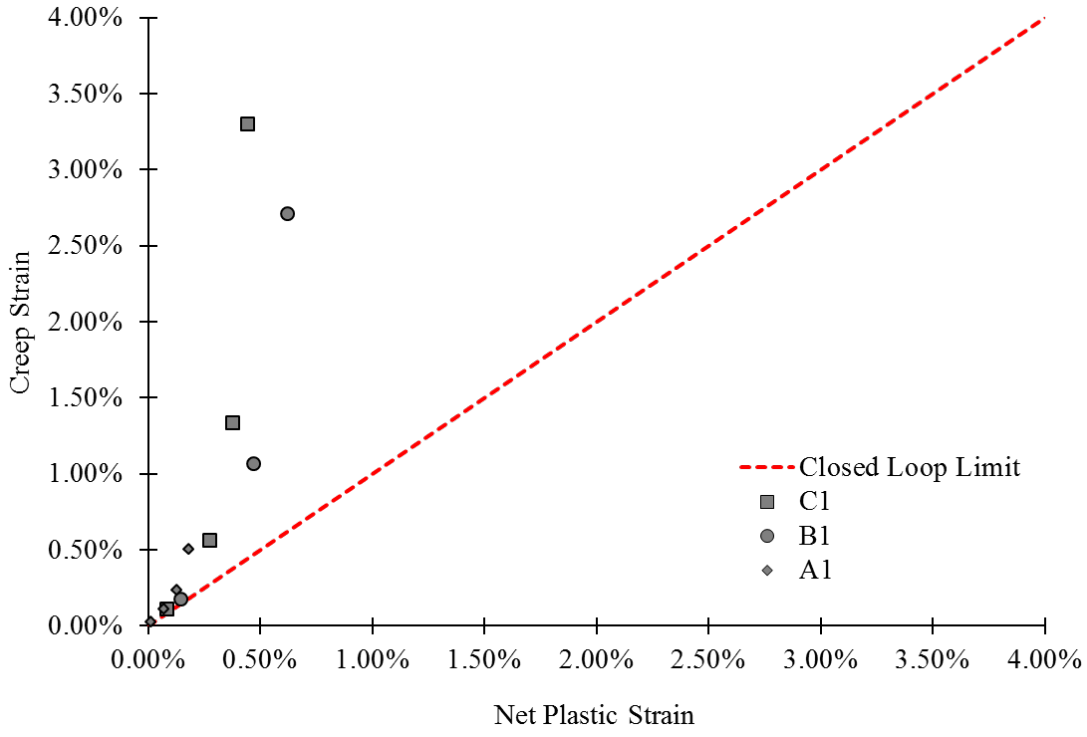

Figure 4.17: Creep ratchetting interaction diagram for different cyclic loading points (Figure 4.4) at increasing creep dwells

If the saturated cycle is an open, the number of cycle to failure due to the creep ratchetting can be evaluated using the strain based equation [54], which is characterised by the ratio between the tensile strain to fail and the calculated ratchet strain per cycle. The creep ratchetting strains per cycle at two temperature conditions are shown in Figure 4.18 for different mechanical loads. For both temperature conditions, it is shown that no ratchetting occurs when the mechanical load is zero, and the increase of this mechanism at each cycle has the same dependency on the applied mechanical load.

The effect of temperature on the creep ratchetting strain per cycle has also been shown in Figure 4.18 against the normalised transverse mechanical load. For a normalised mechanical load of 0.5, the ratchetting strain per cycle increases from 0.7% to 1.4% for the 1000 hours dwell time when the temperature increases from 150 and 175°C. Despite this, it has been observed that the creep damage becomes dominant for longer dwell time and high mechanical load, and higher temperatures enhance it.

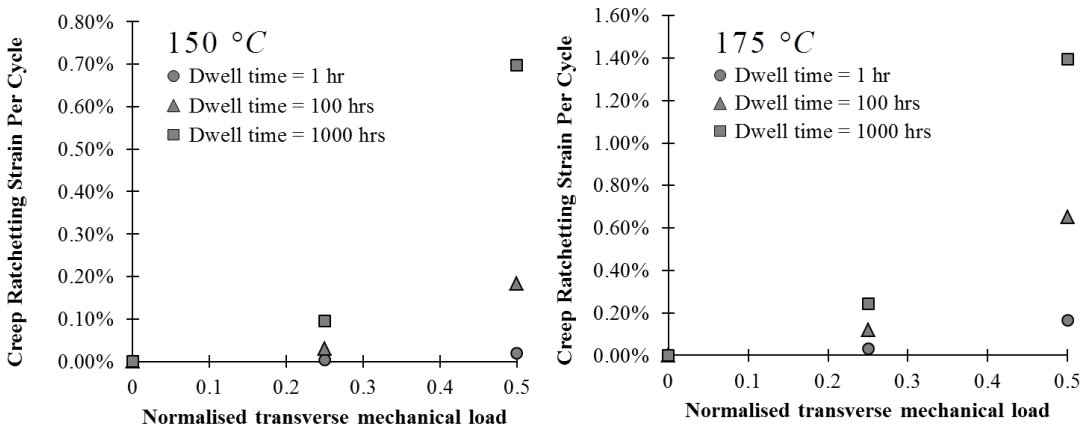

Figure 4.18: Creep ratchetting Strain per cycle at 150 and 175 °C for different transverse constant mechanical load, normalised by the yield of the matrix.

The creep-fatigue life and creep ratchetting life against dwell time are shown in Figure 4.19a for a cyclic temperature of 150°C. Up to 1000 hours, creep-fatigue life (N_{cf}) is almost independent of dwell time, and the fatigue damage dominates due to the low temperature of 150°C considered, making the creep damage negligible. For dwell times longer than 1000 hours creep damage becomes significant and competes with the damage caused by fatigue. The number of cycles to failure calculated using a strain ductility (N_{cr}) approach are higher than the number of cycles to failure due to creep-fatigue interaction (N_{cf}) for dwell time up to 10 hours. After this threshold of 10 hours creep ratchetting becomes dominant and causes the failure rather than the creep-fatigue interaction. In such a case the damage is associated with a large change in the size of cross-section area due to the material necking. A proof of this creep ratchetting mechanism is shown in the contours presented in Figure 4.19b, where both the plastic strain at the unloading phase (left) and the ratchet strain increment per cycle (right) are presented. The magnitude of ratchet strain shown in Figure 4.19b is larger than the plastic strain that occurs during the most dangerous cyclic phase. This means that the damage caused by the creep ratchetting is more significant than the damage produced by creep and fatigue interaction.

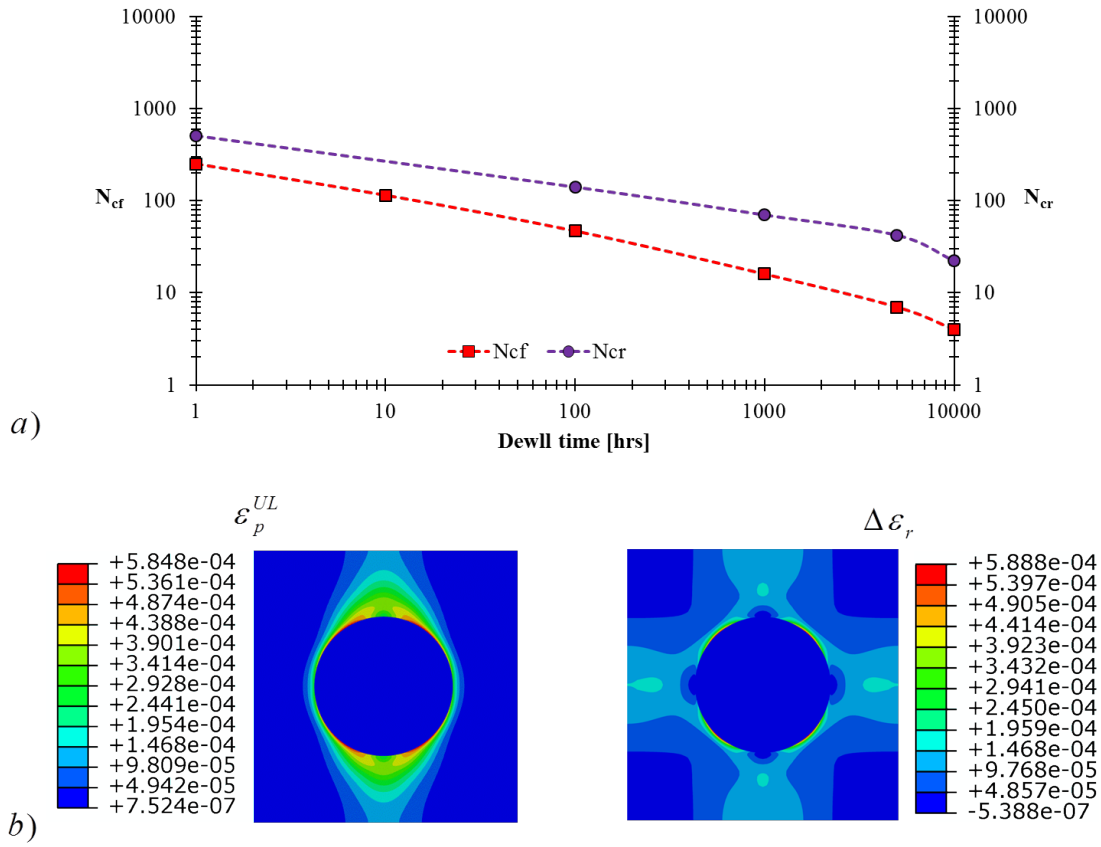

Figure 4.19: a) Creep-fatigue life and creep ratchetting life against dwell time, b) contours of the plastic strain at unloading phase and the creep-ratchetting strain per cycle for a cyclic temperature of $150^{\circ}C$ and a constant mechanical load 0.25 time the yield of the matrix.

In Figure 4.20a, the creep-fatigue life and creep ratchetting life are reported against the dwell time for a temperature of $175^{\circ}C$. For all the dwell times studied creep ratchetting is always less damaging than the combined damage due to fatigue and creep. For such a cyclic loading condition the driving fatigue and creep failure mechanism is the creep-fatigue interaction for intermediate dwell (up to 100 hours) and creep dominated for longer dwell periods (larger than 1000 hours). Figure 4.20b presents the contours of the plastic strain at the unloading phase and the creep ratchetting strain increment per cycle. For this loading case, the two quantities are comparable, but the damage caused by the creep ratchetting strain per cycle is still negligible respect to that caused by combined damage due to the creep and fatigue interaction.

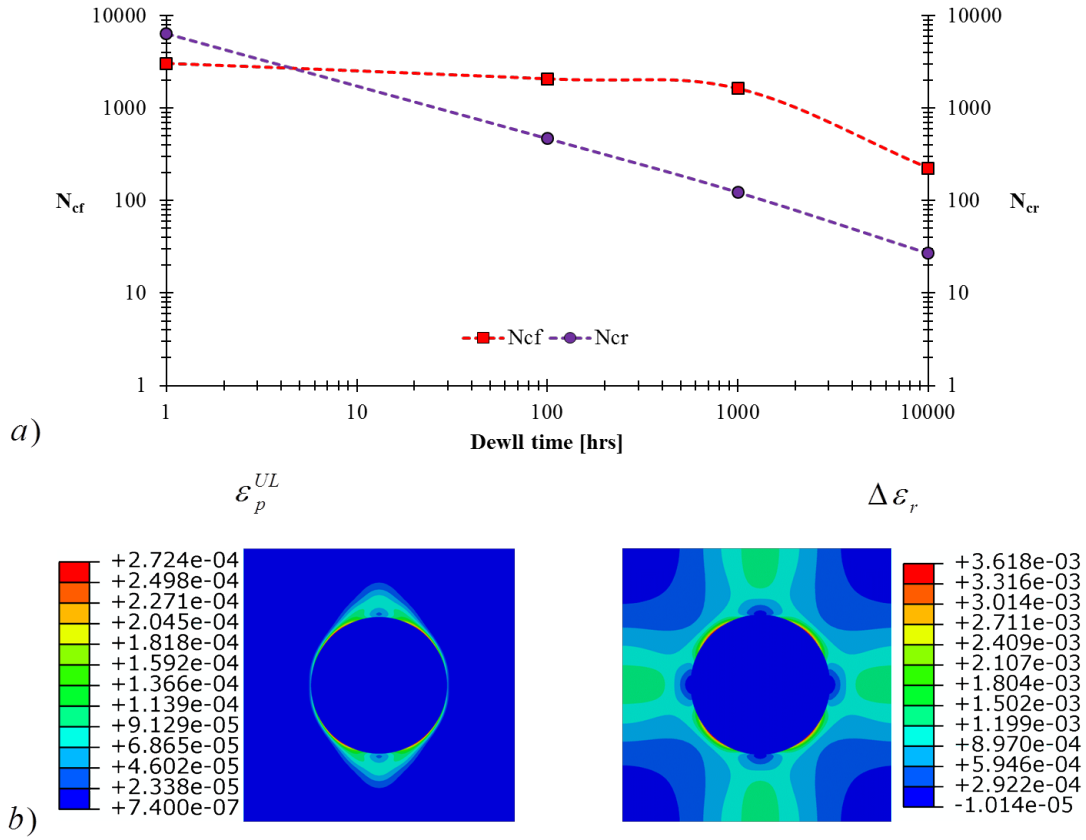

Figure 4.20: a) Creep-fatigue life and creep ratchetting life against dwell time, b) contours of the plastic strain at unloading phase and the creep-ratchetting strain per cycle for a cyclic temperature of $175^{\circ}C$ and a constant mechanical load 0.25 time the yield of the matrix.

4.3.7 Discussion on creep-fatigue crack initiation on MMCs

The research study presented in this chapter investigates the interactions between fatigue and creep damages of a fibre reinforced MMC subjected to a cyclic temperature and constant mechanical load by using the LMM extended DSCA with micromechanical modelling. The MMC is modelled using an idealised plain strain model, where both matrix and fibre materials are modelled as elastic-perfectly plastic. The time-dependent creep behaviour is modelled using the Norton-Bailey relationship.

A detailed study on MMC responses to different cyclic load points within the shakedown limit is performed. The primary load level and dwell time are confirmed to be the two most important parameters for creep-fatigue interaction. When the dwell time is small enough (e.g. 1 hour) a closed hysteresis loop can be observed for a low level of primary load. Conversely when dwell time increases creep ratchetting become significant. The increasing dwell time increases the total strain range, by increasing the plastic strain increment during unloading phase, due to the stress relaxation during the creep dwell period. Once the steady state creep stress is reached at the end of the creep dwell no more increase of plastic strain increment is possible. Typically for a long dwell time (more than 1000 hours), creep ratchetting is present with an inelastic strain accumulation at each cycle, the magnitude of which increases almost linearly with the

dwell time. When the primary load is zero, creep ratchetting does not take place for any thermal load level and dwell times.

In addition to these results, a discussion on the failure mechanisms is presented for the most critical cyclic load point (B_2), showing a full unit cell view. The main contribution to the MMC damaging is the stress relaxation and redistribution during the dwell period, which makes it possible to yield regions which normally don't exhibit a plastic behaviour without the creep dwell. Overall, the life and integrity of MMC are reduced by the combined action of creep and fatigue damages, as well as the accumulated inelastic strain per cycle due to the creep ratchetting mechanism. At this high level of mechanical load, dwell time has a substantial impact on the failure mechanism. For dwell times up to 1000 hours, the creep-fatigue failure is dominated by creep damage. Otherwise, for extremely long dwell times (up to 10000 hours), the monotonic creep rupture occurs.

The effect of temperature on creep ratchetting is also investigated, and it has been demonstrated that for a low temperature of $150°C$, creep ratchetting is dominant over the creep-fatigue interaction after a critical dwell period when a mechanical load is applied. Conversely, at a higher temperature of $175°C$, the damage caused by creep ratchetting is less significant than the damage resulting from creep-fatigue interaction, where creep and fatigue damages are comparable for dwell times between 1 and 100 hours. However at such a higher temperature condition, when the dwell period is beyond 100 hours, creep damage dominates. The accuracy and efficiency of the LMM extended DSCA for the evaluation of cyclic plastic creep behaviour of MMC has been confirmed by direct comparisons with a set of ABAQUS step-by-step analyses. All the comparisons demonstrate that LMM is capable of providing accurate solutions, with reduced computational efforts.

4.4 Crack initiation assessment on dissimilar weld joint

4.4.1 The Dissimilar weld joint problem

High-temperature structures play an important role in the power industry, due to the increasing necessity of more efficient coal-fired [92, 93], cost competitive concentrating solar power plants [94], and for the IV generation high-temperature reactors [95]. This latter class of structures pose significant challenges, for both material science and structure integrity. Indeed it is known that the next high-temperature reactors will have an outlet temperature of about $700 - 850°C$, and it is planned to be increased up to $1000°C$ [96]. It is recognised that the interfaces between dissimilar metals and welds are the most probable location of crack initiation. A typical dissimilar material joint is composed of a reactor pressure vessel steel (SA508), a nickel based filler material and a structural stainless steel (316L(N)) [97].

Crack initiation can be triggered by several phenomena, which can be categorized into two types. The first one regards the welding process of the joint, which can be affected by the cooling rate during the welding process, the welding technique adopted, the weld metal composition at the fusion line where hard-brittle martensite microstructure can develops and Post Welding Heat treatment. The second one regards the operating condition and material properties of the DMW. Thermal fatigue is typically caused by the Coefficient of Thermal Expansion (CTE) mismatch, and by heat-up and cool-down cycles. Moreover, if a creep dwell is introduced within the load cycle, dangerous mechanisms can occur. The importance of creep has been highlighted by [98], further confirming the tendency of strain to be accumulated during the creep dwell in a localised area near the weld/steel interface. Moreover, high-temperature creep can enhance the cyclic plasticity and in extreme case introduces an incremental collapse mechanism known as creep-ratchetting [65].

In this subsection the previous study on ratchet limit for a pipe intersection with dissimilar weld metal joint performed by [18] is extended to consider creep-fatigue interaction. High-temperature fatigue and creep-fatigue interaction are investigated to understand the impact of different loading conditions. The effects of a thermal shock during the cycle, and creep dwell length on the failure mechanism are considered .

4.4.2 Dissimilar metal weld joint numerical model

The component is composed of a main pipe, a weld and a branch pipe showed in Figure 4.21a. All the geometry parameters are resumed in Figure 4.21b. The main pipe is made of 316L(N) stainless steel (green), and it has a radius of 120 mm and a thickness of 15 mm. The branch pipe is made of structural steel SA508 (grey), with a radius of 16.5 mm and a thickness of 3.5 mm. They are connected with a nickel based weld material (red), which has a thickness of 3.5 mm, and the face forms an angle of 45 degrees to the main pipe.

The mesh has been refined around the critical location of the weld region, leading to a model with a total of 4038 20-nodes solid isoparametric elements with reduced integration scheme. Due to the symmetry condition of the model, a quarter of the pipe intersection is considered. Furthermore, both ends of the pipes are constrained to expand in-plane.

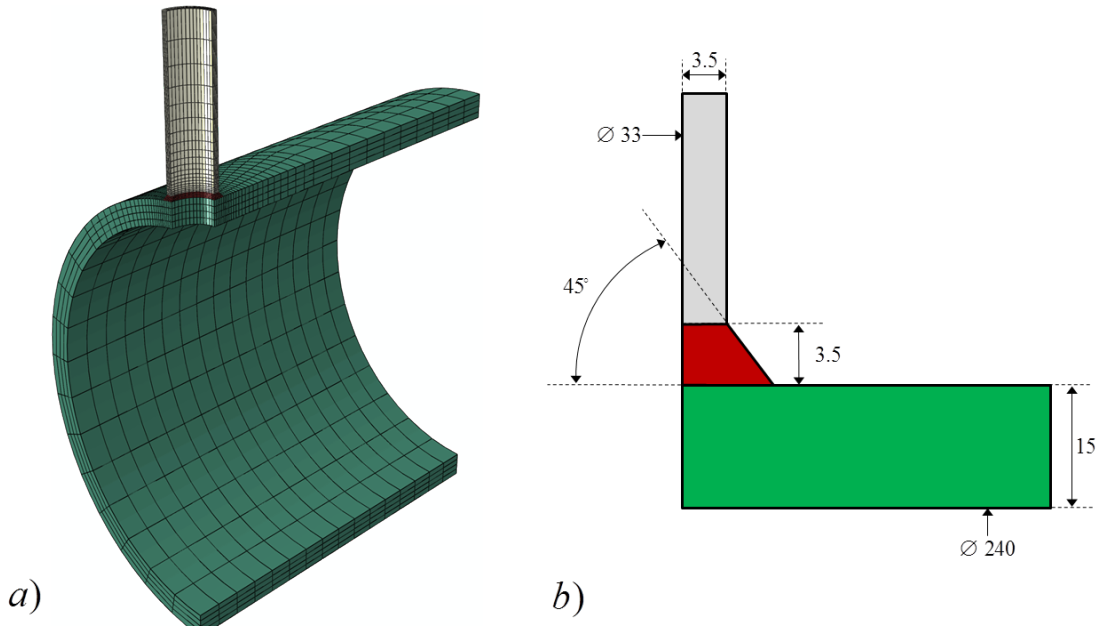

Figure 4.21: a) Dissimilar Metal Weld joint finite element model, b) geometry measurements of the DMW joint expressed in mm.

Two case studies have been analysed within this work, in both the effect of thermal stress has been assumed larger than any mechanical load. The first considers a cyclic homogeneous high temperature across the entire component. This condition is expected to be the most common, small temperature gradients are neglected in this study and the temperature is expected to vary smoothly across the small thickness. Instead the second case takes into account the effect of thermal shocks on the DMW life. For the first case, 3 load points are considered to simulate the steady state cycle. Two of these points are at high temperature and the third one is at room temperature. When thermal shock is considered, a total of 4 load points are required. At the first load point, the internal temperature is θ_0 and the outer is $\theta_0 + \Delta\theta$. Then the entire component is at $\theta_0 + \Delta\theta$. At the third one, temperature is held constant to consider the effect of creep dwell. Finally at the fourth load point, the temperature of the entire component returns to θ_0. Three dwell times of 1, 10 and 100 hours have been considered to study the impact of the creep dwell.

The elastic and plastic material properties of the dissimilar weld joint are obtained from literature [99] and are presented in Table 4.5 for a wide range of temperature. The plastic response is modelled using the Elastic Perfect Plastic assumption. The yield stress thermal degradation caused by the thermal gradient existing between the inner and outer walls is considered. The steady state creep and creep rupture time caused by the high temperature hold period are modelled by the Norton law and time fraction rule respectively.

The Norton law coefficients and creep rupture are reported in Table 4.6 for a wide range of temperatures and for $550°C$ respectively. However, for the IN82 more conservative creep rupture stresses are predicted at low load level as shown if Figure 4.22 (red continuous line). This is due to the lack of experimental results in the low stress range which has been pointed out also by [98].

Table 4.5: Elastic and plastic material properties of the dissimilar metal weld joint.

	Temperature $[°C]$	20	150	300	450	550	600	650
Young's	SA508	200000	192000	176671	158000	144000	129000	115000
Modulus	SS 316L(N)	195000	189000	178000	165000	156000	153000	147000
[MPa]	IN82	156000	147000	137000	129000	125000	123000	121000
Yield	SA508	472	465	430	345	298	221	142
Stress	SS316L(N)	262	206	161	152	149	141	138
[MPa]	IN82	265	238	212	196	190	189	180

Table 4.6: Secondary creep and creep rupture properties of the dissimilar weld joint.

	Temperature $[°C]$	500	550	600	650
	SA508	$8.99 \cdot 10^{-20}$	$2.67 \cdot 10^{-16}$	$9.25 \cdot 10^{-12}$	$9.40 \cdot 10^{-7}$
A	IN82	$1.0094 \cdot 10^{-24}$	$3.94 \cdot 10^{-16}$	$4.47 \cdot 10^{-15}$	$5.08 \cdot 10^{-14}$
	SS316L(N)	$9.27 \cdot 10^{-25}$	$3.97 \cdot 10^{-19}$	$1.71 \cdot 10^{-17}$	$7.16 \cdot 10^{-16}$
	SA508	7.87	6.53	4.87	3.05
n	IN82	4	6.270	6.644	7.018
	SS316L(N)	9.97	8.2	8.2	8.16
Creep rupture	SA508	$B = 1.397 \cdot 10^{21}$ k $= -8.620$			
parameters at	IN82	$t_f = 0.1559 \cdot \sigma^2 - 140.85 \cdot \sigma + 31765$			
$550°C$	SS316L(N)	$B = 1.24 \cdot 10^{28}$ k $= 9.904$			

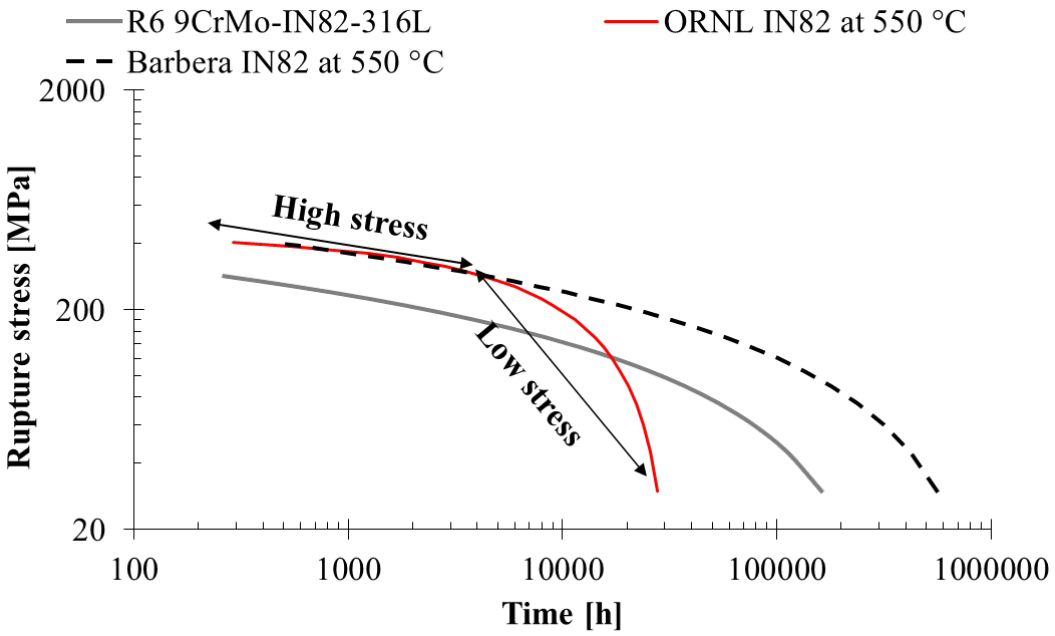

Figure 4.22: Rupture curves for IN82 form ORNL research program and DMW design curve from R6 at $550°C$.

For this reason an extrapolation has been done in order to obtain a more realistic rupture curve. The old creep rupture curve obtained by [100] is accurate only for high stresses, but the strength has an abrupt decrease for low stresses. This behaviour is not realistic compared to others design curves, such as the one obtained from R6

for a nickel based dissimilar metal weld. A new curve is obtained using the following equation, which replicate better the behaviour at low stress:

$$t_f = A \cdot e^{(b \cdot \sigma)} \tag{4.7}$$

where σ is the rupture stress, $A = 989345$ (hours) and $b = -0.019$ (MPa^{-1}) are the material parameters for the temperature considered.

4.4.3 Results for high temperature fatigue

When the temperature is imposed to vary in an homogeneous way across the entire pipe, the most critical location is located at the interface between the weld and the main pipe. This is due to the significant coefficient of thermal expansion mismatch. The cyclic maximum temperature for this case is $550°C$, and the loading cycle is represented in Figure 4.23a. The von Mises stress during the loading and unloading is shown in Figure 4.23b. The homogeneous temperature clearly affects, in both phase, the area where the constraint caused by the CTE mismatch is the highest. This loading condition is expected when the component operate in normal condition and no thermal gradient is present. Conversely, if a very high thermal gradient is considered the results are remarkably different. This is shown in Figure 4.24 where the von Mises history is reported for each cyclic load point.

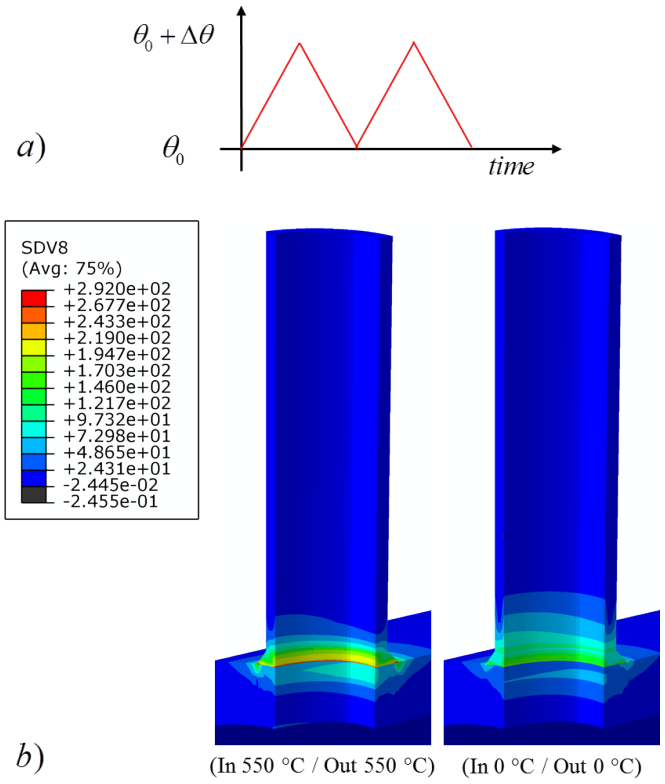

Figure 4.23: a) cyclic loading history of the thermal load, b) von Mises stress during the loading and unloading phase.

During the first stage the temperature is higher inner the component than outside. This generates a significant level of stress in the outer part of the small pipe (Figure 4.24). However, the yield stress of the materials adopted are temperature dependent. Due to this, when temperature becomes homogeneous the stress relaxation and redistribution occur. The outer surface, which is at high temperature, exhibits a lower yield stress. In according with this, the stresses accumulated in the previous cyclic load point must be redistributed. For this reason during the second phase the stresses appear to decrease. When the unloading phase starts, stress raises at the interface between the small pipe and the weld as shown in Figure 4.24.

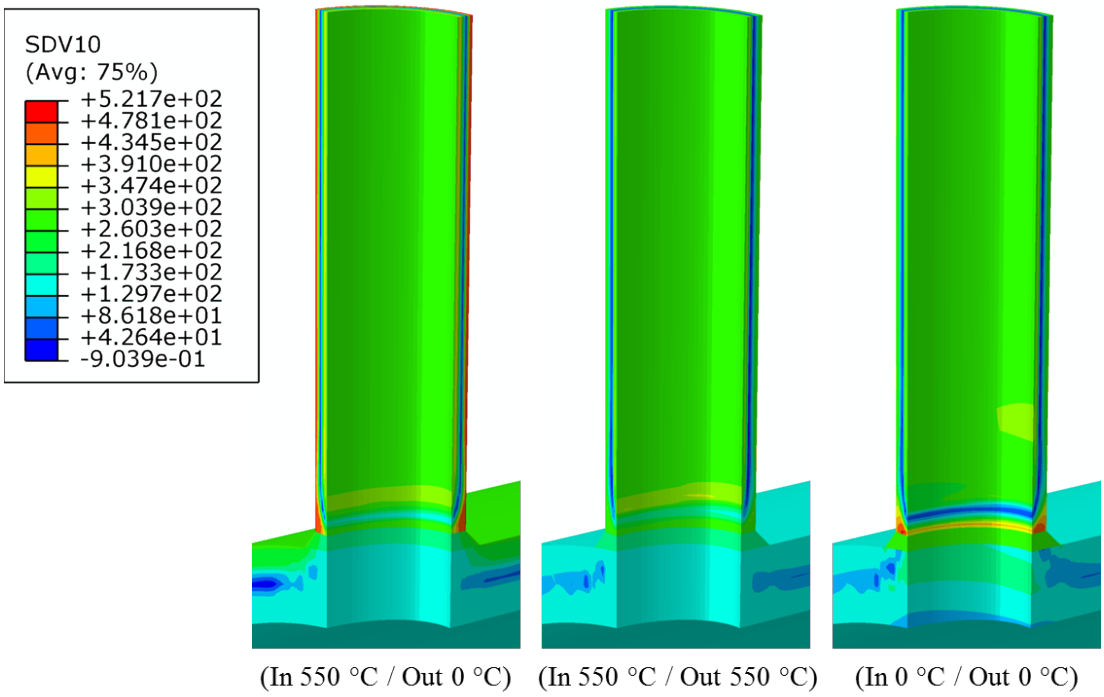

Figure 4.24: von Mises stress history during the thermal loading and unloading phase, considering the thermal gradient between the internal an external face.

These different responses lead to two different failure mechanisms, which are shown in Figure 4.25. The failure expected for thermal fatigue is located at the interface between the weld and the main pipe, as shown in Figure 4.25a. The cycles to cause such a failure are estimated using the fatigue life obtained from [101], and a total of 55185 cycles are expected. This calculation does not considered any hardening of the material and for this reason it is conservative. Figure 4.25b presents the failure mechanism when the thermal shock affects the DMW during the first part of the loading cycle. The location of the predicted failure is completely different and located at the weld interface, next to the small pipe. For this case a semicircular crack is expected and the number of cycles to fail is significantly low, 52. This latter failure mechanism has been spotted in other real power plant components, which experienced severe thermal cycling due to design errors or sudden changes of the operating load cycle.

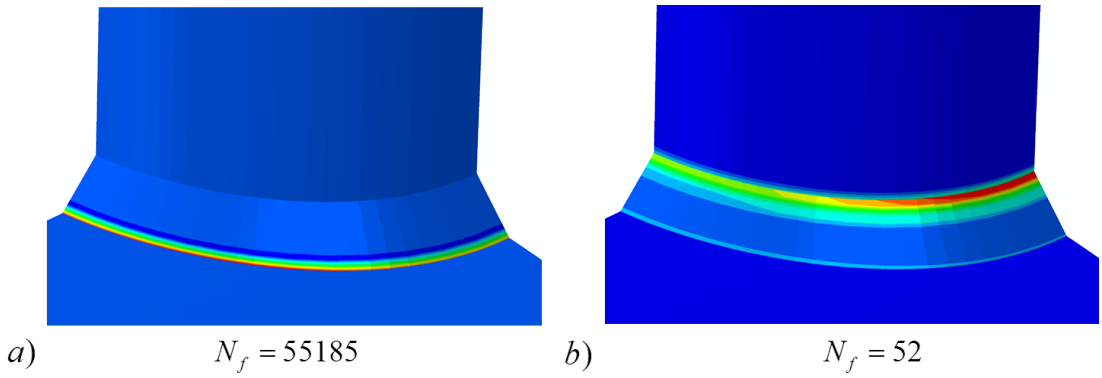

Figure 4.25: a) Failure mechanism for loading cycle without thermal shock, b) failure mechanism for the loading cycle with thermal shock.

4.4.4 Results for creep-fatigue interaction without thermal shock

The first effect of creep dwell on the component is to enhance the reversed plasticity through the stress relaxation. This mechanism has been described also by the recent report for MATTER project [102], and it is found to be significant also for DMW. The effect of stress relaxation on the hysteresis loop width can be seen in Figure 4.26a, where the stabilized cycles are reported for pure fatigue and different dwell times. The hysteresis loops presented are calculated at the most critical location on the outer surface of the pipe, at the interface between the weld and the main pipe. The stress relaxation tends to stabilize and it becomes less severe when the dwell time increase. However, its effect on the fatigue life is significant. The fatigue damage is reported in Figure 4.26b (blu circle) and it is dominant for dwell times shorter than 1 hour. Contrary, a significant interaction is expected for dwell between 1 and 10 hours, where the creep and fatigue damages are comparable. For dwell times longer or equal to 100 hours creep damage dominates and develops also in the internal area.

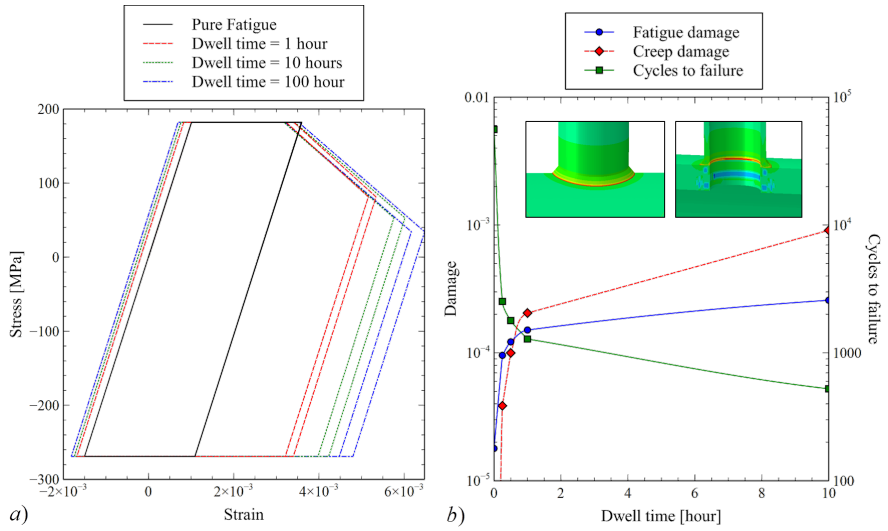

Figure 4.26: a) Stabilised steady state cycles and b) creep-fatigue damages and cycles to failure at the most critical location.

The creep strain develops mainly at the interface between the weld and main pipe as shown in Figure 4.27a. The accumulation of creep strain is very large up to 10 hours. After this threshold it continues by a linear trend. The increase of the dwell time introduces the known phenomenon of creep-ratchetting, which can be identified in Figure 4.26a. For the 100 hours case a small ratchet strain can be identified, this mechanism has been discussed by [65]. Using the creep-ratchetting diagram, shown in Figure 4.27b, the effect of creep strain and reversed plasticity can be seen. All the points analysed are below the closed loop limit. This means that the mechanism is driven by the reversed plasticity. However, the accumulated plastic strain is very small and can be neglected by adopting a more refined plastic material model. For this reason creep-ratchetting is not considered as a damaging mechanism in this case.

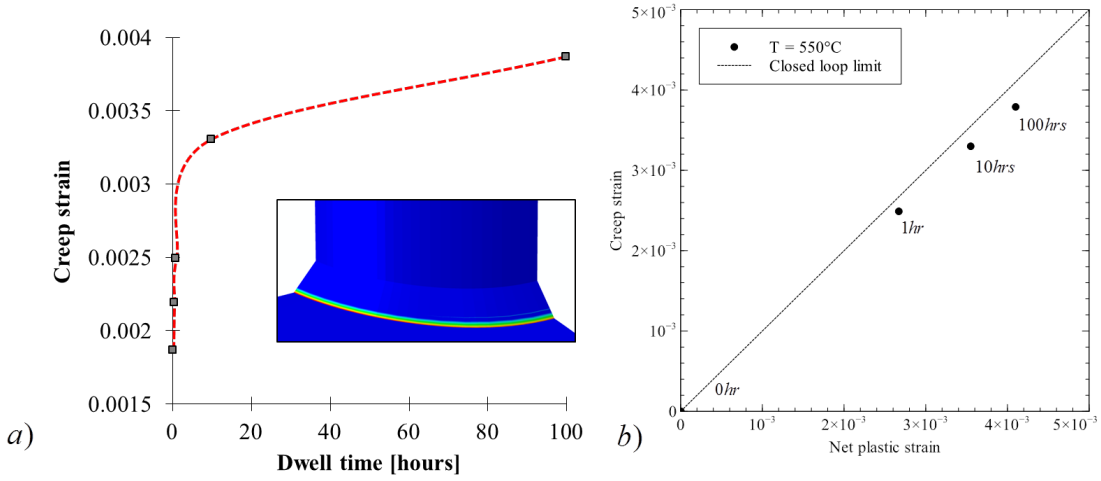

Figure 4.27: a) Creep strain accumulation at the interface between the weld and main pipe, b) creep-ratchetting interaction diagram for different dwell times.

In Figure 4.28 the predicted operating life of the DMW analysed is reported (solid circles). For comparison purposes the experimental results reported by [98] for a DMW made by 2.25CrMo-IN82-316L are shown in Figure 4.28 (solid square). In the same figure also three design curves are presented. The first is for 2.25CrMo-IN82-316L DMW (dotted line), the second for 9CrMo-IN82-316L DMW (continuous double line) and third is for IN82 weld material(continuous line). Both the design limits and the experimental results are based on pure creep test, where fatigue is not involved. However, in this study both fatigue and creep are assessed since the applied load is not monotonic.

The fatigue damage is calculated using the total strain range obtained by the LMM. For each integration point the total strain range is used to calculate the damage per cycle by entering in the E-N curve. At the temperature of $550°C$ the low cycle fatigue life of the three materials is known. If the assessment needs to be done at temperature where this data is not available the MUSM can be used as described in subsection 2.3.1.

The calculation of the creep damage is based on the time fraction rule, using equation 2.30. The average creep rupture stress is used to calculate the rupture time. However, the multi-axial effect needs to be considered. A procedure similar to the one described in R5 V6 for DMW assessment has been adopted. The von Mises stress is divided by the stress triaxiality factor. This makes possible to consider the effect of

Table 4.7: Design curve and parameters for the DMW analysed at $550°C$

Design curve for DMW at $550°C$	$ln(t_f) = \alpha_0 + \alpha_1 log_{10}(\sigma) + \alpha_2\sigma + \alpha_3\sigma^2$
α_0	18.75747
α_1	-4.424
α_2	-0.013
α_3	$-8.5 \cdot 10^{-5}$

multi-axial state of the stress, which is crucial to provide reliable results. Due to the level of uncertainty, as suggested by R5 V6, the rupture stress is multiplied by a factor 1.25. For long dwell, the creep damage has more time to develop and dominates over the fatigue as shown in Figure 4.27b, this kind of failure is the most likely for plant operation.

The results obtained by the LMM for the considered DMW are comparable with other types of dissimilar metal welds. However, a direct comparison with experimental results based on same geometry and material is not possible due to the lack of experimental results in literature. The improved creep rupture curve for IN82 at low stress allows to predict a more accurate creep damage. For this particular case a Creep-Fatigue Crack Initiation curve (CFCI) can be derived. The parameters that characterize the CFCI curve are shown in Table 4.7. By adopting the same methodology other curves can be derived for higher temperature, and a more general formulation can be obtained for design purpose.

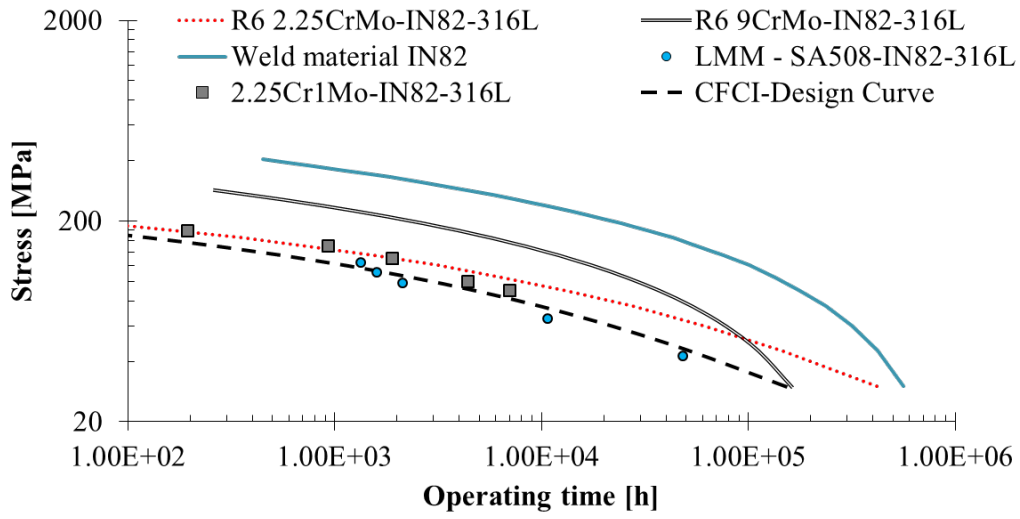

Figure 4.28: Rupture curves for DMWs and single parent and weld material at $550°C$.

4.4.5 Results for creep-fatigue interaction with thermal shock

As discussed in subsection 4.4.3, when within the load cycle a thermal shock is present, the associated failure mechanism remarkably affects the life of the component. The effect of creep on this cyclic loading case needs to be further investigated. By observing

the results, the creep strain accumulates strictly into two areas. The first one is showed in Figure 4.29, it is located outside the component and creep strain accumulates at the interface between the small pipe and the nickel weld filler. For relatively short dwell up to 1 hour, the creep strain accumulation is not significant. Conversely, when the dwell time is larger than 4 hours, the creep strain starts to increase significantly. The area affected by this creeping process is very sensitive due to the dissimilar metal weld, and in such a location the failure is expected to be more likely to initiate. Similar results are shown in Figure 4.30, where the creep strain accumulation at the inner surface of the component is reported for different dwell times. Once again the creep strain accumulates at the interface between the small pipe and the nickel-based weld. However, to correctly estimate the component's endurance the stress-strain history of the most critical location needs to be presented. Due to the large thermal stress introduced, one of the parameters chosen is the total strain range, and the second one is the sign of the most significant principal stress range. This latter one is required to assign the correct sign to the von Mises stress when the hysteresis loop is constructed. This strategy has been developed by [78] for multi-axial stress problems, where the stress direction is not easily identified. The principal maximum direction has been observed to cause the high-stress range at the location where the total strain range is maximum.

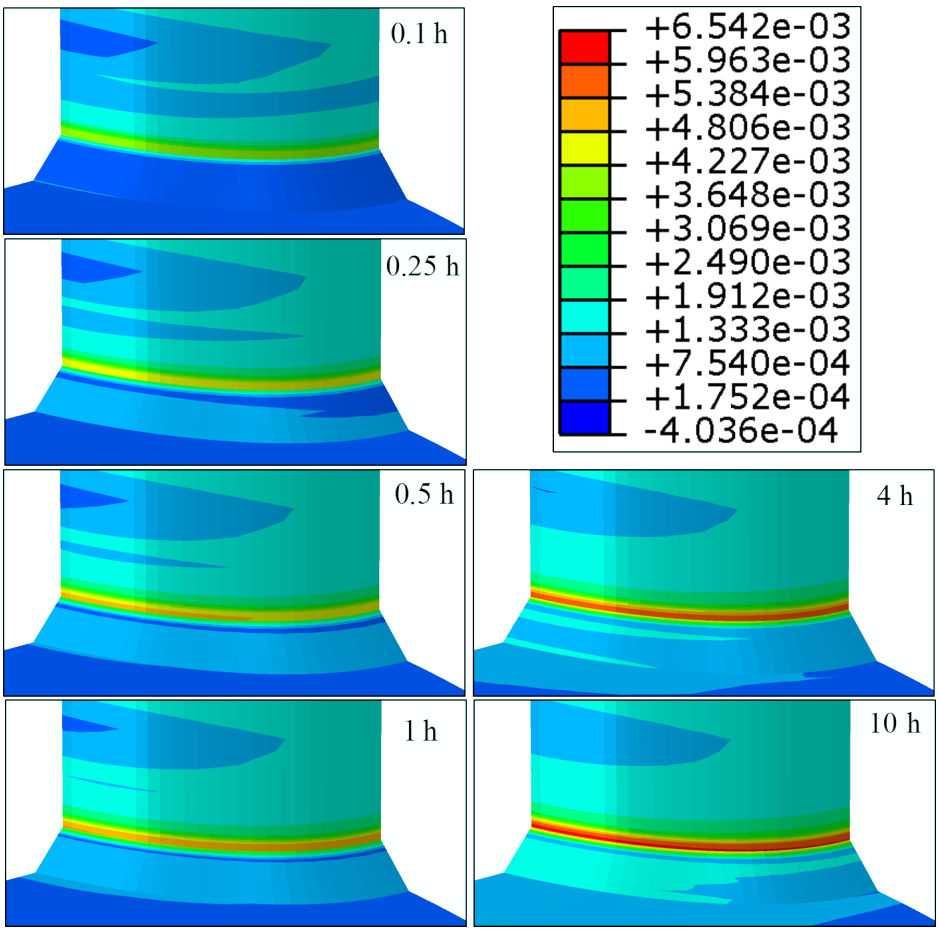

Figure 4.29: Equivalent creep strain on the outer side of the component, at the interface between small pipe and weld for different dwell times up to 10 hours.

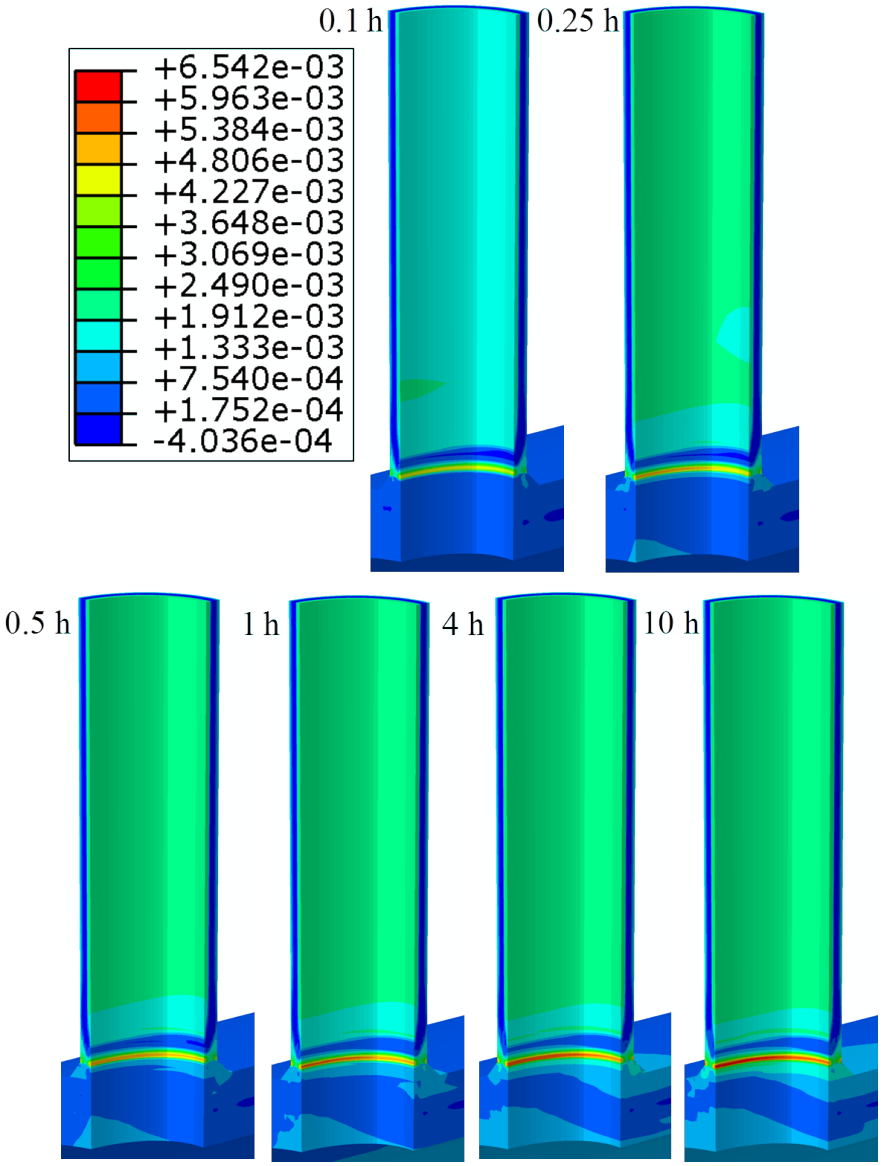

Figure 4.30: Equivalent creep strain on the inner side of the component, at the interface between small pipe and weld for different dwell times up to 10 hours.

By analysing the response of the most critical location, a large stress relaxation is observed with the increase of the dwell time. This is shown in Figure4.31a, where the equivalent von Mises stress at the most critical location is reported at different dwell times. The stress at the start of the creep dwell is 182.64 MPa, and in less than 5 hours it relaxes to 53 MPa. After 20 hours no significant stress relaxation occurs and the steady state stress has been considered to be achieved. Despite this large stress relaxation, the life of the component is not affected by the introduction of the creep dwell. This is depicted by Figure 4.31b, where the total damage and the number of cycles to failure have been reported against the dwell time. The estimated life reduces with the increase of the dwell time, but this change is negligible 4.4.3.

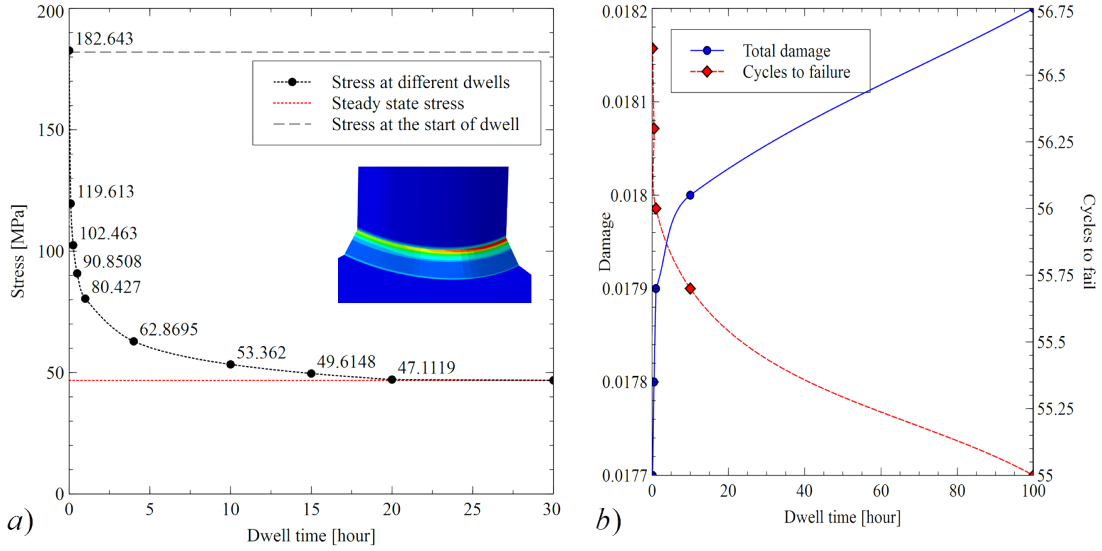

Figure 4.31: a) Stress relaxation at the most critical location for an increasing dwell time, b) total damage and cycles to failure against dwell time.

This can be explained by understanding the stress state when creep occurs within the load cycle. Due to the thermal load applied the creep dwell starts during a compressive phase, this means that no creep damage can be produced. Furthermore, the relaxation caused by the creep dwell allows preventing additional plasticity during the unloading phase. However, this mechanism also has the side-effect of enhancing the subsequent loading phase. The final effect is to improve the fatigue endurance of the DMW for short dwell and to reduce it for longer. In all the cases the failure is dominated by fatigue damage, and a transgranular cracking it is expected. The location of the failure, shown in Figure 4.31a, is the same determined for the pure thermal fatigue case with the thermal shock. This result is reasonable due to the severity of the loading scenario simulated. It also highlights the importance to avoid or limit such phenomenon within the life of the component. In this case study, the effect of thermal stress and temperature distribution are further enhanced by the material mismatch. The interface between the small pipe and the weld is the most affected. To validate the results obtained a SBS analysis has been performed for the same loading case, considering a dwell time equal to 1 hour. Same material models have been used, considering elastic-plastic-creep materials. A visual comparison between the stress field predicted by the LMM and the SBS is shown in Figure 4.32. For each load instance considered the stress field predicted by the LMM is very close to that one calculated by the SBS.

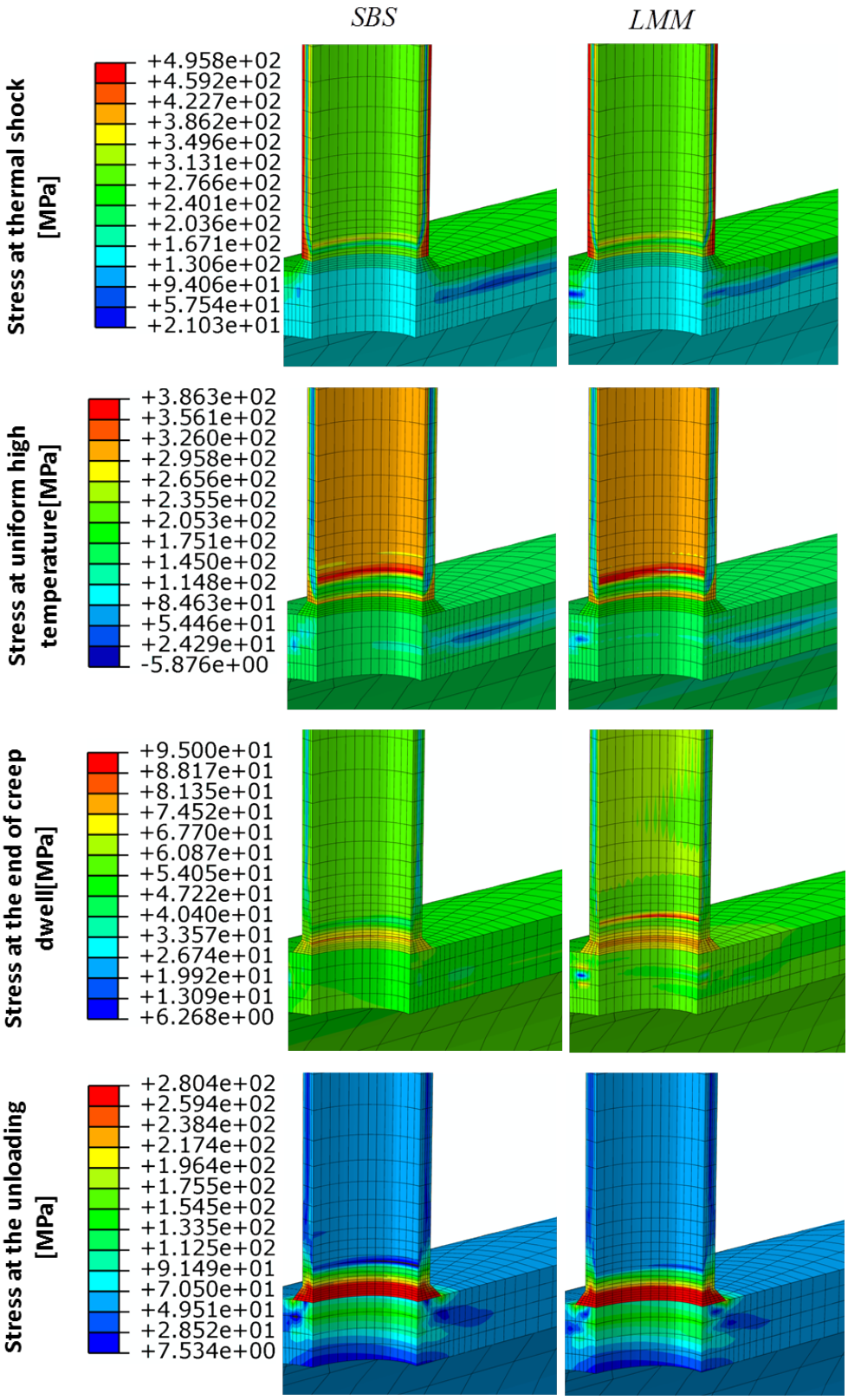

Figure 4.32: von Mises stress field at different load point for the Step-By-Step and LMM analyses.

Table 4.8: Equivalent stress and strain at the most critical location for the LMM and SBS analyses.

	Stress due to thermal shock [MPa]	Stress at high temperature [MPa]	Stress at the end of creep dwell [MPa]	Stress at unloading [MPa]
LMM	477	298	94.07	279.1
SBS	472	297	98.03	280.4
	Plastic strain due to thermal shock	Plastic strain at high temperature	Creep strain	Plastic strain at unloading
LMM	$6.144 \cdot 10^{-2}$	$5.718 \cdot 10^{-2}$	$5.559 \cdot 10^{-3}$	$8.557 \cdot 10^{-3}$
SBS	$6.121 \cdot 10^{-2}$	$5.733 \cdot 10^{-2}$	$5.164 \cdot 10^{-3}$	$8.282 \cdot 10^{-3}$
	Computational cost [seconds]			
LMM	766			
SBS	14680			

The effect of thermal shock, material mismatch and stress relaxation are fully replicated by the LMM, demonstrating its effectiveness. Furthermore, in Table 4.8 a detailed comparison between the LMM and the SBS is proposed. The stress and strain predicted at the most critical location are showed for each load instance. The results predicted by the LMM are always very close to those predicted by the incremental finite element analysis. It worth noting that the computational time required by the LMM is smaller than the traditional SBS. The LMM takes 766 seconds to calculate the steady state cycle response against the 14680 required by the SBS. This important feature is made possible by the direct calculation of the steady state cycle, which requires for this case study 200 increments. Conversely, SBS requires more than 26800 increments to reach the stabilised cycle. This final outcome shows the effectiveness of the eDSCA analysis for creep-fatigue crack initiation assessment.

4.4.6 Discussion on crack initiation on DMWs

A creep-fatigue structural assessment against crack initiation has been carried out for a dissimilar metal weld joint. The structural components are made of SA508 (branch pipe) and SS316L(N) (main pipe), and the weld is made of a nickel filler material IN82. The branched pipe structure is modelled using a quarter 3D model, which replicates a real plant component. The two structural steels and weld filler are modelled adopting the elastic-perfect plastic assumption. The time-dependent creep behaviour is modelled using the Norton relationship.

The cyclic behaviour of the dissimilar weld joint and the associated crack initiation process have been studied for two load cases. The first considered a homogeneous high temperature across the entire component. The second one included the addition of a thermal shock during the initial loading phase. For both cases, the effect of creep dwell duration has been investigated. In all the studies done the effect of internal pressure is neglected, due to the high thermal stress.

For the homogeneous high-temperature case the effect of the coefficient of thermal

expansions mismatch is significant. The crack initiation for the pure fatigue case is located at the interface between the weld and main pipe. However, when creep affects the component the crack is predicted to initiate at an earlier stage. The fatigue damage increases due to the creep-enhanced reverse plasticity, which tends to increase the width of the saturated cycle. A significant interaction between fatigue and creep occurs for dwell times between 10 and 100 hours. However, creep dominates for hold period longer than 100 hours, leading to intergranular cracking. A design curve for the component studied has been generated for the specific temperature of $550°C$. The predictions obtained are comparable with other experimental tests done on similar DMW. It worth noting that since now, no experimental results are available in the literature for the specific DMW analysed.

When the thermal shock is considered, the response of the structure changes remarkably and the crack initiation process drastically changes. The thermal fatigue cracking is significantly enhanced and also the steady state response is much different. The location of the expected crack is located at the interface between the small pipe and the weld, in the form of a semicircular crack. When creep affects the load cycle, results does not change for short hold period. Hence, the creep dwell starts in a compressive stress state, and no damage is directly generated. However, when the creep dwell becomes longer it enhances the loading phase and consequentially the fatigue damage.

The results have been verified through full inelastic analyses, and very good agreement is observed. The computational cost required by the eDSCA has been found to be lower than standard step-by-step analysis.

4.5 Conclusions

In this chapter, the creep-fatigue crack initiation has been assessed for two problems. In both the problems the crack-initiation process has been confirmed to be highly localised in a small region of the component. The initiation of the crack is largely affected by the loading history, the type of loads applied (primary or secondary) and the length of the creep dwell. The type of crack predicted is also affected by the magnitude and interaction of creep and fatigue damage. When fatigue damage tends to dominate for very short creep dwell or when compressive dwell are present. In this case the crack is predicted to start from the surface, and it is located in areas where the strain range is the highest. It is important to underline, how the effect of stress relaxation due to the creep dwell can drastically enhance the fatigue damage. This has been identified and demonstrated for both the case studies, and it has been very important especially for pure secondary load. Conversely for long creep dwells creep damage dominates, and the location of the crack initiation can vary depending on the stress redistribution and creep strain accumulation.

Within this work, it has been demonstrated how direct methods, such as the LMM, can be a valuable tool for researchers. The results obtained are accurate and the level of accuracy can be improved by adopting more refined material models. However, this does not limit the method's applicability especially when only reduced material data is available. This feature is very important for initial design studies. The method is capable of calculating both fatigue and creep damage assessing directly the steady state

cycle. This is done by directly calculating the residual stress field of each load instance and the associated inelastic strain. The iterative procedure ensures the convergence to a unique and accurate solution, and this has been demonstrated by the several case studies analysed. The detailed Step-by-Step analyses have confirmed the accuracy of all the results obtained. It worth mentioning that the computational cost required by the eDSCA is lower than any traditional finite element approach.

However, the method needs to be enhanced in order to calculate more accurate creep damage. This can be done by implementing the stress modified ductility exhaustion method. This feature will be described in the next chapter, where a detail discussion on strain based creep damage methods will be done. For the calculation done in this chapter, the time fraction rule has been adopted successfully. The creep rupture stress was properly modified by using the triaxiality factor when required. The time fraction rule is a good compromise when detailed creep ductility data is not available, and the start of the creep dwell is not at a very high stress. In this latter case, the time fraction rule tends to be overly conservative.

Chapter 5

Improvements to the creep damage assessment by the LMM

5.1 Introduction

As discussed in chapter 2, and further investigated in chapter 4, the evaluation of creep damage is crucial for a safe design and assessment of structures operating at high temperature. The effect of creep could be significant and in some cases even more severe than fatigue. As shown within chapter 2, several methods have been developed and these are divided into stress and strain based methods. Since its early stage, the LMM incorporated the time fraction rule, which belongs to the first category. However, as discussed in chapter 4, the multiaxial stress state and the load type can affect the accuracy of the time fraction rule. This is particularly dangerous when primary loads are very low or negligible. Furthermore, the cyclic behaviour of the structure can change significantly if it is controlled by a secondary load. This last consideration is even more relevant for GEN IV nuclear reactors, where components will experience very high temperature and very low mechanical load. In this scenario, if a large stress relaxation occurs during the creep dwell, the time fraction rule can predict too optimistic creep damage.

The actual practice within the UK's R5 is to use the Ductility Exhaustion method, which has been further extended by also considering the effect of the stress. The effectiveness of this method has been proven by several pieces of research over the last 10 years. However, as in other design codes, it relies on the use of elastic analyses and assumption to fully assess the cyclic response of the structure. As previously demonstrated these ruled based methods are capable of providing safe, but overly conservative predictions [103]. Furthermore, this conservatism is expected to be enhanced by the introduction of new operating conditions, which are required for new high-temperature reactors and power industry components [93, 96]. In order to improve the capabilities of the LMM in assessing a whole class of problems, including creep-fatigue crack initiation, in a more efficient and accurate way the Stress Modified Ductility Exhaustion (SMDE) method need to be fully implemented. This will allow combining for the first time the efficiency and robustness of eDSCA, which has been demonstrated in chapter 4, and the accuracy of SMDE.

In this chapter, a review of strain based methods available in the literature is given,

and detail description of the Stress Modified Ductility Exhaustion method is provided. Furthermore, the effect of the stress state is discussed and carefully reviewed. In order to test the updated LMM the life of a Single Edge Notched Bend (SENB) specimen subjected to a cyclic mechanical load at constant high temperature is assessed. In order to properly consider the effect of multiaxial stress state on the creep damage, for the first time, the SMDE approach has been implemented within the LMM. The predicted endurances are compared with the experimental and numerical results obtained by [103, 104] within the Brite-Euram C-FAT BE-5245 project. Furthermore, the impact of creep duration and additional primary load on the steady state cycle response is investigated. All the results demonstrate the method capability of accurately assessing a whole class of loading conditions also not considered during the experimental works.

5.2 Strain based methods for creep damage modelling

5.2.1 Introduction to creep strain ductility under uni-axial load

Several structural steels, when operating under high temperature and tensile loading, fail due to the growth and coalescence of voids. However, the mode of failure, as it was studied by Beere [105] and later by Hales [106], is dependent on the load level and the stress multiaxial state. In his early work Hales identified that the strain to failure was related to the strain rate. Three distinct failure mechanisms or regimes has been identified, and shown in Figure 5.1a [107]. In his work Hales considered only spherical voids, with initial radius r_0, for simplicity. The failure occurs when the radius reaches the critical size of $\frac{\lambda}{2}$, where λ is the cavity spacing. Regime I, shown in Figure 5.1b, occurs for high-stress level and the voids growth is the result of plastic deformation. An elegant mathematical representation of this physical phenomenon is given by Hales, demonstrating how the failure strain is independent of stress and time. For a spherical cavity growing in a steady-state creep regime consider the following growth rate:

$$\dot{r} = B_1 \dot{\varepsilon} \tag{5.1}$$

where $\dot{r}$ is the radius growth rate of the void, B_1 is a material property and $\dot{\varepsilon}$ is the creep strain rate. By integrating equation 5.1 the strain to failure is obtained:

$$\epsilon_f = \dot{\varepsilon} t_f = \frac{\lambda}{2B_1} \tag{5.2}$$

where ϵ_f is the strain to failure and t_f is the failure time. Equation 5.2 shows the existence of an upper bound for the creep ductility, and it can be obtained from hot tensile test or high stress tensile creep test. For intermediate stress level, a transition is observed, Regime II in Figure 5.1c. This change of mechanism between Regime I and II occurs when the cavity growth for diffusion dominates over the plastic hole growth.

In this regime the cavity radius growth rate is linearly related to the stress σ and the material parameter B_2:

$$\dot{r} = B_2 \sigma \tag{5.3}$$

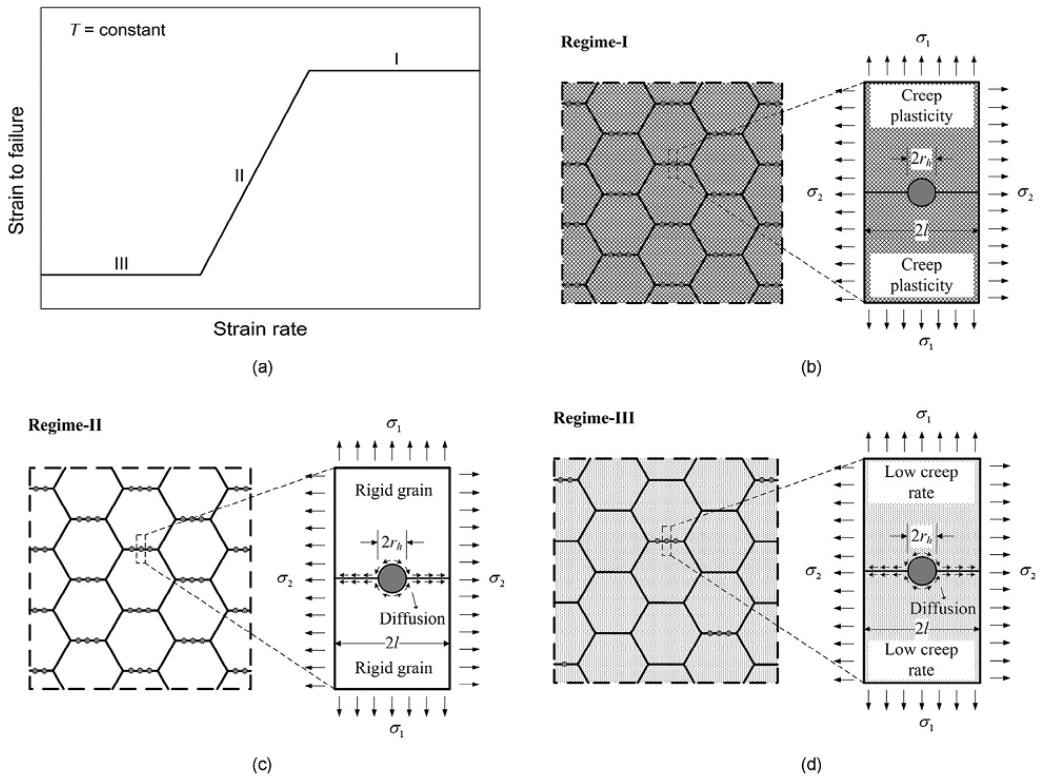

Figure 5.1: Effect of strain rate on the failure ductility. a) Schematic representation of the three regimes depending on the creep strain rate, b) regime-I where plastic cavity growth dominates, c) regime-II where diffusion controlled cavity growth occurs, d) regime-III where constrained diffusion growth takes place. (source: [107])

By integrating equation 5.3 the rupture time is given:

$$t_f = \frac{\lambda}{2B_2\sigma} \tag{5.4}$$

By combining equation 5.4 and the Norton law for steady-state creep the strain to failure as a function of the strain rate, stress multiplier A and stress exponent n is given:

$$\epsilon_f = (\frac{\lambda A^{\frac{1}{n}}}{2B_2})\dot{\epsilon}^{\frac{(n-1)}{n}} \tag{5.5}$$

Equation 5.5 clearly shows how the strain to failure is a function of the strain rate, and it is related to both the material properties and load condition. However, when a low stress is applied the constrained diffusion mechanism dominates and Regime III starts as presented in Figure 5.1d. For this regime, the strain to failure is represented by a constant value. The stress at cavitation boundaries relaxes, producing a stress redistribution. This local mechanism stops when the local strain rate, due to the cavitation process, is equal to that present in the remote area. This physical behaviour can be expressed by the following equation, which is a fixed value function of the vacancy spacing λ and grain size d:

$$\epsilon_f = \frac{\pi \ \lambda}{6d} \tag{5.6}$$

This physical and mathematical representation of the creep ductility, as reviewed by [108], can be used to estimate the creep damage in structures operating in creep regime. The so-called strain based methods have recently been further enhanced by [109, 110] using the local approach based on scalar damage. However, the stress based methods have serious drawbacks in terms of sensibility to the material parameters, such as α and the stress level. Even when CDM is not employed and the time fraction rule is adopted the results can be unsatisfactory. For load cycles where the creep dwell starts at the maximum strain, the time fraction becomes overly conservative. Moreover, it becomes less conservative for load cycles with a small strain range with the creep dwell starting at the maximum strain. Despite this, this method is adopted in several design codes such as the ASME-NH and RCC-MR. However, the strain based methods are progressively becoming more reliable and accurate than stress based.

The stress independent ductility exhaustion method has been extended by [59] to consider the effect of stress and the impact of multiaxial stress state. The creep damage per cycle is calculated by the following formulation:

$$d_c = \int_0^{t_h} \frac{\dot{\bar{\varepsilon}}_c}{\bar{\varepsilon}_f \left(\dot{\bar{\varepsilon}}_c, \sigma_1, T\right)} dt \tag{5.7}$$

where t_h is the hold time, $\dot{\bar{\varepsilon}}_c$ is the creep strain rate and $\bar{\varepsilon}_f \left(\dot{\bar{\varepsilon}}_c, \sigma, T\right)$ is the von Mises strain to failure. The strain to failure is a function of the creep strain rate, the temperature and the stress. The contribution of the stress has been demonstrated to be important to better approximate the cavity nucleation process. The creep uniaxial ductility can be represented by the following equation:

$$\varepsilon_f = A_1 \cdot \exp\left(\frac{\Delta G}{RT}\right) \cdot \dot{\bar{\varepsilon}}_c^{n_1} \cdot {\sigma_1}^{-m_1} \tag{5.8}$$

where A_1, ΔG, n_1 and m_1 are material parameters obtained by using a multi linear interpolation of the creep ductility data. Also the effect of the material composition has been implemented by [111] to account different chemical compositions of the steel considered.

5.2.2 The effect of stress and stress state on the creep ductility

The triaxial state of stress has a significant impact on the failure of industrial components since due to the manufacturing requirements they contain many cross-sectional area changes, grooves or welds. In these locations, the equivalent stress is higher than other areas and are more likely to develop cracks. However, when creep and fatigue interact the damage caused by creep can be enhanced by the stress triaxiality. The triaxial stress commonly develops within the surface, at a distance of several hundred microns from the stress concentrator as observed in notched specimens experiments [112–115]. It has been further demonstrated by [11] that the effect of the stress triaxiality is to significantly reduce the creep ductility. This has also been outlined by

the review work done by [107] where a detailed overview of several multiaxial ductility factors (MDF) is given.

The MDF models can be divided into three categories: Physically Based MDF, Semi-Empirical MDF and Empirical MDF. The first consists of those MDFs that incorporate the physical impact of multiaxial stress state to the creep fracture. The creep fracture is recognised to be governed by two mechanisms, the growth and the coalescence of microvoids. One of the most famous multiaxial ductility factors is the one created by Cocks and Ashby [116]. It is capable of modelling the grain-boundary cavity growth due to the creep power law of the surrounding matrix:

$$\frac{{\epsilon_f}^*}{\epsilon_f} = \frac{sinh[\frac{2}{3}(\frac{n-0.5}{n+0.5})]}{sinh[2(\frac{n-0.5}{n+0.5})]\frac{\sigma_m}{\bar{\sigma}}} \tag{5.9}$$

where n is the secondary creep stress exponent, σ_m is the mean stress and $\bar{\sigma}$ is the von Mises stress. As reported by [11] and recently by [107] equation 5.9 becomes less effective for small changes of n leading to overestimated values for the ductilities. A significant enhancement has been done by [110] by introducing a new physically based MDF:

$$\frac{{\epsilon_f}^*}{\epsilon_f} = \frac{exp[\frac{2}{3}(\frac{n-0.5}{n+0.5})]}{exp[2(\frac{n-0.5}{n+0.5})]\frac{\sigma_m}{\bar{\sigma}}} \tag{5.10}$$

Another physical based MDF is represented by the one developed by [59], which has been considered for implementation within the eDSCA numerical procedure. Two different cavity growth mechanisms are evaluated, the diffusion and the creep power law controlled growth. It has been demonstrated by [11, 106] that when the strain rate exponent n_1 is smaller than the theoretical one obtained by $(n-1)/n$, where n is the secondary creep stress exponent, the cavity growth mechanism is coupled with the diffusion and the creep power law mechanism. In this case, the modified Cavity Growth Factor (CGF) introduced is:

$$CGF_{modified} = \frac{\bar{\sigma}}{\sigma_1} \exp\left(\frac{1}{2} - \frac{3\,\sigma_p}{2\,\bar{\sigma}}\right) \tag{5.11}$$

The first term of equation 5.11 $\left(\frac{\bar{\sigma}}{\sigma_1}\right)$ is used to properly describe the diffusion mechanism affected by the principal stress. The second term $\left(\exp\left(\frac{1}{2} - \frac{3\sigma_p}{2\bar{\sigma}}\right)\right)$ is used to model the creep power law cavity growth [117] and it is based on the model developed by [118] for hole growth in the plastic deformation regime.

To better evaluate the effect of multiaxial stress state on the creep ductility the plot of multiaxial ductility factor against the stress triaxiality is presented in Figure 5.2. The uniaxial stress case is represented by a circle, all of the models presented pass from this point when the stress triaxiality is 0.33. All the experimental results reported from the literature [119–124] for a multiaxial stress state are present for stress triaxiality up to 1.6 [107]. It is worth mentioning that no cases are available for a low level of stress triaxiality below 0.33. However, this region is important and should be investigated more for its relevance in real practical cases. From Figure 5.2 it is clear that the three physical methods give reasonable results. However, the most accurate are provided by the Spindler CGF and the newest developed by Wen and Tu. These

two MDFs return very close results for stress triaxiality over 1.2. For stress triaxiality between 0.6 and 1.2, the Spindler CGF looks more accurate especially for austenitic stainless steels and for CrMoV. Conversely, the MDF from Wen-Tu is more accurate for the others, providing a better lower-bound for 316H at a high level of triaxiality. However, the model proposed by Wen and Tu is still slightly insensitive to changes of stress exponent n.

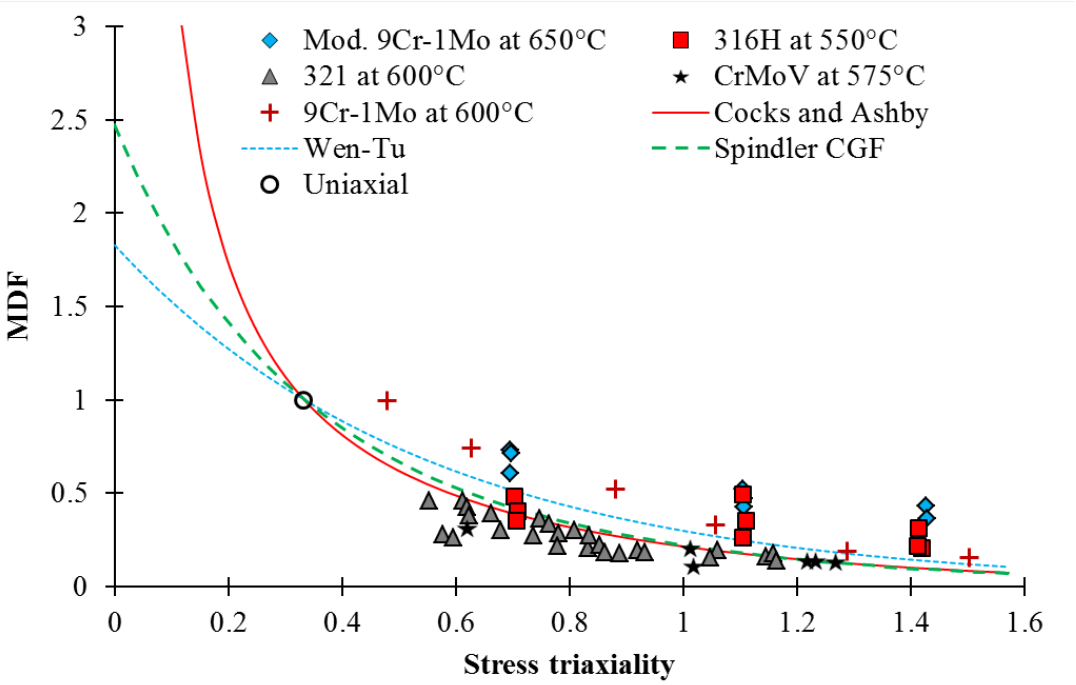

Figure 5.2: Effect of stress triaxiality on the multiaxiality ductility factor for different physical models, and experimental results on notched bar specimen at high temperature.

Both the MDFs provide a good starting point for the assessment of creep ductility when comprehensive multiaxial data is not available. It can be concluded that both these approach are robust enough to be used for structural integrity. However, due to the better performances of the Spindler CGF with the CrMoV and other structural steels, and its implementation within the UK's R5, it has been implemented within the LMM.

5.3 Numerical example: SENB Specimen

5.3.1 Finite element model and material properties

The same test specimen adopted by [104] has been used for this study. Due to the symmetry conditions, only half of the entire model is analysed. The model is composed of 1425 plain strain quadrilateral elements, with a reduced integration scheme. As shown by Figure 5.3, the mesh is refined near the round notch, which has a radius of 6 mm. Symmetry conditions are applied to the left side on the x-axis (Figure 5.3), and the translation is constrained with boundary conditions applied on the right part

of the model. A Load Point Displacement (LPD) is imposed as shown by Figure 5.3, producing the desired elastic stress field necessary to perform the LMM eDSCA analysis.

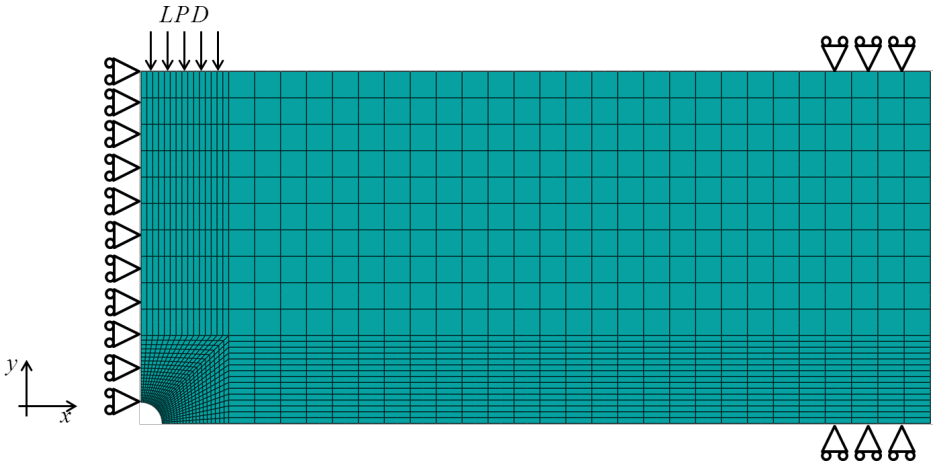

Figure 5.3: Finite element model and mesh of the SENB specimen.

The SENB specimen is subjected to different fully reversed LPDs in a 0.268 0.5 mm range, considering dwell time of 0, 0.5 and 16 hours. Furthermore, an additional pure axial load of 200 MPa has been considered for the study.

Table 5.1: Material properties for elastic, plastic and creep behaviour in MPa and hours.

1CrMoV at $550°C$			
Youngs modulus [MPa]		151700	
Poissons ratio		0.3	
Ramberg-Osgood	B = 646.67		beta = 0.1092
Norton-Bailey	A = $2.5 \cdot 10^{-30}$	n = 10.5	m = -0.6

The 1CrMoV material properties adopted for this work has been largely obtained from Japanese NIMS database, and are shown in Table 5.1. The cyclic-stress strain behaviour of this alloy is modelled using the Ramberg-Osgood relationship:

$$\frac{\Delta\varepsilon}{2} = \frac{\Delta\sigma}{2E} + \left(\frac{\Delta\sigma}{B}\right)^{\frac{1}{\beta}} \tag{5.12}$$

where $\frac{\Delta\varepsilon}{2}$ is the total strain amplitude, $\Delta\sigma$ is the total stress range, B and β are material parameters. The Ramberg-Osgood constants are obtained by the locus of the tips of the steady state cycle response at $550°C$ [22] for different total strain ranges. Due to the homogenous high temperature, the creep deformation that occurs during the dwell period is calculated using the Norton-Bailey relationship defined as:

$$\dot{\varepsilon}^{cr} = A \cdot \sigma^{n} \cdot t^{m} \tag{5.13}$$

where $\dot{\varepsilon}^{cr}$, σ and t are creep strain rate, stress and time, respectively, and A, n and m are material parameters. In order to calculate the most accurate creep damage due to

Table 5.2: Parameters for DE and SMDE creep ductility models.

DE	SMDE
$A_1 = 19.005$	$A_1 = 1.5489$
$n_1 = 0.3489$	$n_1 = 0.2953$
	$m_1 = 0.2111$

the hold time, the creep uniaxial ductility is calculated. To avoid overly conservative results, the local rupture strain is calculated by the reduction of area measured during the creep test [104]. The data used for the material property extrapolation has been obtained from the NIMS database. Figure 5.4 shows the scattering data (symbols) and both the lower and upper shelves and transition part generated (dashed line). A total of 10 different batches of data are used to fully describe the material ductility. For high strain rate, also the tensile results are adopted and an upper shelf has been identified (Figure 5.4a). When the component operates at such a high level of average strain rate, the creep damage mechanism is governed by the matrix deformation. In Figure 5.4a also the lower shelf is shown, and it starts for average strain rates lower than $2 \cdot 10^{-6}$ h^{-1}. In this case, the creep damage is mainly caused by the grain boundary cavitation mechanism. Between the upper and lower shelf, a transition region is present. Figure 5.4a shows the transition law obtained using the DE formulation. For comparison, the SMDE parameters are also obtained using multi-linear regression. The results are shown in Figure 5.4b, where the experimental points are interpolated and the parameters obtained are reported in Table 5.2 for both the model.

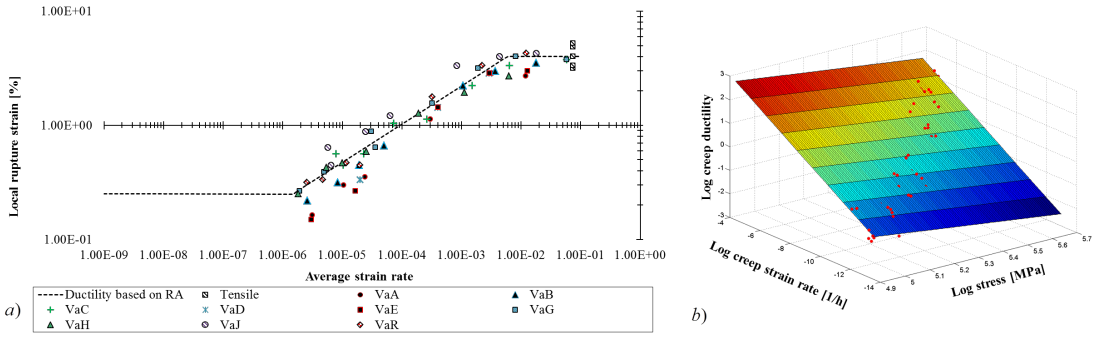

Figure 5.4: a) Local rupture strain based on reduction of area against the average strain rate to failure, b) Creep ductility using the stress modified exhaustion method by multi linear regression.

The fatigue data is obtained from the R66 Issue 8 [125] database, for 1CrMoV at $550°C$. The data are obtained from isothermal low cycle fatigue tests at different strain ranges. The number of cycles to failure is defined as the number of cycles required to obtain a 2% stress drop in the steady state cycle. The fatigue damage per cycle is obtained by $d_f = 1/N_0$, where N_0 is the cycle to failure associated with the total strain range calculated by the eDSCA. Creep damage (d_c) per cycle can be calculated with both stress or strain based methods. When TF rule is used the average creep stress during the dwell is obtained to determine the rupture time required by equation 2.30. Conversely, for DE and SMDE the creep strain increment and the multiaxial creep ductility are calculated for the associated creep dwell. Hence, the total damage per cycle

is defined as the linear sum of fatigue and creep damages, subsequently the predicted endurance is defined as $N_f = (d_f + d_c)^{-1}$. By knowing the experimental endurance for each load case, the total damage based on the total creep damage D_c and total fatigue damage D_f can be calculated. D_{tot} must be lower than unity to prevent crack initiation, otherwise the component is likely to exhibit crack initiation. The unity limit is an empirical rule, and it is based on direct comparison with experimental results [22].

5.3.2 Comparison with simplified method

The accuracy of the creep-fatigue crack initiation assessment is related to the capability of estimating the parameters required. The most relevant are the stress at the start of the creep dwell, the stress drop due to the hold time, and the total strain range. R5 adopts different approximated methods in order to calculate the aforementioned quantities. The effect of creep on the total strain range is considered by summing the stress drop to the maximum elastic stress range. The ratio between this revised stress range and the effective Young's modulus gives the revised elastic strain range. The cyclic strain range, including the plastic strain, is calculated by adopting the Neuber rule and using the cyclic data obtained by the Ramberg-Osgood relationship.

The calculation of the stress at the start of the creep dwell has three different options available within the R5 [4]. In this comparison the same one used by [103] has been adopted, where the start of the creep dwell stress is limited by the yield at the creep end. A factor of 1.25 is applied to provide a better estimate than a non-conservative solution as required by R5 [4]. The entire procedure described relies upon only elastic analyses, and for this reason, it is always conservative.

Instead, the LMM directly calculates the residual stress field caused by plastic behaviour for an assigned cyclic load point, using the Elastic Perfect Plastic material model or adopting the more accurate Ramberg-Osgood model. Using this method, more accurate stress levels are obtained, improving the accuracy of the assessment. The stress at the start of the creep dwell obtained by the LMM is 345 MPa against the 369 MPa obtained by the R5 procedure. In terms of stress drop, the LMM predicts for the 0.5 hour case a drop of 52 MPa against the 69 MPa of the less conservative R5 option. The total strain ranges obtained are 1.12% and 1.55% for LMM and R5 respectively. The approximated method always gives a more conservative assessment of the fatigue damage.

In terms of creep damage, the LMM is capable of providing a more accurate prediction of the damage within each analysed cyclic load point. The calculation of the creep and plastic flow stress considers the full interaction between creep and plasticity response, which generates stress relaxation and redistribution. This feature is fundamental for the accurate assessment of the component, especially where notches, grooves and changes of section are present. This is not accurately represented by methods based on elastic analyses and enhances the conservatisms of the rule-based methods. These differences are shown in Figure 5.5 where the creep damage predicted for the 0.5 hour dwell at different LPDs is plotted. The LMM always produces a less conservative prediction, which makes the predicted endurance closer to the observed life.

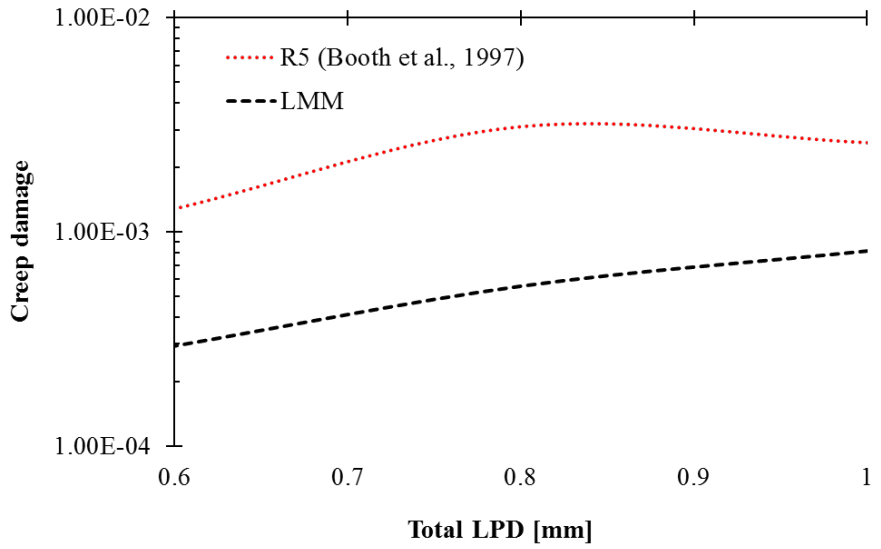

Figure 5.5: Comparison between creep damage per cycle predicted by R5 procedure (dotted line), and LMM (dashed line).

5.3.3 Predicted endurance by LMM

A benchmark test has been performed to demonstrate the differences between the various creep damage models available within the numerical procedure. A total of four case studies have been analysed, one without creep and three with creep dwell at different positions within the load cycle (Table 5.3). From the results obtained the fatigue damage is enhanced by the creep dwell. Time Fraction rule (TF) gives the most conservative result, and for high levels of stress at the start of the tensile dwell it produces the most conservative result. However, it is capable of identifying the compressive dwell producing a very low damage. The Ductility Exhaustion (DE) method predicts overly optimistic results and is overly conservative when a compressive creep dwell is considered. This is one of the drawbacks of this method. The Stress Modified Ductility Exhaustion (SMDE) performs well in all the cases considered because it is capable of combining the strengths of both stress and strain based methods. For these reasons only DE and SMDE methods will be used for the SENB assessment.

Table 5.3: Fatigue and creep damages per cycle calculated for different loading cycles of SENB specimen subjected to a total displacement of 0.8 mm and a dwell time of 0.5 hours at $550°C$.

Load cycle	Fatigue damage	Creep damage		
		DE	SMDE	TF
Pure fatigue	$1.030 \cdot 10^{-3}$	-	-	-
Tensile peak dwell	$1.097 \cdot 10^{-3}$	$3.19 \cdot 10^{-4}$	$5.57 \cdot 10^{-4}$	$1.92 \cdot 10^{-2}$
Compressive peak dwell	$1.099 \cdot 10^{-3}$	$3.36 \cdot 10^{-3}$	$2.17 \cdot 10^{-7}$	$2.06 \cdot 10^{-6}$
Tensile and compressive dwell	$1.182 \cdot 10^{-3}$	$3.32 \cdot 10^{-3}$	$1.03 \cdot 10^{-3}$	$1.92 \cdot 10^{-2}$

The entire assessment is summarised in Figure 5.6, where the observed number of cycles to failure are plotted against those predicted. The continuous line represents the interpolation of the observed endurance (solid square) of the SENB specimen subjected

to different loading conditions. The LMM predictions are plotted for different dwell times, loading conditions and creep damage models. The results for different creep damage models are represented by diamonds (DE) or circles (SMDE). Good agreement is shown by the SMDE for all analysed cases, while DE has been demonstrated to be slightly non-conservative but always within a factor of 2. Accurate predictions are obtained for long creep dwell (16 hours) by the SMDE. The endurances predicted by the SMDE are never less conservative than the observed ones, except for a single case. For all the cases analysed, the predicted cycles to failure are never more conservative than those calculated by [103]. Very good accuracy is demonstrated when an additional axial load of 200 MPa and a dwell time of 0.5 hours are considered. For this case the life predicted by the LMM is 661 and 570 cycles for DE and SMDE respectively, which is very close to that observed (576 cycles). The solution obtained is far less conservative than the R5 procedure and comparable to the fully inelastic analysis, which predict 108 and 526 cycles to failure respectively [103]. It is worth noting that the computational cost and the number of material parameters required are both significantly lower than full inelastic analyses.

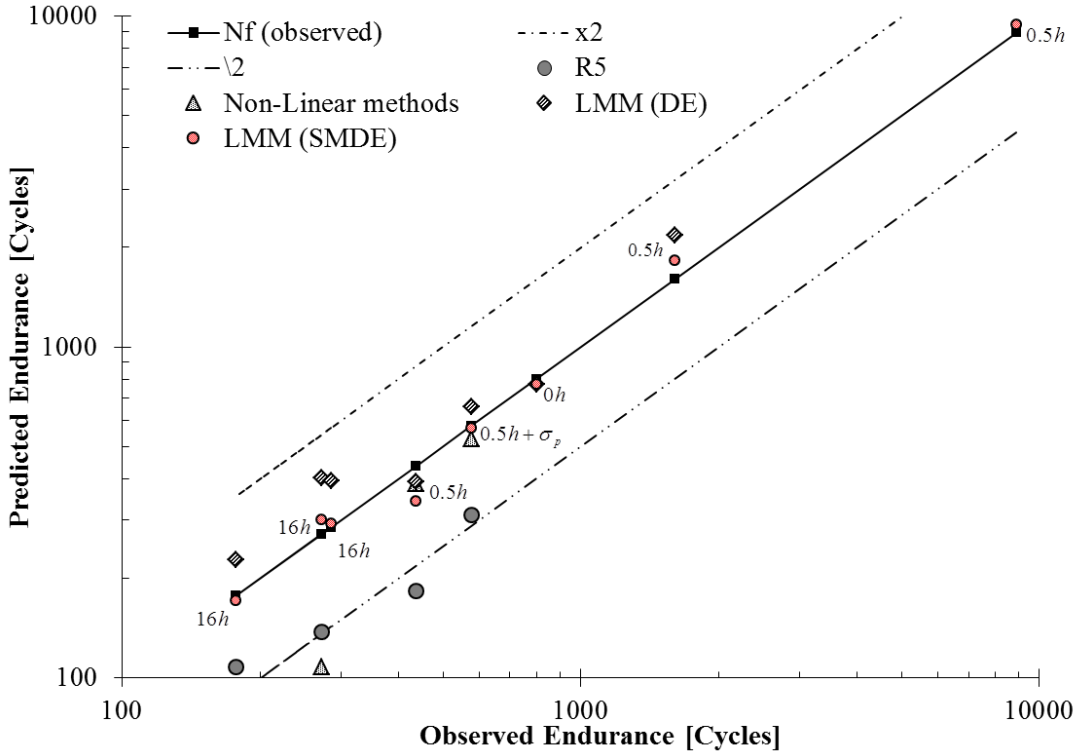

Figure 5.6: Endurance plot representing the observed cycles to failure (solid square), the LMM predictions (diamond, and circle) for different dwell times and loading cycle, R5 predictions (solid circle), inelastic analyses prediction (triangle).

The effect of the dwell time duration on the failure mechanism is shown in Figure 5.7 where the creep and fatigue damages per cycle are plotted against the load point displacement applied for the two dwell times. Figure 5.7a shows the creep and fatigue damage for a dwell time of 0.5 hour. For such a dwell there is a strong interaction between creep and fatigue. However, as discussed by [115], for low strain cases (small

LPD) creep damage is dominant over fatigue. Conversely, for high strains, fatigue damage dominates. Significant creep-fatigue interaction occurs for a total LPD between 0.45 and 0.55 mm. This behaviour completely changes for longer dwell, as is shown in Figure 5.7b. In that case, the creep damage is always greater than fatigue.

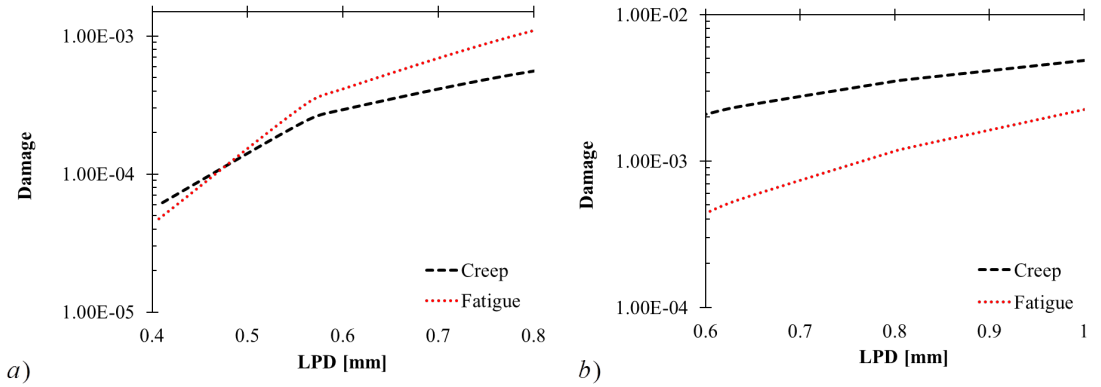

Figure 5.7: Creep and fatigue damage per cycle for different Load Point Displacement applied for a dwell time of a) 0.5 and b) 16 hours.

When creep damage dominates the failure is expected to initiate from inside the specimen, at a depth of several hundred micro-meters from the notch root. This behaviour is highlighted in Figure 5.8 where the total damage is shown in the form of contour plots for two dwell times under the same applied mechanical load. Figure 5.8a shows the total damage, that is dominated by the creep damage. Conversely, Figure 5.8b shows a much lower damage which is dominated by a fatigue mechanism. By comparing these two contours, it is evident how the damage initiates in a much larger and deeper area (Figure 5.8a) when creep is dominant.

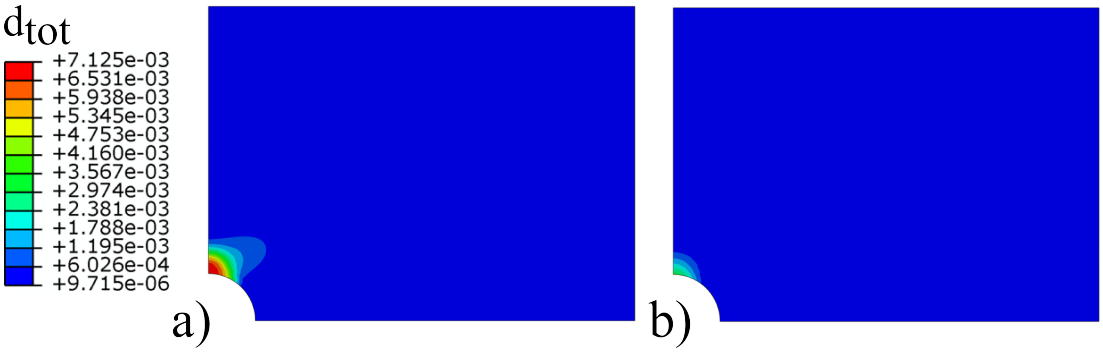

Figure 5.8: Total damage per cycle calculated for an applied LPD 1.0 mm at a) 16 hours and b) 0.5 hour creep dwell.

The importance of the principal stress in the failure mechanism is also crucial to accurately predict the failure of a component. Due to the triaxiality of the stress state, the principal stress is expected to be larger than the von Mises stress. In Figure 5.9 the stress state and the triaxiality factor is plotted against the cross section of the notched specimen. The creep damage contour calculated is superimposed to the plot. The von Mises stress at the start of the creep dwell is subjected to a large relaxation.

As expected the principal stress is larger than the von Mises stress and the triaxiality factor is remarkably higher inside the bar. In that location, as depicted by Figure 5.9, the maximum damage per cycle is observed, which is about 1000 micrometres from the surface as observed by many experi-mental and numerical works on notched specimens[112–114].

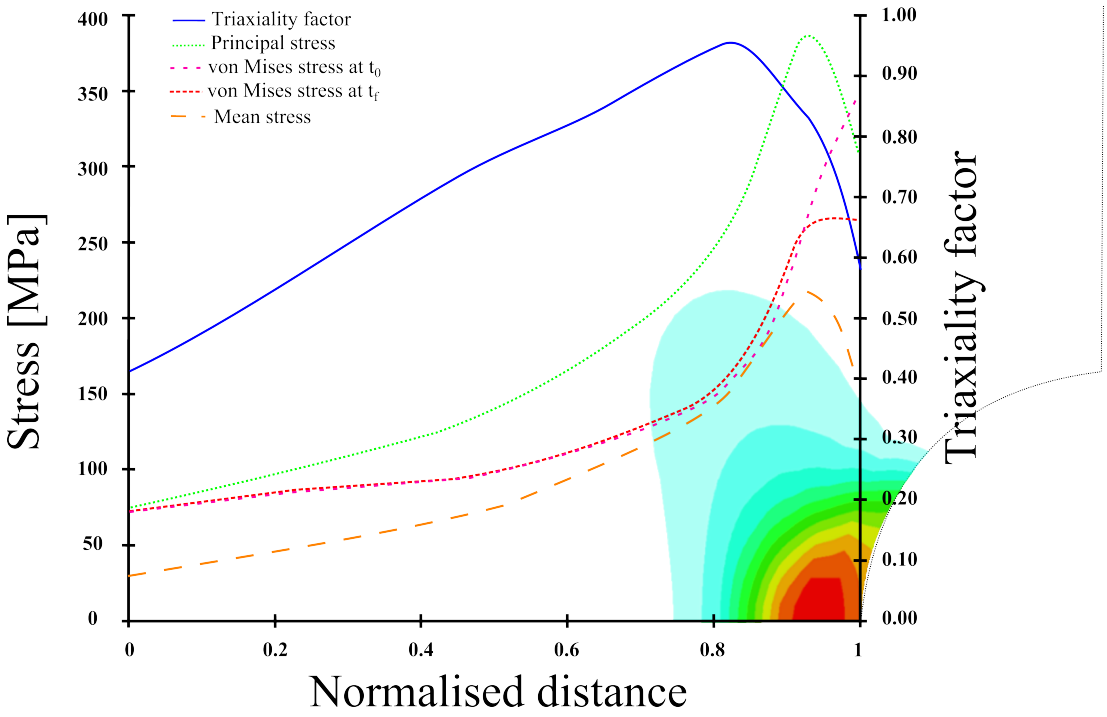

Figure 5.9: Impact of stress state on creep damage. Stress and triaxiality factor distribution in the cross sec-tion of the notched specimen and superimposed contour of the creep damage for a LPD of 1.0 mm and a dwell time of 16 hours.

A parametric study has been performed to investigate the effect of the superimposed primary load on the component's response, considering a 0.5 hour creep dwell, a total LPD of 0.8 mm and an increasing superimposed load of 50, 100, 150, 200, 250 and 300 MPa. Up to 200 MPa the failure is always dominated by creep and fatigue interaction. However, creep ratchetting develops but it still negligible. The total damage per cycle produced by the creep-fatigue interaction, the creep-fatigue and the creep ratchetting endurances are reported in Figure 5.10. For the superimposed load of 100 MPa creep-fatigue interaction dominates, with a predicted life of 542 and 1360 cycles for creep-fatigue and creep ratchetting respectively. For the 200 MPa load case the predicted life due to the two mechanisms is comparable and affect two close areas in the notch groove as shown in Figure 5.10. If the axial load is increased up to 300 MPa the response changes and the predicted cycles to failure due to creep-ratchetting is 117 against the 344 of creep-fatigue mechanism. The locations where the damages initiate do not coincide, but are close enough to be likely to interact especially during the crack growth process. The superimposed primary load as expected reduces the component life and introduces an incremental mechanism, which affects the notch root area. Tong [126, 127]introduced and demonstrated that the ratchetting at the crack tip is a driving

mechanism for the crack growth process. The notch can be divided into three distinct areas: i) creep fatigue dominated, ii) creep-fatigue and creep ratchetting interaction area and iii) creep ratchetting dominated area. If a crack initiates in the second area the concept introduce by Tong [126] becomes relevant. The surrounding material ahead the crack exhibits creep-ratchetting affecting also secondary cracks, leading to a much more complex scenario in terms structural integrity of the defective body.

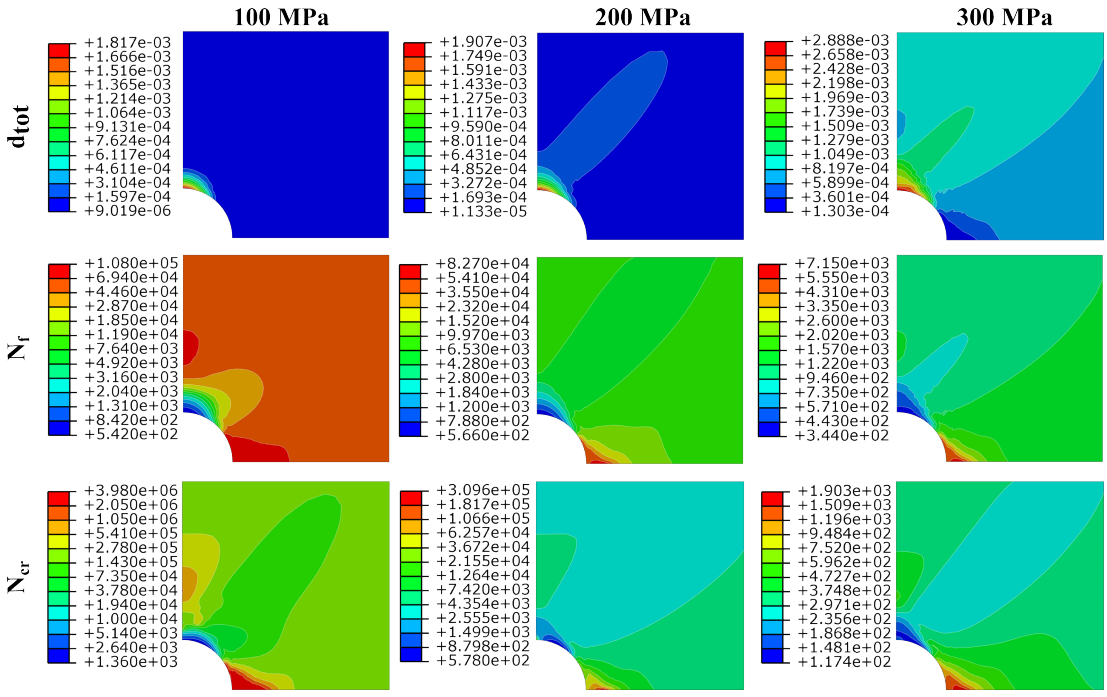

Figure 5.10: Contours of total damage per cycle, creep-fatigue life and creep-ratchetting life for a superimposed primary load of 100, 200 and 300 MPa.

A final overview of all the results obtained is given in Figure 5.11 , where the creep-fatigue linear damage summation diagram is shown for the different loading cases considered. All the endurances predicted, except two, are in the crack initiation area as expected (Figure 5.11). These results can be divided into three types of failure mechanism, fatigue dominated (above the dot-dash line), creep dominated (below the dot-dash line) and creep-fatigue interaction for points that lie closer to the depicted limit (dot-dash line). For the first type, transgranular cracking is predicted to initiate from the surface of the notched area, and the mechanism is strongly affected by the total strain range of the cyclic load condition. The second type exhibits intergranular damage, which initiates within the specimen, and the principal stress is a driving parameter. In the last case, the interaction between creep and fatigue is more complex and both surface and interior cracking are expected. Such a scenario occurs for intermediate applied loads and for short dwell times (0.5 hours, diamond symbol).

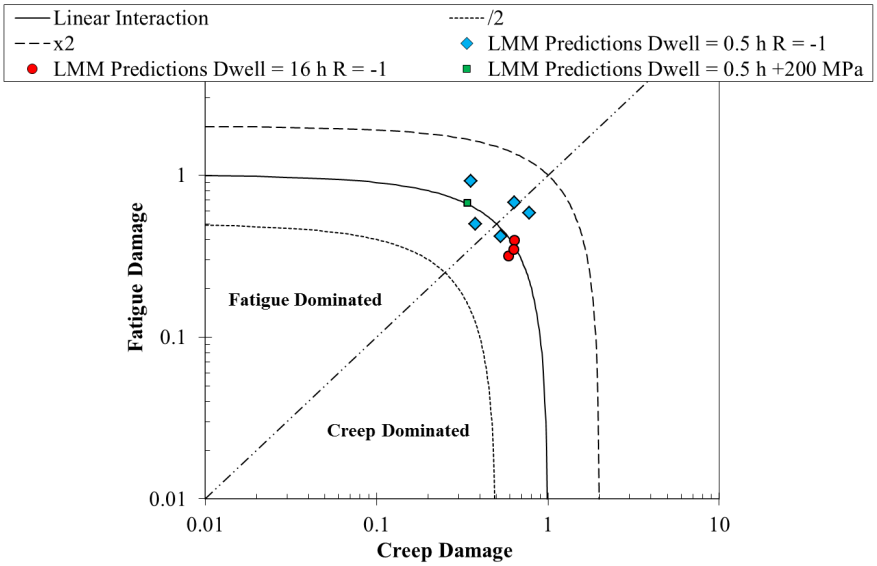

Figure 5.11: Creep-fatigue linear damage summation diagram for the cyclic loading conditions exanimated by LMM and SDME.

In order to further verify the accuracy of the adopted method, a comparison between metallography inspections on experimental results obtained by [128], and the numerical prediction have been presented in Figure 5.12. Figure 5.12a shows the multiple crack initiation occurred in the SENB component subjected a fully reversed total LPD of 0.8 mm, and an additional axial load of 200 MPa with a dwell time of 0.5 hour. The damage develops from the surface of the specimen, demonstrating that the crack initiation is fatigue driven. This failure mechanism has been identified by the numerical solution. This is shown in Figure 5.11 where the load point (square) is largely within the fatigue dominated area. Furthermore, in Figure 5.12b the distribution of the total damage is shown, and the area of maximum damage has a total width of about 2 mm, which is comparable to the area where multiple cracks have occurred.

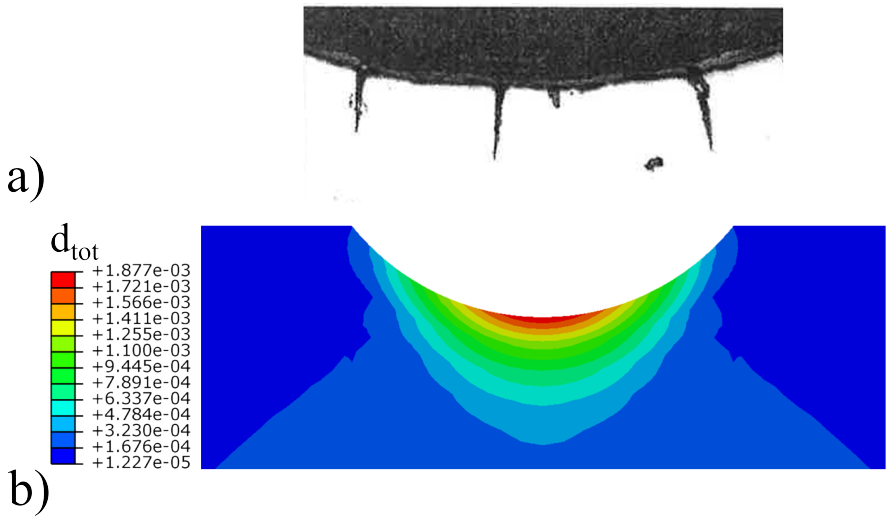

Figure 5.12: a) Creep-fatigue crack initiation and early growth at groove root for 1CrMoV SENB specimen by Holdsworth [128], and b) total damage per cycle calculated by the LMM for a 0.4 mm displacement and additional 200 MPa axial load, with a dwell time of 0.5 hour.

5.4 Conclusions

In this chapter, the LMM eDSCA method has been successfully improved by implementing the Stress Modified Ductility Exhaustion delivering a study on the creep-fatigue interaction Single Edge Notch Bend specimen. The cyclic response has been identified and discussed pointing out its implication on the structural integrity. The main results obtained within this research work are as follow:

1. Implementing the Stress Modified Ductility Exhaustion approach with the Cavity Growth Factor into the eDSCA leads to very accurate life predictions. Excellent agreement has been demonstrated for cyclic loads when a primary load is introduced. All the failure mechanisms have been properly identified and match with the experimental observations available in the literature.

2. The physical effect of the associated load level on the crack initiation mechanism has been properly modelled with the proposed numerical procedure. Load levels confirmed to be important in influencing the type of failure mechanism. Furthermore, the stress triaxiality, which has a severe effect on creep ductility, has been investigated and modelled properly.

3. A new and more detailed numerical study has been performed varying the superimposed primary load. For a superimposed primary load up to 200 MPa the creep-fatigue crack initiation dominates. Conversely, the failure is driven by creep-ratchetting affecting a different location. For this specific case creep-ratchetting is expected to enhance the crack growth process.

4. The results obtained further demonstrate the capabilities of the LMM eDSCA, in assessing structures subjected to cyclic loading conditions when a limited number of experimental data is available.

Chapter 6

Unexpected plastic strain during creep dwell

6.1 Introduction

Mechanical structures are designed to withstand defined loading conditions, which includes monotonic and cyclic thermal and mechanical loads. Different international design and assessment codes are currently adopted, like the UK's R5 procedure [4] and the ASME NH [3]. For each code, it is important that the structure does not fail during operative life, even in the case of severe accidents or malfunctions. This important issue can be tackled by adopting a fail-safe design and making sure that the safety margins are correctly estimated. Due to the severe consequences of chemical and radiation release on the society, these industrial structures have rigid requirements in terms of safety. However, after the dramatic multiple meltdowns at Fukushima Daichi nuclear power plant, in March 2011, it has been demonstrated how the integrity of components must be designed to withstand even more critical scenario. To do this, several aspects need to be considered and one of these is the accurate prediction of structural response of component subjected to an extreme load. The estimate of the deformations and times to failure in such an extreme scenario will contribute in supporting field engineers while facing an emergency, but also improve the resilience of the design. Furthermore, by investigating the behaviour of structures under off-design load it is possible to identify new unexpected failure mechanism.

The study proposed in this chapter is relevant for component's safety when extreme or non-conventional loading conditions occur, leading to the detrimental accumulation of inelastic strain, with emphasis on high-temperature conditions. A new failure mechanism associated with the increase of the plastic strain during the creep dwell is discussed. The novel mechanism has been identified by numerical finite element analyses on notched bars, subjected to high mechanical load level and high-temperature. Notched bars are considered due to their capability of representing more realistically the multiaxial stress state in real components. Two material models for cyclic plastic response have been considered, the Elastic Perfect Plastic (EPP) material model widely adopted for structure assessment and the more refined combined hardening model. Monotonic load has been considered as well, and the plastic behaviour has been modelled using the stress-strain curve. In order to prove that this mechanism

is not a numerical artefact, both the element type and mesh sensitivity have been investigated. The aim of this chapter is to identify, discuss and explain this new failure mechanism.

6.2 Material models adopted

For both the monotonic and cyclic load case the EPP material model have been used to study the impact of the model accuracy on the mechanism by understanding its effect on the magnitude and structural integrity significance of the new failure mechanism.

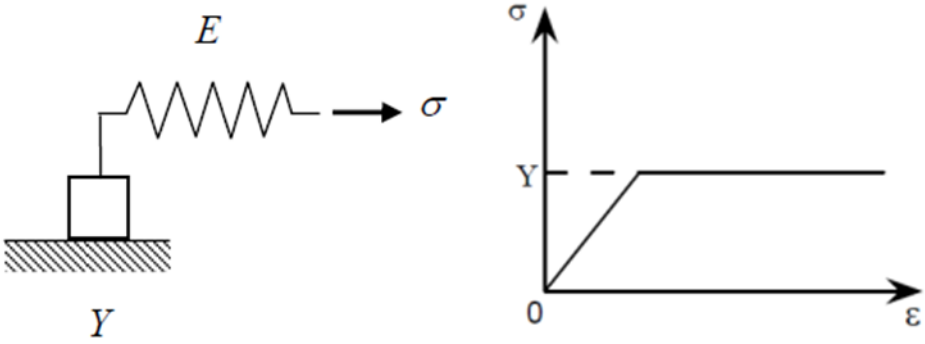

Figure 6.1: Schematic representation of the Elastic Perfect Plastic material model.

The EPP material model has been used extensively in the past and represents one of the most used model for limit analysis of metallic structures, especially for initial design calculation. It can be represented by a very simple mass-spring model, shown in Figure 6.1. When the applied load σ is below the yield only elastic strain accumulates, and the mass is still fixed. However, when the applied load reaches the yield limit, plastic strain accumulates, and the mass starts to move. If the load is removed, the mass cannot return in its own original position, since there is no recall force, and this reflects the physical aspect of the plastic strain.

For the most complex cyclic load case, the EPP can be overly conservative and inaccurate, especially for material that exhibit complex responses under cyclic load such as the Bauschinger effect or cyclic hardening/softening. The combined hardening model has been used to fully characterize the isotropic and kinematic hardening of the material.

The isotropic hardening is used to describe the change of size of the yield surface to an associated accumulated plastic strain as shown in Figure 6.2a. This mechanism can be represented by a scalar function R, known as the drag stress introduced by [129]. The rate of change of this function is expressed by the following equation:

$$\dot{R} = b(Q - R)\dot{\varepsilon}_p \tag{6.1}$$

where $\dot{R}$ is the rate of change of the drag stress during the progressive hardening associated to a plastic strain rate $\dot{\varepsilon}_p$. By integrating equation 6.1 with respect to the

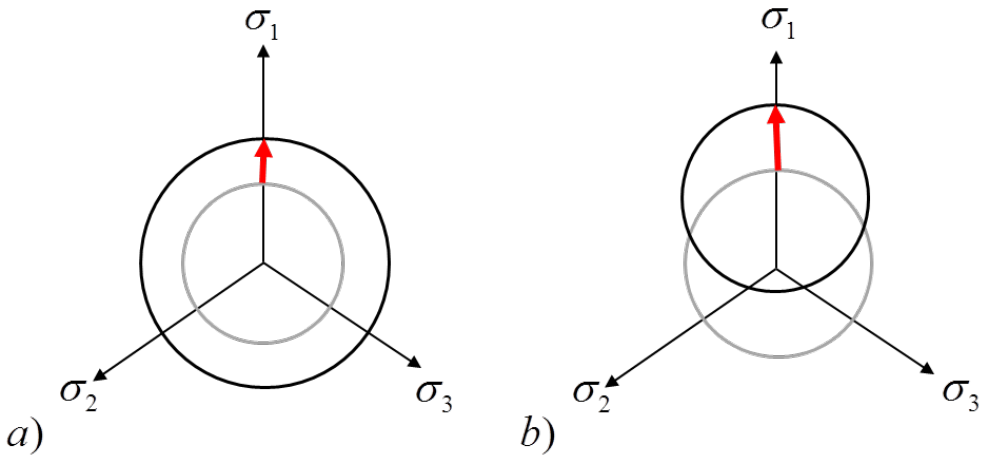

Figure 6.2: Schematic representation of a) isotropic and b) kinematic hardening.

time the dimensional change of the updated yield surface σ_0 is given by:

$$\sigma_0 = \sigma_y + Q_\infty \left(1 - e^{-b\varepsilon_p}\right) \tag{6.2}$$

where σ_y is the initial yield stress, Q_∞ represents the asymptotic value of the yield stress, b defines the rate of change of the yield surface for an associated plastic strain ϵ_p. The yield criterion then can be expressed using the von Mises function:

$$f = |\sigma| - \sigma_0 = 0 \tag{6.3}$$

The isotropic hardening is capable of modelling the cyclic hardening by increasing the elastic limit $(\sigma_y + R)$ for an associated plastic strain. Furthermore, the isotropic softening can be modelled as well by considering a negative Q_∞, which tends to reduce the final saturated yield strength.

Conversely, the kinematic hardening adopts a completely different concept to simulate the hardening/softening of materials. Rather than varying the yield surface dimension, the centre of the yield surface is rigidly translated within the stress plane as shown in Figure 6.2b. This modelling strategy is very important when tensile and compressive loads are present, and the Bauschinger effect needs to be considered. The yield surface drift is associated to a kinematic hardening parameter α, known as the back stress. The rate of change of the back stress is defined by the Armstrong-Frederick relationship as follow:

$$\dot{\alpha}_i = C_i \frac{1}{\sigma_0} (\sigma - \alpha) \dot{\bar{\varepsilon}}_p - \gamma_i \alpha_i \dot{\bar{\varepsilon}}_p \tag{6.4}$$

where the first term presents the linear hardening, introduced earlier by Prager in 1949, and the second term expresses the non-linear behaviour introducing the recall coefficient γ. The non-linear recall effect is coupled with the plastic strain rate. C_i and γ_i are both material constants, and for each back stress a couple of parameters need to be calculated. The overall back stress is calculated by the sum of each back

stress component. The number of back stresses used affects directly the accuracy of model adopted and three back stresses are normally used to fully describe the material behaviour for a wide strain range. However, in this chapter a single back stress is used due to the material constants provided by third part. All the material properties used for this research work are shown in Table 6.1. Both isotropic and kinematic hardening have been adopted in a combined the combined form keeping separate creep and plastic strain calculation.

Table 6.1: Kinematic and isotropic hardening material properties

Kinematic hardening			Isotropic hardening	
σ_y	C_1	γ_1	Q_∞	b
175	12374	150	99.8	37.7

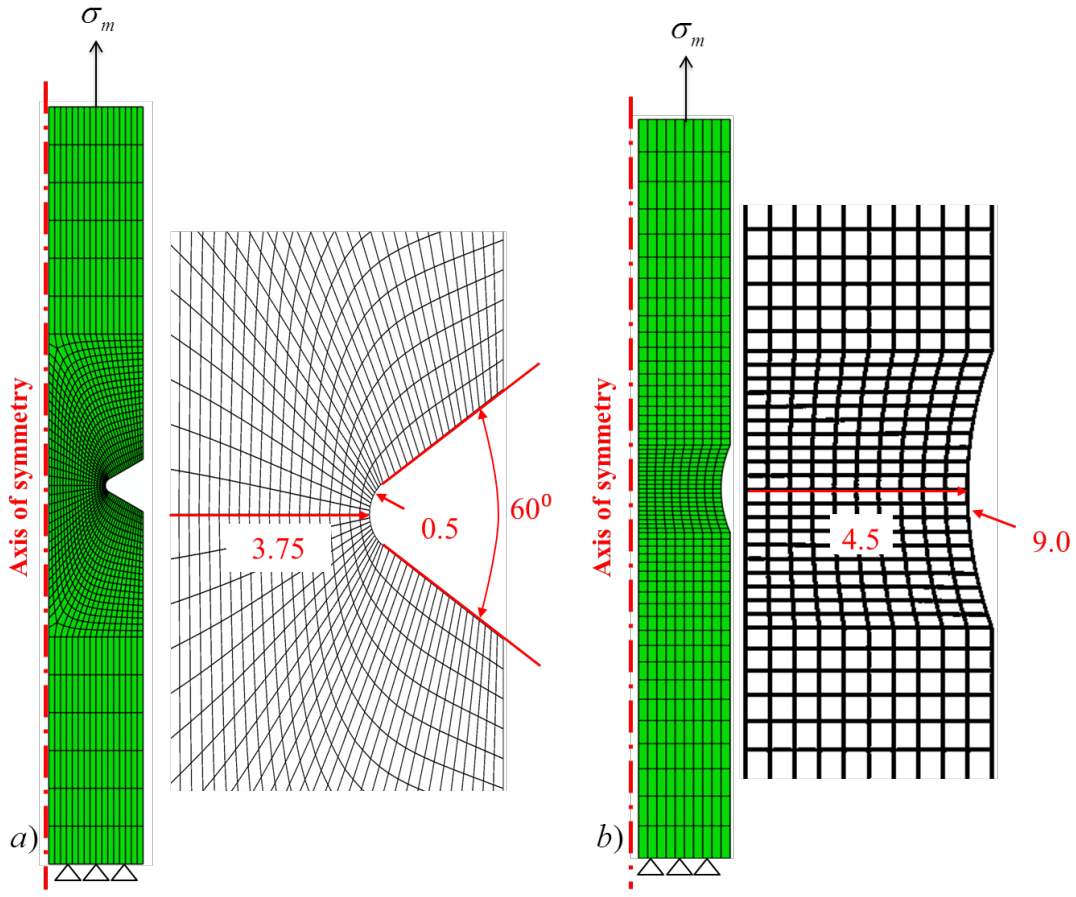

Figure 6.3: Finite element model and geometry properties for the a) v-notched bar and b) c-notched bar.

6.3 Numerical study

The v-notched bar is shown in Figure 6.3a and all the geometrical properties are reported as well. The mesh is refined in the notched area, and the entire model is composed of 1394 elements. The semicircular notched bar is shown in Figure 6.3b, the radius is 9 mm and the throat depth is 4.5 mm. The mesh is refined in the notched area, and the entire model is composed of 600 elements. For both the numerical models a 2D axis-symmetric 8 node quadrilateral element mesh with reduction integration scheme is adopted. A monotonic load with a subsequent creep dwell is considered in this study for both the models, and the time is increased to evaluate the response to a long term. The v-notched bar has a Kt equal to 5, which will lead to an extremely high level of stress with a relative small applied load, instead, the semicircular notched bar has a Kt equal to 1.4.

6.3.1 v-notched and c-notched bar: monotonic load

In this subsection, the results for the v-notched and c-notched bars analyses using the EPP and isotropic tensile hardening model are reported for several load cases. The effect of the load level is investigated by performing 3 analyses at 45, 60 and 90 MPa for the v-notched bar. The stress along the notch throat are reported in Figures 6.4a,b,c. In Figure 6.4a the von Mises stress at the start of the dwell (t_0) and at its end (t_f) is shown. At the start of the creep dwell only the most exterior area of the notch is at the yield. When the creep dwell starts, stress relaxation occurs and rapidly a stress redistribution takes place. For this load case, no increase of the plastic strain is observed. However, by increasing the load up to 60 MPa the plastic strain accumulation starts during the creep dwell. At the end of the hold period, as shown in Figure 6.4b, the stress is only partially relaxed and a small region still at the yield. In this region the accumulation of plastic strain is maximum. When the applied load is increased to 90 MPa the yielded area is larger than the 60 MPa case, and it is shown in Figure 6.4c. The von Mises stress contours at the start and end of the creep dwell are shown in Figure 6.4d. At the start of the creep dwell a larger area of the notch is yielded. However, the stress redistributes during the creep dwell, apart a small area that still at the yield. As for the previous load case in this area the plastic strain accumulation is significant.

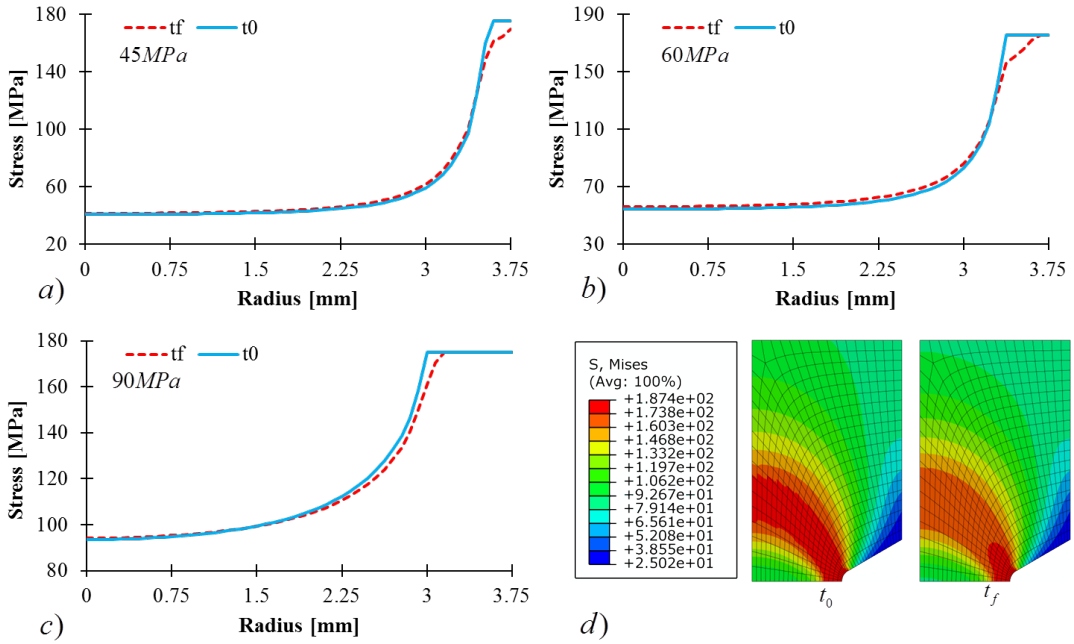

Figure 6.4: von Mises equivalent stress evolution along the notched bar throat for a) 45 MPa ,b) 60 MPa and c) 90 MPa, d) von Mises equivalent stress contours for the 90 MPa load case using the EPP model and a creep dwell of 1 hour.

In order to justify the increase of plastic strain, the only reasonable hypothesis is that a non-zero residual stress must be generated during the creep dwell. This condition, with the equivalent stress at the yield, can justify the increase of plastic strain. In Figure 6.5 the axial residual stress and the plastic strain increment are presented for two load case. For a load of 45 MPa, Figure 6.5a, the residual stress is non-zero. However, for this case, the equivalent stress is not at the yield, and no plastic strain accumulates during the dwell. Conversely for the second case, depicted in Figure 6.5b, both the condition are satisfied and an increase of the plastic strain is observed. In all the numerical cases presented since now the dwell time is equal to one hour. When a longer dwell is considered, the plastic strain accumulation becomes more severe.

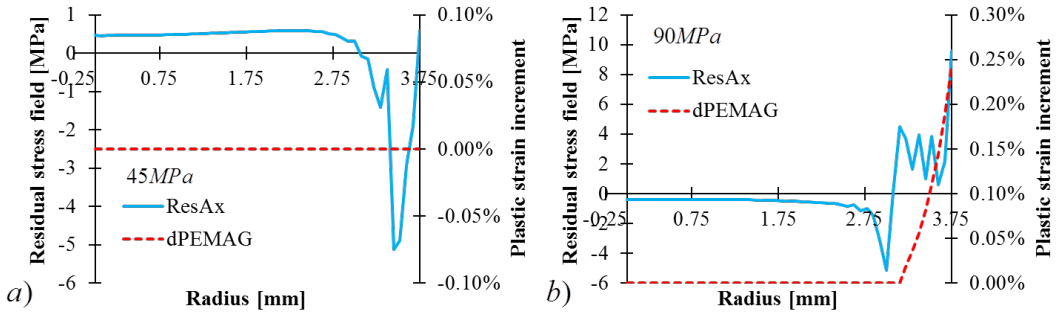

Figure 6.5: Axial residual stress (continuous line) and plastic strain increment (dashed line) for an applied load of a) 45 MPa and b) 90 MPa, using the EPP model and a creep dwell of 1 hour.

A dwell time up to 300 hours and a load of 100 MPa are considered. For this numerical test the maximum plastic strain accumulated increase significantly. In Figure 6.6 the stress along the notch throat, the plastic strain magnitude and creep strain magnitude are shown. When the creep dwell starts, the initial plastic strain accumulated in the most critical location is around the 2% and in less than 100 hours it is doubled. After 100 hours the increase of plastic strain is linear and reach the 6% at 300 hours. The von Mises stress tends to relax progressively and to redistribute. However, at the most critical location it still at the yield. It worth mentioning that the creep strain accumulated over the 300 hours is significantly smaller than the plastic strain as shown in Figure 6.6b. This highlight how this mechanism is significant for the failure analysis of a component operating under such load conditions.

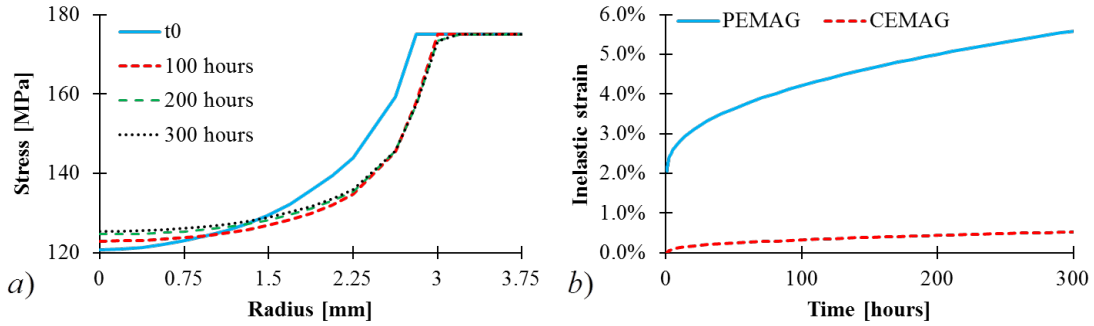

Figure 6.6: a) von Mises stress history with increasing dwell time using the EPP model, b) plastic and creep strain accumulation against dwell time at the notch throat.

Similar results are obtained when considering the circular notched bar. However, the magnitude of the mechanism is largely reduced. Also for this case study the applied load is found to be crucial. When an axial load of 130 MPa is applied the stress relax in the most critical location and increases within the bar, as it is shown in Figure 6.7a. This behaviour is expected and already reported in many research papers dealing with creep in notched specimens. The plastic strain does not change during the dwell time as depicted in Figure 6.7b, and it is always lower than the creep strain magnitude. This further confirms the importance of the stress level for this mechanism. The equivalent stress evolution is presented in Figure 6.7c. Due to the fast and significant stress relaxation, that occurs in the first 2 hours, the response is creep dominated for most of the time.

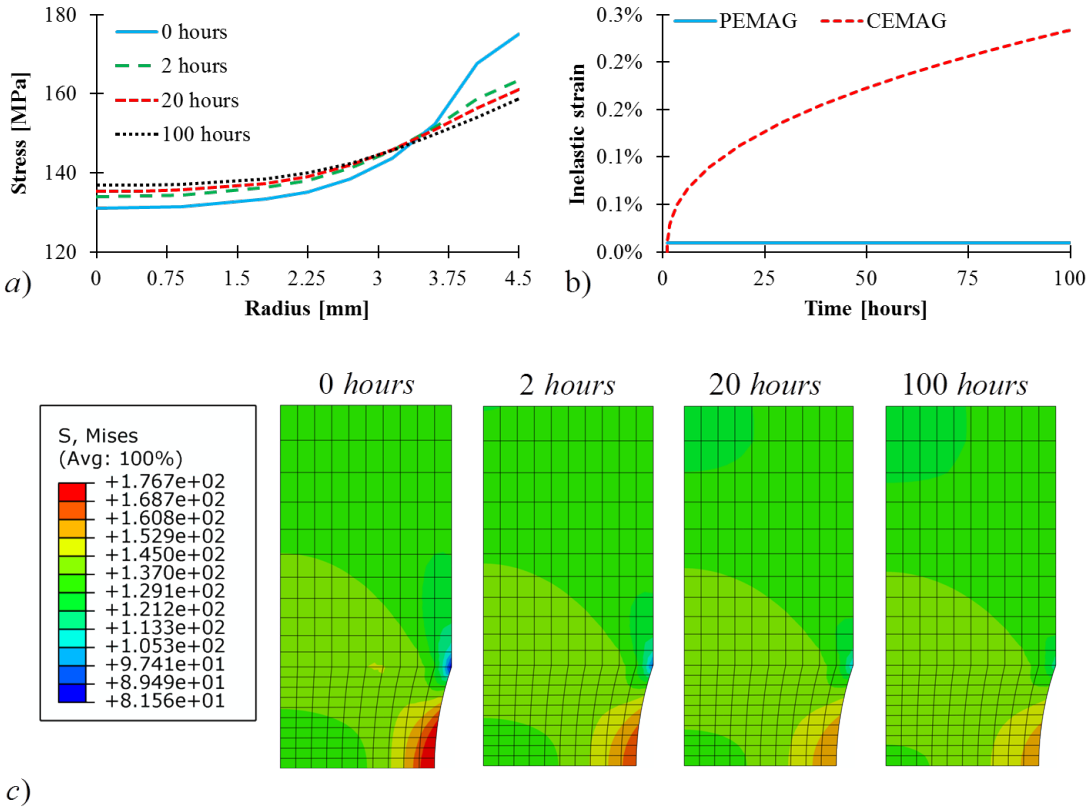

Figure 6.7: a) von Mises stress history along the notch throat, b) comparison between plastic strain and creep strain magnitude, c) plastic strain increment at the most critical location for an applied load of 130 MPa using the isotropic hardening model for a dwell time of 100 hours.

The results change for an applied load of 150 MPa, and are summarized in Figure 6.8. Also in this case the stress tends to redistribute. However, as it is depicted in Figure 6.8a, where the von Mises history is reported for different time steps, the stress does not fully relax. Even after 100 hours a very small location still at the yield, and in this area the increment of plastic strain is observed. Despite this, the plastic strain magnitude is not larger than the creep strain magnitude (Figure 6.8b). In Figure 6.8c the equivalent stress is presented in the form of contours from 0 to 100 hours. The largest stress relaxation and redistribution is observed in the first 20 hours, after which only small changes are observed. The area where the stress is at the yield becomes very localized.

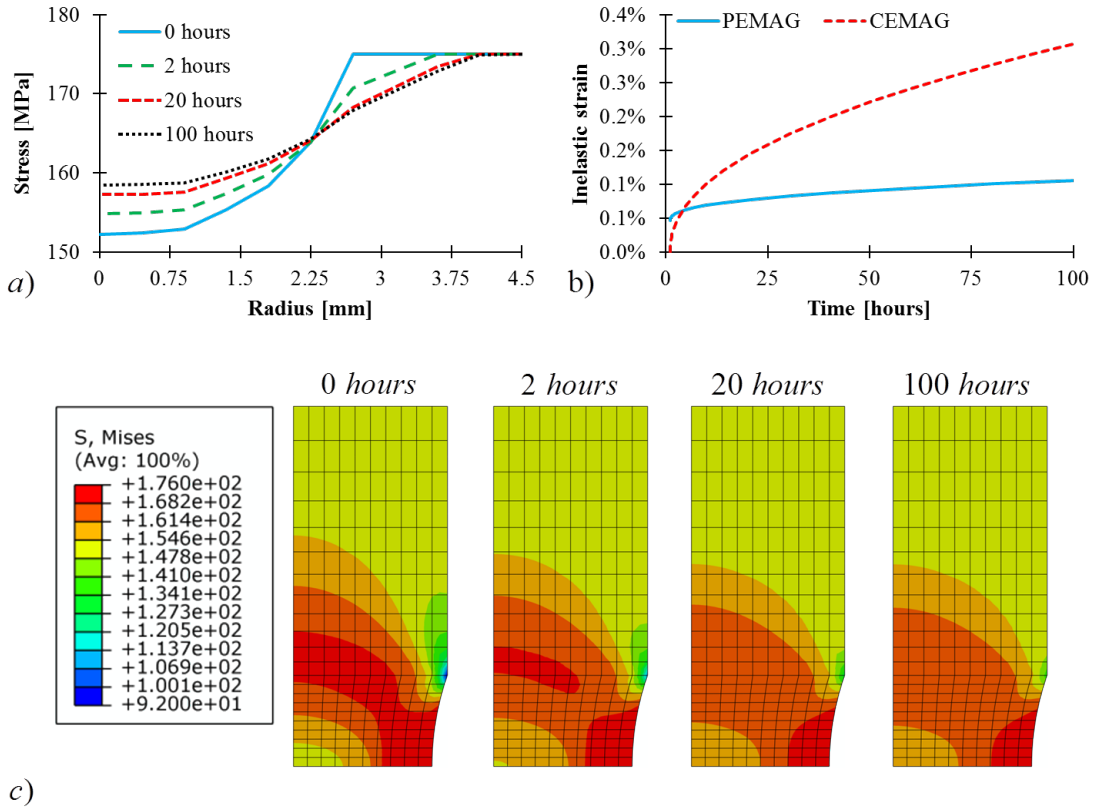

Figure 6.8: a) von Mises stress history along the notch throat, b) comparison between plastic strain and creep strain magnitude, c) plastic strain increment at the most critical location for an applied load of 150 MPa using the EPP model for a dwell time of 100 hours.

The residual stress and the associated plastic strain increment are monitored and reported in Figure 6.9 for both load conditions. For the first case the axial residual stress is non zero, Figure 6.9a. However, as shown before the equivalent stress in the most critical location is not at the yield during the creep dwell. For this reason no plastic strain increment is observed. Conversely, for the second load case both the condition are satisfied simultaneously and plastic strain increment is observed. It worth mentioning that the increase of plastic strain for the circumferential notched bar is smaller than the v-notched bar. From this point all the results presented will consider only the v-notched bar.

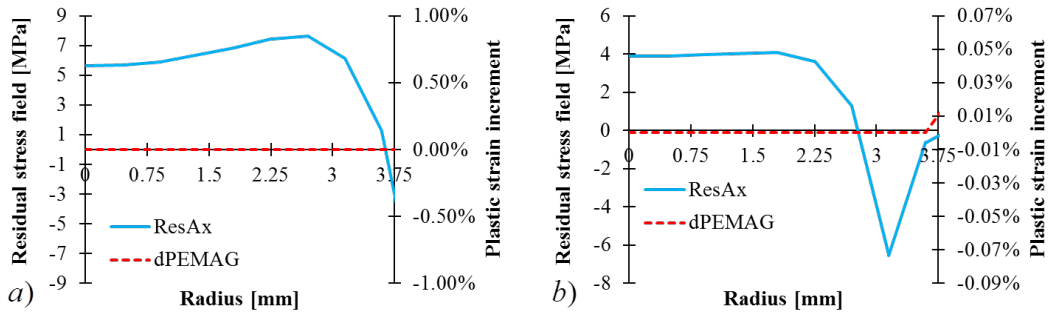

Figure 6.9: Axial residual stress (continuous line) and plastic strain increment (dashed line) for an applied load of a)130 and b) 150 MPa using the EPP model for a dwell time of 100 hours.

In order to further verify the significance of this mechanism, a more refined plastic model have been used. The isotropic hardening model is used to model the hardening during the hot tensile testing. This is done by providing the post yield stress strain response. At 90 MPa no increase of plasticity during the dwell is observed. However, for a higher mechanical load, 100 MPa, the mechanism is present. In Figure 6.10a the evolution of the stress is presented for the most significant time points. The largest stress redistribution occurs in the first 20 hours, affecting mostly the area between the centre of the bar up to 2.5 mm. After 20 hours only slight increase is observed. Conversely, at the notch surface the stress does not change significantly. The history of the axial residual stress is depicted in Figure 6.10b. The residual stress tends to increase in absolute value with the dwell time, leading to a progressive increase in the accumulated plastic strain (Figure 6.10c). By analysing the plastic strain increment shown in Figure 6.10c a reduction of the accumulated plastic strain is observed. This is reasonable due to the use of the isotropic tensile hardening, which allows less conservative estimate of the plastic strain. Furthermore, for lower mechanical load the plastic strain accumulation occurs only during the first few hours due to the progressive stress relaxation. A significant results is shown in Figure 6.10d, where the comparison between plastic strain magnitude and creep strain magnitude is reported. For this case study the plastic strain accumulated over the dwell is higher up to 75 hours. After this threshold the creep strain magnitude becomes more significant than plastic magnitude. This can be explained by the contribution of two factors, the high stress at the most critical location, and the more accurate plastic strain calculated by the isotropic hardening model.

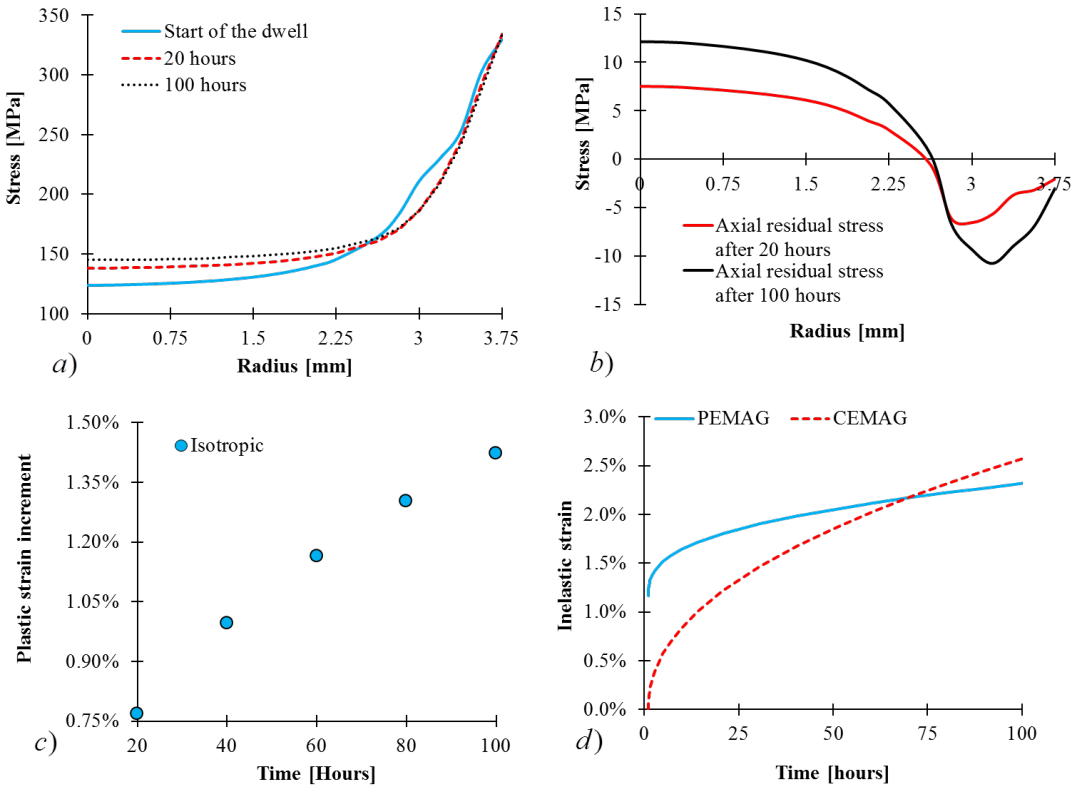

Figure 6.10: a) von Mises stress history along the notch throat, b) axial residual stress history, c) plastic strain increment, and d) plastic strain and creep strain magnitude at the most critical location for an applied load of 100 MPa

By exterminating all the results obtained the concept can be well represented by the schematic shown in Figure 6.11. This graphical representation depicts both the scenario described previously. For clarity in this case, the material model used to describe the mechanism is the EPP. In Figure 6.11a the classical behaviour is represented. In this case the stress during creep dwell relaxes and there is no possibility, even if a residual stress is generated, to have additional plastic strain. This can be summarized by the following mathematical statement:

$$\bar{\sigma}(\sigma(t_1)) = \sigma_y \rightarrow \bar{\sigma}(\sigma(t_2)) \leq \sigma_y \Rightarrow \Delta\varepsilon^p = 0 \tag{6.5}$$

where $\bar{\sigma}$ is the equivalent stress, σ_y is the yield stress, t_1 and t_2 are the time instances before and after creep dwell respectively and $\Delta\varepsilon^p$ is the plastic strain increment. When no stress relaxation occurs, as shown in Figure 6.11b, it is possible that a plastic strain increment is generated for an associated residual stress $\bar{\rho}$. It worth nothing that the residual stress in this case is generated by the creep dwell rather than an unloading phase. It is important to underline that the equivalent stress will not relaxes, but the stress components will be affected generating a residual stress. This can be summarized by the following mathematical statement:

$$\left.\begin{array}{c} \bar{\sigma}(\sigma(t_1)) = \sigma_y \rightarrow \bar{\sigma}(\sigma(t_2)) = \sigma_y \\ \Delta\rho_{ij} = \sigma_{ij}\,(t_2) - \sigma_{ij}\,(t_1) \rightarrow \bar{\sigma}\,(\Delta\rho_{ij}) \neq 0 \end{array}\right\} \Rightarrow \Delta\varepsilon^p \neq 0 \tag{6.6}$$

where σ_{ij} is the stress tensor and $\bar{\sigma}(\Delta\rho_{ij})$ is the equivalent stress associated to the residual stress tensor. This further highlight the importance of the multiaxial stress state for such a mechanism. Indeed, for a pure uniaxial stress, there is no possibility to have at the same time a residual stress, and the equivalent stress at the yield.

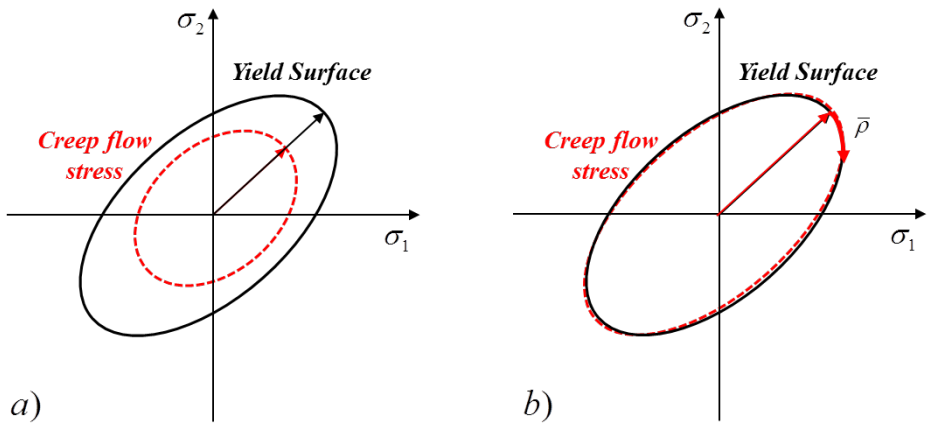

Figure 6.11: a) Stress history with the stress relaxation occurs during the creep dwell, and b) when no significant relaxation takes place allowing the possibility to generate a plastic strain increment associate to a residual stress.

These numerical tests further confirm that this mechanism can exist, if the equivalent stress is at the yield and a non-zero residual stress is present. Due to its significance, in the next subsection a more detailed study is done for the cyclic load case.

6.3.2 v-notched bar: cyclic load

In this subsection, the v-notched bar is subjected to a cyclic load condition, and both the combined hardening and elastic-perfect plastic material model are used. The aim of this study is to understand the possible impact of additional unexpected plasticity on the component's integrity. The main hypothesis is that a ratcheting mechanism can be enhanced by the additional plastic strain accumulated during the creep dwell. For both the material model considered the same loading condition is applied, an axial load of 90 MPa with R=0. The creep dwell considered is up to 20 hours for a total of 5 full cycles for a total 100 hours. The results obtained from the EPP model are significant and are resumed in Figure 6.12a. A progressive accumulation of the plastic strain occurs during each dwell period within each cycle. The final total plastic strain in very large, around the 3.5%. However, if the more refined combined hardening model is adopted the strain accumulation is very small. This is reasonable due to the capability of the material to enlarge and move the yield surface leading to a progressive material hardening. For this reason, a higher loading case is studied up to 110 MPa. The results are depicted in Figure 6.12b, where the plastic strain history from the combined model at 110 MPa is compared to the one from the EPP at 90 MPa. At higher loading level, even using the more refined material model, the plastic strain continues to increase during the creep dwell.

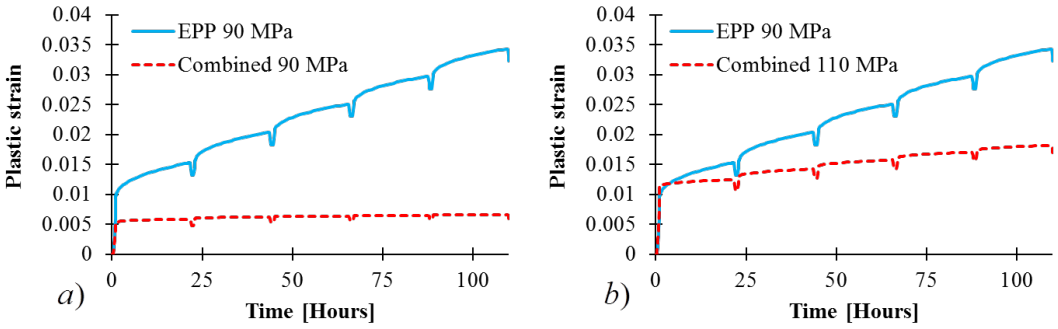

Figure 6.12: a) Plastic strain history for the EPP and combined hardening model at 90MPa and b) comparison between the results of EPP at 90MPa and the combined at 110 MPa.

Furthermore, for longer numerical tests that involve more than 50 full cycles the plastic strain accumulation does not stop as shown in Figure 6.13a. For this load case, the cyclic response is ratcheting. However, for this test the plastic strain continues to accumulate during the creep dwell, and no sign of reduction is present. This is shown in Figure 6.13b, where the plastic strain history is presented for a particular load cycle during the 20 hours creep dwell.

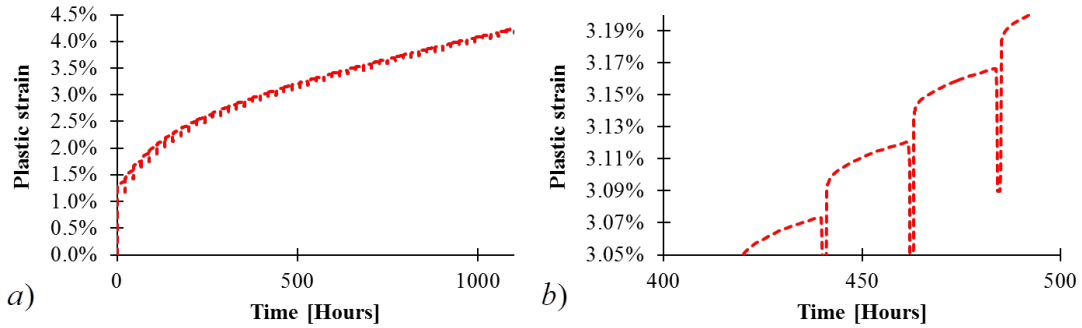

Figure 6.13: a) Plastic strain history for combined hardening model at 110 MPa and b) detail plot showing the plastic strain accumulation during each creep dwell.

To have a clear picture of the cyclic response of the component the hysteresis loop is presented in Figure 6.14.

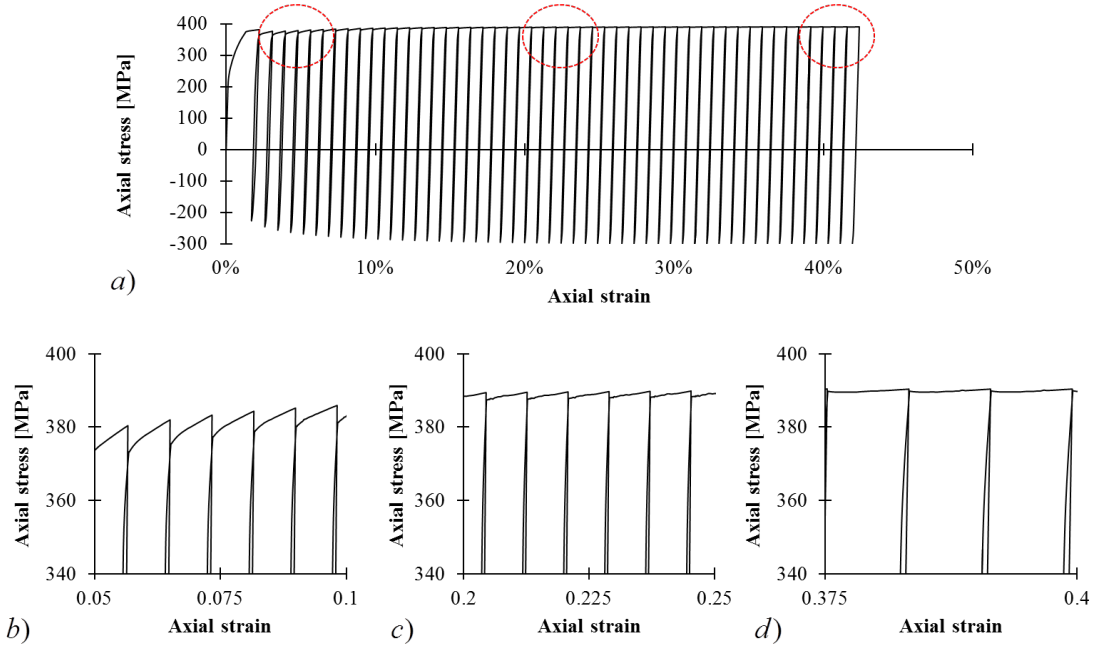

Figure 6.14: a) Plastic strain history for combined hardening model at 110 MPa and detail plot showing the plastic strain accumulation during each creep dwell b) $\varepsilon < 10\%$, c) $20\% < \varepsilon < 30\%$ and d) $\varepsilon > 40\%$ axial strain.

The entire stress-strain history is showed in Figure 6.14a, for the axial direction. The cyclic behaviour is ratchetting, and a strain accumulation up to 40% is observed after 50 cycles. The cyclic response has reached the steady state when the total axial strain is at the 15%. The cyclic behaviour is shown in detail in Figure 6.14b,c and d. A progressive stress stabilization occurs during the creep dwells. At the beginning stress increases non-linearly with the strain. However, a progressive saturation of the stress is observed (Figure 6.14c), and the associated plastic strain increases enhancing the incremental mechanism. When half of the total number of cycles have been passed, the stress tends to exhibit a small relaxation as shown in Figure 6.14d. The contribution of this plastic

strain accumulation is about the 5% of the overall inelastic strain accumulated. For this load case, creep produces the largest amount of inelastic strain, causing the component to exhibit creep-ratcheting. It worth mentioning that the plastic strain accumulated is larger than the creep strain magnitude for shorter dwell times or when only small number of load cycles are considered. However, this is strongly related to the material's creep properties. For some particular structural steels, the creep properties can make the plastic accumulation process dominant even for long dwells or number of cycles. This last finding further proves the importance of this mechanism, which enhances the creep-ratcheting mechanism by introducing an extra plastic strain at each load cycle. Furthermore, more extensive numerical test should be performed investigating the impact of the creep properties.

6.3.3 Mesh study

The potential contribution of the mesh element type and size on this unexpected mechanism have been investigated by undertaking two specific studies. There are many sources of numerical error in a finite element model, one of these is the element type chosen. The linear and quadratic elements have been tested. In Figure 6.15 the comparison between linear and quadratic axisymmetric elements is presented. The mechanism is present for both the type of element. For the V-notched bar (Figure 6.15a), the difference is more evident, and the quadratic element predicts a higher accumulated plastic strain during the creep dwell. Conversely, for the C-notched bar (Figure 6.15b), very close results are obtained with the EPP model. Also in this last case, the quadratic element predicts a higher plastic strain. This investigation excludes the mesh type effect on the mechanism, which is always present when both conditions, previously discussed, are satisfied. The different stiffness of the element will affect only the magnitude of the phenomenon, but not its order which is always comparable.

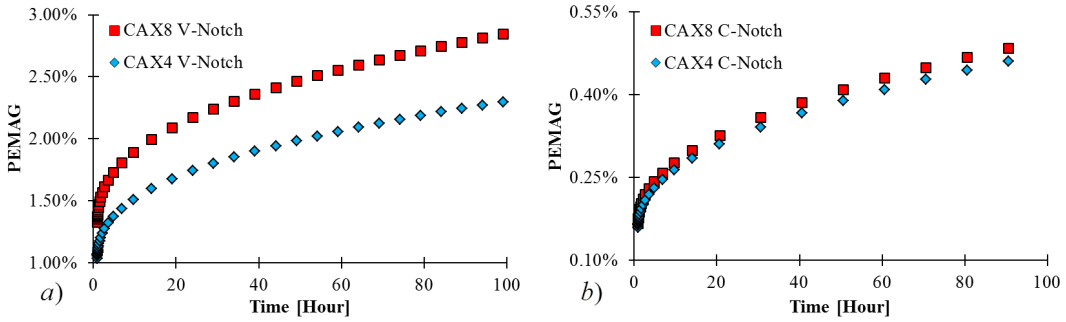

Figure 6.15: Effect of mesh element type on the failure mechanism for the a) v-Notched bar and b) c-Notched bar.

The second aspect investigated is the effect of the element size on the mechanism, and for this study, three meshes with an increasing number of elements have been used. The study focused on the v-notched bar using the EPP model. The element type adopted is a quadratic axisymmetric element with reduced integration scheme (CAX8). In Figure 6.16 the results obtained for the most critical location are reported. The mechanism is always present and affects the component despite the mesh refinement considered. The coarser mesh gives always the smallest amount of plastic strain

accumulation. The results tend to converge due to the mesh refinement and a more stable value is obtained for the finer mesh. The mesh with 3660 elements predicts the same mechanism of the coarser one with 1394. However, a strong increase is observed from the coarsest mesh of 670. It worth mentioning that any subsequent increase in the mesh density at the most critical location, does not improve the magnitude of the mechanism. It is possible to conclude that the mesh size is not the cause of the mechanism, and it only affects its magnitude.

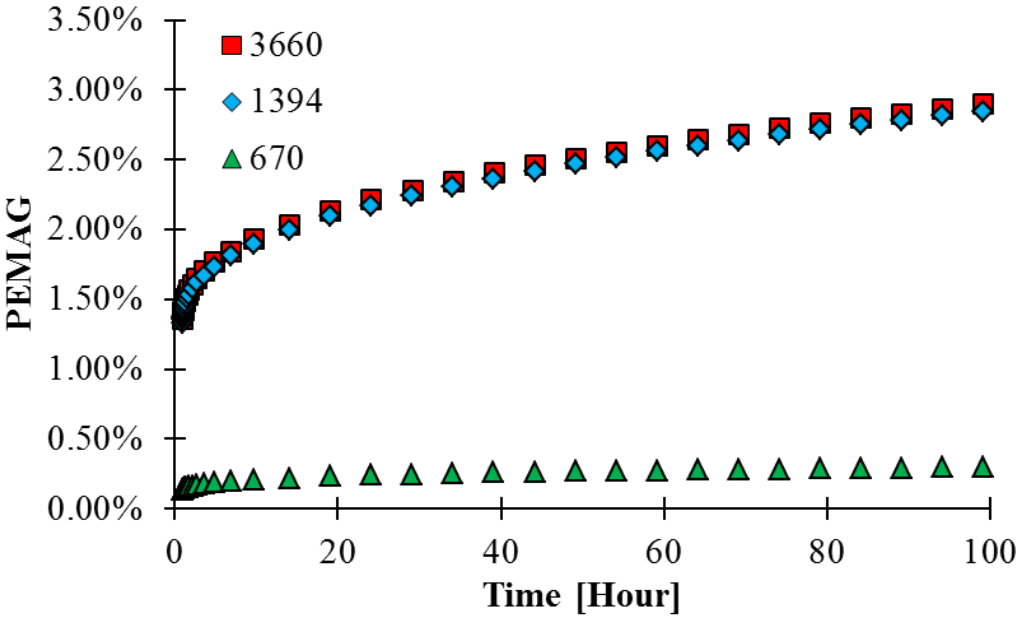

Figure 6.16: Effect of the mesh element size on the failure mechanism for the v-Notched bar.

6.4 Discussion and conclusions

In this chapter, a new failure mechanism has been investigated and identified by an extensive use of numerical analyses. Two notched bars have been considered, a v-notched and a c-notched bar. The mechanism occurs during the high-temperature dwell when two conditions are both satisfied at the same time. In all the cases observed the plastic strain starts to accumulate only when the following conditions are both satisfied for the same integration point:

1. The stress is at the yield or the yield condition is verified during the dwell.
2. A non-zero residual stress must exist where condition 1 is satisfied.
3. In order to allow the existence of a non-zero residual stress a creep dwell must exist.

When this mechanism occurs, no stress relaxation has been observed in a small area of the notched bar. Four major considerations can be made: (i) the geometry of the notch plays a crucial role by introducing a multi-axial stress field. The v-notched bar has the highest plastic strain accumulation, meaning that this mechanism will be more severe

for sharp notches. (ii) The applied load level must be high enough, or close to the limit load of the structure based on the EPP model. This condition has been found to be directly related to the geometry. (iii) The accuracy of the plastic model does not affect the existence of the mechanism. However, more refined plastic models can produce less conservative predictions. When a cyclic load is considered, the mechanism produces a significant plastic strain during the dwell. This makes the mechanisms even more dangerous especially during off design cyclic loading. iv) The creep dwell is relevant for the development of the residual stress, but also for the stress relaxation process which is influenced by the creep properties. In order to clarify if this mechanism is an artefact or not, the mesh effect has been studied as well. Both the element type and size do not affect the existence of the mechanism when condition 1 and 2 are satisfied. The effect of the mesh is minimal, and only slightly affects the magnitude of the unexpected plastic strain during the dwell. In conclusion with a coarse mesh and a very simple material model the mechanism can be observed, even using the built-in ABAQUS material models for plasticity and creep.

For all the previous discussions, this mechanism is considered not an artefact, and should be investigated more due to its impact on the safety of components subjected to extreme load conditions at high temperature.

Chapter 7

Conclusions, Discussion and Future work

7.1 Summary of the Thesis

The work presented in this dissertation is focused on testing and further developing the capabilities of the Linear Matching Method Framework on high-temperature failure assessment including creep-fatigue interaction. Furthermore, new insights on high temperature structural integrity have been delivered. This has been achieved by delivering the following results:

1. A comprehensive review of the current state of art on creep-fatigue damage assessment by detailed non-linear finite element analyses or design codes.
2. The previous creep rupture assessment procedure has been improved by considering a robust and accurate creep rupture stress interpolation method.
3. Studies on creep-fatigue interaction and crack initiation on practical problems using the eDSCA have been performed.
4. A more accurate creep damage model, using the stress modified ductility exhaustion method has been successfully implemented within the LMM.
5. Extending the knowledge on high-temperature behaviour, investigating a new failure mechanism.

Currently, the common practice is to use design codes and finite element elastic analyses to calculate all the design limits of high-temperature structures. In literature, there are many works on modelling creep damage by using detailed damage models. However, this approach is very sensitive to the material parameters, and it has been demonstrated to be also inefficient in terms of computational cost. The LMM represents a valid tool to help engineers in performing better design and assessment of components, especially for creep rupture and creep-fatigue crack initiation. The creep rupture limit calculation has been discussed in chapter 3, where a more accurate algorithm has been developed to interpolate and extrapolate creep rupture stresses. The solutions provided by the LMM for creep rupture are always more accurate than the solutions obtained

by R5 [4] or ASME NH [3]. The R5 approach of using a reference stress leads always to unnecessary overly conservative results, limiting the designed life.

For creep-fatigue interaction, a lot must be done to further understand the combined effect of creep and fatigue on the cyclic response, and the dangerous phenomenon of creep-ratcheting. Within this work, efforts have been done in using the eDSCA to solve practical problems. The effect of different load conditions on the creep-fatigue life has been investigated, and several results are discussed in chapter 4. It has been observed how reversed plasticity can be significantly enhanced by the abrupt stress relaxation, caused by a creep dwell. This increase of reversed plasticity has been found to increase the fatigue damage, causing fatigue dominated failure, especially for very short dwell. In other cases, the reversed plasticity has the beneficial effect on limiting the start of the creep-ratcheting mechanism. Assuming that the stress during the loading and creeping phase has the same direction, the only possibility to recover the creep strain accumulated is to experience more plastic strain during the unloading. This has been found to be possible in most of the cases for short dwell time or when the primary load is not too high. When this does not occur creep ratcheting can initiate, becoming a potential threat to the component integrity. Since now there is no proof of direct interaction between creep-ratcheting and creep-fatigue damage. For this reason, in this work, these mechanisms have been assessed separately. However, this should be investigated more, performing also specific experimental studies.

The creep damage model available within the eDSCA has been enhanced including both the stress and strain based method. This has been discussed in depth in chapter 5. The user now has a much more wide choice depending on the assessment code used or material data available. However, the use of strain based method should be preferred due to the higher level of accuracy and less dependency on the model parameters. Furthermore, stress-based methods like the time fraction rule, are in some cases too conservative producing very short and impractical lifetimes. The major drawback of strain based methods is the necessity of detailed creep tensile tests. Particular attention needs to be given on the effect of stress multiaxiality, which has been demonstrated to be crucial for accurate assessment. It is worth mentioning that the accuracy of stress-based methods is strongly related to the stress ranges adopted during the experiments. For most of the experimental data results are available at stress levels higher than those present at plant-like load condition. This is crucial especially for GEN IV nuclear reactors, where low stress and long-term tests need to be performed to achieve a high level of confidence.

The overall development of numerical procedure such as the Linear Matching Method has been accompanied by the deep investigation of the high-temperature response of structures. This has been culminated in the analyses of a new behaviour never reported before in literature. In chapter 6 the increase of plastic strain during high temperature creep dwell has been discussed. Within this chapter, a comprehensive study has been done to understand if the observed phenomenon is real or a numerical artefact. The numerical tests involved the study of the mesh, effect of the geometry, the impact of the creep dwell and load level effect. All the results confirm that this mechanism can exist, and the conditions required have been identified and verified.

7.2 Future work

The research work included in this thesis forms the basis for a further extension of the LMM in assessing high-temperature components. The actual assessment practice has been demonstrated to be overly conservative. The LMM has the capabilities of delivering a more accurate assessment against creep-fatigue crack initiation and creep-ratcheting. Furthermore, the several case studies have demonstrated the capability of being efficient and versatile. However, some areas should be investigated in the future:

1. The possibility to consider more complicated creep models is very important. This is currently, one of the most crucial aspects and it will be investigated by the author during a three months project sponsored by the EPSRC Impact Acceleration Account. This will improve significantly the applicability of the eDSCA analysis to a more wide range of materials, increasing the impact over the industrial and academic community.

2. By adopting the eDSCA analyses more comprehensive analyses should be done on the effect of complex loading cycle on the creep-fatigue life of components. In this research work the load cycle considered up to 4 loading instances, with a creep dwell always at the tensile and/or compressive peak. In the future, the effect of intermediate creep dwell on the creep-fatigue interaction is recommended to be done. Furthermore, the effect of multiple creep dwells on the residual stress should provide new insight on the structural integrity point of view.

3. Up to now the LMMF does not contain an user plug-in for the post-processing of the results. This represents a significant bottleneck for the dissemination of the method through the industrial partners. For creep-fatigue interaction, it is advisable to provide a software tool capable of post-process the result files from ABAQUS CAE. The plug-in will allow the user selecting the design code to be adopted, and based on material data provide automatically the component life.

4. The last and most important aspect that must be done in the future is the use of LMM for creep-fatigue crack growth assessment. The use of a direct method for such a task is totally new. This represents the biggest challenge for the next future. The crack growth assessment is an important aspect of the structural integrity assessment. This research work can be delivered within a more articulated research project, and currently it is author interest to apply for funding in order to start the research activity on this topic.

References

[1] J. MacCarthy, T. Murrells, Y. Pang, N. Passant, J. Ramirez Garcia, G. Thistlethwaite, N. Webb, S. Choudrie, S. Forden, S. Gilhespy *et al.* Uk greenhouse gas inventory, 1990 to 2014. 2016.

[2] M. ODonnell, R. Bradford, D. Dean, C. Hamm and M. Chevalier. High temperature issues in advanced gas cooled reactors (agr). 2011.

[3] T. A. S. of Mechanical Engineers. *ASME boiler & pressure vessel code : an international code*, volume Division 1 - Subsection NH. 2013.

[4] E. Energy. *Assessment procedure for the high temperature response of structures, R5 Issue 3.* 2014.

[5] M. Lytwyn, H. Chen and M. Martin. Comparison of the linear matching method to rolls royce's hierarchical finite element framework for ratchet limit analysis. *International Journal of Pressure Vessels and Piping*, 125: 13–22, 2015. 10.1016/j.ijpvp.2014.11.001.

[6] H. Chen. Lower and upper bound shakedown analysis of structures with temperature-dependent yield stress. *Journal of Pressure Vessel Technology*, 132(1): 011202, 2010.

[7] H. Chen and A. R. S. Ponter. Structural integrity assessment of superheater outlet penetration tubeplate. *International Journal of Pressure Vessels and Piping*, 86(7): 412–419, 2009.

[8] H. Chen and A. R. S. Ponter. On the behaviour of a particulate metal matrix composite subjected to cyclic temperature and constant stress. *Computational Materials Science*, 34(4): 425–441, 2005.

[9] A. R. S. Ponter and M. Engelhardt. Shakedown limits for a general yield condition: implementation and application for a von mises yield condition. *European Journal of Mechanics - A/Solids*, 19(3): 423–445, 2000.

[10] R. Priest, P. Cairns, D. Gladwin and D. Miller. Creep-fatigue assessment of a welded steel component. *Creep: Characterization, Damage and Life Assessments, Lake Buena Vista*, pages 423–429, 1992.

[11] M. Spindler. The multiaxial creep ductility of austenitic stainless steels. *Fatigue & Fracture of Engineering Materials & Structures*, 27(4): 273–281, 2004.

[12] T. Hyde, C. Hyde and W. Sun. *Applied creep mechanics.* McGraw-Hill Professional, 2013.

[13] K. Naumenko, A. Kutschke, Y. Kostenko and T. Rudolf. Multi-axial thermo-mechanical analysis of power plant components from 912 *Engineering Fracture Mechanics*, 78(8): 1657–1668, 2011.

[14] K. Naumenko and Y. Kostenko. Structural analysis of a power plant component using a stress-range-dependent creep-damage constitutive model. *Materials Science and Engineering: A*, 510: 169–174, 2009.

[15] B. Dyson. Use of cdm in materials modeling and component creep life prediction. *Journal of pressure vessel technology*, 122(3): 281–296, 2000.

[16] D. Hibbitt, B. Karlsson and P. Sorensen. Abaqus 6.12. 3 manual. 2012.

[17] M. Lytwyn, H. Chen and A. R. S. Ponter. A generalised method for ratchet analysis of structures undergoing arbitrary thermo-mechanical load histories. *International Journal for Numerical Methods in Engineering*, 104(2): 104–124, 2015.

[18] J. Ure, H. Chen and D. Tipping. Calculation of a lower bound ratchet limit part 2 application to a pipe intersection with dissimilar material join. *European Journal of Mechanics - A/Solids*, 37: 369–378, 2013.

[19] H. Chen, A. R. S. Ponter and R. A. Ainsworth. The linear matching method applied to the high temperature life integrity of structures. part 1. assessments involving constant residual stress fields. *International Journal of Pressure Vessels and Piping*, 83(2): 123–135, 2006.

[20] H. Chen, A. R. S. Ponter and R. A. Ainsworth. The linear matching method applied to the high temperature life integrity of structures. part 2. assessments beyond shakedown involving changing residual stress fields. *International Journal of Pressure Vessels and Piping*, 83(2): 136–147, 2006.

[21] R. P. Ginsztler, J.and Skelton. *Component reliability under creep-fatigue conditions*. Springer, 1998.

[22] R. Skelton. *High temperature fatigue: properties and prediction*. Springer Science et Business Media, 2012.

[23] J. T. Boyle. The creep behavior of simple structures with a stress range-dependent constitutive model. *Archive of Applied Mechanics*, 82(4): 495–514, 2012.

[24] K. Naumenko, H. Altenbach and Y. Gorash. Creep analysis with a stress range dependent constitutive model. *Archive of Applied Mechanics*, 79(6-7): 619–630, 2009.

[25] J. Bolton. Analysis of structures based on a characteristic-strain model of creep. *International Journal of Pressure Vessels and Piping*, 85(1-2): 108–116, 2008.

[26] F. R. Larson and J. Miller. A time-temperature relationship for rupture and creep stresses. *Trans. ASME*, July(74): 765–775, 1952.

[27] S. Manson and A. Haferd. A linear time-temperature relation for extrapolation of creep and stress rupture data. Report NACA-TN-2890, Lewis Flight Propulsion Laboratory, 1953.

[28] R. L. Orr, O. D. Sherby and J. E. Dorn. Correlations of rupture data for metals at elevated temperatures. Report, DTIC Document, 1953.

[29] E. Pink. Physical significance and reliability of larson miller and manson haferd parameters. *Materials science and technology*, 10(4): 340–346, 1994.

[30] L. M. Kachanov. Rupture time under creep conditions. *International journal of fracture*, 97(1-4): 11–18, 1999.

[31] I. N. Rabotnov. *Creep problems in structural members*. North-Holland series in applied mathematics and mechanics, v. 7. North-Holland Pub. Co, Amsterdam, London, 1969.

[32] Y. Liu and S. Murakami. Damage localization of conventional creep damage models and proposition of a new model for creep damage analysis. *JSME international journal. Series A, Solid mechanics and material engineering*, 41(1): 57–65, 1998.

[33] T. Hyde, M. Saber and W. Sun. Creep crack growth data and prediction for a P91 weld at 650 °C. *International Journal of Pressure Vessels and Piping*, 87(12): 721–729, 2010.

[34] C. J. Hyde, W. Sun, T. H. Hyde, M. Saber and A. A. Becker. Application of the liu and murakami damage model for creep crack growth predictions in power plant steels. 2014.

[35] M. S. Haque and C. M. Stewart. A novel sin-hyperbolic creep damage model to overcome the mesh dependency of classic local approach kachanov-rabotnov model. *ASME 2015 International Mechanical Engineering Congress and Exposition*. 2015.

[36] J. Bree. Elastic-plastic behaviour of thin tubes subjected to internal pressure and intermittent high-heat fluxes with application to fast-nuclear-reactor fuel elements. *The Journal of Strain Analysis for Engineering Design*, 2(3): 226–238, 1967.

[37] L. Coffin Jr. A study on the effects of cyclic thermal stress on a ductile metal. *Trans. ASME*, 76, 1954.

[38] S. S. Manson. *Behavior of materials under conditions of thermal stress*, volume TN 2933. NACA, 1954.

[39] S. S. Manson. A simple procedure for estimating high-temperature low-cycle fatigue. *Experimental Mechanics*, 8(8): 349–355, 1968.

[40] U. Muralidharan and S. Manson. A modified universal slopes equation for estimation of fatigue characteristics of metals. *Journal of Engineering Materials and Technology*, 110(1): 55–58, 1988.

[41] J.-H. Park and J.-H. Song. Detailed evaluation of methods for estimation of fatigue properties. *International Journal of Fatigue*, 17(5): 365–373, 1995.

[42] M. Meggiolaro and J. Castro. Statistical evaluation of strain-life fatigue crack initiation predictions. *International Journal of Fatigue*, 26(5): 463–476, 2004.

[43] S. Manson. Fatigue: a complex subjectsome simple approximations. *Experimental mechanics*, 5(7): 193–226, 1965.

[44] A. Karakas and J. Szusta. Monotonic and low cycle fatigue behaviour of 2024-T3 aluminium alloy between room temperature and 300 °C for designing vawt components. *Fatigue & Fracture of Engineering Materials & Structures*, 2015.

[45] A. Lipski and S. Mrozinski. Approximate determination of a strain-controlled fatigue life curve for aluminium alloy sheets. *Journal of Polish CIMAC*, 6: 107–118, 2011.

[46] R. Hales. A quantitative metallographic assessment of structural degradation of type 316 stainless steel during creep-fatigue. *Fatigue & Fracture of Engineering Materials & Structures*, 3(4): 339–356, 1980.

[47] X.-L. Yan, X.-C. Zhang, S.-T. Tu, S.-L. Mannan, F.-Z. Xuan and Y.-C. Lin. Review of creepfatigue endurance and life prediction of 316 stainless steels. *International Journal of Pressure Vessels and Piping*, 126127(0): 17–28, 2015.

[48] D. Miller, R. Priest and E. Ellison. A review of material response and life prediction techniques under fatigue-creep loading conditions. *High-temperature materials and processes*, 6(3-4): 155–194, 1984.

[49] W. Plumbridge. *Metallography of high temperature fatigue*, pages 177–228. Springer, 1987.

[50] M. Kobayashi, N. Ohno and T. Igari. Ratchetting characteristics of 316FR steel at high temperature, part ii: Analysis of thermal ratchetting induced by spatial variation of temperature. *International Journal of Plasticity*, 14(45): 373–390, 1998.

[51] N. Ohno, M. Abdel-Karim, M. Kobayashi and T. Igari. Ratchetting characteristics of 316FR steel at high temperature, Part I: Strain-controlled ratchetting experiments and simulations. *International Journal of Plasticity*, 14(45): 355–372, 1998.

[52] J. Bree. Incremental growth due to creep and plastic yielding of thin tubes subjected to internal pressure and cyclic thermal stresses. *The Journal of Strain Analysis for Engineering Design*, 3(2): 122–127, 1968.

[53] H. Chen, W. Chen and J. Ure. A direct method on the evaluation of cyclic steady state of structures with creep effect. *Journal of Pressure Vessel Technology*, 136(6): 061404–061404, 2014. 10.1115/1.4028164.

[54] A. Kapoor. A re-evaluation of the life to rupture of ductile metals by cyclic plastic strain. *Fatigue & Fracture of Engineering Materials & Structures*, 17(2): 201–219, 1994.

[55] E. Wei, B. Postberg, T. Nicak and J. Rudolph. Simulation of ratcheting and low cycle fatigue. *International Journal of Pressure Vessels and Piping*, 81(3): 235–242, 2004.

[56] R. I. Jetter. Subsection nh-class 1 components in elevated temperature service. *American Society of Mechanical Engineers, New York*, pages 369–404, 2002.

[57] R. Skelton and D. Gandy. Creep fatigue damage accumulation and interaction diagram based on metallographic interpretation of mechanisms. *Materials at High Temperatures*, 25(1): 27–54, 2008.

[58] M. Sheridan, D. Knowles and O. Montgomery. Comparison of R5 and ASME NH creep-fatigue damage assessment methodologies. *ASME 2013 Pressure Vessels and Piping Conference*. American Society of Mechanical Engineers.

[59] M. W. Spindler. An improved method for calculation of creep damage during creepfatigue cycling. *Materials Science and Technology*, 23(12): 1461–1470, 2007.

[60] M. Spindler. The prediction of creep damage in type 347 weld metal. part i: the determination of material properties from creep and tensile tests. *International journal of pressure vessels and piping*, 82(3): 175–184, 2005.

[61] M. W. Spindler. The prediction of creep damage in type 347 weld metal: part ii creep fatigue tests. *International Journal of Pressure Vessels and Piping*, 82(3): 185–194, 2005.

[62] R. Ainsworth. R5 procedures for assessing structural integrity of components under creep and creep–fatigue conditions. *International materials reviews*, 2013.

[63] J. Ure, H. Chen and D. Tipping. Integrated structural analysis tool using the linear matching method part 1 software development. *International Journal of Pressure Vessels and Piping*, 120121: 141–151, 2014.

[64] M. Sauzay, M. Mottot, L. Allais, M. Noblecourt, I. Monnet and J. Prinet. Creep-fatigue behaviour of an aisi stainless steel at 550 c. *Nuclear Engineering and Design*, 232(3): 219–236, 2004.

[65] D. Barbera, H. Chen and Y. Liu. On creep fatigue interaction of components at elevated temperature. *Journal of Pressure Vessel Technology*, 2015. 10.1115/1.4032278.

[66] J. Chaboche. Anisotropic creep damage in the framework of continuum damage mechanics. *Nuclear Engineering and Design*, 79(3): 309–319, 1984.

[67] T. Hyde, L. Xia and A. Becker. Prediction of creep failure in aeroengine materials under multi-axial stress states. *International Journal of Mechanical Sciences*, 38(4): 385–403, 1996.

[68] H. Chen and A. R. Ponter. Linear matching method on the evaluation of plastic and creep behaviours for bodies subjected to cyclic thermal and mechanical loading. *International Journal for Numerical Methods in Engineering*, 68(1): 13–32, 2006.

[69] H. Chen, M. J. Engelhardt and A. R. S. Ponter. Linear matching method for creep rupture assessment. *International Journal of Pressure Vessels and Piping*, 80(4): 213–220, 2003.

[70] A. R. Ponter, P. Fuschi and M. Engelhardt. Limit analysis for a general class of yield conditions. *European Journal of Mechanics-A/Solids*, 19(3): 401–421, 2000.

[71] W. Koiter. *General Theorems for Elastic-plastic Solids*. North-Holland Amsterdam, 1960.

[72] A. Mendelson, E. Roberts Jr and S. Manson. Optimization of time-temperature parameters for creep and stress rupture, with application to data from german cooperative long-time creep program. Report, DTIC Document, 1965.

[73] M. T. Whittaker, M. Evans and B. Wilshire. Long-term creep data prediction for type 316H stainless steel. *Materials Science and Engineering: A*, 552: 145–150, 2012.

[74] R. L. Burden. *Numerical analysis*. Pacific Grove, CA : Brooks/Cole, 2001. 7th ed.

[75] H. F. Abdalla, M. M. Megahed and M. Y. A. Younan. A simplified technique for shakedown limit load determination. *Nuclear Engineering and Design*, 237(12-13): 1231–1240, 2007.

[76] M. Martin and D. Rice. A hybrid procedure for ratchet boundary prediction. *ASME 2009 Pressure Vessels and Piping Conference*, pages 81–88. American Society of Mechanical Engineers.

[77] Y. Wada, K. Aoto and F. Ueno. Creep-fatigue evaluation method for type 304 and 316fr ss. Technical report, 1997.

[78] S. Manson and G. R. Halford. *Fatigue and durability of metals at high temperatures*. ASM International, 2009.

[79] H. Qing. 2d micromechanical analysis of sic/al metal matrix composites under tensile, shear and combined tensile/shear loads. *Materials & Design*, 51(0): 438–447, 2013.

[80] H. Qing. Automatic generation of 2d micromechanical finite element model of siliconcarbide/aluminum metal matrix composites: Effects of the boundary conditions. *Materials & Design*, 44(0): 446–453, 2013.

[81] M. N. Yuan, Y. Q. Yang, C. Li, P. Y. Heng and L. Z. Li. Numerical analysis of the stressstrain distributions in the particle reinforced metal matrix composite sic/6064al. *Materials & Design*, 38(0): 1–6, 2012.

[82] S. Guo, G. Kang and J. Zhang. Meso-mechanical constitutive model for ratchetting of particle-reinforced metal matrix composites. *International Journal of Plasticity*, 27(12): 1896–1915, 2011.

[83] Y. Schneider, E. Soppa, C. Kohler, R. Mokso and E. Roos. Numerical and experimental investigations of the global and local behaviour of an al(6061)/al2o3 metal matrix composite under low cycle fatigue. *Procedia Engineering*, 10: 1515–1520, 2011.

[84] T. Baxevanis and N. Charalambakis. A micromechanically based model for damage-enhanced creep-rupture in continuous fiber-reinforced ceramic matrix composites. *Mechanics of Materials*, 42(5): 570–580, 2010.

[85] W. J. Fleming and J. M. Temis. Numerical simulation of cyclic plasticity and damage of an aluminium metal matrix composite with particulate sic inclusions. *International Journal of Fatigue*, 24(10): 1079–1088, 2002.

[86] R. Echle and G. Z. Voyiadjis. Simulation of damage evolution in a uni-directional titanium matrix composite subjected to high cycle fatigue. *International Journal of Fatigue*, 21(9): 909–923, 1999.

[87] R. Pandorf and C. Broeckmann. Numerical simulation of matrix damage in aluminium based metal matrix composites. *Computational Materials Science*, 13(13): 103–107, 1998.

[88] H. Chen and D. Giugliano. On the behaviour of fibre reinforce metal matrix composites under loading and thermal cycling conditions, 2015.

[89] Y. Gorash and H. Chen. Creep-fatigue life assessment of cruciform weldments using the linear matching method. *International Journal of Pressure Vessels and Piping*, 104(0): 1–13, 2013.

[90] Y. Gorash and H. Chen. On creep-fatigue endurance of tig-dressed weldments using the linear matching method. *Engineering Failure Analysis*, 34(0): 308–323, 2013.

[91] J. T. Maximov, G. V. Duncheva, A. P. Anchev and M. D. Ichkova. Modeling of strain hardening and creep behaviour of 2024t3 aluminium alloy at room and high temperatures. *Computational Materials Science*, 83(0): 381–393, 2014.

[92] P. Weitzel. Steam generator for advanced ultra-supercritical power plants 700 to 760 °C. 2011.

[93] P. S. Weitzel, J. Tanzosh, B. Boring, N. Okita, T. Takahashi and N. Ishikawa. Advanced ultra-supercritical power plant (700 to 760 °C) design for indian coal. *Power-Gen Asia, Bangkok, Thailand*, 2012.

[94] C. K. Ho and B. D. Iverson. Review of high-temperature central receiver designs for concentrating solar power. *Renewable and Sustainable Energy Reviews*, 29: 835–846, 2014.

[95] S. J. Zinkle and G. S. Was. Materials challenges in nuclear energy. *Acta Materialia*, 61(3): 735–758, 2013.

[96] P. Sabharwall, S. M. Bragg-Sitton and C. Stoots. Challenges in the development of high temperature reactors. *Energy Conversion and Management*, 74: 574–581, 2013.

[97] H. Hnninen, A. Brederholm, I. Virkkunen, P. Aaltonen, U. Ehrnsten, H. Gripenberg, A. Toivonen and J. Pitkaenen. Dissimilar metal weld joints and their performance in nuclear power plant and oil refinery conditions. Report, VTT Technical Research Centre of Finland, Espoo (Finland), 2006.

[98] J. N. DuPont and R. E. Mizia. Review of dissimilar metal welding for the ngnp helical-coil steam generator. *Idaho National Laboratory, Idaho Falls, ID, Report No. INL/EXT-10-18459*, 2010.

[99] P. Scott, R. Olson, J. Bockbrader, M. Wilson, B. Gruen, R. Morbitzer, Y. Yang, C. Williams, F. Brust, L. Fredette *et al.* Battelle integrity of nuclear piping(binp) program final report. summary and implications of results. 2005.

[100] R. Klueh and J. King. Creep and creep rupture of ernicr-3 weld metal. *Journal of Nuclear Materials*, 98(1-2): 173–189, 1981.

[101] C. Brinkman, J. Strizak and J. King. Elevated temperature fatigue characterization of transition joint weld metal and heat affected zone in support of breeder steam generator development. *Fatigue testing of weldments*. ASTM International, 1978.

[102] P. Rami, H. Stefan and L. Hyeong-Yeon. Recommendation for creep and creep-fatigue assessment for P91 components. *International Journal of Fatigue*, 4.6, 2016.

[103] P. Booth, P. Budden, I. Bretherton, S. Bate and Holdsworth. Validation of the shakedown route in R5 for the assessment of creep fatigue crack initiation, 1997.

[104] H. S.R. Prediction of creep-fatigue behaviour at stress concentrations in 1crmov rotor steel. *Conference on Life Assessment and Life Extension of Engineering Plant, Structures and Components*, pages 137–146.

[105] W. Beere and J. Gittus. Cavities and cracks in creep and fatigue. *Mechanism maps. Applied Science Publisher, New York*, pages 29–57, 1981.

[106] R. Hales. The role of cavity growth mechanisms in determining creep-fatigue under multiaxial stresses. *Fatigue & Fracture of Engineering Materials & Structures*, 17(5): 579–591, 1994.

[107] J.-F. Wen, S.-T. Tu, F.-Z. Xuan, X.-W. Zhang and X.-L. Gao. Effects of stress level and stress state on creep ductility: Evaluation of different models. *Journal of Materials Science & Technology*, 2016.

[108] D. Barbera and H. Chen. Creep rupture assessment by a robust creep data interpolation using the linear matching method. *European Journal of Mechanics - A/Solids*, 54: 267–279, 2015.

[109] J.-F. Wen, S.-T. Tu, X.-L. Gao and J. Reddy. Simulations of creep crack growth in 316 stainless steel using a novel creep-damage model. *Engineering Fracture Mechanics*, 98: 169–184, 2013.

[110] J.-F. Wen and S.-T. Tu. A multiaxial creep-damage model for creep crack growth considering cavity growth and microcrack interaction. *Engineering Fracture Mechanics*, 123: 197–210, 2014.

[111] L. Binda, S. R. Holdsworth and E. Mazza. The exhaustion of creep ductility in 1crmov steel. *International Journal of Pressure Vessels and Piping*, 87(6): 319–325, 2010.

[112] S. Goyal, K. Laha and M. D. Mathew. Creep life prediction of modified 9Cr-1Mo steel under multiaxial state of stress. *Procedia Engineering*, 86: 150–157, 2014.

[113] N. Isobe, K. Yashirodai and K. Murata. Creep damage assessment considering stress multiaxiality for notched specimens of a crmov steel. *ICMFF10*.

[114] Y. Takahashi. Comparison of notched bar creep behavior of various alloys. *ASME 2010 Pressure Vessels and Piping Division/K-PVP Conference*, pages 485–491. American Society of Mechanical Engineers.

[115] S. Holdsworth. Creep-fatigue failure diagnosis. *Materials*, 8(11): 5418, 2015.

[116] A. Cocks and M. Ashby. Intergranular fracture during power-law creep under multiaxial stresses. *Metal science*, 14(8-9): 395–402, 1980.

[117] K. Hellan. An approximate study of void expansion by ductility or creep. *International Journal of Mechanical Sciences*, 17(5): 369–374, 1975.

[118] J. R. Rice and D. M. Tracey. On the ductile enlargement of voids in triaxial stress fields. *Journal of the Mechanics and Physics of Solids*, 17(3): 201–217, 1969.

[119] N. Isobe, K. Yashirodai and K. Murata. Creep damage assessment for notched bar specimens of a low alloy steel considering stress multiaxiality. *Engineering Fracture Mechanics*, 123: 211–222, 2014.

[120] C.-S. Oh, N.-H. Kim, Y.-J. Kim, C. Davies, K. Nikbin and D. Dean. Creep failure simulations of 316H at 550°C: Part i–a method and validation. *Engineering Fracture Mechanics*, 78(17): 2966–2977, 2011.

[121] S. Goyal, K. Laha, C. Das, S. Panneerselvi and M. Mathew. Effect of constraint on creep behavior of 9Cr-1Mo steel. *Metallurgical and Materials Transactions A*, 45(2): 619–632, 2014.

[122] K. Yoshida and M. Yatomi. Creep damage evaluation for HAZ of Mod. 9Cr-lMo steels under multi-axial stress conditions. *Procedia Engineering*, 10: 490–495, 2011.

[123] A. D. Bettinson. *The influence of constraint on the creep crack growth of 316H stainless steel*. Ph.D. thesis, Imperial College London (University of London), 2002.

[124] L. Allais, Q. Auzoux, M. Reytier and A. Pineau. Fissuration en relaxation des jonctions soudées en aciers inoxydables austénitiques. *Mécanique & industries*, 6(1): 45–54, 2005.

[125] E. Energy. *AGR Materials Data Handbook R66 Revision 9*. 2011.

[126] J. Tong, L. Zhao and B. Lin. Ratchetting strain as a driving force for fatigue crack growth. *International Journal of Fatigue*, 46: 49–57, 2013.

[127] J. Tong, B. Lin, Y.-W. Lu, K. Madi, Y. Tai, J. Yates and V. Doquet. Near-tip strain evolution under cyclic loading: In situ experimental observation and numerical modelling. *International Journal of Fatigue*, 71: 45–52, 2015.

[128] S. Holdsworth. Creep-fatigue crack growth from a stress concentration. *Materials at high temperatures*, 15(2): 111–116, 1998.

[129] J. Chaboche and G. Rousselier. On the plastic and viscoplastic constitutive equationspart i: Rules developed with internal variable concept. *Journal of Pressure Vessel Technology*, 105(2): 153–158, 1983.